Synthesis of Titanium Dioxide and Zinc Oxide Nanowires for Excitonic Solar Cells

A DISSERTATION SUBMITTED TO THE FACULTY OF THE GRADUATE SCHOOL OF THE UNIVERSITY OF MINNESOTA BY

Janice Elaine Boercker

IN PARTIAL FULFILLMENT OF THE REQUIREMENTS FOR THE DEGREE OF DOCTOR OF PHILOSOPHY

Eray S. Aydil

August, 2009

Acknowledgements

I would like to thank my family for all their support during my time in graduate school. They are always ready and willing to help me through the tough times and are my biggest fans. I am also grateful for all the friends I have made in Minnesota and for all their help and support. They give balance to my life and never cease to astonish me with their talent, wit and friendship.

I am also very thankful for my advisor, Eray Aydil. Not only did he teach me science, he taught me how to think about and approach problems and I will be able to use these lessons throughout my career. Eray has perfected the art of being an advisor. He always let me explore the ideas I found interesting and was there with encouragement and good ideas when I needed them. He is also a wonderful role model both professionally and personally and I hope to be able to follow his example.

I would also like to thank my Aydil Lab group members who have helped me with my research. I am particularly grateful for the help from Mike Behr, Emil Enache-Pommer, Kurtis Leschkies, Bin Liu, Seong Ho Jeong, and Ankur Khare. I also am extremely grateful to all the talented undergraduate students, Damien Brewer, Yasuhide Nakamura, Spencer Schaber and Jillian Schmidt who have worked tirelessly with me on characterizing the ZnO nanowire growth. I also thank Brook Timp for her help with the XPS experiments.

I am grateful to Prof. Norris, and Prof. Gladfelter and their research groups for their scientific and professional advice during my graduate school career.

I am thankful for the financial support from the Minnesota Initiative for Renewable Energy and the Environment (IREE), the National Science Foundation Integrative Graduate Education and Research Traineeship (IGERT) program, the National Science Foundation under the Nanoscale Interdisciplinary Research Team (NIRT) program and the University of Minnesota. Finally, this research made extensive use of the University of Minnesota Characterization Facility and I am grateful to the staff for all their help.

To My Family

Abstract

Dye-sensitized, quantum-dot sensitized, quantum-dot, and hybrid organic/inorganic solar cells are promising excitonic photovoltaic devices for the generation of low cost, carbon free energy. Wide-band gap semiconductor nanowire photoanodes have the potential to increase the efficiencies of these excitonic solar cells. Controlling and tailoring the dimensions of the nanowires (i.e. nanowire height, diameter, and planar number density) for each solar cell type is important for efficiency improvement. Obtaining such control will require a detailed and fundamental understanding of the nanowire growth process. Towards this end, the synthesis of TiO_2 and ZnO nanowire films in aqueous solutions was studied.

Anatase TiO_2 nanowire films were grown on flexible titanium foil substrates using a three step hydrothermal synthesis. First, the top surface of the titanium foil was transformed to $Na_2Ti_2O_4(OH)_2$ nanotubes through hydrothermal oxidation in NaOH. Next, the $Na_2Ti_2O_4(OH)_2$ nanotubes were converted to $H_2Ti_2O_4(OH)_2$ nanotubes by ion exchange. Finally, the $H_2Ti_2O_4(OH)_2$ nanotubes were converted to polycrystalline anatase nanowires through a topotactic transformation. The film morphology evolution, crystal structure transformations, and growth mechanism were examined in detail. Dye-sensitized solar cells (DSSCs) were assembled from these TiO_2 nanowire films. Transient photocurrent and photovoltage spectroscopies were used to measure the electron transport and recombination rates in these solar cells. Compared to TiO_2 nanoparticle DSSCs the electron collection efficiency in the TiO_2 nanowire DSSCs was increased due to decreased electron recombination. However, the electron transport in the nanowire DSSCs was similar to that of TiO_2 nanoparticle DSSCs.

The synthesis of ZnO nanowires from aqueous solutions of methenamine (HMT) and zinc nitrate hexahydrate on substrates was studied in detail. A ZnO nanowire growth mechanism was proposed which predicts that the precursor is a zinc-methenamine complex (Zn-HMT^{2+} and Zn-HMT-Zn^{4+}) which reacts at the hydroxyl terminated nanowire surface. This growth mechanism was supported by examining the growth with several experimental techniques, kinetic modeling, and thermodynamic calculations. In addition, the ZnO nanowire film growth, on ZnO seeded substrates, was found to be mass

transport limited. This results in an inverse relationship between the nanowire planar number density and the height and diameter of the nanowires. By stirring the solution the growth rate is increased by approximately a factor of four.

TABLE OF CONTENTS

LIST OF FIGURES

LIST OF TABLES

Chapter 1 : Introduction

1.1 The Energy Problem

Humankind is facing a serious energy crisis. The Intergovernmental Panel on Climate Change (IPCC) predicts that the global energy need will increase by almost a factor of five over the next century, from 10 TW to near 46 TW by 2100.[1] The IPCC also predicts that burning fossil fuels alone will not be able to meet this requirement and, in order to meet global energy needs, at least 10 TW, will have be provided from alternative energy sources by 2050.[1] In addition, the burning of fossil fuels releases almost 7 Gt of carbon dioxide into the atmosphere each year.[1] Carbon dioxide is a greenhouse gas and has been linked to global temperature rise through detailed analysis of the CO_2 content in air pockets trapped in ice cores obtained by drilling in Antarctica and Greenland.[2] Atmospheric CO_2 has increased by 30% from 280 to 370 ppm by volume since the beginning of the 20^{th} century and the industrial revolution. This increase is thought to be a result of 160 billion tons of CO_2 released in to the atmosphere.[3] This is the same increase in CO_2 that naturally occurred starting approximately 110,000 year ago and was partially responsible for a 6 $^{\circ}$C temperature increase and the end of the last ice age. During the last 100 years, we have introduced, into the atmosphere, the amount of CO_2 that took the earth thousands of years to produce through natural means.[3] If this amount of CO_2 helped to end an ice age, similar dramatic changes may occur as a result of anthropogenic CO_2 increases with potentially negative consequences for life on earth. One of the predicted consequences of anthropogenic CO_2 increase is an average global temperature rise of almost 6 °C by 2100. Such a dramatic rise would cause thermal expansion of the oceans as well melting of the polar ice caps, resulting in floods and storms that would contaminate drinking water and cause a very serious and global health and safety crisis.[3] The energy crisis facing humankind has the potential for disastrous consequences and solutions need to be pursued with a great sense of urgency.[1]

In order to combat this impending energy crisis, and the catastrophic consequences of global warming, carbon-free alternative energy sources will need to be

used to meet the ever increasing global energy demand. The United States Department of Energy (DOE) is considering a variety of alternative energy sources as a potential solution to the energy problem. The increasing energy demand will probably be met with a combination of bio-energy, nuclear energy, hydroelectric power, hydrogen, solar power, geothermal power, natural gas and wind power.[4]

Direct solar-to-electrical energy conversion using solar cells is one of potential ways to meet the global energy demand without CO_2 emissions because the average power provided by the sun is very large, ~$9x10^{16}$ watts. In fact, averaged over one year, the sun provides almost 10,000 times more power than the current global demand of 10 TW; if just 0.1% of the earth was covered by 10% efficient solar cells all of the current global energy demand could be supplied using solar power. In addition, solar cells are very versatile and can be placed almost anywhere, including roofs, sides of buildings, etc. The barrier to wide-spread use of solar cells is their high cost. Figure 1.1 shows a graph of the cost per kw-hr of electricity from various energy sources. Solar energy is an order of magnitude more expensive than energy obtained from other sources, which makes wide-spread implementation of solar cells with the current technology impractical. Inexpensive solar cells need to be developed in order for solar energy to become a viable economical alternative to burning fossil fuels.

1.2 Excitonic Solar Cells

Excitonic solar cells (XSC) have been studied since the 1950s.[5] Recently, they have been getting much more attention and have emerged as a promising inexpensive solar cell type. The operation of XSCs is fundamentally different than that of conventional silicon solar cells and this difference allows XSCs to be potentially less expensive than conventional solar cells. In conventional silicon solar cells based on the p-n junction, the key steps for solar-to-electric energy conversion, light absorption, charge generation, charge separation and charge transport all take place in the same material. Consequently, these conventional solar cells operate as *minority*-carrier devices with an *electrical potential difference* across the p-n junction driving the carrier transport. In a minority-carrier photovoltaic device electrons travel through hole rich regions of the cell and holes travel through electron rich regions. In contrast, in XSCs, the key solar-to-

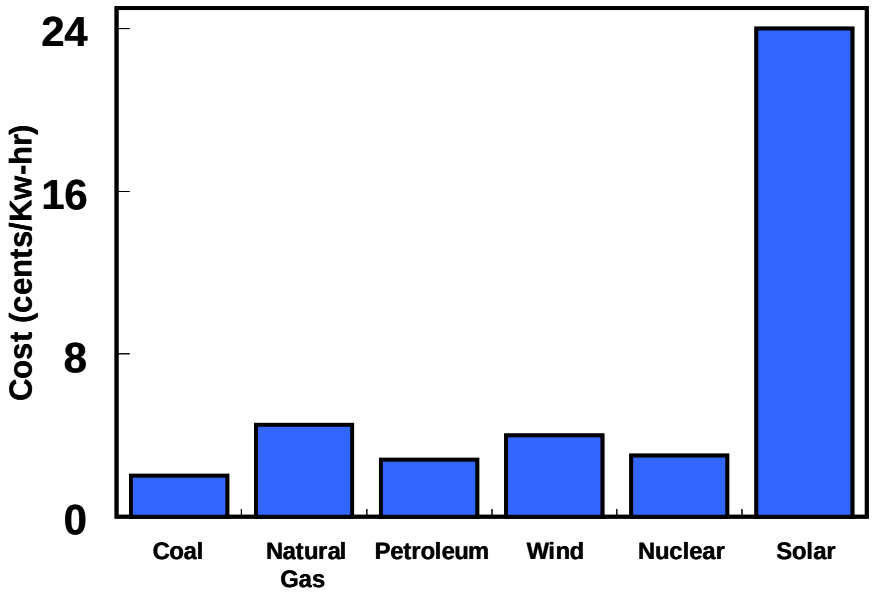

Figure 1.1 Approximate electricity production cost from various energy sources. Electricity from solar energy costs an order of magnitude more than the other methods.[6-10]

electric energy processes are separated into the different materials that comprise the solar cell. This separation of the key steps into different materials allows the cell to operate as a *majority*-carrier device. A majority-carrier photovoltaic device is the opposite of a minority-carrier device, the electrons transport through electron rich materials and the holes transport through hole rich materials. In XSCs, a *chemical potential difference* across the cell is the main driving force for charge separation that leads to the photovoltaic effect.

To allow minority carrier transport without significant recombination, conventional solar cells must be made from materials which must be crystalline, pure and defect free over large length scales. The production of such materials requires expensive fabrication techniques and often involves vacuum equipment and/or high temperatures. The need for very high quality materials makes conventional solar cells expensive to produce. In contrast, charge carriers in XSCs are majority carriers, and the materials for these cells do not have to be as defect-free and as pure as conventional solar cell materials. Thus, XSCs can be made with less expensive materials that can be synthesized using inexpensive methods, including liquid solution crystallization and growth techniques. In addition, XSCs can be made on flexible substrates, a strategy that can potentially reduce manufacturing costs by allowing roll-to-roll processing. The unique operating principles of XCS allow the use of inexpensive materials and manufacturing techniques for economically viable energy production without significant CO_2 emission.

Nanowires of wide band gap semiconductors such as TiO_2 and ZnO find applications in a variety of XCSs as the electron acceptor and conductor. Reasons for preferring TiO_2 and ZnO nanowires in XCSs over other semiconductors will be discussed in Chapter 2 but their main promise rests on their potential to increase the overall power conversion efficiency of these solar cells by providing a high interfacial area for light absorption and charge separation as well as faster electron transport for conduction. However, effective use of nanowires in XCSs require the ability to *control and tailor* their dimensions and morphology (i.e., height, diameter, spacing and planar density). Obtaining such control in turn requires a detailed and fundamental understanding of the nanowire growth process. In addition, an understanding of the nanowire growth will also

allow the nanowire *yield* as well as the *growth rate* to be increased which will help lower the cost of incorporating nanowires into XSCs. With these objectives in mind, this thesis focuses on developing an in depth understanding of the TiO_2 and ZnO nanowire growth on various substrates using liquid solution growth methods.

1.3 Research Goals and Accomplishments in Brief

The goals of my thesis project were to study the growth of TiO_2 and ZnO nanowires in order to obtain a fundamental understanding of the growth process, and to use this understanding in assembling nanowire-based dye-sensitized solar cells. To this end, a novel TiO_2 nanowire hydrothermal synthesis method was developed and the growth mechanism was characterized in detail. The TiO_2 nanowires synthesized using this method were incorporated into one of the first TiO_2 nanowire dye-sensitized solar cells. Also, a well-known, widely-used but poorly understood hydrothermal technique for growing ZnO nanowires was studied in unprecedented detail and a growth mechanism that is consistent with experimental observations was proposed.

1.4 Organization of this Thesis

Chapter 2 establishes the background necessary to understand the motivation for and findings of this thesis project. Specifically, in Chapter 2, I discuss the various types of XSCs, and why nanowires with *controlled and tailored* dimensions can potentially increase the efficiency of XSCs.

Chapter 3 describes the hydrothermal growth of TiO_2 nanowire films in an alkaline solution on titanium foil and their incorporation into nanowire DSSCS. I describe, in detail, the evolution of the film morphology, crystal structure transformations and growth mechanism.

Chapter 4 introduces the solution growth of ZnO nanowires from zinc nitrate hexahydrate and methenamine and presents the various ZnO seeding methods I have explored for the growth of uniform nanowire films. The various seeding methods are compared and the best method for uniform films of aligned ZnO nanowires is highlighted.

Chapter 5 focuses on the growth of ZnO nanowires from an aqueous solution of zinc nitrate hexahydrate and methenamine. A possible growth mechanism is proposed and corroborated with several analytical chemistry techniques as well as thermodynamic reaction equilibrium calculations.

Chapter 6 describes our discovery that ZnO nanowires in aqueous solutions of zinc nitrate and methenamine is mass transport limited. Models of the solution phase species transport and nanowire growth are developed and used to interpret the experimental results. The effect of stirring the solution is also discussed.

Chapter 7 presents a summary of the research in the previous chapters and suggests some possible future research directions.

References

(1) Hoffert, M. I.; Caldeira, K.; Jain, A. K.; Haites, E. F.; Harvey, L. D. D.; Potter, S. D.; Schlesinger, M. E.; Schneider, S. H.; Watts, R. G.; Wigley, T. M. L.; Wuebbles, D. J. *Nature* **1998**, *395*, 881.

(2) Petit, J. R.; Jouzel, J.; Raynaud, D.; Barkov, N. I.; Barnola, J. M.; Basile, I.; Benders, M.; Chappellaz, J.; Davis, M.; Delaygue, G.; Delmotte, M.; Kotlyakov, V. M.; Legrand, M.; Lipenkov, V. Y.; Lorius, C.; Pepin, L.; Ritz, C.; Saltzman, E.; Stievenard, M. *Nature* **1999**, *399*, 429.

(3) Maslin, M. *Global warming: a very short introduction*; Oxford University Press: New York, 2004.

(4) DOE; http://www.energy.gov/energysources/index.htm: July 23, 2009.

(5) Gregg, B. A. *J. Phys. Chem. B* **2003**, *107*, 4688.

(6) PBS; http://www.pbs.org/now/science/coal.html: July 23, 2009.

(7) DOE; http://www.eia.doe.gov/cneaf/electricity/epm/table4_1.html: July 23, 2009.

(8) DOE; http://www1.eere.energy.gov/windandhydro/pdfs/43025.pdf: Jul 23, 2009.

(9) http://nuclearinfo.net/Nuclearpower/WebHomeCostOfNuclearPower: July 23, 2009.

(10) EDN; http://www.edn.com/article/CA6432171.html: July 23, 2009.

Chapter 2 : Background on Excitonic Solar Cells

2.1 Operation of Excitonic Solar Cells

Excitonic solar cells (XSC) can be categorized into five types; organic solar cells (OSC), hybrid organic/inorganic solar cells (HSC), quantum dot solar cells (QDSC), quantum dot sensitized solar cells (QDSSC), and dye sensitized solar cells (DSSC). In this section the architecture and operation of these cells are discussed in detail.

2.1.1 Organic Solar Cells

The photoactive layer in an organic solar cell (OSC) consists of a heterojunction between two organic semiconductor films each ~100-500 nm thick.[1] One of the semiconductors easily accepts electrons and is called the "acceptor" (A), while the other easily donates electrons and is called the "donor" (D). For example, P3HT (poly(3-hexylthiophene)) is a conjugated hole conducting polymer that is commonly used as the donor material because its semicrystalline lamellar structure leads to higher hole mobilities than other conjugated polymers.[2] The C_{60} derivative, PCBM, ((6,6)-phenyl C_{61}-butyric acid methyl ester), is a commonly used acceptor material because of its high electron mobility and excellent electron accepting properties.[3] Figure 2.1 shows the energy band diagram and a schematic of a planar OSC based on a heterojunction between thin P3HT and PCBM layers. The donor and acceptor materials must be carefully selected such that their energy bands form a type II alignment (i.e., the electron affinity of the acceptor must be larger than the electron affinity of the donor, and the ionization potential of the donor must be less than the ionization potential of the acceptor) to favor electron and hole separation at the interface between them. Typically a transparent conducting oxide (TCO) such as indium tin oxide (ITO) is used as a contact to the donor and a low work function metal such as Al or Ca is used as a contact to the acceptor.[4] In general, contact electrodes are selected such that the work function of the donor contact is lower than the HOMO of the donor, and the work function of the acceptor contact is higher than the LUMO of the acceptor.[5]

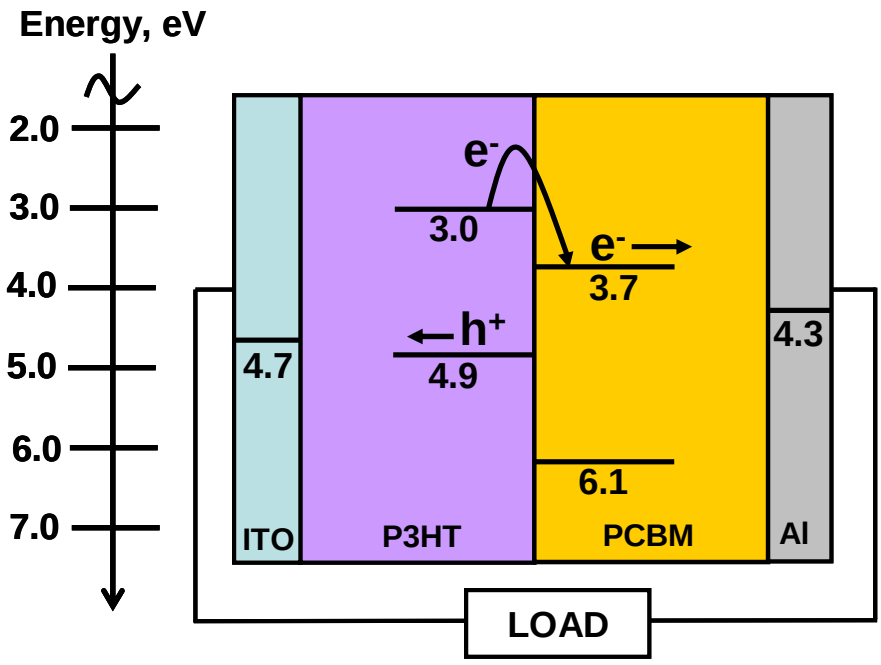

Figure 2.1 Schematic of a planar organic solar cell containing P3HT and PCBM. P3HT acts as the donor and PCBM acts as the acceptor. Energy levels are with respect to vacuum.

Conversion of photons to electrical current in an organic semiconductor takes place in four steps. First, a photon incident onto the cell is absorbed by one of the photoactive layers which creates an exciton (i.e., a bound electron-hole pair), within one of the organic layers. In organic materials the exciton binding energy is typically greater than in semiconductors and the available thermal energy, k_bT, at room temperature. Thus, unlike excitons in typical inorganic semiconductors, the excitons in organic semiconductors do not immediately dissociate. In the example shown in Figure 2.1, both P3HT and PCBM can absorb photons, but most of the light is absorbed by P3HT in the P3HT/PCBM cell, due to better absorption overlap with the solar spectrum.[1,5] In the second step, the exciton diffuses to the interface between the donor and the acceptor (D-A interface). In the third step, the exciton dissociates rapidly at the D-A interface on a sub-picosecond time scale.[6] Electrons are injected into the acceptor and the hole remains behind in the donor. This process separates the electrons from the holes and generates charge carriers that if collected can create photocurrent in an external circuit. This sequence of events differs from those that generate photocurrent in a conventional p-n junction solar cell, where electrons and holes are photogenerated and separated throughout the *bulk* of the material as opposed to at an interface. Lastly, the electrons in the acceptor and the holes in the donor are transported via drift and diffusion to the anode and the cathode, respectively. The electrons flow though the external load, on which they do work, and then to the donor contact to complete the circuit. The driving force for carrier transport in OSCs is the chemical potential difference between the D-A interface and the contacts. This chemical potential difference is due to the higher electron and hole concentrations near the D-A interface relative to the rest of the cell.[7]

The first donor-acceptor OSCs had flat interfaces and had efficiencies of only ~0.04%.[8] The main issue limiting these cells was the mismatch between the exciton diffusion and light absorption length scales. The exciton diffusion length in typical organic materials is 4-20 nm but the optical absorption depth is much larger, ~100 nm.[1] This meant that while excitons could be created throughout the cell only those within the exciton diffusion length (4-20 nm) from the interface could be harvested. Many of the photogenerated excitons would recombine before ever encountering the D-A interface to

dissociate. This limitation was coined the "exciton diffusion bottleneck."[9] In 1995, Yu et al.[10] and Halls et al.[11] overcame this issue at about the same time by blending two organic materials that separated on the nanometer length scale to form two interpenetrating bicontinuous phases. This created a nanostructured morphology where the distance at any point in the active layer of the cell was within an exciton diffusion length away from the D-A interface. Moreover, the interpenetrating bicontinuous morphology provided an interpenetrating donor and acceptor network that connected any point in the material to either of the contacts. This intimate mixing of the two phases created a very large area D-A heterojunction throughout the whole active layer so that and the resulting solar cell is referred to as a bulk heterojunction (BHJ) solar sell. The first BHJ solar cells had efficiencies of ~1%.[10] However, improvements in the device morphology as well as the donor and acceptor materials lead to organic BHJ solar cell efficiencies as high as 5.5 %.[1,12] In addition, recently Kim et al. have made a organic tandem cell with an efficiency of 6.5%.[12] It has been predicted that OSCs could have efficiencies as high as 10-20% if (i) the cell morphology can be improved further, (ii) conjugated polymers with higher carrier mobilities, lower band gaps and wider bandwidths can be synthesized and (iii) the energy level offset between the donor and the acceptor can be minimized to reduce energy loss, while still allowing for electron transfer.[1]

2.1.2 Hybrid Excitonic Solar cells

Organic-inorganic hybrid excitonic solar cells (HSCs) have a similar architecture as OSCs except that the acceptor is replaced with an inorganic semiconductor. The HSC combines the advantages of organic and inorganic materials; specifically, the HSC combines the high electron mobility of inorganic materials with the processability and low cost of organic materials. The electron mobility of the organic materials used in OSCs is typically between ~10^{-9} and 10^{-4} cm^2 V^{-1} s^{-1} and depends on the molecular structure, morphology and the degree of crystallization.[1] In contrast for example, the electron mobility of ZnO films can be as high as ~100 cm^2 V^{-1} S^{-1} and the electron mobility of ZnO nanowires grown from aqueous solutions has been reported to be 1-5 cm^2 V^{-1} S^{-1}.[13,14] In addition, incorporating nanostructured inorganic semiconductor films as the electron acceptor increases the donor-acceptor interface,[15] makes the cells more

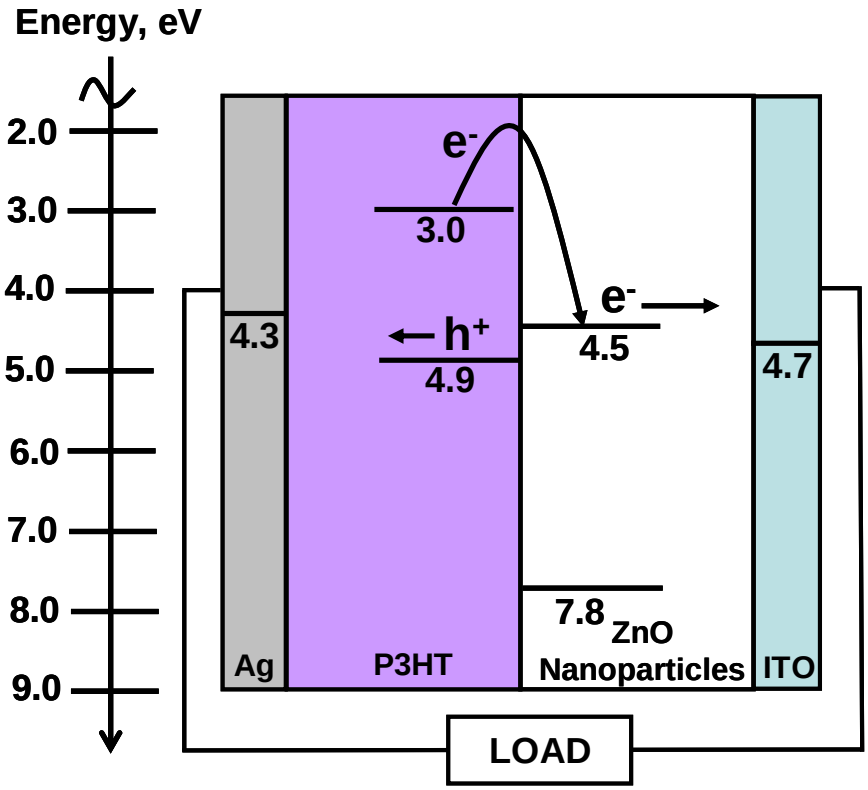

Figure 2.2 Schematic of a hybrid solar cell containing P3HT and ZnO nanoparticles. The P3HT acts as the donor and ZnO acts as the acceptor. Energy levels are with respect to vacuum.

morphologically stable,[16] increases visible light absorption (if the semiconductor band gap is in the visible region),[17] lowers costs, increases cell lifetime, and allows for more stabile high work function counter electrodes.[15]

HSCs convert sunlight to electricity like OSCs do except that the acceptor is an inorganic semiconductor and is usually deposited on the TCO.[15] Figure 2.2 shows a schematic and energy band diagram of a HSC made from ZnO nanoparticles and P3HT. For clarity, the band diagram in Figure 2.2 shows the ZnO nanoparticles and P3HT as if the junction is planar and formed between two separate layers. However, in HSCs the donor and the acceptor materials are intermixed with the P3HT interpenetrating the ZnO nanoparticles and the ZnO nanoparticles forming a continuous percolated network. Thus, both the inorganic nanoparticles and P3HT form continuous pathways to the TCO and top metal contact, respectively. Similar to OSC, the energy levels of the organic and inorganic materials must be carefully chosen to form a type II heterojunction.

The first HSC was made from a blend of CdSe nanoparticles and the conjugate polymer poly(2-methoxy,5-(2'-ethyl)-hexyloxy-p-phenylenevinylene) (MEH-PPV). This HSC had an overall power conversion efficiency of only 0.1% due to the poor electron transport through the CdSe particles.[17] The efficiency of CdSe HSCs has been increased to ~1.8% by using nanorods[18] and three dimensional CdSe tetrapods[19] as the electron conducting material. The elongated nanorods and branched tetrapods increase the electron transport and, consequently, the overall efficiency. To date, HSCs have been made with several different semiconductors[20] such as $CuInS_2$,[21] Nb_2O_5,[22] PbS,[23] and PbSe.[24] However, the overall power conversion efficiency of these cells are all less than 0.2%.

The most commonly employed inorganic acceptors in HSCs have been TiO_2 and ZnO. They are preferred over other semiconductors like CdSe and PbSe because they are abundant, non toxic and easily synthesized.[25,26] Moreover, many different types of molecules can be attached to a TiO_2 surface without degradation because TiO_2 is a very stable oxide.[1] HSCs made with ZnO nanoparticles have achieved efficiencies as high as 2.4%,[20,27] while HSCs made from TiO_2 nanoparticles have reached efficiencies of

0.42%.[28] One of the issues limiting the efficiency of both the ZnO and TiO_2 nanoparticle HSCs is the low charge carrier mobilities.[28]

2.1.3 Quantum Dot Solar Cells

When the size of a nanocrystal is smaller than the Bohr radii of charge carriers,[29] the electronic energy levels within the nanoparticles become size dependent due to quantum confinement. For this reason, nanocrystals are also known as quantum dots (QDs). Because of their unique photophysical properties, quantum dots are attractive for a variety of applications such as bioimaging, lasers and solar cells.[30] Quantum dots are particularly attractive for solar cells for two reasons. First, due to quantum confinement, the band gap of the nanocrystal can be tuned by changing their size; the effective band gap of a semiconductor nanocrystal increases with decreasing size as the carriers are more confined. This allows the optical absorption of the quantum dots to be matched to the solar spectrum for optimal energy conversion. Second, it has been shown that in quantum dots multiple excitons can be generated from one photon.[31,32] This could potentially lead to higher photocurrents and efficiencies greater than the Shockley-Queissier limit.[33-35]

Quantum dot solar cells (QDSCs) have been made from several different types of semiconductors such as CdTe,[36] CdSe,[36] Cu_2S,[37] PbSe,[38,39] and PbS.[40] Figure 2.3 shows schematics and energy band diagrams of the three different types of QDSCs realized so far. The first architecture shown in Figure 2.3a has been developed by Alivisatos et al.[36] and is similar to OSCs in that it consists of a D-A heterojunction. However, in this cell the D-A interface is made between films of CdTe and CdSe nanorods. The band gaps and electron affinities of CdTe and CdSe are such that a type II heterojunction forms and the CdTe film acts as the electron donor while the CdSe film acts as the electron acceptor. The CdTe and CdSe nanorod films were deposited sequentially to form a bilayer device. These cells had efficiencies of ~3% and were claimed to work as follows. Incident light generates excitons in both the CdTe and CdSe films and these excitons dissociate and create free carriers throughout each layer not just at the interface as in OSCs and HSCs. Excitons can dissociate within each nanorod because the quantum confinement is weaker

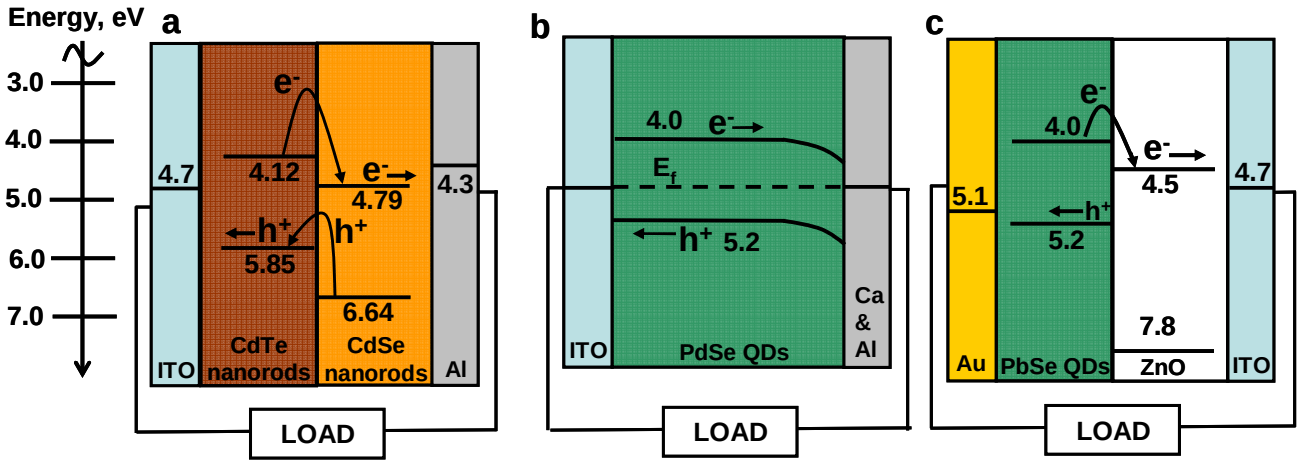

Figure 2.3 Schematics of quantum dot solar cells composed of (a) layers of CdTe and CdSe nanorods[36] (b) PbSe nanocrystals[38] and (c) PbSe nanocyrstals on a ZnO film.[39] Energy levels are with respect to vacuum.

along the length of the nanorods. The free carriers created near the junction between the CdTe and CdSe nanorod films experience an energetic driving force from the type II heterojunction to separate; the holes migrate to the CdTe and the electrons to the CdSe. Once separated, the holes are transported through the CdTe to the ITO contact and the electrons are transported through the CdSe to the top metal contact. As in OSCs the driving force for carrier transport is the chemical potential difference due to the higher carrier concentrations at the interface as well as the potential driving force due to the differences in work functions of the electrodes. Alivisatos et al. have also made a similar cell with less toxic Cu_2S nanocrystals and CdSe nanorods and have achieved a power conversion efficiency of 1.6%.[37]

An alternative QDSC architecture is fashioned after Schottky-type solar cells (Figure 2.3b) and consists of a thin film of semiconductor quantum dots sandwiched between an indium tin oxide and an evaporated metal contact. This type of QDSC has been realized using PbSe[38] as well as PbS quantum dots.[40] The record efficiency for this type of solar cells is 2.1%.[38] The operation principle of this QDSC is similar to that of a conventional Schottky-type solar cell. A Schottky barrier forms between the p-type nanocrystals and the metal contact and a field develops within the depletion region at the interface between the PbSe nanocrystal and the metal contact. This field separates the excitons and free carriers photogenerated within the depletion layer, the electrons are driven to the top metal contact and the holes to the indium tin oxide.

The third type of QDSC has only very recently been developed (Figure 2.3c) and consists of a film of PbSe quantum dots sandwiched between a ZnO film and an evaporated metal contact.[39] The authors argue that these cells are like excitonic solar cells and have achieved an efficiency of 1.6%.[39] In this type of solar cell, the donor PbSe quantum dots absorb the light while ZnO acts as the as the acceptor. The details of what happens after a photon generates an exciton in the PbSe quantum dot film is unclear and still under investigation.[39] The photogenerated excitons could do one of three things (1) recombine, (2) dissociate within the film or (3) diffuse to the interface as an exciton and then dissociate.[39] If the excitons dissociate within the film the free electrons and holes carriers may diffuse or drift to the opposite electrodes under the influence of the electric

field generated by the difference in work functions of the counter electrodes.[39] If the exciton dissociates at the ZnO-PbSe nanocrystal interface then the electron will inject into the ZnO because sufficiently small PbSe quantum dots and ZnO form a type II heterojunction. This electron would then transport through the ZnO to the anode. The hole will remain in the PbSe and drift and diffuse to the cathode.[39] The driving forces for carrier transport in this cell are probably similar to other excitonic solar cells, a combination of the chemical potential gradient from the charge separation at the ZnO/PbSe interface and the potential difference between the contacts.

2.1.4 Dye Sensitized Solar Cells

The dye sensitized solar cell (DSSC) is the most efficient excitonic solar cell with laboratory power conversion efficiencies over 11%.[41] DSSCs are currently being commercialized by several companies around the world; these companies include Dyesol in Australia, 3Gsolar in Israel, and G24 Innovations in Wales. A schematic of the DSSC and the energy levels of the cell's components are shown in Figure 2.4. The DSSC is composed of three main components: (1) a 2-20 μm thick, porous, wide band gap semiconductor film (typically TiO_2 or ZnO) composed of crystalline nanoparticles abutting one another, (2) a monolayer of dye adsorbed onto these nanocrystals, and (3) a liquid electrolyte interpenetrating the nanocrystalline semiconductor network. This arrangement creates the large area semiconductor-dye-electrolyte interface needed for cell operation. (Again, for clarity, the band diagram in Figure 2.4 shows the complicated three dimensional semiconductor-dye-electrolyte interface as a planar trilayer.) The nanoparticle film is referred to as the photoanaode as is deposited on a TCO substrate. A platinized counter electrode spaced 10-50 μm from the nanoparticle film forms the cathode. The semiconductor nanoparticles and the liquid electrolyte form continuous pathways to the anode and cathode, respectively.

Solar radiation excites electrons in the dye from the highest occupied molecular orbital (HOMO) to the lowest unoccupied molecular orbital (LUMO). Electrons excited to the LUMO levels are injected into the semiconductor nanocrystals and travel through the semiconductor to the photoanode and then through the load to the cathode where they

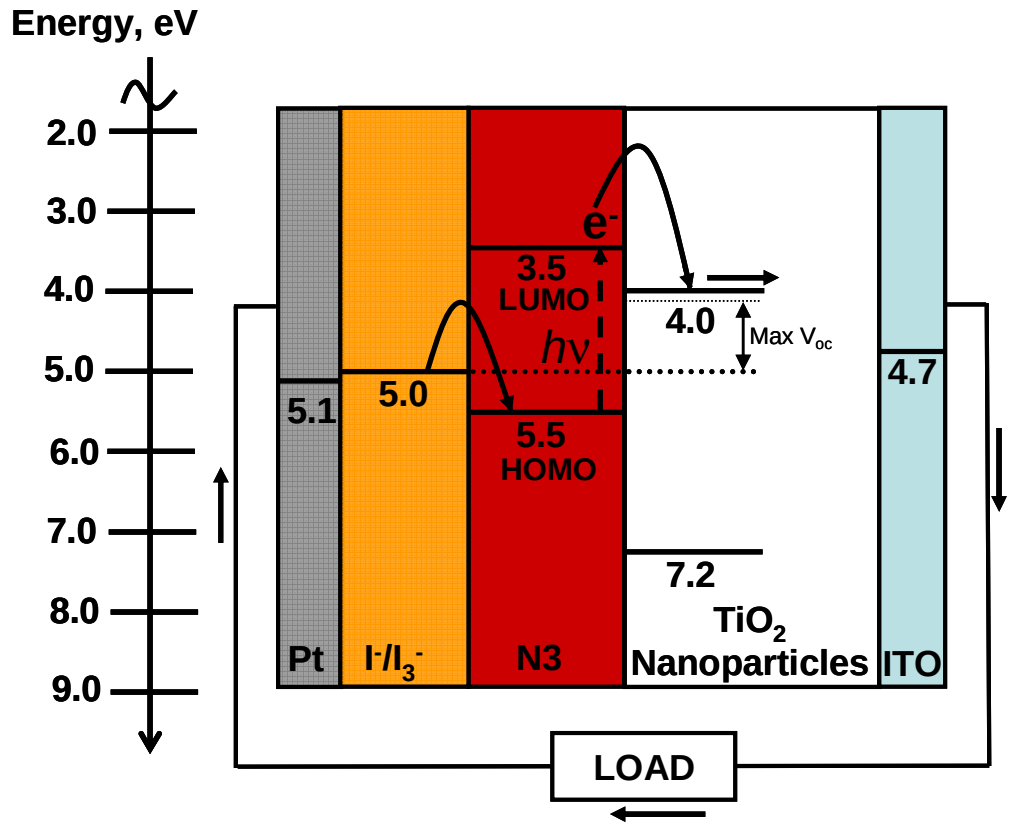

Figure 2.4 Schematic of a dye sensitized solar cell composed of TiO_2 nanoparticles, N3 organometallic dye (Solaronix) and a liquid electrolyte containing the redox pair iodide/triiodide . The dashed arrow represents the dye absorbing a photon and promoting an electron from the HOMO level to the LUMO level. The solid arrows represent the path of the electron during cell operation. The maximum possible open circuit voltage, V_{oc}, is the potential between the redox level of the electrolyte and the quasi-Fermi level in the semiconductor under illumination. Energy levels are with respect to vacuum.

reduce the oxidant in the electrolyte (typically I_3^- of the I^-/I_3^- couple). A thin platinum or carbon layer catalyzes the electrochemical reduction. The reductant (e.g., I^-) completes the circuit by reducing the photooxidized dye. As shown in Figure 2.4 the maximum open circuit voltage, which is the potential at which no current flows through the cell, is the difference between the energy of the quasi-Fermi level in the semiconductor under illumination and the electrochemical potential of the redox mediator. The driving force for the carrier transport through the nanoparticle film and electrolyte is the chemical potential difference created across the cell, which is due to the build up of carriers at the dye-semiconductor-electrolyte interface. Because the nanoparticles are smaller than the Debye length in the semiconductor and the electrolyte has high ionic strength, the electric fields within the nanoparticles are very effectively screened and charge transport in the nanoparticle network is thought to be diffusive.[7]

Research on DSSCs started in the early 1970's,[7,42-44] however efficiencies were <1% until Grätzel and O'Regan's breakthrough work in 1991,[45] when they changed the morphology of the wide band gap semiconductor from a smooth surface to a TiO_2 nanoparticle film. This was the key to a substantial efficiency increase since it provided the large surface area needed for enough dye to be adsorbed such that the nearly 100% of the light at the dye's absorption maximum could be absorbed. Grätzel and O'Regan's first nanoparticle DSSC had a power conversion efficiency of ~8%[45] and has since increased to ~11%[41] largely due to the improvements in dye optical density in the red region of the electromagnetic spectrum,[46] optimization of the TiO_2 photoanode processing parameters,[47] and better optical engineering by addition of light scattering layers.[48-50] DSSC photoanodes have also been made with other semiconductors besides TiO_2, including, ZnO,[51] SnO_2,[52] Nb_2O_5,[53] $SrTiO_3$[54] and Zn_2SnO_4[55] nanoparticles as well as core shell nanostructures such as TiO_2 coated nanoporous SnO_2.[56] TiO_2 nanoparticle DSSCs are the most efficient by far at over 11%.[41] ZnO nanoparticle DSSCs are the second most efficient nanoparticle based DSSC with efficiencies of ~6.5%.[51] While these efficiencies are substantial, there is the potential for further improvement as will be discussed below.

2.1.5 Quantum Dot Sensitized Solar Cells

Another type of excitonic solar cell which incorporates quantum dots as the light absorber is the quantum dot sensitized solar cell (QDSSC). The QDSSC has a similar architecture to the DSSC except that a quantum dot acts as the light absorber instead of an organic dye. One could argue that the QDSSC was modeled after the DSSC.[57] Figure 2.5 shows the schematic of a typical QDSSC and its energy level diagram. In this example, the QDSSC is made from TiO_2 nanoparticles and CdS quantum dots, interpenetrated with an iodide/triiodide electrolyte. Although the schematic shows the TiO_2 nanoparticles, CdS quantum dots and electrolyte as a trilayer, in the actual QDSSC the nanoparticles are blended together to form the photoanode and the electrolyte penetrates the pores of the resulting film to form a three dimensional TiO_2-CdS-electrolyte interface network. As in the DSSC, the TiO_2 nanoparticles and the liquid electrolyte form continuous conduction layers to the anode and cathode, respectively. The operating principle of the QDSSC is similar to that of DSSCs. Excitons are generated upon light absorption by the quantum dots. If the exciton recombination is slow compared to electron injection time scale, the electron will be transferred to the wide band gap semiconductor. The hole remaining behind in the quantum dot will be reduced through an electrochemical reaction with the reductant in the electrolyte. The electrons injected into the semiconductor flow to the contact at the anode, through the load and to the cathode where they reduce the oxidant in the electrolyte to complete the circuit. The driving force for carrier transport in the wide band gap semiconductor is the chemical potential difference created across the film as electrons are injected across the quantum-dot-semiconductor interface. Similarly, the oxidant and the reductant shuttle charge across the electrolyte via diffusion. There is no field to drive the transport because, as mentioned previously, electric fields can not be sustained in the semiconductor nanoparticles or in liquid electrolyte, except in few angstroms thick space charge layers near solid surfaces.[7]

QDSSC have been made with several different types of semiconductor quantum dots, wide band gap semiconductors and electrolytes. For example, QDSSC have been

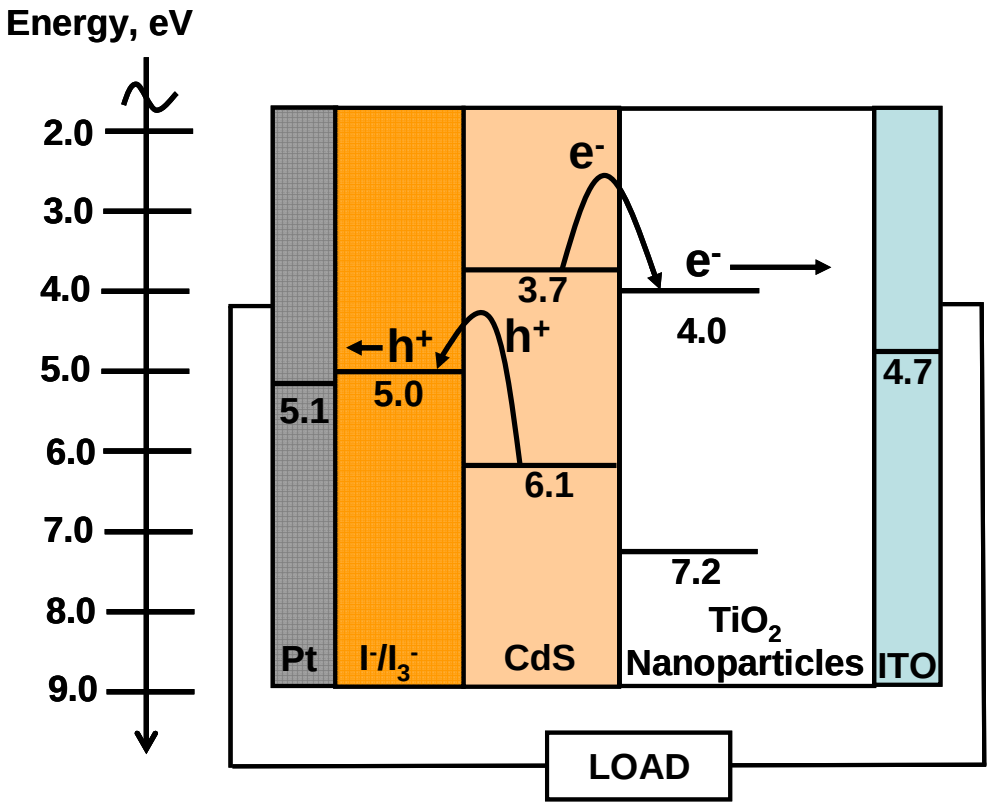

Figure 2.5 Schematic of a quantum dot sensitized solar cell consisting of TiO_2 and CdS nanoparticles and a liquid electrolyte containing the redox pair iodide/triiodide. The electrolyte interpenetrates the intermixed TiO_2 and CdS nanoparticles. Energy levels are with respect to vacuum.

made using PbS,[58] CdS,[58,59] CdSe,[59] InAs,[60] InP,[61] Ag_2S,[58] Sb_2S_3[58] and Bi_2S_3[58] quantum dots on TiO_2 nanoparticles using polysulfide,[58,59] cobalt,[60] ferricyanide,[62] and iodine[61] electrolytes. QDSSC have also been made with ZnO, SnO_2, Nb_2O_5 and Ta_2O_5 nanoparticles as the acceptor.[58] Some of the highest QDSC power conversion efficiencies are ~3% and have been realized using CdSe quantum dots on porous ordered TiO_2 inverse opal films[63] and CdSe/CdS quantum dots on TiO_2 nanoparticles.[59]

2.2 Nanowires for Excitonic Solar Cells

Replacing the wide band gap semiconductor nanoparticle photoanode in XSCs with nanowires can potentially improve the solar cell performance. Nanowires increase the electron collection efficiency (i.e., the fraction of electrons injected into the semiconductor which flow through the load.)[64-67] This increases the XSCs efficiency by allowing thicker semiconductor films covered with more light absorbing material to be utilized. Furthermore, for HSCs and QDCS nanowires allow light absorption and exciton dissociation to be independently optimized thus increasing the overall efficiency.[1]

2.2.1 Nanowires for Hybrid Excitonic Solar Cells

Eliminating the exciton diffusion bottleneck[68] and increasing charge transport[1,15] are two issues which must be addressed to improve the present HSCs. These are the same issues that limit OSCs. The exciton diffusion bottleneck exists because the absorption length of a typical conjugated polymer is on the order of ~100 nm while the exciton diffusion length is on the order of 4-20 nm.[1] Thus, only those excitons generated within a diffusion length away from the D-A interface will dissociate to create charge carriers. Therefore, for planar HSCs, there is a trade off between making the film thick enough to absorb more of the light and thin enough to collect and dissociate the majority of the excitons generated upon light absorption. This trade off limits the thickness of the organic layer and hence the overall efficiency. In addition, once the excitons successfully diffuse to the interface and dissociate the charge transport through the donor and the acceptor must be faster than recombination in order to obtain high photon to current collection efficiencies. Recombination refers to an electron in the acceptor recombining with a hole in the donor without flowing though the load.

One strategy for eliminating the exciton diffusion bottleneck is to decouple the absorption and exciton diffusion lengths into two orthogonal directions within the solar cell. This can be achieved by growing the inorganic semiconductor as a nanowire array with the nanowires separated from each other approximately by the exciton diffusion length in the absorber. The space between the nanowires is filled with the absorber (Figure 2.6). In this way, the absorber can be made much thicker than the exciton diffusion length to harvest as many photons as possible even though the exciton diffusion length may be very short. The short distance between the nanowires increases the probability that an exciton created in the absorber will encounter a D-A interface. Thus, using nanowires in this manner allows one to optimize light absorption and exciton dissociation independently. Moreover, this structure not only eliminates the exciton diffusion bottleneck but also has the potential to increase the electron transport rate if the nanowires are defect free and single crystalline. Such high quality nanowires can provide a more direct path for electrons and hence increased electron mobility and collection efficiency.[69] Therefore, inorganic nanowires are ideal for HSCs,[1] and have the potential to increase their overall power conversion efficiency, especially for low optical density polymers with broad absorption spectra.[70]

HSCs composed of ZnO nanowires and P3HT as the organic conjugated polymer[71] have been constructed but their efficiencies are low (0.53%).[71] Efficiencies of these HSCs have been increased to as high as 2.7% by blending P3HT with PCBM.[15,70] In these cells the ZnO nanowires act only as the electron collector and not as the electron acceptor.[70] The excitons dissociate at the P3HT/PCBM interface and the electron is transferred first to the PCBM and then to the ZnO nanowires. HSCs with efficiencies of 0.2% have also been made with ZnO nanorods coated with an amphiphilic dye and P3HT.[72] In addition, a HSC consisting of ZnO nanowires coated with TiO_2 and P3HT has been constructed with an efficiency of 0.29%.[68]

Several researchers have found that using semiconductor nanowires instead of planar bilayers in HSCs results in higher efficiencies due to increased surface area[68,71] as well a improved electron collection.[70] As mentioned earlier, HSCs have been made with CdSe nanorods[18] and tetrapods[19] and these cells showed improved efficiency over CdSe

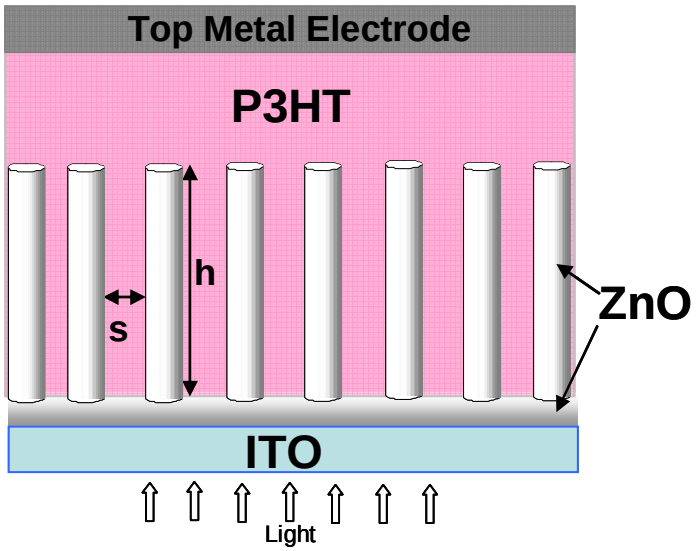

Figure 2.6 Schematic of a nanowire hybrid solar cell containing ZnO nanowires and P3HT. The nanowire spacing is denoted as s and the nanowire height is denoted as h. For optimal performance s needs to be on the order of the exciton diffusion length in P3HT. The nanowire height, h, can be made much larger than the exciton diffusion length to absorb as many photons as possible.

nanoparticle HSCs.[17] However, ZnO nanowire HSCs made with just P3HT (not P3HT and PCBM) have not reached the same efficiencies as ZnO-P3HT nanoparticle based HSCs (0.53%[71] vs. 2.4%[27]). Also, HSCs made with interconnected TiO_2 nanorod networks (η=0.71%)[73] have not shown much efficiency improvement as compared to TiO_2 nanoparticles HSCs (η=0.42%.)[28] Thus, nanowire based HSCs have shown either no improvement or marginal improvement as compared to nanoparticle HSCs.

One reason for this lower performance is that a nanowire film with the optimal spacing between the wires for HSCs has yet to be realized.[68] For maximum exciton collection the spacing must be on the order of the exciton diffusion length (4-20 nm)[1] in the polymer. However if the nanowires are too densely packed, the polymer is not able to properly infiltrate throughout the whole nanowire film.[68] Thus the ideal nanowire spacing is as small as possible while still allowing for proper polymer filling. If the nanowire growth could be *controlled and tailored* such that the nanowire spacing can be made to be this ideal distance the power conversion efficiencies of HSCs could be improved.

It has been recently discovered that the hole transport through the organic layer can also limit the efficiency of some HSCs.[1] Therefore, in order to increase the efficiency of HSCs, it will also be important to optimize the hole transport through the conjugated polymer layer as well as the electron transport though the inorganic semiconductor. Also, high rates of back electron transfer[74] as well as poor charge separation at the semiconductor-polymer interface[68] must also be addressed to further improve the efficiency of HCSs.

2.2.2 Nanowires for Quantum Dot Solar Cells

A schematic of a QDSC with ZnO nanowires incorporated as the electron transport material is shown in Figure 2.7. The operation of the nanowire QDSC is exactly the same as the QDSC made with a flat ZnO films shown in Figure 2.3c and discussed in section 2.1.3. The only difference between the solar cells is the morphology of the ZnO which has been changed from a flat surface to a nanowire film. The nanowires increase the efficiency of QDSCs in the same way they increase the efficiency of HSCs; the nanowires allow the light absorption and exciton collection to be optimized simultaneously and independently. Additionally, the nanowires provide a direct path for

the electrons, which should increase the electron transport to the contact. Also, as compared to the QDSC made with a flat ZnO surface, the nanowires can increase the efficiency by providing a larger D-A interface. As was the case for HSCs, for optimal performance the nanowire spacing needs to be on the order exciton diffusion length through the quantum dots. Thus the development of methods for growing inorganic nanowire films with *controlled and tailored* height, diameter and spacing may also help improve the power conversion efficiency of QDSC.

Nanowire QDSCs are have not been published yet but my colleague Kurtis Leschkies has made a QDSC with PbSe QDs and ZnO nanowires with an efficiency of ~2%.[75] This is three times the efficiency of a comparable QDSC made with just a flat ZnO film (0.7%).[75]

2.2.3 Nanowires for Dye Sensitized Solar Cells

Assuming a dye band gap of 2 eV the ultimate theoretical DSSC efficiency, according to the Shockley-Queisser limit, is ~24%.[33] Thus there is the potential to increase the DSSC efficiency. One issue which limits the further improvement of nanoparticle DSSC efficiency is that only ~46% of the incident solar power is absorbed by the cell.[45] Another issue is that the electrolyte iodide/triiodide (I^-/I_3^-) is almost exclusively used because it is the only known redox couple for which recombination with the electrons in the conduction band of the TiO_2 is much slower than the electron transport. This large ratio of the recombination time constant to the electron transport time constant guarantees that nearly all electrons injected into the semiconductor are collected.[76] The V_{oc} is determined by the difference between the redox potential of the electrolyte and conduction band edge of the wide band gap semiconductor. Thus, if other electrolytes could be used, one with a lower redox potential than iodide/triiodide, like the pseudohalogen $(SeCN)_2/(SeCN^-)$,[77] could be selected which could increase the open circuit voltage and the overall power conversion efficiency.

One way to increase the absorption efficiency beyond ~46% of the incident solar energy would be to increase the thickness of the nanoparticle layer. This would increase the available surface area so more dye could be adsorbed which would in turn result in

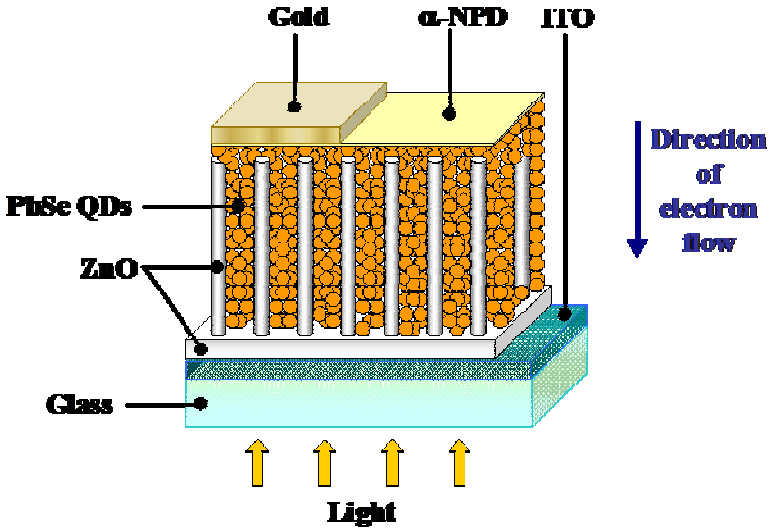

Figure 2.7 Schematic of a nanowire quantum dot solar cell composed of PbSe quantum dots fully interpenetrating ZnO nanowires. α-NPD is on organic coating which is placed between the gold contact and the PbSe quantum dots to protect the quantum dots from physical damage during the metal contact evaporation process and to prevent electrons from interjecting into the gold contact during cell operation. Courtesy of Leschkies et al.[75]

more light absorption and hence an increase in overall power conversion efficiency. However, the DSSC nanoparticle efficiency increases with nanoparticle thickness only up to thicknesses of ~10-20 μm. This is because as the electrons hop from particle to particle to the anode[78] sometimes they get trapped on the surface of a nanoparticle and recombine with the electrolyte without going through the load.[79] This limits the diffusion length, L_n, through the nanoparticle layer to ~10-20 μm.[80] Thus, when the nanoparticle layer is thicker than ~10-20 μm, more dye is adsorbed and more light is absorbed but electrons injected further than L_n away from the anode are less likely to be collected. This means that as the nanoparticle thickness increases beyond L_n the electron collection efficiency starts to decrease which causes the efficiency to saturate once the nanoparticle layer thickness reaches L_n.

To increase the efficiency of DSSCs by making the photoanode thicker, the electron collection efficiency must be improved by increasing the electron transport and/or decreasing the recombination rates. Increasing the electron transport rate would also allow for different electrolytes with faster recombination kinetics but lower redox potentials to be used, which can result in higher open circuit voltages. One way to increase the electron transport and/or decrease the electron recombination is to change the morphology of the photoanode from nanoparticles to nanowires or nanotubes.[14,64,69] A schematic of a ZnO nanowire DSSC is shown in Figure 2.8. The operation of the DSSC with nanowires as the photoanode is exactly the same as with nanoparticles, the only difference is that the nanoparticles have been replaced by nanowires. The nanowires can increase electron transport by providing a direct electron pathway to the anode. Also, the nanowires do not necessarily have to be ordered and vertically oriented; disordered, horizontal nanowires which are each connected to either another nanowire or the anode could also increase electron transport.

Nanowire DSSCs have been assembled using ZnO nanowires,[14,69] ZnO nanotubes,[81] TiO_2 nanowires,[82] TiO_2 nanotubes,[64,83] SnO_2 nanowires,[84] single-walled carbon nanotubes and TiO_2 nanoparticles,[85] ZnO nanowires coated with MgO,[86] Al_2O_3[87] and TiO_2,[87] as well as Nb_2O_5 nanobelts.[88] The highest efficiency (9.3%)[82] nanowire DSSC made to date was assembled with single crystal anatase TiO_2 nanowires with

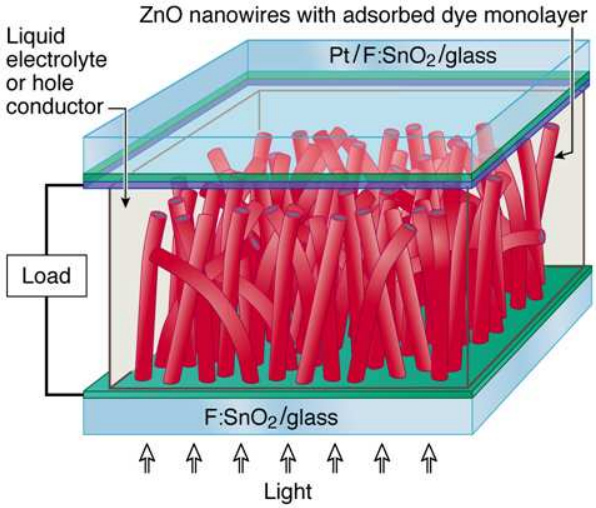

Figure 2.8 Schematic of a ZnO nanowire dye sensitized solar cell. Courtesy of Baxter et al.[88]

length and diameter of 20 ± 10 nm and 5 ± 2 nm, respectively. These nanowires were grown homogeneously and drop cast onto conducting oxide substrates. With aspect ratios of ~5 these nanowires are actually very close to nanoparticles.

It has been shown that the incorporation of nanowires/nanotubes into DSSCs as the photoanode does increase the electron collection efficiency relative to nanoparticles. In particular, when ZnO nanowires are used, it has been found that the electron transport is increased while the recombination rate remains the same relative to nanoparticles.[65-67] In contrast, with TiO_2 nanotubes and nanowires the opposite has been found; the electron recombination rate is slower and the electron transport rate is similar to that measured with nanoparticles.[64,89] The electron transport and recombination rates were found to be 10 times faster and 100 times slower, respectively, in SnO_2 nanowires as compared to TiO_2 nanoparticles.[84] However, so far, nanowire DSSCs have not achieved overall power conversion efficiencies as high as nanoparticle DSSCs because the nanowire surface area is an order of magnitude lower than the surface area of nanoparticle films.[14,90] The lower surface area results in less dye adsorbed onto the photoanode which in turn results in lower light absorption and lower overall power conversion efficiencies.

If nanowires films with surface area equivalent to that of nanoparticle films could be grown then thicker photoanodes with more adsorbed dye could be made and the efficiency of DSSC could be increased. If the nanowire height, diameter and planar density could be *controlled and tailored* then high surface area nanowire films could be made by making the nanowires as long, thin and as densely packed as possible.

2.2.4 Nanowires for Quantum Dot Sensitized Solar Cells

The performance of QDSSCs may also be improved by the incorporation of nanowires. A schematic of nanowire QDSSC composed of ZnO nanowires and CdSe QDs is shown in Figure 2.9. Like DSSCs, the increased electron collection provided by the nanowires will allow thicker semiconductor photoanodes to be used in QDSSCs. Thicker photoanodes will provide more surface area for the QDs to adsorb, leading to more light absorption and higher overall efficiencies. Nanowire QDSSC have been realized using CdSe,[57] CdTe,[91] and CdS[92] QDs on ZnO nanowires as well as CdTe[93] and

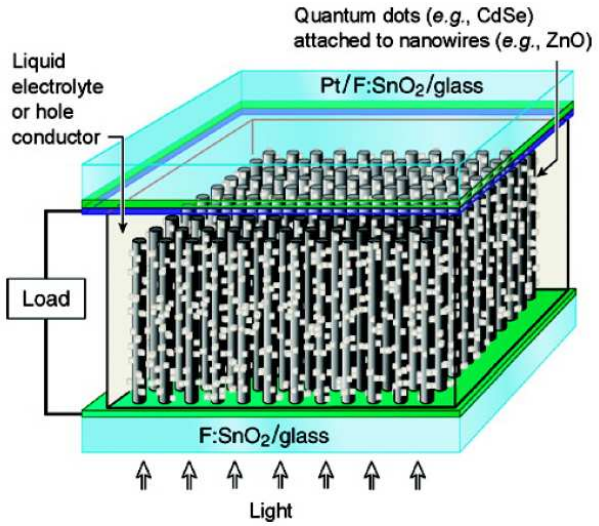

Figure 2.9 Schematic of a nanowire quantum dot sensitized solar cell. Courtesy of Leschkies et al.[57]

CdSe[94] on TiO_2 nanotubes. However, the efficiency of these nanowire QDSSCs (~0.4%[57]) are lower than the QDSSC made with nanoparticles (~3%[59,63]). This, as is the case with the DSSC, is due to the lower surface area of the nanowires as compared to nanoparticles; fewer QDs can be adsorbed onto the nanowires which limits the overall efficiency.[57] Thus, nanowire based QDSSCs can also be improved if the nanowire height, diameter and planar density can be *controlled and tailored* such that nanowire films with larger surface area can be synthesized.

A recurring theme that arises time and time again within this section is the idea that being able to *control and tailor* the growth of wide band gap nanowire films is the key to increasing the power conversion efficiency of all types of excitonic solar cells. In addition, improving the nanowire growth by increasing the *yield* as well as the *growth rate* will also help lower the cost of nanowire based XSCs. Therefore, studying the growth of ZnO and TiO_2 nanowires in order to develop a fundamental understanding which can be used to *control and tailor* the nanowire dimensions as well as to improve the *yield* and *growth rate* is a worthwhile endeavor. It should be noted that although, nanowires have the potential to increase the efficiency of several different types of XSCs this thesis focuses on the incorporation of nanowires into *dye sensitized solar cells*. Other colleagues in our group have used and continue to use these nanowires in other XSCs including the QDSCs.[57]

2.3 Properties of TiO_2 and ZnO

TiO_2 and ZnO are good candidate materials for nanowire photoanodes in XSCs because they are non-toxic, abundant and inexpensive to synthesize.[26,95] They are also stable against photocorrosion because they have wide band gaps; TiO_2 and ZnO only absorb light with wavelengths in the UV or higher.[95] This allows them to be more stable in XSCs than other semiconductor materials with narrower band gaps. In addition, the positions of their conduction bands make TiO_2 and ZnO good DSSC materials. ZnO and TiO_2 have band gaps of 3.3 eV and 3.2 eV respectively, and the electron affinities of ZnO and TiO_2 are such that their conduction band edges are lower but not too far from the LUMO levels of typical dyes and electron donors used in XCSs. For example, Figure

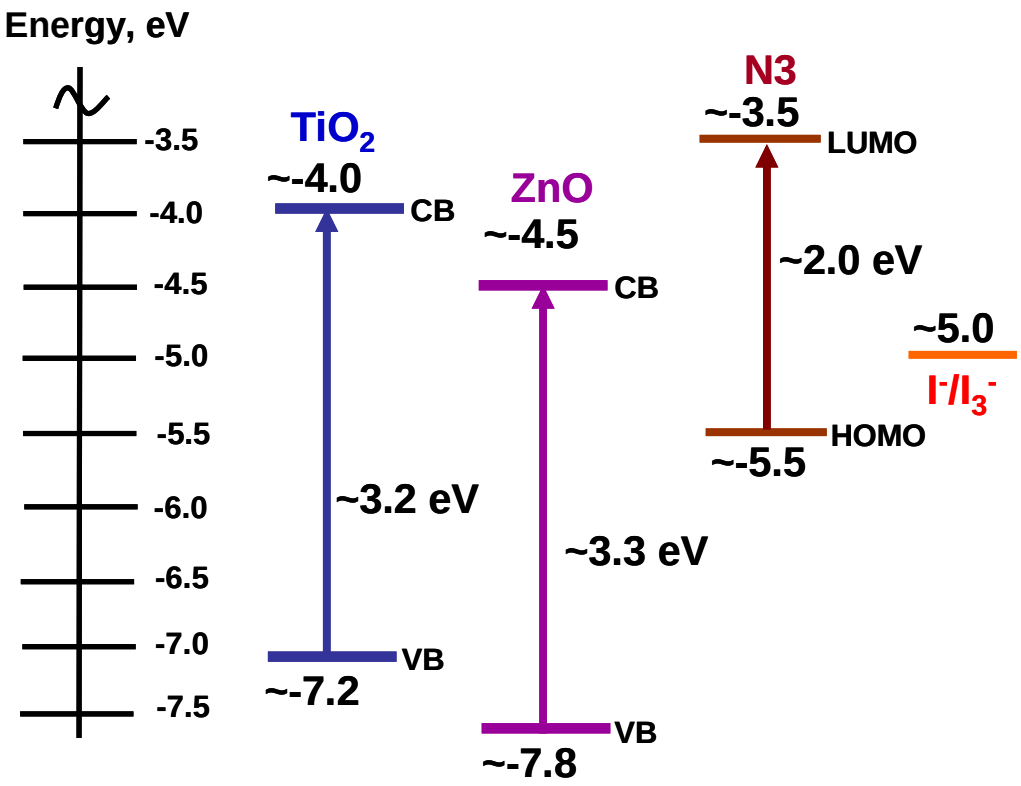

Figure 2.10 Energy levels of the conduction (CB) and valance bands (VB) of TiO_2 and ZnO, the HOMO and LUMO levels of the N3 dye (Solaronix), and the redox level of iodide/triiodide. The energy levels are such that dye sensitized solar cell operation is possible. Energy levels are respect to vacuum.

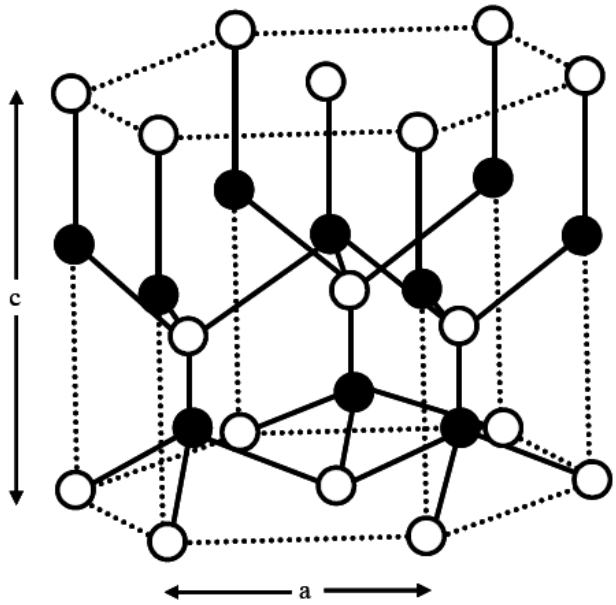

Figure 2.11 Ball and stick representation of wurtzite ZnO. Open circles represent oxygen atoms and filled circles represent zinc atoms.[85]

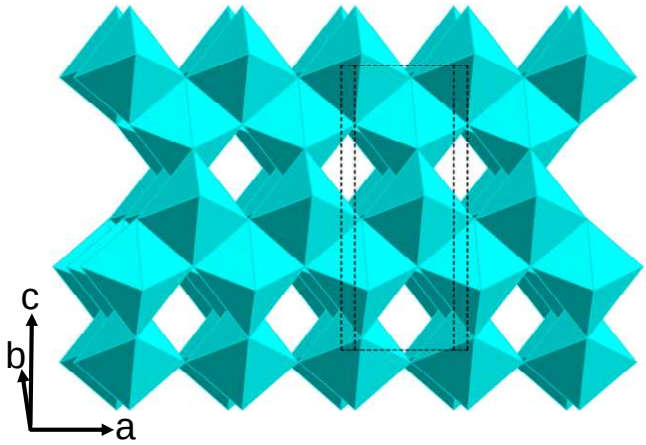

Figure 2.12 Polyhedral representation of anatase TiO_2. Each octahedron represents one Ti atom with six oxygen atoms surrounding it in an octahedral fashion. Each octahedron shares four sides with other octahedra. The dash black line denotes one unit cell.

2.10 shows the energy levels of TiO_2, ZnO, I^-/I_3^-, and the organometallic dye N3 from Solaronix. The LUMO level of the dye is higher in energy than that of the semiconductor conduction band such that it is energetically favorable for electrons to be transferred to the nanowire. However, the conduction band edge and the dye LUMO levels are still close to each other so that only a fraction of the energy is lost to phonons (heat) upon electron transfer from the dye to the wide band gap semiconductor. Similarly, the redox level of the electrolyte is higher in energy than the dye's HOMO level such the electrolyte can reduce the dye.

Zinc oxide has three crystal structures, rocksalt (B1), zinc blende (B3), and wurtzite (B4).[96] Rocksalt is only formed at high pressures and zinc blende is formed only when the zinc oxide is grown on cubic substrates.[96] Wurtzite is the most common of the three structures because it is the thermodynamically stable crystal structure at ambient conditions.[96] Zinc oxide wurtzite structure can be thought of as two interpenetrating hexagonal close packed (hcp) lattices one consisting of oxygen atoms and the other of zinc atoms. The two hcp structures are offset along the c-axis by 0.375 c, where c is the c-axis lattice parameter, Figure 2.11.[97] Each zinc atom exhibits tetrahedral coordination to four oxygen atoms and vice versa for the oxygen atoms. Tetrahedral bonding is sp^3 hybridized covalent bonding but ZnO actually also has significant ionic character making it the "ionic extreme" of the tetrahedrally coordinated semiconductors.[98]

The most common TiO_2 crystal structures of TiO_2 at ambient conditions are anatase (C5) and rutile (C4). While the nanoparticles used in XCS are most commonly anatase, it has been found that the performance of anatase (C5) and rutile (C4) nanoparticles in DSSCs are similar.[99] Anatase has four-fold symmetry and belongs to the body-centered tetragonal crystal system (Figure 2.12). The building block of the anatase phase is an octahedron which is composed of one Ti atom in the center and six oxygen atoms surrounding it at the corners of the octahedron. These octahedra come together and share four sides to form the anatase crystal structure.

References

(1) Coakley, K. M.; McGehee, M. D. *Chem. Mater.* **2004**, *16*, 4533.

(2) Coakley, K. M.; Srinivasan, B. S.; Ziebarth, J. M.; Chiatzun, G.; Yuxiang, L.; McGehee, M. D. *Adv. Funct. Mater.* **2005**, *15*, 1927.

(3) He, C.; He, Q. G.; He, Y. J.; Li, Y. F.; Bai, F. L.; Yang, C. H.; Ding, Y. Q.; Wang, L. X.; Ye, J. P. *Sol. Energy Mater. Sol. Cells* **2006**, *90*, 1815.

(4) Shrotriya, V.; Li, G.; Yao, Y.; Chu, C. W.; Yang, Y. *Appl. Phys. Lett.* **2006**, *88* 073508.

(5) Al-Ibrahim, M.; Roth, H. K.; Zhokhavets, U.; Gobsch, G.; Sensfuss, S. *Sol. Energy Mater. Sol. Cells* **2005**, *85*, 13.

(6) Yu, G.; Gao, J.; Hummelen, J. C.; Wudl, F.; Heeger, A. J. *Science* **1995**, *270*, 1789.

(7) Gregg, B. A. *J. Phys. Chem. B* **2003**, *107*, 4688.

(8) Sariciftci, N. S.; Braun, D.; Zhang, C.; Srdanov, V. I.; Heeger, A. J.; Stucky, G.; Wudl, F. *Appl. Phys. Lett.* **1993**, *62*, 585.

(9) Peumans, P.; Uchida, S.; Forrest, S. R. *Nature* **2003**, *425*, 158.

(10) Yu, G.; Heeger, A. J. *J. Appl. Phys.* **1995**, *78*, 4510.

(11) Halls, J. J. M.; Walsh, C. A.; Greenham, N. C.; Marseglia, E. A.; Friend, R. H.; Moratti, S. C.; Holmes, A. B. *Nature* **1995**, *376*, 498.

(12) Kim, J. Y.; Lee, K.; Coates, N. E.; Moses, D.; Nguyen, T. Q.; Dante, M.; Heeger, A. J. *Science* **2007**, *317*, 222.

(13) Kaidashev, E. M.; Lorenz, M.; von Wenckstern, H.; Rahm, A.; Semmelhack, H. C.; Han, K. H.; Benndorf, G.; Bundesmann, C.; Hochmuth, H.; Grundmann, M. *Appl. Phys. Lett.* **2003**, *82*, 3901.

(14) Law, M.; Greene, L. E.; Johnson, J. C.; Saykally, R.; Yang, P. D. *Nat. Mater.* **2005**, *4*, 455.

(15) Olson, D. C.; Piris, J.; Collins, R. T.; Shaheen, S. E.; Ginley, D. S. *Thin Solid Films* **2006**, *496*, 26.

(16) Beek, W. J. E.; Wienk, M. M.; Janssen, R. A. J. *J. Mater. Chem.* **2005**, *15*, 2985.

(17) Greenham, N. C.; Xiaogang, P.; Alivisatos, A. P. *Phys. Rev. B: Condens. Matter* **1996**, *54*, 17628.

(18) Huynh, W. U.; Dittmer, J. J.; Alivisatos, A. P. *Science* **2002**, *295*, 2425.

(19) Sun, B. Q.; Marx, E.; Greenham, N. C. *Nano Lett.* **2003**, *3*, 961.

(20) Gonzalez-Valls, I.; Lira-Cantu, M. *Energy Environ. Sci.* **2009**, *2*, 19.

(21) Arici, E.; Sariciftci, N. S.; Meissner, D. *Adv. Funct. Mater.* **2003**, *13*, 165.

(22) Lira-Cantu, M.; Norrman, K.; Andreasen, J. W.; Krebs, F. C. *Chem. Mater.* **2006**, *18*, 5684.

(23) McDonald, S. A.; Konstantatos, G.; Zhang, S. G.; Cyr, P. W.; Klem, E. J. D.; Levina, L.; Sargent, E. H. *Nat. Mater.* **2005**, *4*, 138.

(24) Cui, D. H.; Xu, J.; Zhu, T.; Paradee, G.; Ashok, S.; Gerhold, M. *Appl. Phys. Lett.* **2006**, *88* 183111.

(25) Sahu, D. R.; Lin, S. Y.; Huang, J. L. *Appl. Surf. Sci.* **2006**, *252*, 7509.

(26) Lori E. Greene; Matt Law; Joshua Goldberger; Franklin Kim; Justin C. Johnson; Yanfeng Zhang; Richard J. Saykally; Peidong Yang *Angew. Chem. Int. Ed.* **2003**, *42*, 3031.

(27) Oosterhout, S. D.; van Bavel, S. S.; Wienk, M. M.; Janssen, R. A. *Abstr. Excitonic Solar Cell Conference,* Warwick, UK, 9-12 September, 2008, p. 96.

(28) Kwong, C. Y.; Choy, W. C. H.; Djurisic, A. B.; Chui, P. C.; Cheng, K. W.; Chan, W. K. *Nanotechnology* **2004**, *15*, 1156.

(29) Norris, D. J.; Vlasov, Y. A., "*Quantum dot Photonic Crystals*" in *Semiconductor Nanocrystals, From Basic Principles to Applications*, edited by Al. L. Efros, D. J. Lockwood, and L. Tsybeskov, New York: Kluwer, **2003**.

(30) Norris, D. J.; Efros, A. L.; Erwin, S. C. *Science* **2008**, *319*, 1776.

(31) Schaller, R. D.; Klimov, V. I. *Phys. Rev. Lett.* **2004**, *92*, 186601.

(32) Ellingson, R. J.; Beard, M. C.; Johnson, J. C.; Yu, P.; Micic, O. I.; Nozik, A. J.; Shabaev, A.; Efros, A. L. *Nano Lett.* **2005**, *5*, 865.

(33) Shockley, W.; Queisser, H. J. *J. Appl. Phys.* **1961**, *32*, 510.

(34) Klimov, V. I. *Appl. Phys. Lett.* **2006**, *89*, 123118.

(35) Hanna, M. C.; Nozik, A. J. *J. Appl. Phys* **2006**, *100*, 074510.

(36) Gur, I.; Fromer, N. A.; Geier, M. L.; Alivisatos, A. P. *Science* **2005**, *310*, 462.

(37) Wu, Y.; Wadia, C.; Ma, W. L.; Sadtler, B.; Alivisatos, A. P. *Nano Lett.* **2008**, *8*, 2551.

(38) Luther, J. M.; Law, M.; Beard, M. C.; Song, Q.; Reese, M. O.; Ellingson, R. J.; Nozik, A. J. *Nano Lett.* **2008**, *8*, 3488.

(39) Leschkies, K. S.; Beatty, T. J.; Kang, M. S.; Norris, D. J.; Aydil, E. S. *ACS nano* **2009**, *accepted*.

(40) Koleilat, G. I.; Levina, L.; Shukla, H.; Myrskog, S. H.; Hinds, S.; Pattantyus-Abraham, A. G.; Sargent, E. H. *ACS nano* **2008**, *2*, 833.

(41) Chiba, Y.; Islam, A.; Watanabe, Y.; Komiya, R.; Koide, N.; Han, L. Y. *Jpn. J. Appl. Phys. Part 2* **2006**, *45*, L638.

(42) Gerischer H. *Photochem. and Photobio.* **1972**, *16*, 243.

(43) Memming R. *Photochem. and Photobio.* **1972**, *16*, 325.

(44) Matsumura, M.; Nomura, Y.; Tsubomura, H. *Bull. Chem. Society Jpn* **1977**, *50*, 2533.

(45) O'Regan, B.; Grätzel, M. *Nature* **1991**, *353*, 737.

(46) Nazeeruddin, M. K.; Pechy, P.; Renouard, T.; Zakeeruddin, S. M.; Humphry-Baker, R.; Comte, P.; Liska, P.; Cevey, L.; Costa, E.; Shklover, V.; Spiccia, L.; Deacon, G. B.; Bignozzi, C. A.; Gratzel, M. *J. Am. Chem. Soc.* **2001**, *123*, 1613.

(47) Barbé, C. J.; Arendse, F.; Comte, P.; Jirousek, M.; Lenzmann, F.; Shklover, V.; Grätzel, M. *J. Am. Ceram. Soc.* **1997**, *80*, 3157.

(48) Wang, Z. S.; Kawauchi, H.; Kashima, T.; Arakawa, H. *Coord. Chem. Rev.* **2004**, *248*, 1381.

(49) Usami, A. *Chem. Phys. Lett.* **1997**, *277*, 105.

(50) Hore, S.; Vetter, C.; Kern, R.; Smit, H.; Hinsch, A. *Sol. Energ Mater. Sol. C.* **2006**, *90*, 1176.

(51) Saito, M.; Fujihara, S. *Energ. Environ. Sci.* **2008**, *1*, 280.

(52) Ferrere, S.; Zaban, A.; Gregg, B. A. *J. Phys.Chem. B* **1997**, *101*, 4490.

(53) Sayama, K.; Sugihara, H.; Arakawa, H. *Chem.Mater.* **1998**, *10*, 3825.

(54) Lenzmann, F.; Krueger, J.; Burnside, S.; Brooks, K.; Grätzel, M.; Gal, D.; Ruhle, S.; Cahen, D. *J. Phys. Chem. B* **2001**, *105*, 6347.

(55) Tan, B.; Toman, E.; Li, Y. G.; Wu, Y. Y. *J. Am. Chem. Soc.* **2007**, *129*, 4162.

(56) Chappel, S.; Chen, S.-G.; Zaban, A. *Langmuir* **2002**, *18*, 3336.

(57) Leschkies, K. S.; Divakar, R.; Basu, J.; Enache-Pommer, E.; Boercker, J. E.; Carter, C. B.; Kortshagen, U. R.; Norris, D. J.; Aydil, E. S. *Nano Lett.* **2007**, *7*, 1793.

(58) Vogel, R.; Hoyer, P.; Weller, H. *J. Phys.Chem.* **1994**, *98*, 3183.

(59) Lee, Y. L.; Huang, B. M.; Chien, H. T. *Chem. Mater.* **2008**, *20*, 6903.

(60) Yu, P. R.; Zhu, K.; Norman, A. G.; Ferrere, S.; Frank, A. J.; Nozik, A. J. *J. Phys. Chem. B* **2006**, *110*, 25451.

(61) Zaban, A.; Micic, O. I.; Gregg, B. A.; Nozik, A. J. *Langmuir* **1998**, *14*, 3153.

(62) Liu, D.; Kamat, P. V. *J. Phys.Chem.* **1993**, *97*, 10769.

(63) Diguna, L. J.; Shen, Q.; Kobayashi, J.; Toyoda, T. *Appl. Phys. Lett.* **2007**, *91* 023116.

(64) Zhu, K.; Neale, N. R.; Miedaner, A.; Frank, A. J. *Nano Lett.* **2007**, *7*, 69.

(65) Martinson, A. B. F.; McGarrah, J. E.; Parpia, M. O. K.; Hupp, J. T. *Phys. Chem. Chem. Phys.* **2006**, *8*, 4655.

(66) Galoppini, E.; Rochford, J.; Chen, H. H.; Saraf, G.; Lu, Y. C.; Hagfeldt, A.; Boschloo, G. *J. Phys. Chem. B* **2006**, *110*, 16159.

(67) Enache-Pommer, E., University of Minnesota, 2009.

(68) Greene, L. E.; Law, M.; Yuhas, B. D.; Yang, P. D. *J. Phys. Chem. C* **2007**, *111*, 18451.

(69) Baxter, J. B.; Aydil, E. S. *Appl. Phys. Lett.* **2005**, *86*, 53114.

(70) Takanezawa, K.; Hirota, K.; Wei, Q. S.; Tajima, K.; Hashimoto, K. *J. Phys. Chem. C* **2007**, *111*, 7218.

(71) Olson, D. C.; Shaheen, S. E.; Collins, R. T.; Ginley, D. S. *J. Phys. Chem. C* **2007**, *111*, 16670.

(72) Ravirajan, P.; Peiro, A. M.; Nazeeruddin, M. K.; Graetzel, M.; Bradley, D. D. C.; Durrant, J. R.; Nelson, J. *J. Phys. Chem. B* **2006**, *110*, 7635.

(73) Wang, H.; Oey, C. C.; Djurisic, A. B.; Xie, M. H.; Leung, Y. H.; Man, K. K. Y.; Chan, W. K.; Pandey, A.; Nunzi, J. M.; Chui, P. C. *Appl. Phys. Lett.* **2005**, *87* 023507.

(74) Coakley, K. M.; McGehee, M. D. *Appl. Phys. Lett.* **2003**, *83*, 3380.

(75) Leschkies, K. S.; Jacobs, A. G.; Norris, D. J.; Aydil, E. S. *Appl. Phys. Lett.* **2009**, *submitted*.

(76) Frank, A. J.; Kopidakis, N.; van de Lagemaat, J. *Coordin. Chem. Rev.* **2004**, *248*, 1165.

(77) Oskam, G.; Bergeron, B. V.; Meyer, G. J.; Searson, P. C. *J. Phys. Chem. B* **2001**, *105*, 6867.

(78) Benkstein, K. D.; Kopidakis, N.; van de Lagemaat, J.; Frank, A. J. *J. Phys. Chem. B* **2003**, *107*, 7759.

(79) Huang, S. Y.; Schlichthorl, G.; Nozik, A. J.; Gratzel, M.; Frank, A. J. *J. Phys. Chem. B* **1997**, *101*, 2576.

(80) Peter, L. M.; Wijayantha, K. G. U. *Electrochim. Acta* **2000**, *45*, 4543.

(81) Martinson, A. B. F.; Elam, J. W.; Hupp, J. T.; Pellin, M. J. *Nano Lett.* **2007**, *7*, 2183.

(82) Adachi, M.; Murata, Y.; Takao, J.; Jiu, J. T.; Sakamoto, M.; Wang, F. M. *J. Am. Chem. Soc.* **2004**, *126*, 14943.

(83) Mor, G. K.; Shankar, K.; Paulose, M.; Varghese, O. K.; Grimes, C. A. *Nano Lett.* **2006**, *6*, 215.

(84) Gubbala, S.; Chakrapani, V.; Kumar, V.; Sunkara, M. K. *Adv. Funct. Mater.* **2008**, *18*, 2411.

(85) Brown, P.; Takechi, K.; Kamat, P. V. *J. Phys. Chem. C* **2008**, *112*, 4776.

(86) Plank, N. O. V.; Snaith, H. J.; Ducati, C.; Bendall, J. S.; Schmidt-Mende, L.; Welland, M. E. *Nanotechnology* **2008**, *19* 465603.

(87) Law, M.; Greene, L. E.; Radenovic, A.; Kuykendall, T.; Liphardt, J.; Yang, P. D. *J. Phys. Chem. B* **2006**, *110*, 22652.

(88) Wei, M. D.; Qi, Z. M.; Ichihara, M.; Zhou, H. S. *Acta Mater.* **2008**, *56*, 2488.

(89) Enache-Pommer, E.; Boercker, J.; Aydil, E. S. *Appl. Phys. Lett.* **2007**, *91*, 123116.

(90) Baxter, J. B.; Walker, A. M.; van Ommering, K.; Aydil, E. S. *Nanotechnology* **2006**, *17*, S304.

(91) Cao, X. B.; Chen, P.; Guo, Y. *J. Phys. Chem. C* **2008**, *112*, 20560.

(92) Zhang, Y.; Xie, T. F.; Jiang, T. F.; Wei, X.; Pang, S.; Wang, X.; Wang, D. *Nanotechnology* **2009**, *20* 155707.

(93) Gao, X. F.; Li, H. B.; Sun, W. T.; Chen, Q.; Tang, F. Q.; Peng, L. M. *J. Phys. Chem. C* **2009**, *113*, 7531.

(94) Kongkanand, A.; Tvrdy, K.; Takechi, K.; Kuno, M.; Kamat, P. V. *J. Am. Chem. Soc.* **2008**, *130*, 4007.

(95) Lenzmann, F.; Kroon, J. M. *Adv. OptoElectronics* **2007**, 65073.

(96) Özgür, U.; Alivov, Y. I.; Liu, C.; Teke, A.; Reshchikov, M. A.; Dogan, S.; Avrutin, V.; Cho, S. J.; Morkoc, H. *J. Appl.Physics* **2005**, *98* 041301.

(97) Baxter, J. B., University of California, Santa Barbara, 2005.

(98) Meyer, B.; Marx, D. *Phys. Rev. B* **2003**, *67*, 035403.

(99) Park, N. G.; van de Lagemaat, J.; Frank, A. *Phys. Chem. B* **2000**, *104*, 8989.

Chapter 3 : Growth Mechanism of TiO_2 Nanowires for Dye-Sensitized Solar Cells*

3.1 Introduction

One-dimensional TiO_2 nanostructures for DSSCs have been synthesized by a variety of methods such as, surfactant-assisted self assembly,[1] potentiostatic anodization of titanium films,[2-4] electrospinning,[5] templating using anodic alumina membranes,[6] and hydrothermal alkali treatment of titanium or titania nanoparticles.[7-12] The latter methods[7-12] follow Kasuga et al.[13,14] who pioneered the homogenous growth of titania nanotubes from the alkali treatment of TiO_2 powder. Indeed, polycrystalline and amorphous nanotubes are the most commonly used one-dimensional morphology for making DSSCs. Recently, it has been found that TiO_2 nanowire films can be grown heterogeneously on titanium foil with alkali treatments similar to those used for growing nanotubes,[15-17] however the growth mechanism is not well understood.

In this chapter, I describe a method for growing TiO_2 nanowire films on titanium foil for use in DSSCs and explain the growth mechanism in detail. The synthesis is based on formation of sodium titanate nanotubes through hydrothermal oxidation of the titanium foil surface and subsequent transformation of these tubes to hydrogen titanate nanotubes by ion exchange and finally to anatase nanowires through annealing. I also show that these TiO_2 nanowire films are suitable for use as the wide band gap semiconductor photoanode in a DSSC.

3.2 Experimental Details

3.2.1. TiO_2 Nanowire Synthesis and Characterization

TiO_2 nanowires were synthesized on titanium foil (0.127 mm thick, Aldrich) following the three-step chemical synthesis described by Zhao et al.[15] In the first step, a ~2.5 × ~2 cm^2 piece of titanium foil was placed on the bottom of a 125 mL Teflon lined pressure vessel (Parr Instrument Company) with 60 mL 10 M NaOH and 4 mL 35 wt%

*This chapter is adapted from:
Boercker, J. E.; Enache-Pommer, E.; Aydil, E. S. *Nanotechnology* **2008**, *19*, 095604.

H_2O_2. Mixing H_2O_2 with NaOH at room temperature formed a slushy film at the surface of the clear NaOH solution. After heating the vessel at 220 °C for four hours, a ~7 μm thick film of sodium titanate nanotubes formed (see below) on the titanium foil surface in contact with the bottom of the vessel, this surface looked slightly brown when viewed at acute angles. After the hydrothermal growth, the solution was no longer clear and contained large white precipitates. The titanium foil with sodium titanate nanotubes was removed from the vessel and washed with deionized water and dried under Ar flow. A ~100 μm thick film of white precipitate also formed on the surface of the titanium foil which was not in contact with the bottom of the vessel. This film was removed from the surface by wiping and rinsing before the next step. In the second step, the titanium foil with nanotubes was immersed in 0.57 M HCl for one hour to exchange the Na^+ with H^+ and thus transform the sodium titanate nanotubes to hydrogen titanate nanotubes. Visual appearance of the film did not change after the ion exchange. The nanotube film was removed from the HCl solution and rinsed with deionized water and dried under Ar flow. In the third step, the hydrogen titanate nanotube coated titanium foil turned white as it was heated at 500 °C for one hour to convert the nanotubes to anatase TiO_2 nanowires. Hereafter, these three consecutive steps are referred to as the hydrothermal growth step, the ion-exchange step and the annealing step.

The nanostructured film on the titanium foil was examined at different stages of the synthesis with X-ray microdiffraction, (XRD, Bruker-AXS Microdiffractometer) scanning electron microscopy (SEM, JEOL 6700) and transmission electron microscopy (TEM, FEI Tecnai T12) to determine their crystal structure and morphology. The nanotube and nanowire films on the titanium foil were placed directly into the microdiffractometer with no alterations to obtain the XRD spectra. TEM samples were prepared by sonicating the nanotubes and nanowires off the titanium foil into isopropanol and then drop casting a few drops of this solution onto a 400 mesh carbon coated copper TEM grid (Ladd Research). Approximate elemental composition of the nanowires and the nanotubes was determined with energy dispersive spectroscopy (EDS, Thermo-Noran Vantage System) on a scanning electron microscope (JEOL 6500.)

3.2.2 TiO_2 Nanowire Dye-Sensitized Solar Cell Assembly

Dye-sensitized solar cells were assembled using the TiO_2 nanowires grown on titanium foil as the photoanode. Prior to dye adsorption, the TiO_2 nanowires were placed in a 0.05 M $TiCl_4$ solution at 70 °C for 30 minutes. After rinsing with deionized water, the $TiCl_4$ treated nanowire film was air dried and annealed at 450 °C for 30 minutes.[18] Immediately before dye adsorption, the titanium foil with TiO_2 nanowires was placed in an oxygen plasma for 10 minutes. *cis*-diisothiocyanato-bis(2,2'-bipyridyl-4,4'-dicarboxylato) ruthenium(II) bis(tetrabutylammonium) dye (N-719 as received from Solaronix) was absorbed onto the surface of the TiO_2 nanowires by immersing the titanium foil in a 0.3 mM dye solution in absolute ethanol for 72 hours. Solar cells were assembled by placing the titanium foil covered with TiO_2 nanowires face-to-face with a fluorine doped tin oxide glass (FTO, Hartford Glass) coated with a thin platinum layer (~1.5 nm). Twenty-five micron thick Teflon spacers (Pike Technologies) were used between the titanium foil and Pt covered FTO glass to prevent electrical shorts. A liquid electrolyte containing the redox couple I^-/I_3^- (Iodolyte TG-50 from Solaronix with 0.5 M 4-tert-butylpyridine added) was injected in the space between the nanowires and the platinized FTO cathode to complete the cell assembly.

3.2.3 Solar Cell Characterization

The solar cell characterization was done in collaboration with my colleague Emil Enache-Pommer.[19,20] The main technique used to characterize the solar cells is the current-voltage measurement. In this measurement the current through the solar cell is measured while a voltage is applied to the terminals of the solar cell. I-V characteristics are obtained by scanning the voltage in the dark and while illuminating the solar cell. A Keithley 2400 Series SourceMeter was used for the I-V measurements along with an Oriel 100 W Xe-arc lamp with an AM1.5 filter. [21]

The schematic in Figure 3.1 shows the sign conventions used in this research for voltage and current. When the cell is producing power from light, the current flows in the opposite direction of the arrow (negative current) shown in Figure 3.1 and is in the fourth quadrant of the I-V plane. Figure 3.2 shows, qualitatively, a typical I-V curve

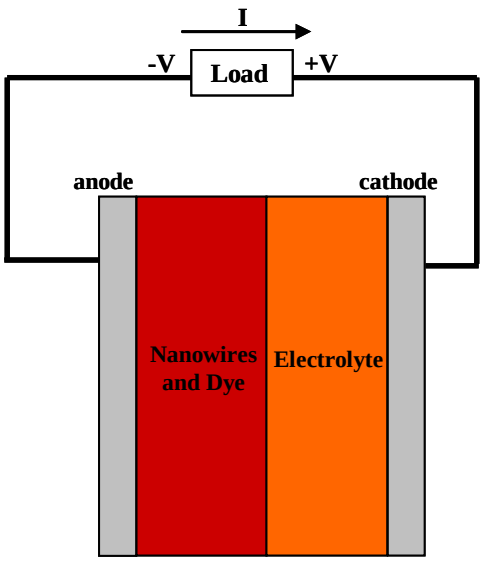

Figure 3.1 A schematic of a nanowire-based DSSC showing the convention for voltage and current. Under normal operation the current is in the opposite direction of the arrow shown.

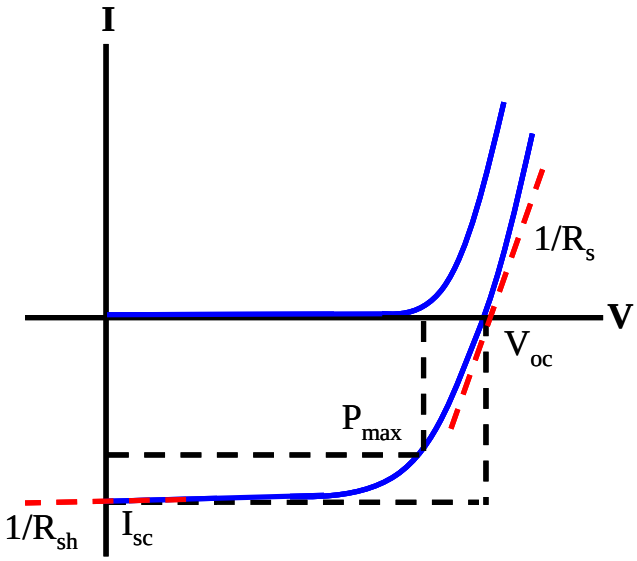

Figure 3.2 A qualitative representation of a typical DSSC solar cell I-V curve. The upper blue line is in the dark and the lower blue line is under illumination. The parameters determined from the I-V curves; the maximum power, P_{max}, the open circuit voltage, V_{oc}, the short circuit current I_{sc} and the shunt and series resistances, R_{sh} and R_s, are shown.

from a nanowire-based DSSC and the important features that are used to characterize the cell. The current that passes through the cell, without bias voltage (V=0) is called the short circuit current, I_{sc}. As the voltage is increased the current decreases until the open circuit voltage, V_{oc}, is reached where no current flows through the cell. When the voltage applied is greater than the open circuit voltage the current flows in the opposite direction to that when the cell is under normal operation (positive current). The maximum power output of the cell, P_{max}, is generated at the point where the current-voltage product is a maximum.

The equivalent circuit shown in Figure 3.3 models the I-V characteristics of a DSSC. The equivalent circuit consists of a current source (I_L), a diode (I_D), two shunt resistors, ($R_{sh\text{-}photo}$ and $R_{sh\text{-}dark}$), and a series resistor (R_s). The current source is the photoabsorption of the dye and subsequent injection into the semiconductor. The combination of the current source, diode and shunt resistors represent the nanowire-dye-electrolyte interface. The diode models the unidirectional nature of the electron injection from the dye into the nanowires. The $R_{sh\text{-}photo}$ and $R_{sh\text{-}dark}$ are the shunt resistances with and without illumination respectively. The shunt resistance is the resistance to current flow from the semiconductor to the electrolyte. The reciprocal of the slope of an I-V characteristic at zero bias voltage is equal to the shunt resistance, R_{sh} (Figure 3.2). A high shunt resistance is desirable for maximum current through the load. R_s is the series resistance which includes the resistance across the contacts, substrates, semiconductor, and electrolyte. The reciprocal of the slope of the I-V curve at $V=V_{oc}$ is the series resistance, R_s (Figure 3.2). A low R_s is ideal to minimize the resistance to current through the cell.

The overall power conversion efficiency, η, of a solar cell is the ratio of the maximum power output of the cell to the power input from the light source,

$$\eta = \frac{P_{\max}}{P_{light}} \quad . \tag{3.1}$$

P_{max} is affected by how much the current decreases from I_{sc} as the voltage is increased. A measure of this deviation is determined by the fill factor, FF,

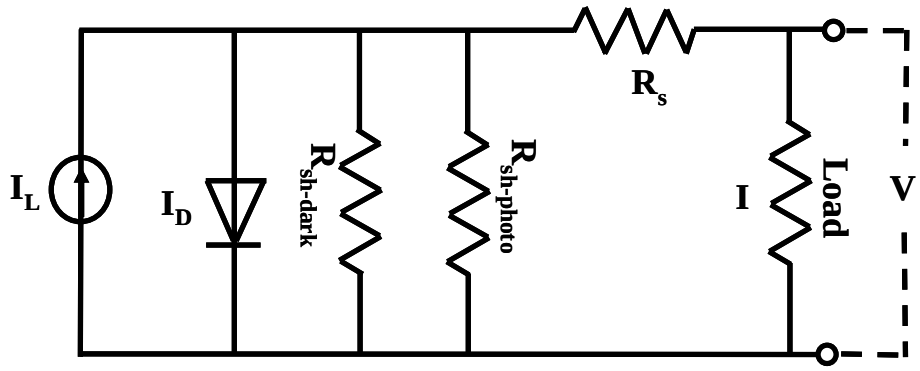

Figure 3.3 The equivalent circuit of a DSSC consists of a current source (I_L), a diode (I_D), a series resistor (Rs), shunt resistors ($R_{sh\text{-}photo}$ and $R_{sh\text{-}dark}$), a voltage drop across the load (V), and a current through the load (I).

$$FF = \frac{P_{\max}}{I_{sc} \times V_{oc}} \quad , \tag{3.2}$$

which compares the actual P_{max} to the hypothetical maximum power that a cell could deliver if I_{sc} remained constant as the voltage is increased to V_{oc}. Typical silicon solar cells and the best DSSCs have FF's near 70%. The FF is higher when the R_{sh} is large and the R_s is small so that the slope of the I-V curve approaches zero at short circuit and infinity at open circuit. Substitution of Equation 3.2 into Equation 3.1 gives a new expression for the overall energy conversion efficiency,

$$\eta = \frac{FF \times I_{sc} \times V_{oc}}{P_{light}} \quad . \tag{3.3}$$

Thus, the important parameters determined from I-V curves are the FF, I_{sc} and V_{oc} and increasing these increases the overall power conversion efficiency of the solar cell. It should be noted that in this thesis, in following with convention, current is presented as current density, J (mA/cm^2), rather than current, I (mA).

In addition to electrical characterization, optical methods were also used to characterize the solar cells. Optical characterization gives insight into factors that limit the efficiency of the solar cells. The photocurrent produced by the solar cells at I_{sc} was measured as a function of the wavelength of incident light to obtain a photocurrent spectrum, also called a photoaction spectrum. This was done by sending the light from the Xe lamp through a monochromator before it was incident on the solar cell and measuring the photocurrent at different incident wavelengths. The incident photon to current efficiency (IPCE) as a function of wavelength can be obtained by dividing the photocurrent spectrum by the number of photons incident on the cell at each wavelength. The IPCE spectrum gives the fraction of the incident photons that are converted to an electron at a particular wavelength. The formula for IPCE is given by

$$IPCE = \frac{1240 \times I_{sc}}{P(\lambda) \times \lambda}. \tag{3.4}$$

Where λ is the wavelength of the incident light and $P(\lambda)$ is the incident radiative flux (i.e., irradiance) between wavelengths λ and $\lambda+d\lambda$. $P(\lambda)$ was measured using a silicon detector (SED033) and a power meter (IL 1700) from International Light.

In order for an incident photon to produce an electron that contributes to the current in a DSSC three things must happen: (1) the photon must be absorbed by the dye to create an excited electron, (2) the excited electron must be injected into the semiconductor, and (3) the electron must be collected at the back contact after passing through the nanowire. Thus, the IPCE is broken down to a product of the efficiencies of each one of these steps and is given by

$$IPCE = LHE \times \eta_{inj} \times \eta_{coll} \quad , \tag{3.5}$$

where LHE is the light harvesting efficiency, η_{inj} is the injection efficiency and η_{coll} is the collection efficiency. The LHE is the fraction of the incident photons that are absorbed by the dye, η_{inj} is the fraction of the absorbed electrons that are injected into the semiconductor, and η_{coll} is the fraction of the injected electrons that are collected at the back contact. Often, these fractions are expressed as percentages.

The absorbance of the dye-coated nanowire thin films can be measured using thin film absorption spectroscopy and the LHE will be calculated from

$$LHE = \left(1 - 10^{-A}\right) \times 100\% \quad . \tag{3.6}$$

The product of η_{inj} and η_{coll} can be obtained from the ratio of IPCE to LHE. This product, $\eta_{inj} \times \eta_{coll}$, is also referred to as the internal quantum efficiency (IQE). The ruthenium based dyes used in the DSSCs have been found to have an injection efficiency of nearly 100%.[22] Thus, for DSSCs the measured IQE is essentially the collection efficiency of the cell. The η_{coll} and LHE give insight into the DSSC's limitations because they quantify the solar cell's absorbance and transport capability respectively.

In addition to characterizing the solar cells with I-V and IPCE measurements the electron transport, τ_c, and recombination, τ_r, time constants were studied using intensity modulated photocurrent spectroscopy (IMPS),[23,24] photocurrent decay,[25,26] and photovoltage decay.[27,28] These characterization techniques are discussed in great detailed in Emil Enache-Pommer's thesis.[20] Briefly, these techniques are transient techniques where the incident light is modulated and the response from the cell, either the I_{sc} or the V_{oc}, can be used to calculate the electron transport and recombination time constants. In particular, in IMPS, the cell is operated at short circuit and the incident light is modulated as a sine wave and the I_{sc} response is recorded as a function of frequency. From the

difference in phases between the light modulation and the I_{sc} response, the electron transport time τ_c can be found.[23] Electron transport time, τ_c, can also be measured using photocurrent decay in which the cell is again operated at short circuit and the incident light is varied as a square wave with a modulation period longer than the electron transport time. The I_{sc} decays exponentially from one steady state value to another as the light is changed from a higher intensity to a lower intensity. Electron transport time, τ_c can be determined by fitting an exponential function to this decay.[25] Photovoltage decay is used to find the electron recombination time constant τ_r. This technique is similar to photocurrent decay in that the light is modulated as a square wave with a modulation period longer than the electron recombination time while the solar cell is maintained at open circuit. The recombination time constant τ_r is found by fitting an exponential function to the V_{oc} decay as the light intensity is changed from a higher value to a lower value.[27]

3.3 Morphology and Structure of the TiO_2 Nanowire Film

Figure 3.4 shows a cross sectional SEM of the TiO_2 nanowires synthesized through the three-step synthesis method described above. XRD of this film shows diffractions only due to anatase TiO_2 and titanium foil (see below). The TiO_2 nanowires are randomly oriented and entangled together to form a nanostructured film with an overall thickness that varies across the titanium foil substrate and has an average value of 7 μm ± 3 μm. At some locations along the foil the thickness of the nanowire film reaches as high as 10 μm while at other points the film is 4 μm or thinner. The nanowires are connected to the titanium foil through a denser mesoporous TiO_2 layer that forms between the nanowires and the unconverted titanium metal. This transition layer is shown in Figure 3.4 and is an intermediate mesoporous structure that forms while the titanium foil is converted to TiO_2 through the three-step synthesis. The most likely reason for the inhomogeneity of the nanowire film thickness is the initial surface structure and surface roughness of the titanium foil. The surface roughness could result in different nucleation and growth rates at various locations on the foil and ultimately in a distribution of nanowire film thicknesses.

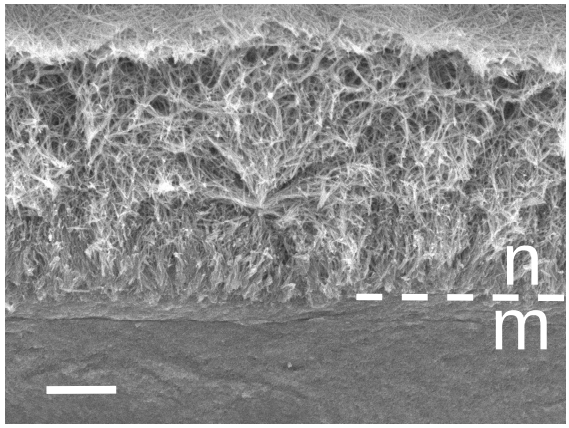

Figure 3.4 Cross-sectional SEM image of a 4 μm thick TiO_2 nanowire film. The nanowire film is connected to a mesoporous TiO_2 layer on the titanium foil. The interface between the nanowire film (n) and the mesoporous transition layer (m) is shown with a dashed line. The scale bar is 1 μm.

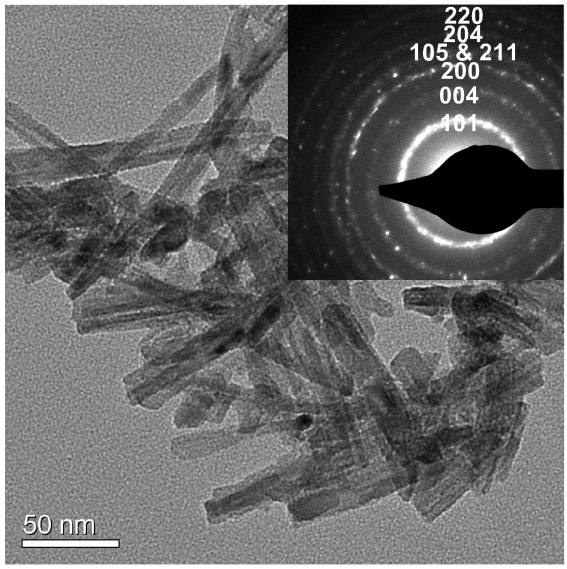

Figure 3.5 TEM image of TiO_2 nanowires with diameters of 20 nm ± 8 nm. Inset shows the selected area electron diffraction pattern from an ensemble of nanowires which can be indexed to anatase TiO_2.

Figure 3.5 shows a TEM of an ensemble of TiO_2 nanowires and the electron diffraction from this ensemble. The TiO_2 nanowires are 20 nm ± 8 nm in diameter and the electron diffraction spots could be indexed to the anatase phase of TiO_2. The lengths of the nanowire segments shown in Figure 3.5 are not representative of the nanowires in the film because the wires break during TEM sample preparation. While difficult to determine, the lengths of the nanowires are estimated to be on the order of the nanowire film thickness and each nanowire meanders through the film. Careful examination of many SEMs show that the nanowires are either connected to the mesoporous transition layer or another nanowire. High resolution TEM (HRTEM, Figure 3.6) shows that the TiO_2 nanowires are polycrystalline with nonequiaxed grains elongated along the nanowire axis. The average grain size measured along the long axis of the grains was 26 ± 17 nm. In all the HRTEMs, the {101} planes of anatase TiO_2 were oriented nearly perpendicular to the local nanowire axis. Careful examination of the angle between the {101} planes and the local nanowire axis, θ (Figure 3.6b), showed that θ varied from 90^o to ~60° with significant majority of the grains oriented with θ ~70°. This orientation is a direct result of the transformation mechanism that yields the TiO_2 nanowires and will be described shortly.

3.4 Morphology and Structure Evolution During Nanowire Synthesis

Figure 3.7 shows top and side view SEMs of the nanostructured film on the titanium foil after each synthesis step, hydrothermal growth, ion exchange, and annealing. This figure shows that the morphology of the film on a micrometer scale is determined during hydrothermal growth by the natural anisotropic growth habit of sodium titanate and is preserved throughout the ion-exchange and annealing steps that eventually lead to TiO_2 nanowires. However, we will show that, on the nanometer scale, the morphology changes from sodium titanate nanotubes to hydrogen titanate nanotubes and finally to polycrystalline TiO_2 nanowires during the ion-exchange and annealing steps, respectively.

Figure 3.8a shows a TEM image of the nanotubes formed after the hydrothermal synthesis step. The nanotubes are identified as $Na_2Ti_2O_4(OH)_2$ through XRD (see below). The nanotubes have outer diameters of 11 ± 2 nm and inner diameters of 4 ± 1 nm. The

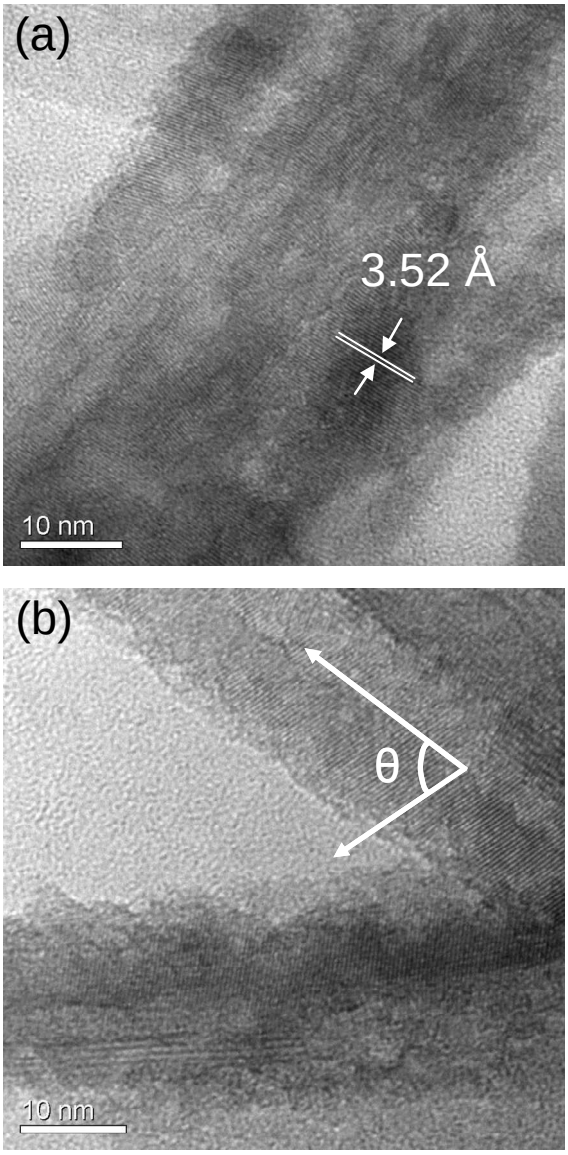

Figure 3.6 HRTEM images of polycrystalline TiO_2 nanowires showing grains elongated along the nanowire axis. Lattice fringes seen in both (a) and (b) are separated by 3.52 Å and correspond to the {101} planes. The angle between the {101} planes and the local nanowire axis, θ, is shown in (b). For the majority of the grains θ was ~70^o.

darker diffraction contrast around the edges indicates that these nanostructures are indeed nanotubes. The HRTEM in Figure 3.8b shows lattice fringes separated by 7.3 Å only at the edges of the tube which further confirms the tube morphology. These lattice fringes correspond to the (200) lattice spacing in $Na_2Ti_2O_4(OH)_2$ and are slightly closer together than the 8.5 Å (200) lattice spacing found from XRD (see below). This difference is due to water desorption from between the (200) planes when the sample is placed in the high vacuum electron microscope: water desorption allows the (200) planes to move closer together. In addition, there are 4 fringes on one side of the tube and 5 on the other indicating that the nanotubes are formed through scrolling of the two dimensional $Na_2Ti_2O_4(OH)_2$ sheets into a spiral.

The $Na_2Ti_2O_4(OH)_2$ nanotubes are transformed to $H_2Ti_2O_4(OH)_2$ nanotubes via

$$Na_2Ti_2O_4(OH)_2 + 2HCl \longrightarrow H_2Ti_2O_4(OH)_2 + 2NaCl \qquad (3.7)$$

whereby Na^+ ions are exchanged with H^+ in a dilute HCl bath. Both XRD and energy dispersive X-ray spectroscopy (EDS) confirm this conversion (see below). Upon annealing at 500 °C for one hour, the $H_2Ti_2O_4(OH)_2$ nanotubes dehydrate and rearrange to form polycrystalline anatase TiO_2 nanowires such as those shown in Figures 3.4 and 3.6. During the annealing step the morphology changes, on the nanometer scale, from nanotubes to nanowires. However, the morphology on the micrometer scale (see for example, Figure 3.7) is maintained despite the crystal structure transformation from body-centered orthorhombic for $H_2Ti_2O_4(OH)_2$ to body-centered tetragonal for anatase TiO_2.

3.5 Crystal Structure Evolution During Nanowire Synthesis

Figure 3.9 shows the X-ray microdiffraction (XRD) from nanotubes and nanowires after each step of the synthesis and the corresponding crystal structures deduced from this data. The XRD from nanotubes (Figure 3.9a) produced through the hydrothermal synthesis step could be indexed to the sodium titanate, $Na_2Ti_2O_4(OH)_2$ which has the body-centered orthorhombic crystal structure shown above the corresponding XRD. The body-centered orthorhombic $Na_2Ti_2O_4(OH)_2$ is made up of TiO_6 octahedra that share edges to form 2-dimensional sheets. These sheets are held together and electrostatically stabilized with Na^+ and OH^- in between the layer. Hydrogen

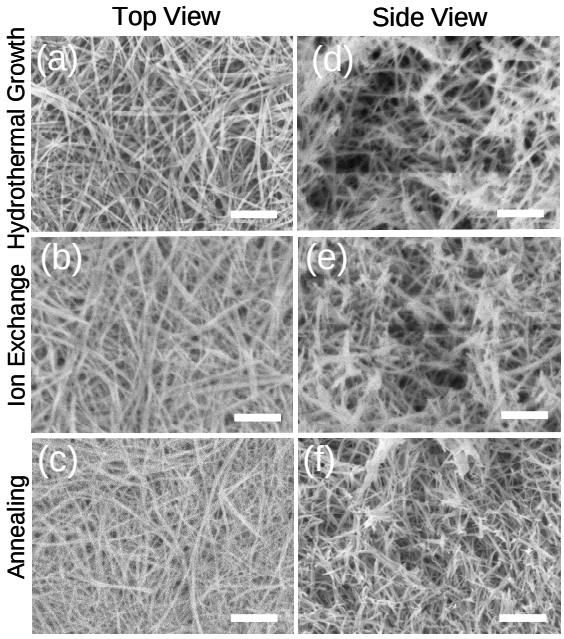

Figure 3.7 Top (left column, a, b and c) and cross-sectional views (right column, d, e, and f) of sodium titanate nanotubes formed after the hydrothermal growth (a and d), hydrogen titanate nanotubes formed after ion exchange (b and e), and anatase TiO_2 nanowires formed after annealing (c and f). Scale bars are 500 nm.

titanate, $H_2Ti_2O_4(OH)_2$, formed by exchanging Na^+ with H^+ (e.g., as in the ion-exchange step) has the same crystal structure albeit with different spacing between the sheets. The XRD from nanotubes obtained after the ion exchange step is shown in Figure 3.9b. The powder diffraction pattern, from the JCPDS file,[29] for $H_2Ti_2O_4(OH)_2$ is also shown (vertical bars) in Figures 3.9a and 3.9b for comparison to the XRD spectra obtained from $Na_2Ti_2O_4(OH)_2$ and $H_2Ti_2O_4(OH)_2$ nanotubes, respectively. Based on the nearly perfect match between the powder diffraction pattern from $H_2Ti_2O_4(OH)_2$ and the nanotubes (Figure 3.9b) obtained after the ion exchange step, we conclude that this material is indeed $H_2Ti_2O_4(OH)_2$. Since $H_2Ti_2O_4(OH)_2$ and $Na_2Ti_2O_4(OH)_2$ have the same crystal structure their XRD patterns are also similar. However, the (200) diffraction peak location in $H_xNa_{2-x}Ti_2O_4(OH)_2$ ($0 \leq x \leq 2$) can vary between ~9.2° and ~10.5° and depends on the distance between the TiO_6 sheets. The distance between TiO_6 sheets in turn depends on the relative amounts of Na^+ and H^+ (e.g., x), and OH^- between the layers.[30] For example, the (200) diffraction peak in the $Na_2Ti_2O_4(OH)_2$ XRD (Figure 3.9a) is at 10.34°, shifted higher by 0.43° relative to the $H_2Ti_2O_4(OH)_2$ (200) peak at 9.91° (Figure 3.9b). The (110), (310), (020), and (220) peaks are also slightly shifted (0.16°, 0.56°, 0.28°, and 0.24°, respectively) in the $Na_2Ti_2O_4(OH)_2$ XRD in comparison to the $H_2Ti_2O_4(OH)_2$ powder diffraction pattern and this could be due to the shift in the distance between the titanate layers due to different degrees of ion incorporation or possibly due to strain induced by the nanotube morphology. Electron diffraction from an ensemble of $Na_2Ti_2O_4(OH)_2$ nanotubes (Figure 3.8a inset) was consistent with XRD from the same sample (Figure 3.9a) and could be indexed to $Na_2Ti_2O_4(OH)_2$.

After the ion-exchange, the TiO_6 octahedra layers remain unchanged but the Na^+ ions are replaced with H^+ ions as shown in the crystal structure in Figure 3.9b. As the H^+ ions replace the Na^+ ions, the distance between the 2-dimensional layers increases and the (200) and (310) peaks shift to a lower diffraction angle and match well to the $H_2Ti_2O_4(OH)_2$ powder diffraction spectra as shown in Figure 3.9b. The (110), (020) and (220) peaks however remain slightly shifted relative to the $H_2Ti_2O_4(OH)_2$ powder diffraction pattern which indicates that these peak shifts may be due to strain induced by the nanotube morphology. The ion exchange also results in the increased intensity of the

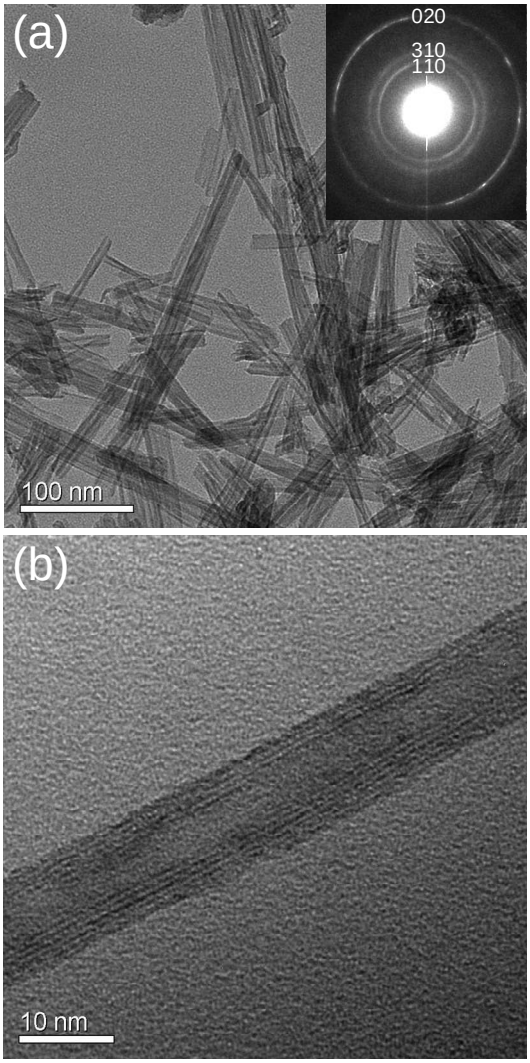

Figure 3.8 (a) TEM image of $Na_2Ti_2O_4(OH)_2$ nanotubes with an average outer diameter of 11 ± 2 nm and an average inner diameter of 4 ± 1 nm. Inset shows the selected area electron diffraction pattern of an ensemble of nanotubes; the diffraction pattern can be indexed to $Na_2Ti_2O_4(OH)_2$. (b) HRTEM of a $Na_2Ti_2O_4(OH)_2$ nanotube showing 4 and 5 lattice fringes on its top and bottom sides, respectively. This indicates that the nanotubes are formed by the spiraling of $Na_2Ti_2O_4(OH)_2$ sheets. The lattice fringes are separated by 7.3 Å and correspond to the {200} planes.

(110) peak relative to the (310) peak, this has been attributed to the replacement of Na^+ ions with H^+ ions [31] as well as to the transformation of the crystal structure.[30] Figure 3.9c shows the XRD pattern of the TiO_2 nanowires formed after the annealing step. The XRD pattern indexes to anatase TiO_2 whose structure is shown above the XRD pattern. Compared to the JCPDS powder diffraction pattern from anatase, the (101) diffraction peak from the TiO_2 nanowires is enhanced relative to the other peaks, which indicates that the grains within the nanowires are oriented with their {101} planes nearly perpendicular to the nanowire axis. This is consistent with the findings from the HRTEM study.

3.6 Nanowire Formation Mechanism

Upon heating to 500 ^oC, the $H_2Ti_2O_4(OH)_2$ nanotubes dehydrate and undergo a topotactic transformation to form anatase TiO_2 nanowires. Figure 3.10 illustrates this transformation which is similar to that proposed previously for the transformation of $H_2Ti_2O_4(OH)_2$ nanotubes to anatase nanorods through hydrothermal treatment at low pH.[30,32-35] Figure 3.10a shows the $H_2Ti_2O_4(OH)_2$ crystal structure viewed along the [001] axis. The edge-sharing octahedra form sheets and a zig-zag pattern in the [010] direction within these sheet. To form the $H_2Ti_2O_4(OH)_2$ nanotubes, these layers are scrolled around the [010] axis as shown in Figure 3.10b (i.e., the sheets in Figure 3.10a scroll out of and back into the page to form the nanotubes). Anatase TiO_2 viewed along the [010] direction is shown in Figure 3.10c. A comparison of Figure 3.10c with Figure 3.10a reveals that the zig-zag pattern formed by the TiO_6 octahedra in the $H_2Ti_2O_4(OH)_2$ layers along the [010] direction is similar to the zig-zag pattern formed by the TiO_6 octahedra in the anatase along the [100] direction.[30,32-35] As the $H_2Ti_2O_4(OH)_2$ nanotubes are heated and dehydrate, the layers in $H_2Ti_2O_4(OH)_2$ approach each other and rearrange to form the polycrystalline anatase nanowire (Figure 3.10d).

Since the sheets spiral such that the nanotube axis is along the [010] direction, the anatase nanowire axis should be aligned with the [100] direction in the tetragonal lattice. Specifically, the {101} planes of anatase form a 68.3° angle with the [100] direction. TEM was used to confirm that the nanowire axis was indeed the [100] direction by measuring the angle between the {101} planes of anatase and the local nanowire axis.

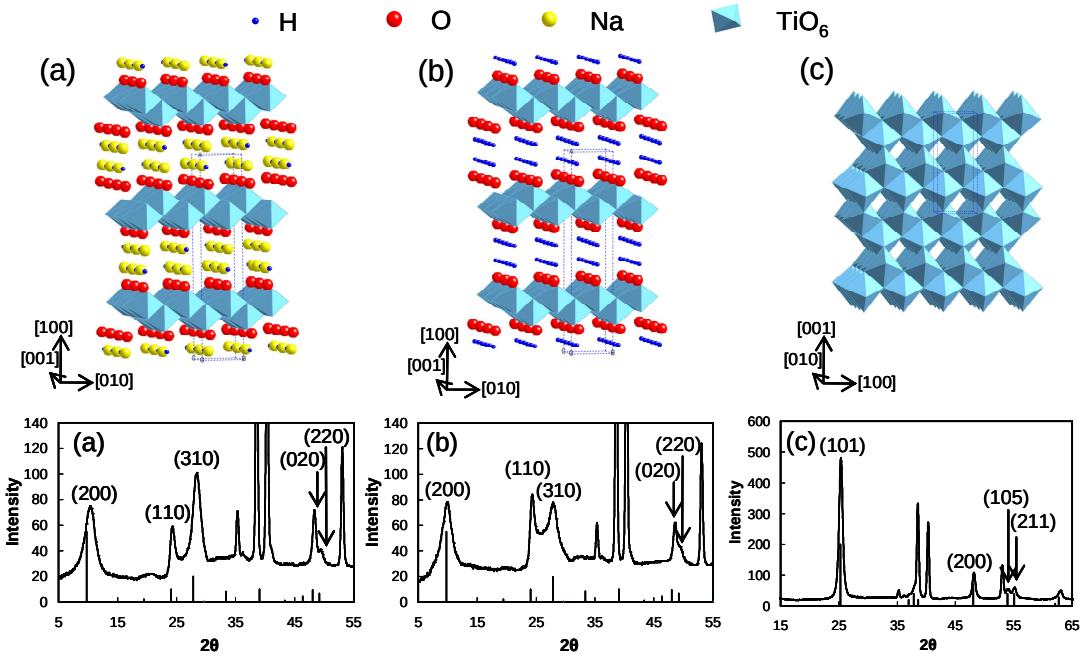

Figure 3.9 X-ray microdiffraction 2θ scans of the nanostructured titanium foil surface after (a) hydrothermal growth, (b) ion exchange and (c) annealing steps. The XRD spectra could be indexed to (a) $Na_2Ti_2O_4(OH)_2$, (b) $H_2Ti_2O_4(OH)_2$ and (c) anatase TiO_2. The corresponding crystal structures are shown above the XRD spectra. The powdered diffraction reference peaks from the JCPDS files in (a) and (b) are of $H_2Ti_2O_4(OH)_2$ and in (c) of anatase TiO_2. Unindexed peaks correspond to the hcp diffractions from the titanium foil substrate. The blue octahedra represent TiO_6 octahedra. The yellow, red and blue spheres represent sodium, oxygen and hydrogen, respectively.

Figure 3.11 shows a typical HRTEM of the anatase nanowires with the angles between the {101} planes and the axis of the nanowires indicated. From a statistically significant number of measurements, an average angle of 75 ± 9° was found between the {101} planes and the nanowire axis. The error in the measurements is almost completely due to the difficulty in determining the nanowire axis to better than ~5°, especially when the crystal being examined is near the center of the wire. When just the crystals near the edges of the nanowires were included in the statistics, an average angle of 71 ± 2° was found. This is remarkably close to the theoretically predicted value and corroborates the proposed dehydration and rearrangement mechanism for the transformation of $H_2Ti_2O_4(OH)_2$ nanotubes to anatase nanowires. The small deviation can be explained since a slight rotation of the nanocrystals is to be expected as the polycrystalline nanowires are formed and there could also be significant amounts of strain in the nanowires.

3.7 Mechanism of $Na_2Ti_2O_4(OH)_2$ Nanotube Formation

The $Na_2Ti_2O_4(OH)_2$ and $H_2Ti_2O_4(OH)_2$ nanotube films were also examined with energy dispersive spectroscopy (EDS), in a scanning electron microscope (6500 JEOL) to understand how the titanium foil is transformed into these nanostructures. Na, Ti and O are detected in the sodium titante nanotubes. Whereas only Ti and O are detected in the hydrogen titanate nanotubes, confirming that within the detection limits of EDS, all the Na^+ ions are replaced by H^+ ions during the ion exchange step. EDS spectra were also collected while scanning across a cross section of the nanotube films to obtain an approximate depth profile of the elemental composition. Figure 3.12 shows the variation of Na, O and Ti content as a function of distance from the surface of the nanotube film down towards the titanium foil. Both the sodium and oxygen concentrations go to zero at the titanium foil and the titanium counts rise rapidly but this is not shown on the figure. At the interface between the nanotube film and the denser mesoporous transition layer there is a drop in both the sodium and oxygen content. This indicates that the overall reaction that leads to $Na_2Ti_2O_4(OH)_2$,

$$2Ti + 2NaOH + 4H_2O_2 \longrightarrow Na_2Ti_2O_4(OH)_2 + 4H_2O \qquad (3.8)$$

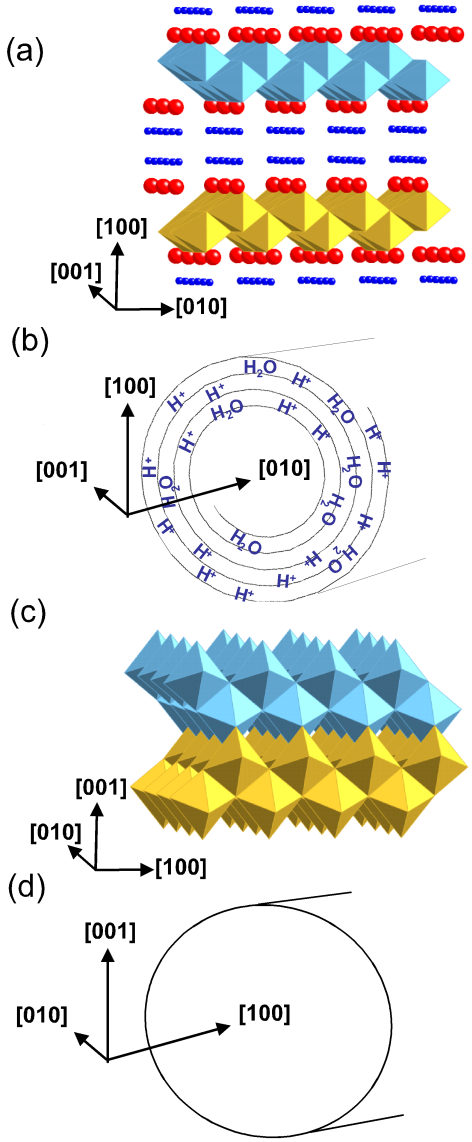

Figure 3.10 Schematic illustrations to aid in visualization of the proposed transformation mechanism from $H_2Ti_2O_5 \cdot H_2O$ nanotubes to anatase TiO_2 nanowires. (a) The $H_2Ti_2O_5 \cdot H_2O$ crystal structure viewed along the [001] axis. TiO_6 octahedra share edges to form sheets with a zig-zag pattern in the [010] direction. (b) The $H_2Ti_2O_5 \cdot H_2O$ layers are scrolled around the [010] axis to form the $H_2Ti_2O_5 \cdot H_2O$ nanotubes. (c) Anatase TiO_2 viewed along the [010] direction. A comparison of (c) with (a) shows that the zig-zag pattern formed by the TiO_6 octahedra in the $H_2Ti_2O_5 \cdot H_2O$ layers along the [010] direction is similar to the zig-zag pattern formed by the TiO_6 octahedra in the anatase along the [100] direction. As the $H_2Ti_2O_5 \cdot H_2O$ nanotubes are heated, the TiO_6 layers approach each other and rearrange to form polycrystalline anatase nanowires.

has progressed to different degrees of completion as one moves from the surface of the film towards the titanium foil. There seems to be a diffuse but well-defined boundary that delineates the nanotube morphology from a region that is in the process of being converted (the mesoporous transition region). This boundary moves with time from the solution-film interface towards the titanium foil. Above the boundary, there is enough sodium and oxygen to create, exfoliate and spiral the $Na_2Ti_2O_4(OH)_2$ sheets into nanotubes. Below the boundary, there is sodium and oxygen but the reaction has not progressed enough to form nanotubes. This region below the boundary is the mesoporous transition layer that forms between the sodium titanate nanotubes and the titanium foil. With increased synthesis time sodium and OH^- reach further into the substrate and the nanotube film and the mesoporous layer both get thicker at the expense of the titanium foil. Within the accuracy of the EDS measurements, the Ti/O and Ti/Na weight percent ratios in the sodium titanate nanotube film (taken from a side view of the film) were on average 1.2 and 2.7, respectively. The Ti/O ratio is between the Ti/O ratio of $Na_2Ti_2O_4(OH)_2$ (1.0) and $Na_2Ti_2O_4$ (1.5) which indicates that there is some dehydration when the sample is placed in the high vacuum electron microscope. The Ti/Na ratio is high compared to the Ti/Na weight percent ratio of 2.1 in $Na_2Ti_2O_4(OH)_2$. This could be due to some Na^+ ions being removed during the deionized water rinse. The variation of the titanium and oxygen concentrations in the hydrogen titanate nanotube films is similar to that shown in Figure 3.12 but no Na^+ can be detected. As in the sodium titanate nanotubes, there is a drop in the oxygen content at the interface between the hydrogen titanate nanotube film and the mesoporous layer. The Ti/O weight percent ratio (also taken from a side view of the film) remains around 1.2, which further supports the conclusion that the 2-dimensional layers made up of Ti and O do not change during the ion exchange and the only structural change is the replacement of Na^+ with H^+.

3.8 TiO_2 Nanowire Dye-Sensitized Solar Cells

The titanium foil with TiO_2 nanowires was used as the photoanode in the DSSC shown in the inset of Figure 3.13. Typically, DSSC photoanodes are assembled on transparent conducting substrates so that they can be illuminated from the anode side; in this way, transmission losses through the platinum coated cathode and the electrolyte are

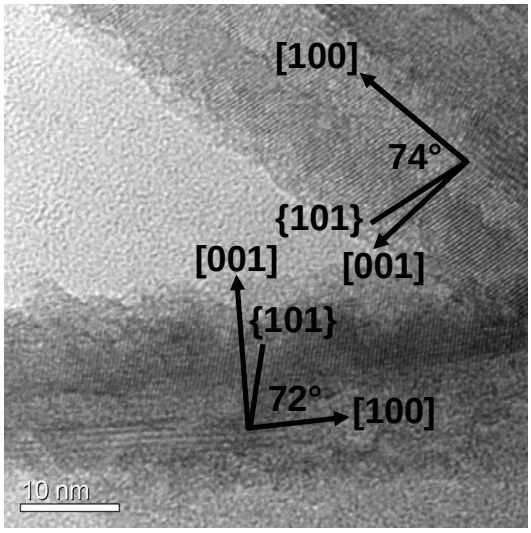

Figure 3.11 A typical HRTEM of the anatase nanowires. The angles between the {101} planes and the nanowire axis are indicated for two typical grains. On average these angles were ~70° which supports the mechanism proposed for the transformation of $H_2Ti_2O_4(OH)_2$ nanotubes to TiO_2 nanowires.

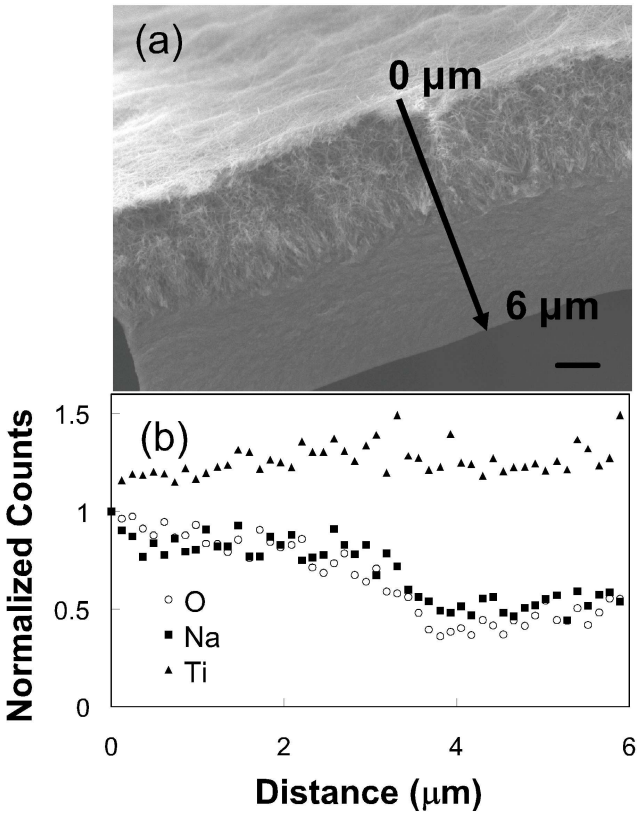

Figure 3.12 (a) Cross-sectional SEM image of $Na_2Ti_2O_4(OH)_2$ nanotubes. The arrow indicates the location of the EDS linescan. The position indicated as 0 µm corresponds to the top surface of the nanotube film and 6 µm corresponds to a position at the bottom of the mesoporous transition layer. Scale bar is 1 µm. (b) Normalized EDS counts of Ti, Na and O as a function of distance along the arrow indicated in (a). The drop in the Na and O counts occurs at the interface between the nanotubes and the mesoporous particle layer.

minimized. However, since the TiO_2 nanowires were grown on the titanium foil, the cells assembled for this study had to be illuminated from the cathode side. The thin platinum layer on the cathode had a transmission of ~60%. The current-voltage characteristic of a representative solar cell assembled using a TiO_2 nanowire film is shown in Figure 3.13. Under 100 mW/cm^2 of AM1.5 illumination, this cell produces a short circuit current of ~5.6 mA/cm^2 with an open-circuit voltage of ~0.62 V and a fill factor of 0.52. The overall power conversion efficiency was 1.8%. Figure 3.14 shows a typical incident photon to current efficiency (IPCE) as a function of wavelength and a photoaction spectrum. The IPCE reaches 50% at 530 nm which is near the absorbance maximum of the dye. This is a promising result considering that the transmission through the cathode is only ~60%. The IPCE drops to zero at ~400 nm because of absorption by the electrolyte.

Electron transport and recombination rates of the TiO_2 nanowire DSSCs as well as a TiO_2 nanoparticle DSSCs, made on Ti foil, were measured using transient photocurrent and photovoltage spectroscopies (details can be found in Emil Enache-Pommer's Ph.D. thesis).[20] The TiO_2 nanoparticle DSSC was assembled using ~15 nm diameter anatase particles purchased from Aldrich (cat #637254-50G). The nanoparticle films were deposited on the Ti foil by suspending the nanoparticles in ethanol and drop casting the solution on to the Ti foil and allowing the film to dry in air. The thickness of the TiO_2 nanoparticle film was ~16 ± 2 μm (Figure 3.15a).

In typical DSSCS, both recombination and transport times exhibit a power law dependence on the short-circuit current density (or light intensity).[2,19] The power law exponents describes the distribution of transport-limiting traps and thus is used to compare the trap density of different DSSCs.[2,36] Figure 3.16 shows the electron transport time constants as a function of short circuit current density (proportional to incident light intensity) found for both the nanowire DSSC and the nanoparticle DSSC. The electron transport time constants for the nanowire DSSCs are shown for two different cells using both IMPS as well as photocurrent decay. There is reproducibility between the different cells as well as the different measurement techniques. The electron transport time

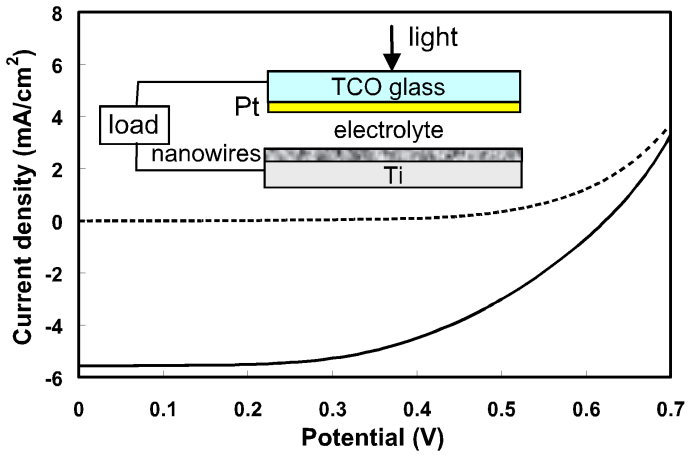

Figure 3.13 A typical current-voltage characteristic of a TiO_2 nanowire DSSC with short circuit current, open circuit voltage, fill factor and overall efficiency of 5.6 mA/cm^2, 0.62 V, 0.52, and 1.8%, respectively. The inset shows a schematic of the TiO_2 nanowire DSSC and the illumination geometry.

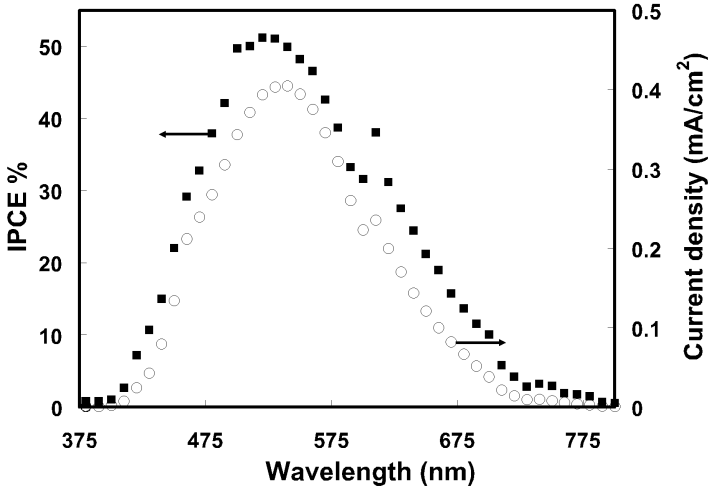

Figure 3.14 Incident photon to current efficiency (IPCE) and photocurrent action spectra of a typical TiO_2 nanowire DSSC.

constants for the TiO_2 nanoparticle DSSC were found using photocurrent decay for one cell. The transport time constants for the nanowire DSSCs varied between 2 and 8 ms whereas the time constants for the nanoparticle DSSC varied between 6 and 45 ms. The power law exponents for the electron transport for the nanowires and the nanoparticles were -0.39 and -0.73 respectively. Since the power law exponents are different, it is likely that the transport limiting trap distributions are different in the TiO_2 nanowires as compared to the TiO_2 nanoparticles. As occurs in most DSSCs, the transport time increases with short-circuit current for both the nanoparticle and nanowire cells. This is because at higher short-circuit currents the electron density is higher in the nanowires/nanoparticle which results in more filled traps and therefore faster transport.[37] While the electron transport through the nanowires in this experiment appears to be between 2-6 times faster than through the nanoparticles, this difference may not be entirely due to the superior electron transport ability of the nanowires, but rather due to other differences between the two cells, such as photoanode thickness, which will be discussed next.

Fair comparison of electron transport time in DSSCs with drastically different morphologies is a complicated issue. Ideally, when the performance of two DSSCs are compared, both cells should have the same photoanode thickness as well as the same roughness factor. In this way, the apparent distance traveled by the electrons as well as the number of injected electrons are the same in both cells. However, it is nearly impossible to achieve this comparison in practice since different photoanode morphologies have different surface areas per unit thickness. Thus, in practice, cells either with similar photoanode thicknesses or with similar roughness factors are compared. An additional difficulty is that the roughness factor is determined by desorbing the dye and measuring the optical absorption of the resulting dye solution, after the cell is assembled, operated and dissassembled.

The nanoparticle and nanowire cells in this experiment had roughness factors and photoanode thicknesses of ~1300 and ~16 ± 2 μm, and ~700 and 7 ± 3 μm, respectively. Thus, the slower electron transport through the nanoparticle DSSCs as compared to the nanowire DSSCs may be explained partly by the nanoparticle film thickness being

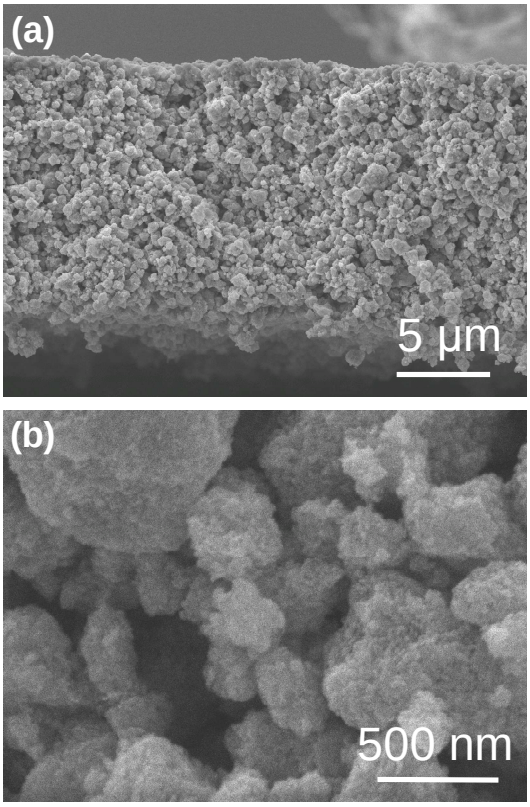

Figure 3.15 (a) Low magnification and (b) higher magnification cross-sectional SEM images of anatase TiO_2 nanoparticles deposited on Ti foil for use in a nanoparticle DSSC. The nanoparticle film layer was 16 ± 2 µm thick and the ~15 nm particles aggregated into larger, >100 nm, particles.

greater than the nanowire film thickness. It is reasonable to presume that thicker nanoparticle films result in slower electron transport because the electrons have to travel a longer distance to the anode than in the nanowire cells. Moreover, we noticed that the ~15 nm TiO_2 nanoparticles aggregated into larger (>100 nm) particles (Figure 13.15b) resulting in reduced connectivity within the nanoparticle film which may also contribute to the slower electron transport rate. Regardless of these details, the mere fact that the TiO_2 nanoparticle films and TiO_2 nanowires have electron transport times within the same order of magnitude is surprising. When nanowires were first proposed as photoanodes in DSSCs, the electron transport rate in nanowires was expected to be several hundred times faster than nanoparticles.[38,39] Indeed, electron transport rates in single crystal ZnO nanowires have been measured to be significantly faster than in nanoparticles.[20,40,41]

The electron recombination times were measured using photovoltage decay for both the nanowire and nanoparticle DSSCs. Figure 3.17 shows the electron recombination time as a function of short circuit current density. The current density was varied by changing the incident light intensity. The nanowire DSSC recombination time constants varied with short circuit current density between 250 and 1300 ms. The recombination time constants were found for two different nanowire DSSCs and were reproducible between cells. As is seen in typical DSSCs, the nanowire recombination times got faster as the short-circuit current increased. This is because at higher short-circuit current densities there is a higher electron density in the nanowires, and since the recombination rate is proportional to square of the electron density,[42] this leads to faster recombination rates at higher short-circuit current densities. The recombination time constants of the nanoparticle DSSC varied with short-circuit current density between 170 and 650 ms which was only slightly faster than in the nanowire DSSCs. The power law exponents for the recombination times for the nanowire and nanoparticles DSSCs were -0.53 and -0.47 respectively. The nanowire cells have slightly slower recombination time constants as compared to the nanoparticle cells but this amount of variation is similar to that seen from cell to cell in nanoparticle DSSCs[2,43] therefore the recombination rates are essentially the same in the nanowire and nanoparticle DSSCs made in this work.

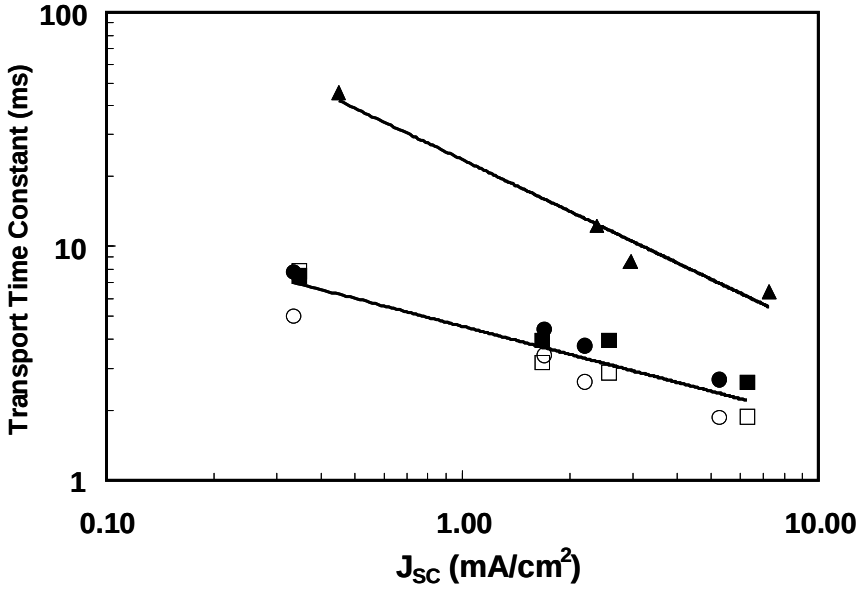

Figure 3.16 Electron transport time constants for TiO_2 nanowire (■,□,●,○) and nanoparticle (▲) DSSCs as a function of short circuit current density (light intensity). Open (□,○) and filled (▲,●,■) symbols represent transport time constants extracted from IMPS and photocurrent decay, respectively. Data for two nanowire DSSCs (■,□) and (●,○) are shown to demonstrate reproducibility. Only one nanoparticle cell was measured.

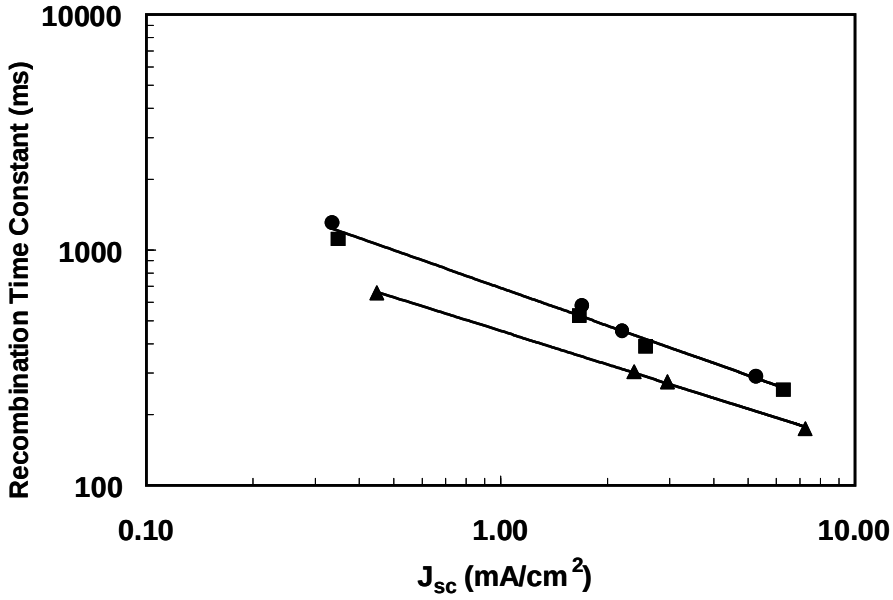

Figure 3.17 Recombination time constants for TiO_2 nanowire (●,■) and nanoparticle (▲) DSSCs as a function of short circuit current density (light intensity). Data for two nanowire DSSCs (●,■) is shown to demonstrate reproducibility. All data was found using photocurrent decay.

Although in this work we found that the electron transport times were faster and the recombination time were slightly slower in the nanowire DSSCs as compared to the particle DSSCs, the opposite is true if the nanowire DSSCs in this work are compared to nanoparticle DSSCs in the literature.[2,43] The electron transport time constants in the TiO_2 nanowire DSSCs in this work are similar to those reported for TiO_2 nanoparticle DSSCs in the literature.[2,43] While the electron recombination time constants in the TiO_2 nanowire DSSCs in this work are an order of magnitude slower than those reported for TiO_2 nanoparticle DSSCs in the literature.[2,43] Electron transport and recombination time constants in TiO_2 nanoparticle DSSCs, made on Ti foil, were measured to be between 1 and 10 ms and 10 and 100 ms, respectively.[2] Thus, the increased electron collection efficiency, η_{coll} , found in the nanowire DSSC in this work is due to slower electron recombination rate and not due to faster electron transport.[19] Zhu et al.[2] have also made similar conclusions regarding polycrystalline TiO_2 nanotube DSSCs.

One reason that the TiO_2 nanowire DSSCs do not demonstrate faster electron transport as compared to TiO_2 nanoparticle DSSCs in the literature could be that the nanowires are polycrystalline. The electrons have to cross grain boundaries in the nanowires to reach the collection electrode, a situation similar to that exists in nanoparticle films wherein the electrons must cross particle-particle interfaces. Thus, one way to improve the transport could be to synthesize single crystal TiO_2 nanowires. In addition, synthesizing these on a transparent conducting oxide would also be desired since it would allow for illumination from the anode side, avoiding absorption by the platinized cathode and the electrolyte and resulting in more light incident on the photoanode. The growth of single crystal rutile TiO_2 nanowires on a transparent conducting oxide has only recently been achieved and published.[44] However, it has been found that the electron transport rates through these single crystal nanowires is surprisingly low (personal communication with Bin Liu, April 8, 2009).[45] This slower electron transport could be due to a high defect density in these nanowires which results in the electrons transporting via a trap to trap hopping mechanism and not via direct transport though the conduction band. While the nanowire/nanotube morphology does result in higher electron collection efficiencies due to lower recombination rates[2,19] it is

not clear if the TiO_2 nanowire/nanotube morphology will result in a significant increase in electron transport as has been predicted.[2,38,39] Further research must be done in order to determine if TiO_2 nanowires are capable of providing significantly increased electron transport.

3.9 Conclusions

Polycrystalline TiO_2 nanowires were grown on titanium foil through a three-step process. In the first step, sodium titanate nanotubes are grown hydrothermally on titanium foil. Next, the sodium ions are exchanged with protons to convert the sodium titanate nanotubes to hydrogen titanate nanotubes. Finally, the hydrogen titanate nanotubes are transformed to anatase TiO_2 nanowires through a topotactic transformation upon heating. The evolution of the morphology and structure throughout the synthesis process was investigated and a detailed mechanism is proposed for the transformation of $H_2Ti_2O_4(OH)_2$ nanotubes to TiO_2 nanowires, wherein the TiO_6 sheets in $H_2Ti_2O_4(OH)_2$ nanotubes rearrange upon heating and bond to form polycrystalline anatase nanowires. The TiO_2 nanowire films on titanium foil were suitable for use as the photoanode in dye-sensitized solar cells. While the electron collection efficiency was increased due to decreased electron recombination the electron transport in the nanowire DSSCs was similar to that of TiO_2 nanoparticles.

References

(1) Adachi, M.; Murata, Y.; Takao, J.; Jiu, J. T.; Sakamoto, M.; Wang, F. M. *J. Am. Chem. Soc.* **2004**, *126*, 14943.

(2) Zhu, K.; Neale, N. R.; Miedaner, A.; Frank, A. J. *Nano Lett.* **2007**, *7*, 69.

(3) Mor, G. K.; Shankar, K.; Paulose, M.; Varghese, O. K.; Grimes, C. A. *Nano Lett.* **2006**, *6*, 215.

(4) Macák, J. M.; Tsuchiya, H.; Schmuki, P. *Angew. Chem. Int. Edit.* **2005**, *44*, 2100.

(5) Song, M. Y.; Kim, D. K.; Ihn, K. J.; Jo, S. M.; Kim, D. Y. *Nanotechnology* **2004**, *15*, 1861.

(6) Yoon, J. H.; Jang, S. R.; Vittal, R.; Lee, J.; Kim, K. J. *J Photoch Photobio A* **2006**, *180*, 184.

(7) Ohsaki, Y.; Masaki, N.; Kitamura, T.; Wada, Y.; Okamoto, T.; Sekino, T.; Niihara, K.; Yanagida, S. *Phys. Chem. Chem. Phys.* **2005**, *7*, 4157.

(8) Uchida, S.; Chiba, R.; Tomiha, M.; Masaki, N.; Shirai, M. *Electrochemistry* **2002**, *70*, 418.

(9) Wei, M. D.; Konishi, Y.; Zhou, H. S.; Sugihara, H.; Arakawa, H. *J. Electrochem. Soc.* **2006**, *153*, A1232.

(10) Pan, K.; Zhang, Q. L.; Wang, Q.; Liu, Z. Y.; Wang, D. J.; Li, J. H.; Bai, Y. B. *Thin Solid Films* **2007**, *515*, 4085.

(11) Pavasupree, S.; Ngamsinlapasathian, S.; Nakajima, M.; Suzuki, Y.; Yoshikawa, S. *J. Photoch. Photobio A* **2006**, *184*, 163.

(12) Tan, B.; Wu, Y. Y. *J. Phys. Chem. B* **2006**, *110*, 15932.

(13) Kasuga, T.; Hiramatsu, M.; Hoson, A.; Sekino, T.; Niihara, K. *Langmuir* **1998**, *14*, 3160.

(14) Kasuga, T.; Hiramatsu, M.; Hoson, A.; Sekino, T.; Niihara, K. *Adv. Mater.* **1999**, *11*, 1307.

(15) Zhao, Y. N.; Lee, U. H.; Suh, M.; Kwon, Y. U. *B. Kor. Chem. Soc.* **2004**, *25*, 1341.

(16) Zhao, Y. N.; Jin, J.; Yang, X. Q. *Mater. Lett.* **2007**, *61*, 384.

(17) Tian, Z. R. R.; Voigt, J. A.; Liu, J.; McKenzie, B.; Xu, H. F. *J. Am. Chem. Soc.* **2003**, *125*, 12384.

(18) Sommeling, P. M.; O'Regan, B. C.; Haswell, R. R.; Smit, H. J. P.; Bakker, N. J.; Smits, J. J. T.; Kroon, J. M.; van Roosmalen, J. A. M. *J. Phys. Chem. B* **2006**, *110*, 19191.

(19) Enache-Pommer, E.; Boercker, J.; Aydil, E. S. *Appl. Phys. Lett.* **2007**, *91*, 123116.

(20) Enache-Pommer, E., University of Minnesota, 2009.

(21) Leschkies, K. S.; Divakar, R.; Basu, J.; Enache-Pommer, E.; Boercker, J. E.; Carter, C. B.; Kortshagen, U. R.; Norris, D. J.; Aydil, E. S. *Nano Lett.* **2007**, *7*, 1793.

(22) Grätzel, M. *Pure Appl. Chem.* **2001**, *73*, 459.

(23) Dloczik, L.; Ileperuma, O.; Lauermann, I.; Peter, L. M.; Ponomarev, E. A.; Redmond, G.; Shaw, N. J.; Uhlendorf, I. *J. Phys.Chem.B* **1997**, *101*, 10281.

(24) Peter, L. M.; Wijayantha, K. G. U. *Electrochim. Acta* **2000**, *45*, 4543.

(25) Nakade, S.; Kanzaki, T.; Wada, Y.; Yanagida, S. *Langmuir* **2005**, *21*, 10803.

(26) Boschloo, G.; Haggman, L.; Hagfeldt, A. *J. Phys. Chem. B* **2006**, *110*, 13144.

(27) Zaban, A.; Greenshtein, M.; Bisquert, J. *Chemphyschem* **2003**, *4*, 859.

(28) Bisquert, J.; Zaban, A.; Greenshtein, M.; Mora-Sero, I. *J. Am. Chem. Soc.* **2004**, *126*, 13550.

(29) Sugita, M.; Tsuji, M.; Abe, M. *B. Chem. Soc. Jpn.* **1990**, *63*, 1978.

(30) Tsai, C. C.; Teng, H. S. *Chem. Mater.* **2006**, *18*, 367.

(31) Yang, J. J.; Jin, Z. S.; Wang, X. D.; Li, W.; Zhang, J. W.; Zhang, S. L.; Guo, X. Y.; Zhang, Z. J. *Dalton T.* **2003**, 3898.

(32) Nian, J. N.; Teng, H. S. *J. Phys. Chem. B* **2006**, *110*, 4193.

(33) Zhu, H. Y.; Gao, X. P.; Lan, Y.; Song, D. Y.; Xi, Y. X.; Zhao, J. C. *J. Am. Chem. Soc.* **2004**, *126*, 8380.

(34) Zhu, H. Y.; Lan, Y.; Gao, X. P.; Ringer, S. P.; Zheng, Z. F.; Song, D. Y.; Zhao, J. C. *J. Am. Chem. Soc.* **2005**, *127*, 6730.

(35) Yu, Y. X.; Xu, D. S. *Appl. Catal. B-Environ.* **2007**, *73*, 166.

(36) van de Lagemaat, J.; Frank, A. J. *J. Phys. Chem. B* **2001**, *105*, 11194.

(37) Benkstein, K. D.; Kopidakis, N.; van de Lagemaat, J.; Frank, A. J. *J. Phys. Chem. B* **2003**, *107*, 7759.

(38) Law, M.; Greene, L. E.; Johnson, J. C.; Saykally, R.; Yang, P. D. *Nat. Mater.* **2005**, *4*, 455.

(39) Baxter, J. B.; Aydil, E. S. *Appl. Phys. Lett.* **2005**, *86*, 53114.

(40) Martinson, A. B. F.; McGarrah, J. E.; Parpia, M. O. K.; Hupp, J. T. *Phys. Chem. Chem. Phys.* **2006**, *8*, 4655.

(41) Galoppini, E.; Rochford, J.; Chen, H. H.; Saraf, G.; Lu, Y. C.; Hagfeldt, A.; Boschloo, G. *J. Phys. Chem. B* **2006**, *110*, 16159.

(42) Fisher, A. C.; Peter, L. M.; Ponomarev, E. A.; Walker, A. B.; Wijayantha, K. G. U. *J. Phys. Chem. B* **2000**, *104*, 949.

(43) Frank, A. J.; Kopidakis, N.; van de Lagemaat, J. *Coordin. Chem. Rev.* **2004**, *248*, 1165.

(44) Liu, B.; Aydil, E. S. *J. Am. Chem. Soc.* **2009**, *131*, 3985.

(45) Enache-Pommer, E.; Liu, B.; Aydil, E. *Phys. Chem. Chem. Phys. submitted* **2009**.

Chapter 4 : Nanowire Seeding Methods

4.1 Introduction

This chapter introduces the chemical bath deposition synthesis of ZnO nanowires, on seeded substrates, from an aqueous solution of zinc nitrate hexahydrate and methenamine which is discussed in great detail in the following chapters. In addition, this chapter explains the various methods explored for seeding the substrates with ZnO and discusses the advantages and disadvantages of each method.

4.2 ZnO nanowire Growth and Seeding

Zinc oxide nanowire films have been grown using a variety of techniques such as vapor phase deposition,[1-3] metalorganic vapor-phase epitaxial growth,[4] electrodeposition,[5] molecular beam epitaxy,[6] and templating using anodic alumina membranes (AAM)[7,8]. While these techniques do yield uniform, well aligned ZnO nanowires most require high vacuum chambers, expensive sapphire substrates, and high processing temperatures, typically above 400 °C. Thus, these techniques are not suitable for making inexpensive, flexible solar cells on plastic substrates since plastics cannot endure temperatures above ~150 °C [9] and expensive high vacuum equipment increases processing costs.

Recently, a chemical bath deposition technique has been demonstrated which produces zinc oxide nanowire films from an aqueous solution of zinc nitrate hexahydrate and methenamine on virtually any substrate, at ambient pressure, and with processing temperatures below 100 °C.[10,11] There are two steps in the synthesis process. First, the substrate is seeded with ZnO by one of several techniques which will be discussed below. Second, the substrate is immersed, with the seeded side of the substrate facing the bottom of the reaction vessel, in an aqueous solution of zinc nitrate hexahydrate and methenamine and heated to 90 °C for 4 hours. ZnO nanowires nucleate on the seed layer and grow heterogeneously on the substrate. The ZnO nanowires synthesized are single crystal and grow along the (0001) axis. In a typical synthesis the nanowires grow ~1 μm in length and ~100 nm in diameter after 4 hours. Due to the majority of the zinc oxide

precursor (the identity of which is discussed in chapter 5) precipitating as homogenous growth in the solution, after 4 hours the heterogeneous growth on the substrate slows. Thus, to grow nanowires longer than ~1 μm the current state of the art is to replenish the reaction solution and allow the reaction to continue for another 4 hours. Each four hour reaction, termed a cycle, increases the nanowire length by ~1 μm. Using multiple cycles wires as long as ~25 μm[12] have been synthesized. These nanowires have relatively high mobilities, 1-5 $cm^2V^{-1}S^{-1}$,[12] and are single crystal,[13] which make them attractive for use as the photoanode in DSSCs.

However there are a couple of disadvantages to using these nanowires in DSSCs. First, the nanowire DSSCs made from these ZnO nanowires have only achieved an efficiency of ~2.4%,[14] due to the surface area being an order of magnitude smaller than that of a typical nanoparticle based DSSC. Second, the majority of the precursor being depleted due to homogeneous growth limits the heterogeneous growth rate as well as the yield (defined as the percentage of zinc in the solution which precipitates as heterogeneously grown nanowires). In order to improve the nanowire surface area, growth rate and yield this nanowire synthesis was studied in great detail as will be discussed in the remaining chapters.

The nanostructured zinc oxide seed layer deposited on the substrate prior to the nanowire growth is key to the successful synthesis of nanowires from the reaction solution. The energy required for heterogeneous nucleation is lower than that required for homogenous growth.[15-17] Thus the ZnO seed layer lowers the energy required for nanowire nucleation and allows ZnO nanowires to nucleate and grow uniformly across the seeded area of the substrate. Figure 4.1 shows the nanowire growth on both a seeded (using the thermal decomposition of zinc acetate method described below) and unseeded substrate. Densely packed, thin nanowires grow only on the seeded substrates. Whereas, micron thick rods grow sparsely on unseeded substrates.

The seed layer is a critical step in the growth process. Therefore, to study the nanowire growth and assemble efficient nanowire DSSCs, the seed layer must satisfy several key requirements. The seeding method must be reproducible, provide uniform

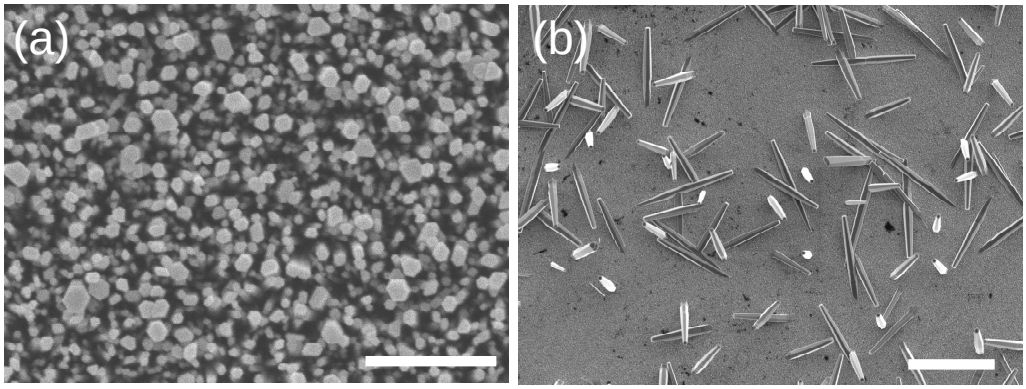

Figure 4.1 Top view SEM images of (a) a densely packed, aligned ZnO nanowires grown on a silicon substrate seeded using the thermal decomposition of zinc acetate method, (b) randomly oriented ZnO rods ~10 μm long and ~1 μm wide grown irregularly on a FTO substrate without a nanostructured seed layer deposited prior to growth. Scale bars are 500 nm in (a) and 10 μm in (b).

nanowire coverage, produce aligned nanowires, and be able to be tailored to change the nanowire number density and diameter. In addition, to maintain a high DSSC efficiency, the seed layer must allow efficient transport of electrons from the nanowires to the substrate. While this last requirement is obviously important it was not studied in detail in this thesis project and seed layers which satisfied as many of the other requirements as possible were utilized. However, Emil Enache-Pommer has studied the effect that different seed layers have on nanowire DSSC performance and those results will be published in his thesis.[18]

Ideally, the seed layer would be able to be tailored to allow for the control of the nanowire diameter, alignment and number density. This would allow for densely packed, thin nanowire films with high surface area to be synthesized. Currently seed layers are able to control nanowire alignment and number density, however, seed layers have a more limited control over the nanowire diameter and diameter size distribution.[16,17,19-23] The reason for the seed layers limited control of the diameter size and distribution is due to a lack of knowledge of how the ZnO nanowires nucleate on the seeds and what determines the nanowire diameter. Several researchers report that multiple wires nucleate from each nucleation site,[11,13,24] however what the defines a nucleation sight (i.e. one seed or multiple seeds), is still unclear. Thus, further understanding of the factors which govern the ZnO nucleation on the seed layer and what determines the nanowire diameter may promote more control over the diameter size and distribution

Several different seeding methods have been used for the synthesis of ZnO nanowire from aqueous solutions. Very thin films (10-250 nm) of zinc oxide deposited by pulsed laser deposition,[25] RF magnetron sputtering,[26] atomic layer deposition,[27] sputtering,[28] or thermal evaporation,[29] have been used as seed layers. These films can be easily patterned and create well aligned nanowire arrays, but the deposition either requires high temperature and/or high vacuum techniques which might limit their utilization in inexpensive DSSCs. We explored two potentially less expensive seeding techniques, drop casting ZnO nanoparticles[13] and thermally decomposing zinc acetate.[30] We ultimately decided that the thermal decomposition of zinc acetate was the best

method to use in the majority of the nanowire growth experiments. These two techniques are described in detail below.

4.3 Nanoparticle Seed Films

Zinc oxide nanoparticles have been synthesized as colloidal solutions using a variety of methods such as double-jet precipitation,[31] sol-gel processing,[32] flame spray pyrolysis,[33] and solution phase precipitation.[34] Solution phase methods are frequently used and usually make use of the reactions of a soluble zinc salt with a hydroxide ion in a nonaqueous solvent.[35] Aqueous solvents are not used because the reactions rapidly produce large particles and are very difficult to control. In nonaqueous solvents, the reactions are slower which allows for greater control.[35] In solution phase synthesis, the zinc oxide nanoparticles nucleate from a homogenous solution when the supersaturation of the ZnO precursor, thought to be $Zn_4O(CH_3OOH)_6$,[36] is sufficiently large. Nucleation continues until the ZnO precursor supersaturation is no longer large enough for homogenous nucleation. At that point nucleation stops but particle growth continues, usually by Ostwald ripening.[37] We have tried two different solution phase methods for synthesizing zinc oxide nanoparticles. Both methods use zinc acetate as the zinc salt and sodium hydroxide as the hydroxide ion source. UV-absorption was used to find the particle size distribution and concentration of the colloidal solutions synthesized and will be discussed in the next section.

One of the methods we used to produce ZnO nanoparticles, which will now be referred to as Method M, was first conceived by Womelsdorf et al. and later altered by Pacholski et al.[34,38] This method creates 5-10 nm ZnO particles in methanol. In Method M, 65 mL of 0.03 M NaOH methanol solution at room temperature was added drop wise at a rate of about 2 drops/second into 125 mL of 0.01 M zinc acetate in methanol at 60 °C with vigorous stirring. After about 30 minutes, all the NaOH solution had been added to the reaction flask creating 6.4 mM of zinc acetate and 10 mM of NaOH. The flask was covered and stirred for 2 hours at 60 °C. At various times during the reaction 2 mL aliquots of the reaction mixture were collected and analyzed using UV-absorption spectroscopy (ocean optics HR2000 spectrophotometer with a 25 μm slit and a resolution

of about 1.5 nm). The ZnO particles are produced though hydrolysis and the overall reaction may be written as

$$Zn(CH_3OO)_2+2NaOH \rightarrow ZnO+2Na(CH_3OO)+H_2O. \quad (4.1)$$

Following this procedure, in some of the synthesis the mixture would turn cloudy after approximately 10 minutes into the addition of the NaOH solution and stay cloudy for the rest of the reaction. In other synthesis the solution would stay clear during the entire reaction time, yielding colloid solutions of 3-4 nm ZnO nanoparticles. Clouding is due to particles in the solution becoming unstable and aggregating to form larger clusters that scatter light.

After examining the ZnO nanoparticle literature, we hypothesize that the irreproducibility of stable ZnO colloid solutions synthesized by Method M is due to fluctuating water content. The amount of water in the reaction mixture was not controlled and could vary from day to day. For example, water could get into the system in several uncontrolled ways. First, fresh methanol contains small but variable amounts of water, on the order of 2 mM, and is also hygroscopic so the water concentration can increase with exposure to the moisture in the air to approximately 30 mM.[39] Second, NaOH is hygroscopic and can absorb water when it is exposed to the air. Finally, the zinc acetate dihydrate contains water in a 2:1 molar ratio of water to Zn^{2+}. Thus, from experiment to experiment depending on the humidity and how fresh the methanol was the small amount of water present in the reaction mixture could have been fluctuating by an order of magnitude.

The fluctuating water content in Method M caused irreproducibility because the stability of the ZnO colloids synthesized is very sensitive to the ratio of H_2O to Zn^{2+}. Searson et al. have found that a H_2O to Zn^{2+} molar ratio of 10:1 is needed to synthesize clear solutions when the solvent is 2-propanol and that this critical ratio increases as the boiling point of the solvent decreases.[40] The boiling point of methanol is 64.7 $^{\circ}$C and that of 2-propanol is 82.4 $^{\circ}$C so the ratio of H_2O to Zn^{2+} has to be greater than 10 to achieve clear solutions in methanol. Searson et al. theorize that water helps to solvate zinc oxide and its precursors and that there is a critical molar ratio of water to Zn^{2+} that needs to be

met for solvation to occur.[40] However, Season et al. also found, with 2-propanol as the solvent, that as the relative H_2O to Zn^{2+} concentration approaches 100:1 the reaction of water with zinc acetate to form zinc oxide becomes a significant side reaction.[39] In addition, Sakohara et al. have analyzed ZnO nanoparticles synthesized from LiOH and zinc acetate with IR spectroscopy.[41] They found that higher zinc acetate to hydroxyl ratios in the synthesis solution resulted in increased absorption of acetate ions on the surface of the nanoparticles and increased colloidal stability. Sakohara et al. concluded that the absorbed acetate ions are responsible for the improved colloidal stability and that the higher the ratio of zinc acetate to hydroxyl ion in the synthesis solution the more stable the resulting colloid.[41] Sakohara et al. did not determine if the stabilization mechanism of the absorbed acetate ions was due to steric or columbic repulsion, but it is most likely steric repulsion because the attached acetate ions are no longer charged. The side reaction of Zn^{2+} with H_2O increases the production rate of ZnO but does not increase the concentration of acetate ions. This essentially decreases the zinc acetate to hydroxyl ratio, making the particles unstable. Therefore, there is an ideal H_2O to Zn^{2+} molar ratio approximately between 10 and 100 that allows zinc oxide and its precursors to be soluble but does not allow a significant amount of water to react with zinc acetate.

Indeed, synthesis with controlled amounts of water addition to the methanol helped synthesize clear nanoparticle solutions. However, synthesis was still not as robust and reproducible as desired; sometimes a certain amount of added water would create a clear solution and sometimes it would not. When a solution became cloudy it was possible to the make it clear again by adding more water. An example of such an experiment is shown in Figure 4.2 which displays the temporal evolution of the absorbance spectra of zinc oxide nanoparticles in methanol during synthesis using Method M with 6.4 mM of zinc acetate and 10 mM of NaOH. After 5 minutes, there is virtually no UV-absorption which means that zinc oxide particles had not yet nucleated by this time. By 10 minutes the solution appeared cloudy, a sign of the presence of large particles that scatter the light in the visible region. The scattering is evident in the absorbance spectra as increased extinction above 387 nm, the wavelength corresponding to the band gap of zinc oxide. Whether these particles were zinc oxide or a precursor is

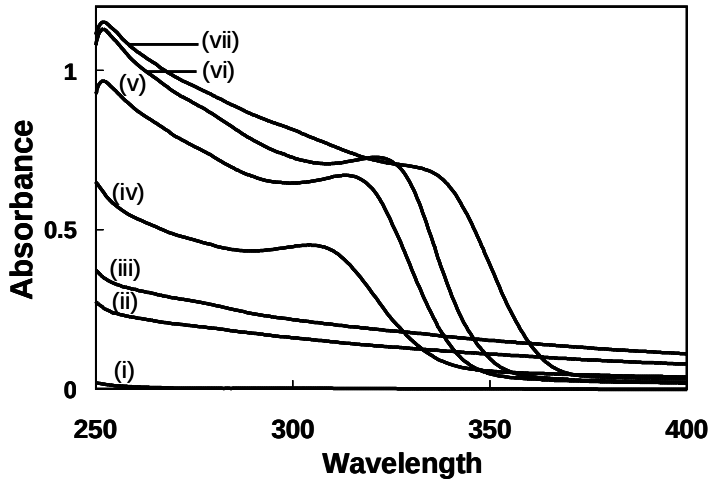

Figure 4.2 The absorbance at progressive time intervals during the synthesis of ZnO nanoparticles from Method M. (i) 5, (ii) 10, (iii) 12, (iv) 13, (v) 15, (vi) 30, and (vii) 120 minutes into the synthesis.

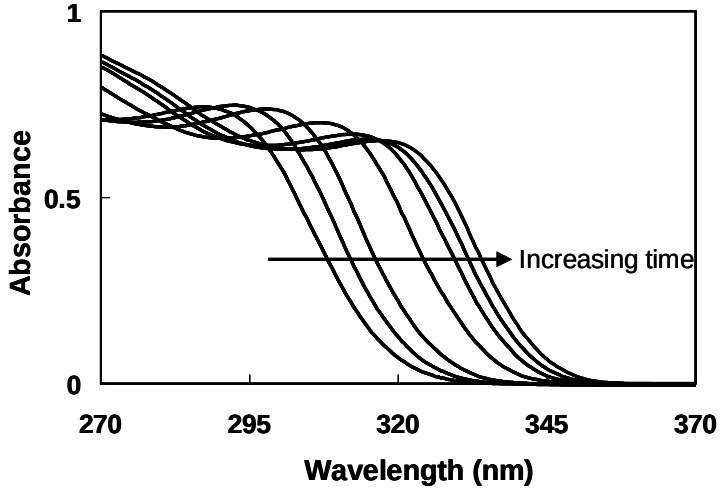

Figure 4.3 Time evolution of the ZnO nanoparticle absorbance spectra between minute 2 and 120 of the Method P synthesis.

not known. At 12.5 minutes 2 mL of deionized and distilled water was added to the solution and by 13 minutes the solution appeared clear again and the absorbance spectra had the characteristic shape of zinc oxide nanoparticle absorption with minimal extinction in the visible (> 387 nm). The solution appeared to remain clear for the rest of the reaction. However, even though the solution looked clear to the eye a small amount of extinction was still seen above the 387 nm band gap of zinc oxide indicating thepossible presence of large unstable particles. These colloidal solutions of ZnO in methanol that appeared clear to the eye during the synthesis were not stable for a long time after the synthesis. They became cloudy within a few days after synthesis. We concluded that water content strongly affects the stability of the zinc oxide colloidal solutions and that the control of the water content from experiment to experiment was too cumbersome and not reproducible enough to gain control of the system. This lack of reproducibility of zinc oxide nanoparticle solutions with known size distribution makes this synthesis method unattractive, especially since a more robust alternative exists.

We used an alternative zinc oxide nanoparticle solution synthesis method developed by Bahnemann et al.[42] and analyzed in detail by Searson et al.[37] This method will now be referred to as Method P. Method P is similar to Method M in that zinc acetate and sodium hydroxide are the precursors. However, in Method P 2-propanol is used as the solvent, the precursors are mixed all at once, and a lower temperature and precursor concentration are used relative to Method M.[43] In Method P, 1 mM of zinc acetate was dissolved in 80 mL of 2-propanol at 50 °C with vigorous stirring. And 2 mM of NaOH was dissolved in 100 mL of 2-propanol at 60 °C also with vigorous stirring. The solutions were then allowed to cool to room temperature and 8 mL of the zinc acetate solution was added to 64 mL of 2-propanol and 8 mL of the NaOH solution was added to 20 mL of 2-propanol. The diluted zinc acetate and NaOH solutions were then each heated to 35 °C in a water bath. Once each solution had reached 35 °C the NaOH solution was quickly added to the zinc acetate solution under vigorous stirring creating a total volume of 100 mL with 1 mM zinc acetate and 1.6 mM NaOH. The reaction was maintained at 35 °C for various lengths of time depending on the size of the particles desired. At various times during the reaction 2 mL aliquots of the reaction mixture were

collected and analyzed using UV-absorption spectroscopy (ocean optics HR2000 spectrophotometer with a 25 μm slit and a resolution of about 1.5 nm). Unlike with Method M the solutions from Method P were always clear and stable for approximately two weeks.

Figure 4.3 shows typical ZnO nanoparticle absorbance spectra found as synthesis Method P proceeds. Sharp absorbance onsets are seen below the ZnO bulk band gap of ~387 nm, indicating that the zinc oxide particles are demonstrating quantum confinement affects. In each spectra a pronounced peak is seen which is proportional to the total concentration of zinc oxide produced in the reaction at that point in time.[39] The height of this peak stays constant from the first measurement at two minutes until the end of the reaction at 120 minutes. This indicates that nucleation happens within the first two minutes of the reaction. The absorbance onsets of the spectra also red-shift with increasing time due to the growth of the particles and the subsequent decrease of the band gap towards the bulk band gap value.

From the absorbance spectra, the normalized, $f(r)$, and unnormalized, $n(r)$, particle size distributions were found as a function of time and are shown in Figures 4.4 and 4.5. The average particle size increases with time and the total number of particles decreases with time, because with a fixed volume of zinc oxide the density of smaller particles is greater than that of larger particles.

Searson et al. found that the growth of the ZnO nanoparticles after nucleation is caused by Ostwald ripening and can be described by the diffusion-limited growth theory developed by Lifshitz, Slyozov and Wagner (LSW theory).[37,44,45] LSW theory is a mathematical model of Ostwald ripening that can either assume a diffusion-limited ripening or surface reaction rate limited ripening.[37] Ostwald ripening occurs because the chemical potential of a solute in equilibrium with solid spherical particles is higher around smaller particles than larger particles. This causes a net flow of solute from the smaller particles to the larger particles resulting in the larger particles growing at the expense of the smaller particles. The Kelvin equation, written assuming an ideal solution, gives the concentration of the solute species in the liquid phase in equilibrium with the solid:

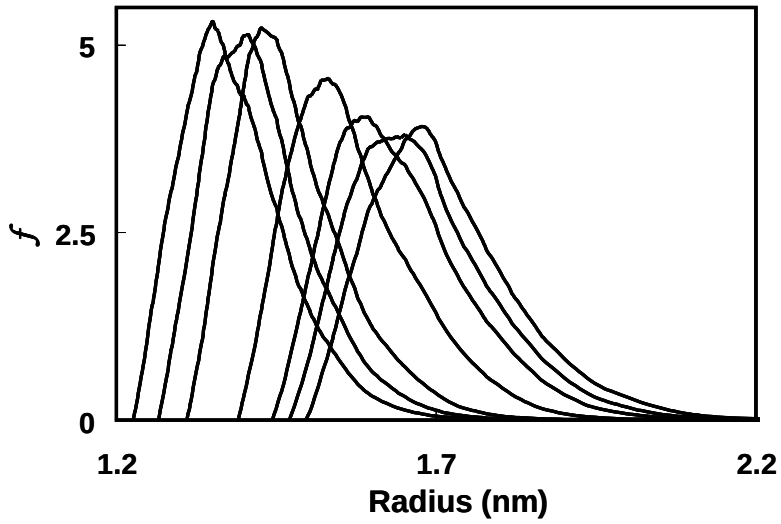

Figure 4.4 Time evolution of the normalized ZnO particle size distribution, $f(r)$, between minute 2 and 120 of the Method P synthesis. The resulting distributions are calculated from the absorbance spectra in Figure 4.3 and are smoothed using a three point averaging.

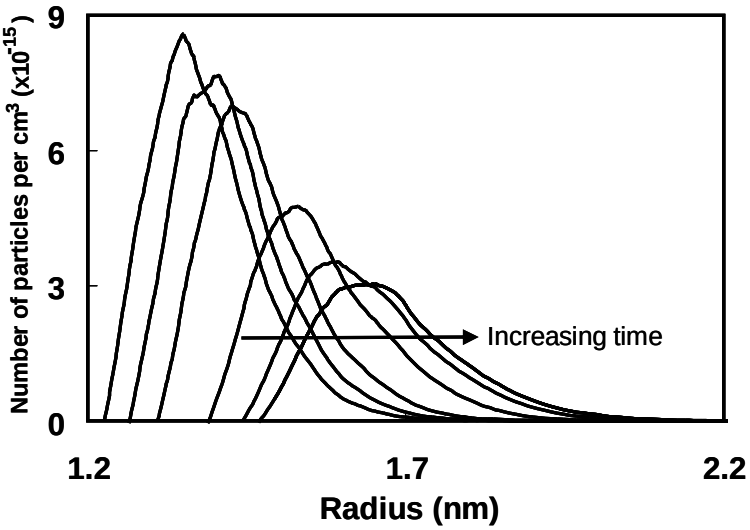

Figure 4.5 Time evolution of the unnormalized ZnO particle size distribution, $n(r)$, between minute 2 and 120 of the Method P synthesis. The resulting distributions are calculated from the absorbance spectra in Figure 4.3 and are smoothed using a three point averaging.

$$C_r = C_\infty e^{\frac{2\gamma V_m}{RT}\frac{1}{r}}. \quad (4.2)$$

Where C_r is the solute equilibrium concentration, r is the radius of the particle, C_∞ is the equilibrium concentration above a flat solid surface (bulk solubility), γ is the interfacial energy, V_m is the molar volume, R is the gas constant and T is temperature. Assuming small concentration deviations, $C_r \approx C_\infty$, then Equation 3.2 can be approximated as:

$$C_r = C_\infty + \left(\frac{2\gamma V_m}{RT}\frac{1}{r}\right). \quad (4.3)$$

Inserting Equation 4.3 into Fick's 1st law the LSW growth law is obtained,[37]

$$\bar{r}^3 - \bar{r}_o^3 = Kt \ , \quad (4.4)$$

where r_o is the average initial particle size, r is the average particle size at any given time, t, and K is the coarsening rate constant given by,[37]

$$K = \frac{8\gamma D V_m^2 C_\infty}{9RT} \ . \quad (4.5)$$

Using the Stokes-Einstein equation the rate constant K can be further simplified,

$$K = \frac{8\gamma V_m^2 C_\infty}{54\pi\eta a N_a}, \quad (4.6)$$

where η is the solvent viscosity, and a is the radius of the solvated ZnO precursor species that diffuses from the small particles to the larger particles. The identity of the ZnO precursor is not clear at this point but is thought to be $Zn_4O(CH_3COOH)_6$.[36]

It can be seen from Equation 4.6 that by changing the time period of the reaction any average ZnO nanoparticle size can be synthesized by Method P. However, Figures 4.4 and 4.5 show that as the particles grow the particle size distribution widens. Thus, if the particles are grown for long time periods the average particle size will increase, but at the cost of the narrowness of the particles size distribution. Therefore, in order to create particle size distributions with large average radii, Method P must be modified so that the initial nuclei are larger so less growth is required to achieve the desired average particle radius. Searson et al. have shown that by changing the solvent and raising the temperature of the reaction, particles can be nucleated with sizes ranging from about 3 nm in diameter to 10 nm in diameter.[40] By utilizing the LSW growth kinetics of the

particles made from Method P, particle size distributions with varying average diameters can be made by tailoring the reaction time and temperature.

When the zinc oxide nanoparticles are deposited on to the substrates it is important that at least a monolayer of nanoparticles are deposited in order to prevent recombination from the FTO to the electrolyte, and to maximize the nanowire density. This means that the zinc oxide nanoparticle solutions must have enough nanoparticles for at least a monolayer of particles. Using the maximum absorbance from the spectra and Beer's law it can be found that the volume percentage of the zinc oxide particle solutions is about 0.02%. The total number of particles/cm^3 is on the order of 10^{15} and the total volume of solution is 100 mL, consequently there are approximately 10^{17} particles available for deposition. The substrates used for DSSCs have a surface area of approximately 4 cm^2, assuming the particles in the dipping solution are on average 3 nm in diameter, covering the substrate with a monolayer of particles would take on the order of 10^{13} particles. Thus, this means that there are approximately four orders of magnitude more particles in the synthesized zinc oxide solution than are needed for a monolayer of particles to be deposited on the substrate. Although the volume percentage of zinc oxide is small, total coverage of the substrate is indeed possible with these zinc oxide nanoparticles solutions, provided the concentration of the solution used for deposition and the deposition method are properly tailored.

Method P is more stable and reproducible than Method M, can be modified to create a range of narrow average particle size distributions, and yields sufficient particles to cover the FTO substrate. Therefore, we chose Method P as the preferred method for making zinc oxide nanoparticle solutions of controllable known size distributions. These solutions were used to seed the ZnO nanowire growth, however the seed layer made from the thermal decomposition of zinc acetate described below turned out to have superior characteristics to the ZnO nanoparticle seed layer and was therefore utilized more often during the ZnO nanowire growth studies.

4.4 Determining Particle Size Distribution

The particle size distribution of the ZnO nanoparticles synthesize by Method M and Method P were determined from the UV-absorbance spectra of the colloid solutions.

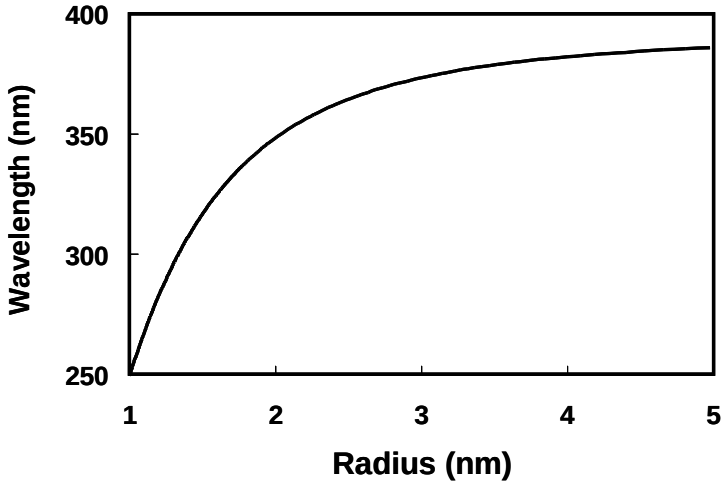

Figure 4.6 The relationship, given by Equation 4.7, between the radius of a quantum particle and the wavelength, λ_{onset}, at which the particle starts to absorb radiation.

The method used to obtain the particle size distribution from the UV-absorbance spectrum was taken from Pesika et al.[46] and is explained below

Pesika et al.[46] found that in the dilute concentration limit the particle size distribution and the total particle concentration can be found from the absorbance spectra. Pesika et al. also confirmed that the PSD obtained from the absorbance spectra was in excellent agreement with the PSD obtained from TEM images of the same zinc oxide particles.[46] The PSD can be determined from the UV-absorbance spectra because when the crystal size approaches the exciton diameter quantum confinement affects the electronic structure and widens the band gap of the particles. The band gap widening is related to the particle diameter; the smaller the particles the larger the widening. In an ensemble of nanoparticles with diameters in the quantum confinement regime, each particle size starts absorbing radiation at different wavelengths. The largest particles will start absorbing at the longest wavelengths and as the wavelength decreases the smaller particles will start to absorb until all the particles are absorbing at the peak of the absorbance spectra.[46,43] The variation in the wavelength at which the particles in the ensemble start to absorb broadens as well as blue-shifts the absorbance spectra as compared to the bulk crystal absorbance spectra. This change in the shape of the absorbance spectra is used to find the PSD.

The effective mass model for spherical particles, derived by Brus,[47] quantifies the band gap widening and relates the band gap energy, E^*, of a particle to its radius r, by the equation

$$E^* \cong E_g^{bulk} + \frac{\hbar^2 \pi^2}{2r^2}\left(\frac{1}{m_e m_o} + \frac{1}{m_h m_o}\right) - \frac{1.8e^2}{4\pi\varepsilon\varepsilon_o r} - \frac{0.124e^4}{\hbar^2(4\pi\varepsilon\varepsilon_o)^2}\left(\frac{1}{m_e m_o} + \frac{1}{m_h m_o}\right)^{-1}, \qquad (4.7)$$

where E^{bulk}_g is the bulk band gap, ε is the relative permittivity, ε_o is the permittivity of free space, h is Planck's constant, e is the charge of an electron, m_o is the free electron mass, and m_e and m_h are the effective masses of the electrons and holes, respectively. Using Equation 4.7 the wavelength at which a particle starts to absorb, λ_{onset}, can be related to the particle radius, i.e. $\lambda_{onset} = \lambda_{onset}(r)$, and is shown in Figure 4.6. At any particular wavelength, λ, only the particles with radii such that λ_{onset} is greater than or equal to λ will contribute to the absorbance. The absorbance can then be thought of as a

function of λ_{onset}, i.e. $A = A(\lambda_{onset}(r))$. From now on the "onset" will be dropped and λ will imply λ_{onset}. Assuming that the particles are spherical and that the absorption coefficient is independent of the particle size, absorbance at wavelength, λ, is proportional to the total volume of particles with radii greater than or equal to r, the radius of particles that start absorbing at λ. So

$$A(\lambda(r)) \propto \int_r^{\infty} \frac{4}{3}\pi(r')^3 n(r')dr' \tag{4.8}$$

where A is the absorbance, r is the radius of the particles, r' is a dummy variable, and $n(r)$ is the unnormalized particle size distribution. $n(r)$ can then be found by taking the derivative with respect to r of $A(\lambda(r))$,

$$n(r) \propto \frac{-\frac{dA(\lambda(r))}{dr}}{\frac{4}{3}\pi r^3} \quad . \tag{4.9}$$

The proportionality constant is obtained by normalizing $n(r)$. This constant gives the normalized particle size distribution, $f(r)$. Using Beer's law, the total number of particles in the solution is given by

$$N = \frac{AV_m}{\varepsilon l \int_0^{\infty} f(r)\frac{4}{3}\pi r^3 dr} \tag{4.10}$$

where ε is the extinction coefficient, A is the absorbance at the peak of the spectrum, which changes for each spectra but is near 330 nm, l is the path length of the light in centimeters, and V_m is the molar volume of ZnO taken to be 14.8 cm^3mol^{-1}. Over the small range of wavelengths considered, ε is taken to be constant at 605 $Lmol^{-1}cm^{-1}$, the value at 330 nm.[43] The unnormalized particle size distribution, $n(r)$, can then be obtained by multiplying the normalized particles size distribution by, N, the total number of particles,

$$n(r) = Nf(r). \tag{4.11}$$

Thus, the ZnO normalized and unnormalized particle size distributions can be determined from the UV-absorption spectra of the zinc oxide nanoparticle solutions. It should be

noted however that, at small particle sizes, the tight binding model developed by Viswanatha et al.[52] predicts ZnO nanoparticle size better than the effective mass model.

4.5 Applying the Nanoparticles to the Substrate

Before the ZnO nanoparticles were drop cast, the substrates were cleaned by sonication in 1:1:1 by volume acetone, isopropanol and deionized water. The nanoparticles were applied to the substrate by drop casting 200 μL of the ZnO particle solution onto the substrate three times. After each coating the substrate was allowed to dry in air. The substrates were then annealed at 450 °C for 30 minutes to make sure the particles adhered to the substrate surface. Next, after the substrates were cooled in air, they were rinsed with deionized water to remove sodium acetate salt deposited on the surface. The whole coating process was repeated to ensure complete coverage of the substrate with ZnO nanoparticles. As mentioned previously, there are ~10^{15} particles/cm^3 in the ZnO nanoparticle solution, and ~10^{13} 3 nm particles are required to coat a monolayer on a 4 cm^2 substrate. Therefore, since ~10^{15} particles were deposited on the substrate a monolayer coating of nanoparticles was assured. Also, to study how the nanoparticle seed layer thickness affects the DSSC performance thicker nanoparticle films were made by concentrating the ZnO nanoparticle solution using a rotary evaporator (Buchi Rotavapor R-200).[18] It should be noted that since the sodium and acetate ions from the ZnO nanoparticle precursors were not removed from the solution sodium acetate salt was deposited during the drop casting step. Nanowires do not grow where the salt deposits which leads to inhomogenous nanowire growth. Rinsing the substrates with deionized water after the annealing step removes the salt and allows more particles to deposit where the salt was during the second drop casting step. This allows for more uniform coverage of ZnO nanoparticles.

The advantage of this seeding process is that the size of the seed particles can be varied by changing the particle synthesis. In addition, the nanowire number density can be controlled by changing the concentration of the ZnO nanoparticle solution. Some disadvantages of this seeding technique are that since the nanoparticle seeds are randomly oriented the nanowires are not aligned and that pattering the nanowires on the substrate,

which is important to some solar cell applications,[48] is difficult due to the lack of control of where the solution is drop casted.

4.6 Seeding Using Zinc Acetate

Substrates were also seeded using a technique based on the thermal decomposition of zinc acetate, developed by Greene et al.,[30] which deposits a thin (~5-10 nm) polycrystalline ZnO film on to virtually any substrate. Growth from these seed layers results in vertically aligned nanowires, Figure 4.7. In this method, we first cleaned the substrates by sonicating them in 1:1:1 by volume acetone, isopropanol and deionized water. One drop of a 5 mM zinc acetate ethanol solution was spread uniformly across each substrate by slowly rotating and gently tilting the substrate manually. After ~10 seconds, the substrate was rinsed with a brief squirt of ethanol and blown dry with argon. This wetting and rinsing process was repeated for a total of five times before the substrates were annealed at 350 $^{\circ}$C in air for 20 min. After the substrates were cooled to room temperature the wetting and annealing process was repeated. Greene et al.[30] found that the annealing processes decomposes the zinc acetate molecules adsorbed on the surface of the substrate, creating a ~10 nm thick seed layer of zinc oxide nanocrystalline "islands" that have their c-axis oriented parallel to the substrate.

This seeding method is an art and subtle variations to the method result in morphological changes. It is important that *only one drop* of the zinc acetate ethanol solution be applied to the ~4 cm^2 substrate. As the ethanol is allowed to evaporate the substrate must be grasped with tweezers at one corner and rotated in a circular motion using ones wrist. The ethanol must be allowed to dry, while the substrate is being rotated, until drying patterns of rainbow colors start to be seen. Then, the solution must be rinsed with a relatively strong squirt of ethanol and immediately blown dry with an Ar stream. Inhomogeneities in the film occur if too much zinc acetate solution is applied and not rinsed right when rainbow drying patterns start to form, Figure 4.8. Also the seed layer is made more uniform if the substrate is held, with tweezers, by different corners for each wetting and rinsing step. It is also critical for optimum nanowire alignment that the substrates not have an RMS roughness greater than ~2 nm (ITO substrates with <1 nm RMS roughness are available from Thin Film Devices, Inc.).[30] In addition, studies have

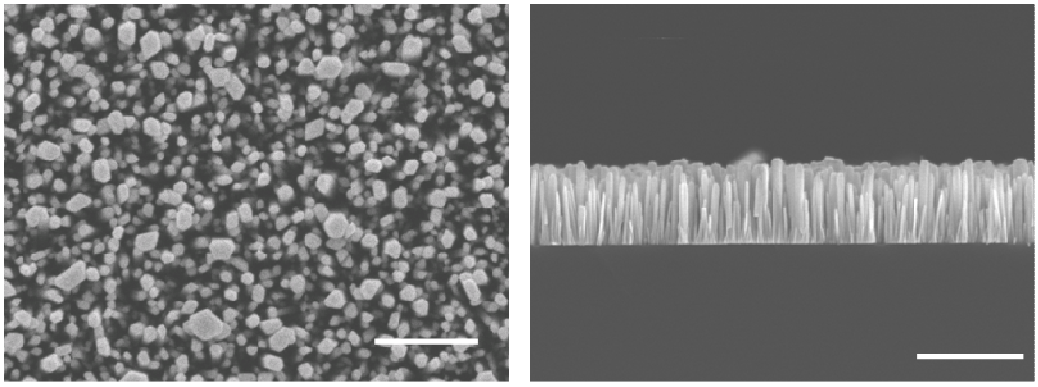

Figure 4.7 (a) Top view and (b) side view SEM images of ZnO nanowires grown on a silicon substrate seeded with ZnO using the thermal decomposition of zinc acetate method. Scale bars are 500 nm in (a) and 1 μm in (b).

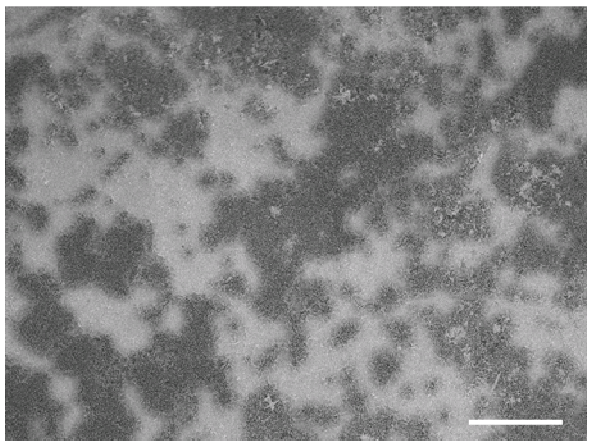

Figure 4.8 Top view SEM image of ZnO nanowires on an FTO substrate seeded with the thermal decomposition of zinc acetate method using too much solution and not squirting with ethanol at the appropriate moment during the drying process. The excess zinc acetate results in inhomogeneities in the nanowire film on the ~100 μm scale. The scale bar is 50 μm.

shown that the relative humidity, RH, during the seeding process influences the nanowire alignment, density and size.[24] The optimum RH was found to be ~35%, when the RH was too high the nanowire diameters became more polydispersed and when the RH was too low the number density and alignment of the nanowires decreased. Lee et al. propose that a small amount of water is required to hydrolyze the zinc acetate to an insoluble zinc hydroxide which is converted to ZnO upon annealing.[24] However, too much water results in higher seed layer densities and less uniform nanowire diameters.[24] This reasoning makes sense because we saw a similar sensitivity to water in the ZnO nanoparticle synthesis (Method M) mentioned above.

After experimenting with seeding the substrates by drop casting nanoparticles and with the thermal decomposition of zinc acetate we decided, due to its better characteristics that the decomposition of zinc acetate technique would work best for our ZnO nanowire growth experiments. This method is reproducible (once the art of the wetting and rinsing process is mastered), results in uniform aligned nanowires and the number density can be controlled by changing the concentration of the zinc acetate ethanol solution (see Chapter 6). One issue which limits the surface area of these nanowire films is that since the nanowires are so aligned and densely packed, which is good for high surface area, the nanowire diameters become large enough that the nanowires coalesce and eventually become a continuous film.

The addition of a surfactant such as polyethyleneimine (PEI) reportedly helps to hamper the diameter growth rate, by adsorbing on the sides of the nanowires, and leads to longer individual wires.[12,49-51] We grew ZnO nanowires on silicon substrates, seeded with the decomposition of zinc acetate, in the standard reaction solution of 16 mM zinc nitrate hexahydrate and 25 mM methenamine with PEI present (number average molecular weight, M_n= 423, Aldrich cat# 468533). The reaction was done at 90 °C without preheating. We found that the pH of the reaction solution increased dramatically, from 7.5 to 10.5, with PEI (M_n=423) concentrations greater than 6 mM. Due to the higher pH values nanowires did not grow with PEI concentrations greater than 6 mM. Thus, PEI concentrations of 2 mM and 6 mM were explored. It was found that the addition of PEI (M_n=423) actually lowered the nanowire aspect ratio. This is contrary to reports in

literature which claim that the addition of PEI increases the nanowire aspect ratio.[12,49-51] PEI can be purchased in a wide variety of molecular weights (M_n=423-60,000, Aldrich) and several different PEI molecular weights have been used in literature.[12,50,51] Furthermore, it is not always explicitly stated in the literature which molecular weight PEI was used.[12,51] The nanowire aspect ratio might be sensitive to the PEI molecular weight and maybe at M_n=423 PEI lowers the aspect ratio, whereas at different molecular weights it might increase the aspect ratio. Exploring the effects of different molecular weight PEI samples in different concentrations would be worth while in order to understand the effect PEI has on the nanowire growth.

References

(1) Cheng, A.-J.; Tzeng, Y.; Zhou, Y.; Park, M.; Wu, T.-h.; Shannon, C.; Wang, D.; Lee, W. *Appl. Phys. Lett.* **2008**, *92*, 092113.

(2) M. H. Huang; Y. Wu; H. Feick; N. Tran; E. Weber; P. Yang *Adv. Mater.* **2001**, *13*, 113.

(3) Tang, H.; Zhu, L.; Ye, Z.; He, H.; Zhang, Y.; Zhi, M.; Yang, F.; Yang, Z.; Zhao, B. *Mater. Lett.* **2007**, *61*, 1170.

(4) Park, W. I.; Kim, D. H.; Jung, S.-W.; Yi, G.-C. *Appl. Phys. Lett.* **2002**, *80*, 4232.

(5) Dloczik, L.; Engelhardt, R.; Ernst, K.; Lux-Steiner, M. C.; Könenkamp, R. *Sensor. Actuat. B-Chem.* **2002**, *84*, 33.

(6) Heo, Y. W.; Varadarajan, V.; Kaufman, M.; Kim, K.; Norton, D. P.; Ren, F.; Fleming, P. H. *Appl. Phys. Lett.* **2002**, *81*, 3046.

(7) Li, Y.; Meng, G. W.; Zhang, L. D.; Phillipp, F. *Appl. Phys. Lett.* **2000**, *76*, 2011.

(8) Martinson, A. B. F.; Elam, J. W.; Hupp, J. T.; Pelline, M. J. *Nano Lett.* **2007**,7, 2183.

(9) Cui, J. B.; Daghlian, C. P.; Gibson, U. J.; Pusche, R.; Geithner, P.; Ley, L. *J. Appl. Phys.* **2005**, *97*, 044315.

(10) Vayssieres, L. *Adv. Mater.* **2003**, *15*, 464.

(11) Lori E. Greene; Matt Law; Joshua Goldberger; Franklin Kim; Justin C. Johnson; Yanfeng Zhang; Richard J. Saykally; Peidong Yang *Angew. Chem. Int. Edit* **2003**, *42*, 3031.

(12) Law, M.; Greene, L. E.; Johnson, J. C.; Saykally, R.; Yang, P. D. *Nat. Mater.* **2005**, *4*, 455.

(13) Baxter, J. B.; Walker, A. M.; van Ommering, K.; Aydil, E. S. *Nanotechnology* **2006**, *17*, S304.

(14) Guo, M.; Diao, P.; Wang, X.; Cai, S. *J. Solid State Chem.* **2005**, *178*, 3210.

(15) Markov, I. V. *Crystal. Growth for Beginners*; World Scientific: New Jersey, 2003.

(16) Guo, M.; Diao, P.; Cai, S. M. *J. Solid State Chem.* **2005**, *178*, 1864.

(17) Wang, S. F.; Tseng, T. Y.; Wang, Y. R.; Wang, C. Y.; Lu, H. C. *Ceram. Int.* **2009**, *35*, 1255.

(18) Enache-Pommer, E., University of Minnesota, 2009.

(19) Song, J.; Lim, S. *J. Phys. Chem. C* **2007**, *111*, 596.

(20) Cui, J. B.; Daghlian, C. P.; Gibson, U. J.; Pusche, R.; Geithner, P.; Ley, L. *J. Appl.Phys.* **2005**, *97*, 044315.

(21) Liu, S.-Y.; Chen, T.; Wan, J.; Ru, G.-P.; Li, B.-Z.; Qu, X.-P. *Appl Phys. A- Mater.* 2009; Vol. 94, p 775.

(22) Huang, J.-S.; Lin, C.-F. *J. Appl. Phys.* **2008**, *103*, 014304.

(23) Boyle, D. S.; Govender, K.; O'Brien, P. *Chem. Commun.* **2002**, *80*, 80.

(24) Lee, Y.-J.; Sounart, T. L.; Scrymgeour, D. A.; Voigt, J. A.; Hsu, J. W. P. *J. Cryst. Growth* **2007**, *304*, 80.

(25) Y. Sun; G. M. Fuge; N. A. Fox; D. J. Riley; M. N. R. Ashfold *Adv. Mater.* **2005**, *17*, 2477.

(26) Liou, S.-C.; Hsiao, C.-S.; Chen, S.-Y. *J. Cryst. Growth* **2005**, *274*, 438.

(27) Li, Q.; Kumar, V.; Li, Y.; Zhang, H.; Marks, T. J.; Chang, R. P. H. *Chem. Mater.* **2005**, *17*, 1001.

(28) Peterson, R. B.; Fields, C. L.; Gregg, B. A. *Langmuir* **2004**, *20*, 5114.

(29) Tak, Y.; Yong, K. *J. Phys. Chem. B* **2005**, *109*, 19263.

(30) Greene, L. E.; Law, M.; Tan, D. H.; Montano, M.; Goldberger, J.; Somorjai, G.; Yang, P. *Nano Lett.* **2005**, *5(7)*, 1231.

(31) Zhong, Q. P.; Matijevic, E. *J. Mater. Chem.* **1996**, *6*, 443.

(32) Sakohara, S.; Tickanen, L. D.; Anderson, M. A. *J. Phys. Chem.* **1992**, *96*, 11086.

(33) Tani, T.; Watanabe, N.; Takatori, K. *J. Nanopart. Res.* **2003**, *5*, 39.

(34) Womelsdorf, H.; Hoheisel, W.; Passing, G. Germany Patent #20040241085, 2000.

(35) Hu, Z.; Oskam, G.; Penn, R. L.; Pesika, N.; Searson, P. C. *J. Phys. Chem. B* **2003**, *107*, 3124.

(36) Tokumoto, M. S.; Briois, V.; Santilli, C. V.; Pulcinelli, S. H. *J. Sol-Gel Sci. Techn.* **2003**, *26*, 547.

(37) Wong, E. M.; Bonevich, J. E.; Searson, P. C. *J. Phys. Chem. B* **1998**, *102*, 7770.

(38) Pacholski, C.; Kornowski, A.; Weller, H. *Angew. Chem. Int. Edit.* **2002**, *41*, 1188.

(39) Hu, Z.; Ramirez, D. J. E.; Cervera, B. E. H.; Oskam, G.; Searson, P. C. *J. Phys. Chem. B* **2005**, *109*, 11209.

(40) Hu, Z.; Herrera Santos, J. F.; Oskam, G.; Searson, P. C. *J. Colloid Interf. Sci.* **2005**, *288*, 313.

(41) Sakohara, S.; Ishida, M.; Anderson, M. A. *J. Phys. Chem. B* **1998**, *102*, 10169.

(42) Bahnemann, D. W.; Kormann, C.; Hoffmann, M. R. *J. Phys. Chem.* **1987**, *91*, 3789.

(43) Hu, Z.; Oskam, G.; Searson, P. C. *J. Colloid Interf. Sci.* **2003**, *263*, 454.

(44) Lifshitz, I. M.; Slyozov, V. V. *J. Phys. Chem. Solids* **1961**, *19*, 35.

(45) Wagner, C. *Z. Elektrochem* **1961**, *65*, 581.

(46) Pesika, N. S.; Stebe, K. J.; Searson, P. C. *J. Phys. Chem. B* **2003**, *107*, 10412.

(47) Brus, L. *J. Phys. Chem.* **2002**, *90*, 2555.

(48) Leschkies, K. S.; Beatty, T. J.; Kang, M. S.; Aydil, E.; Norris, D. J. *ACS nano* **2009**, *submitted*.

(49) Wu, W.; Hu, G.; Cui, S.; Zhou, Y.; Wu, H. *Cryst. Growth Des.* **2008**, *8*, 4014.

(50) Zhou, Y.; Wu, W.; Hu, G.; Wu, H.; Cui, S. *Mater. Res. Bull.* **2008**, *43*, 2113.

(51) Cheng, H.M.; Chiu, W.H.; Lee, C.H.; Tsai, S.Y.; Hsieh, W.F. *J. Phys. Chem. C* **2008**, *112*, 16359.

(52) Viswanatha, R.; Sapra, S.; Satpati, B.; Satyam, P. V.; Dev, B. N.; Sarma, D. D. *J. Mater. Chem.* **2004**, *14*, 661.

Chapter 5 : Mechanism of ZnO Nanowire Growth from Aqueous Solutions of Methenamine and Zinc Nitrate

5.1 Introduction

Although the synthesis of ZnO nanowires from an aqueous solution of zinc nitrate hexahydrate and methenamine (also called hexamethylenetetramine, hexamine and HMT, molecular formula $C_6H_{12}N_4$) was reported several years ago[1-3] the role of methenamine and the ZnO nanowire growth mechanism is still widely debated.[4-11] The most commonly suggested growth mechanism is based on the hydrolysis of methenamine to form ammonia which equilibrates with water to form ammonium ions (NH_4^+) and hydroxyl ions (OH^-). By hydrolyzing slowly, methenamine is thought to act as a pH buffer and supply OH^-, which reacts with the zinc ions to form ZnO.[4-6,11] This sequence of reactions is most often represented as follows:

$$C_6H_{12}N_4 + 6H_2O \longrightarrow 6HCHO + 4NH_3 \qquad (5.R1)$$

$$NH_3 + H_2O \longleftrightarrow NH_4^+ + OH^- \qquad (5.R2)$$

$$Zn^{2+} + 2OH^- \longrightarrow ZnO_{(s)} + H_2O \qquad (5.R3).$$

Some researchers[6,8] hypothesize that since solid $Zn(OH)_2$ is less stable in the reaction solution it forms first upon precipitation, and that ZnO forms over time from the solid $Zn(OH)_2$ by dissolution followed by reprecipitation or by phase transformation. Based on infrared spectroscopy experiments Sugunan et al.[9] conclude that methenamine does not decompose at all during the reaction. In addition, they and several other researchers[7,10,11] hypothesize that since methenamine is a non-polar chelating agent it preferentially binds to the non-polar sidewalls of the wires and inhibits lateral growth which leads to the anisotropic nanowire growth. However, by using NMR to examine the methenamine concentration during the reaction Ashfold et al.[6] conclude that methenamine decomposition does occur and is independent of the reactions producing ZnO. Still, other researchers think that a zinc methenamine complex (Zn-HMT^{2+}) is present in the solution,[10] yet others disagree with this hypothesis.[8,9] Furthermore, based on electron energy loss spectroscopy experiments as well as the observation of hollow ZnO particles,

Li et al.[4] and Chou et al.[7] hypothesize that the ZnO nanowire nuclei is a zinc-nitrate-water-methenamine organometallic complex $[Zn(H_2O)_2(HMT)_2](NO_3)_2$ or $[Zn(H_2O)_4(HMT)_2](NO_3)_2$.[12,13]

In this chapter we suggest a detailed growth mechanism for the formation of ZnO nanowires from methenamine and zinc nitrate hexahydrate. We propose and show evidence that a zinc methenamine complex (Zn-HMT^{2+} and Zn-HMT-Zn^{4+}) is the precursor and reacts at the surface of the hydroxyl terminated ZnO nanowires. To support our proposed growth mechanism we examined the growth with several experimental techniques, kinetic modeling, and thermodynamic calculations.

5.2 Experimental

5.2.1 Nanowire Growth

ZnO nanowires were grown heterogeneously on silicon (100) substrates, seeded with ZnO, from aqueous solutions of zinc nitrate hexahydrate ($Zn(NO_3)_2 \cdot 6H_2O$) (Fisher #Z45-500) and methenamine (Mallinckrodt #5180). All chemicals were used as received. Methenamine is a cyclic amine and is shown in Figure 5.1. The initial concentration of zinc nitrate hexahydrate was varied between 0 mM and 33.6 mM and the initial methenamine concentration was varied between 4 mM and 100 mM to explore the effects of methenamine concentration on the reaction rate.

In growing the ZnO nanowires, aqueous solutions of zinc nitrate hexahydrate and methenamine were heated by one of two different methods. In the first method, separate solutions of zinc nitrate hexahydrate and methenamine with twice the initial reaction concentration (i.e., between 0 and 67.2 mM zinc nitrate hexahydrate and between 8 mM and 200 mM methenamine) and half the total reaction volume were heated in an oven or on a hot plate to the growth temperature. These preheated reactants were mixed together and placed in a preheated oven. The instant at which the preheated reactants were mixed was taken to be the start of the reaction (time, $t = 0$). The substrates (along with the aluminum substrate holder) were also preheated to the reaction temperature and immersed in the mixed solution at $t=0$. This method of growth and the nanowires grown using this protocol will be referred to as "preheated". This protocol aims to grow the

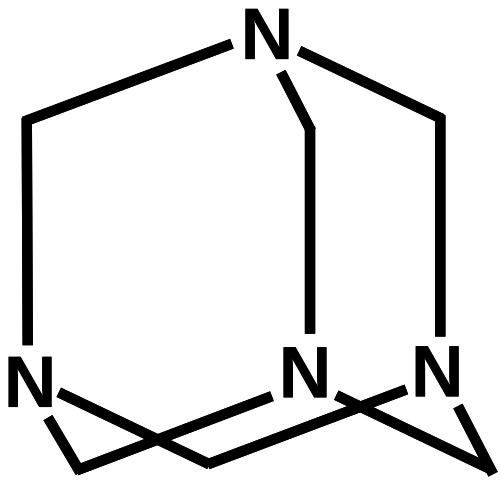

Figure 5.1 Structure of methenamine ($C_6H_{12}N_4$).

nanowires under well-controlled isothermal conditions. In the second method, the reactants were mixed together at room temperature and placed in a preheated oven to heat up over time to the growth temperature. The start of the reaction ($t = 0$) for this growth method was taken to be the instant the reactants were mixed and placed in the oven. This method of growth and nanowires grown using this protocol will be referred to as "not preheated". This is the most common protocol used in the literature for growing nanowires even though the growth conditions are very ill-defined and the temperature-time history of the solution and the substrate depends on the volume of the liquid solution, beaker size and even the precise model and configuration of the oven used for growth. Nevertheless, this protocol produces nanowires with desired properties and is used widely. Difficulty with reproducibility as well as large differences in morphology due to small variations in time-temperature history is often encountered though not well-documented in the literature.

5.2.2 Substrate Seeding for Heterogeneous Growth

To grow a dense film of ZnO nanowires on silicon substrates the silicon surfaces were seeded with a thin (~5-10 nm) layer of ZnO using a method developed by Greene et al.[14] In this seeding method, one drop (~0.05 mL) of 5 mM zinc acetate in ethanol was drop cast on the substrate and evenly distributed by rotating the sample with a gentle rotating motion of one's wrist while the sample was held with tweezers. After ~10 seconds of rotation, the substrate was rinsed with ethanol and then immediately dried with a stream of Ar. The drop casting, rotating, rinsing and drying were repeated three times. The substrate was then annealed at 350 °C for 20 minutes. The entire seeding process was repeated to ensure complete coverage of the substrate with the ZnO seeds.

5.2.3 Homogeneous Growth Characterization

In addition to growing heterogeneously on seeded substrates, the ZnO nanowires nucleate and grow homogeneously and precipitate out of solution. We monitored the rate of homogeneous precipitation by growing ZnO nanowires in 15 mL centrifuge tubes and measuring the mass of the ZnO precipitate as a function of time. In these experiments, each centrifuge tube was filled with 10 mL of the same reaction solution. The centrifuge tubes were capped and placed up right in a "bouquet" fashion in a large beaker. The

reactants were not preheated. The tubes were placed into a 95 °C oven at *t=0* and it took ~1 hr for the reaction solution in the centrifuge tubes to reach 90 °C. Periodically, one centrifuge tube was removed from the oven and the ZnO precipitates were centrifuged out of the solution. The residual salts in the ZnO precipitates were removed by suspending the particles in water and then recentrifuging the particles. This washing step was repeated three times. The particles were then suspended in acetone, dispensed on a watch glass of known weight, dried in an oven and immediately weighed. It was important that the particles were immediately weighed after drying since water condensing on the particles would cause inaccurate weight measurements. In addition, to further improve accuracy, the empty watch glasses were also heated in the oven and immediately weighed.

To examine the morphology and crystal structure of the homogeneously grown ZnO nanowires the synthesis was carried out with 300 mL of the growth solution containing 16.8 mM zinc nitrate hexahydrate and 25 mM methenamine. Periodically, 15 mL of the reaction solution was sampled and the residual salts were removed by centrifuging and washing with water three times. The ZnO particles were then dispersed in acetone and drop-cast on a silicon substrate for examination with scanning electron microscopy (SEM) and X-ray diffraction (XRD). Homogeneous nanowire precipitates from both preheated and not preheated reactions were examined.

5.2.4 Growth Solution Characterization

In addition to ZnO that has precipitated out of solution, zinc is present in the growth solution as zinc ions such as Zn^{2+}, $Zn(OH)_n^{2-n}$, $Zn(NH_3)^{2+}$ Zn-HMT^{2+} etc. Which ions are present in the solution will be discussed below. Titration with ethylenediaminetetraacetic acid (EDTA) was used to measure the total concentration of all ions containing zinc. Hereafter, this concentration will be referred to as the "total zinc ion concentration". The EDTA titration is described in the analytical chemistry text by Harris.[15] To determine the temporal variation of the total zinc ion concentration during growth, 3 mL aliquots of the solution was removed from the beaker periodically. The ZnO particles were removed from this aliquot using a 0.2 μm GHP Pall acrodisc filter. which removes all particles larger than 200 nm. Following, 1 mL of the filtered growth

solution was mixed with 25 mL of deionized water, 5 mL of ammonia pH 10 buffer (Sigma-Aldrich product #33582) and 3 drops of an eriochrome black T indicator solution. The indicator solution was made up of 0.1 g of eriochrome black T metal indicator (Acros #22836100), 7.5 mL of triethanolamine (Sigma-Aldrich product #33729) and 2.5 mL of absolute ethanol. The indicator is purple when bound to zinc and is blue otherwise. EDTA binds in a 1:1 ratio to zinc and has a larger binding constant (logK=16.5) than both the indicator and all the other zinc complexes present in the solution. Thus, when the filtered aliquot mixed with the indicator is titrated with and aqueous solution of EDTA (Acros #40997-1000), the solution changes color from purple to blue when the number of moles of EDTA added is equal to the number of zinc ions present in the solution. The total zinc ion concentration is determined from the concentrations and volumes of the EDTA solution added and the filtered growth solution.

The methenamine concentration was measured as a function of time during growth using 300 MHz proton Nuclear Magnetic Resonance (NMR). For these experiments, growth was carried out in 50 mL of D_2O (Sigma-Aldrich #151882). Both protocols with and without preheating of the reactant solutions were studied. For NMR experiments, 3 mL aliquots were removed periodically from the growth solution filtered with a 0.2 μm GHP Pall acrodisc filter to remove the ZnO particles. One mL of this filtered solution was mixed with between 10 and 100 μL of D_2O containing 0.75 wt% sodium 3-(trimethylsilyl)propionate-2,2,3,3,-d_4 (TSP) (Sigma-Aldrich #293040) and 0.7 mL of this solution was placed in an NMR tube. The TSP was used as a standard. It was found that adding too much TSP caused white particles to precipitate out of solution. The identity of these particles was not determined. However, when the amount of TSP solution added was between 10 and 100 μL precipitation was not observed. For consistency, the same amount of TSP was added to all aliquots from a specific growth experiment. The area of the methenamine proton peak was integrated relative to the TSP standard peak and used to determine the methenamine concentration. Varian NMR (Vnmr) software was used for the peak integration. Absolute methenamine concentrations were determined by comparing the methenamine proton peak areas to that found from a 25 mM standard methenamine solution. The effect of pH on the

methenamine proton NMR with and without zinc present was also examined. For these experiments, NMR spectra were collected from D_2O solutions containing only methenamine and from solutions containing methenamine and zinc nitrate hexahydrate with varying pH values. The solution pH values were lowered to various levels by adding different volumes of a dilute (~12 mM) HCl D_2O solution.

The temporal variation of the solution temperature and pH were measured simultaneously using an Oakton pH probe with a double junction combination electrode (model #110).

5.2.5 Nanowire Characterization

The nanowire morphology and crystal structure were determined using SEM (JEOL 6700) and x-ray microdiffraction (XRD, Bruker-AXS Microdiffractometer), respectively. The surface of the nanowires was characterized using x-ray photoelectron spectrscopy (XPS, Physical Electronic phi 5400) as well as attenuated total reflectance-Fourier transfer infrared spectroscopy (ATR-FTIR, Nicollet Magna 550).

XPS studies were conducted on ZnO nanowires which were grown on seeded silicon substrates from 16.8 mM zinc nitrate hexahydrate and 25 mM methenamine at 90 °C for 4 hours. The solution was not preheated and the nanowires were rinsed with deionized water and dried in air before being placed in the XPS chamber which was at 10^{-9} torr.

For the ATR-FTIR measurements the nanowires were grown directly on to a Ge ATR crystal from 16.8 mM zinc nitrate hexahydrate and 25 mM methenamine at 90 °C for 4 hours. The solution was not preheated. The ATR crystal was removed from the solution and allowed to dry without rinsing before the FTIR spectrum was recorded. This spectrum is referred to as that of the unwashed wires. Following, the ATR crystal with the nanowires was washed with deionized water and allowed to dry before taking a second FTIR spectrum. This spectrum is referred to as that of the washed wires. An ATR crystal with a ZnO seed layer but without the nanowires was used as the background. To help interpret the FTIR spectra obtained a few milliters of various aqueous solutions including methenamine and zinc nitrate hexahydrate were dried directly on to a pristine Ge ATR crystal and FTIR spectra were taken with the pristine ATR crystal as the

background. The samples were determined to be “dry” once the IR peaks due to liquid water disappeared and the spectra stopped changing.

5.3 Effect of Temporal Temperature Profile

Figure 5.2a shows the temporal evolution of the growth solution temperature for two cases, when the reactant solutions were (i) preheated and (ii) not preheated. When the reaction reactant solutions are preheated and mixed the temperature of the growth solution remains at ~90 °C during the entire growth and all the reactions may be considered isothermal. In contrast, when the reactant solutions are not preheated, the growth solution takes ~100 minutes to reach ~90 °C.

It should be noted that in the experiment shown in Figure 5.2 the temperature of the oven was set to 95 °C and the internal air temperature was confirmed to be 95 °C with a thermocouple. However, as Figure 5.2a shows both the preheated (i) and not preheated (ii) growth solutions reach only ~90 °C. Thus the solution temperature does not reach complete thermal equilibrium with the oven within the time of the reaction (~2 hours). When the reactants were preheated for ~2 hours before they were mixed, they also reach ~90 °C. Although the growth solution does not seem to reach thermal equilibrium with the oven surroundings within the time scale of the reaction, they remain steady at a known temperature within ~5 °C of the oven temperature. The reaction temperatures quoted in this chapter will be the measured temperature of the growth solutions and not that of the oven temperature. For growth experiments where the solutions are not preheated, the temperature quoted is the temperature the solution reaches at the end of the reaction (i.e., 90 °C for experiment ii in Figure 5.2a.)

Figure 5.2b shows the temporal variation of the solution pH corresponding to the experiments in Figure 5.2a. When the solution is not preheated (ii) the pH decreases from 6.8 at $t=0$ to 5.79 on a time scale of ~100 minutes, the same as that it takes the temperature to increase from ~33 °C to ~90 °C. The pH of the solution is determined by the quasi-equilibrium reached between various rapid equilibrium reactions involving protons and hydroxyl ions. These reactions are:

$$HMT + H_2O \Leftrightarrow H - HMT + OH^- \quad (5.R4)$$

$$Zn^{2+} + HMT \Leftrightarrow Zn - HMT \quad (5.R5)$$

$$H^+ + OH^- \Leftrightarrow H_2O \quad (5.R6)$$

$$NH_3 + H^+ + \Leftrightarrow NH_4^+ \quad (5.R7).$$

The fact that the pH follows the temperature indicates that the temperature dependence of these equilibria as well as the changes in the concentration of NH_3 is responsible for this change in pH. The ammonia is not directly added to the solution but is a product of the decomposition of the methenamine, as will be discussed in detail below. As the temperature is raised, methenamine decomposes slowly and NH_3 is released into the solution (see below). The reactions (5.R4)-(5.R7) reach equilibrium on a time scale much faster than the variation of the temperature and ammonia concentration. Thus, these reactions are at a quasi-equilibrium that follows the solution temperature variation (i.e., they come to equilibrium very rapidly at the new temperature T when it is increased.) Thermodynamic equilibrium calculations reveal (see below) that as the temperature is raised, reaction (5.R5) moves further to the right creating more Zn-HMT^{2+} complexes. When zinc complexes with methenamine it competes for lone pairs on the nitrogens so that fewer nitrogens are available for protonation (reaction (5.R4)). This in turn results in the pH decreasing as the temperature is raised.

When the reactants are preheated and mixed the pH remains approximately constant around ~5.8. However, when the temporal evolution of the solution pH is examined in detail (Figure 5.2c), there are some subtle changes in pH over the course of the reaction. For example, the pH starts at ~5.8 and drops down to ~5.75 in the first 30 minutes. After this drop, the pH starts to climb up slowly reaching ~5.83 after 2 hours into the reaction. McPeak et al.[16] and Ashfold et al.[6] describe a similar temporal pH evolution for the reaction of zinc nitrate hexahydrate and methenamine at 90 °C. This subtle pH variation with time can be explained by examining the reactions occurring in the solution. As the methenamine and zinc nitrate hexahydrate solutions are preheated separately their pH rises because the water equilibrium constant increases as the temperature is increased.[17] The methenamine solution pH rises from ~7.6 to ~8.2 and the zinc nitrate hexahydrate solution pH rises from ~5.3 to 5.75. Thus, when the preheated

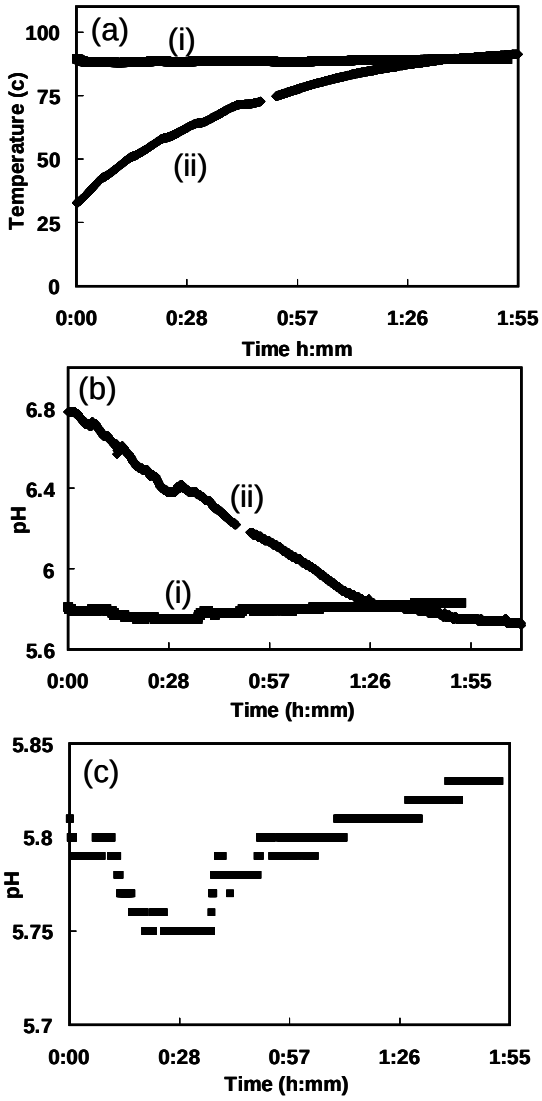

Figure 5.2 (a) Temperature and (b) pH of the growth solution as a function of time for (i) preheated and (ii) not preheated growth. Solution volume, $Zn(NO_3)_26H_2O$ and HMT concentrations were 100 ml, 16.8 mM and 25 mM, respectively. (c) Curve (i) in (b) on expanded scale; the small steps are due to the digitization limit of the probe.

solutions are first mixed, there is a relatively large concentration of OH^- relative to other points in time during the reaction. The solution instantly turns cloudy when the preheated reactants are mixed at 90 °C as some fraction of the Zn^{2+} ions react with the OH^-, via reaction (5.R3), and precipitate as $ZnO_{(s)}$.[16] Reaction (5.R3), however, only occurs at the beginning of the reaction when the pH and temperature are such that reaction (5.R3) is possible. As reaction (5.R3) proceeds during the initial moments after mixing of the reactants, the pH decreases as OH^- is consumed. The pH continues to decrease during the first ~24 minutes of the reaction (Figure 5.2c), until it arrives at value such that reaction (5.R3) reaches equilibrium and $ZnO_{(s)}$ is not longer formed from reaction (5.R3). While reaction (5.R3) is occurring methenamine is also slowly decomposing to form NH_3. Thus, after ~24 minutes into the reaction enough NH_3 has been produced and equilibrated with water through (5.R7) such that the pH of the solution starts to increase. Between ~24 minutes and the end of the reaction the methenamine continuous to decompose and the pH continues to rise (Figure 5.2c).

During the reaction of zinc nitrate hexahydrate with methenamine, ZnO nanoparticles are formed both homogeneously in the solution and heterogeneously on a substrate immersed in the solution. The homogeneous growth looks like white particles which form throughout the solution and make the solution look cloudy due to light scattering. The nanowires grow heterogeneously on substrates covered with a ZnO seed layer. This seed layer enhances the nanowire nucleation density. When the reactants are mixed at room temperature and then heated, homogenous nucleation begins when the solution reaches ~60 ° which occurs at ~22 minutes into heating for a growth solution volume of 100 ml. In contrast, precipitation occurs instantaneously upon mixing when the reactants are preheated to 90 °C.

Figure 5.3 shows that the temporal evolution of the solutiontemperature has a dramatic effect on the dimensions of the ZnO nanowires produced both heterogeneously and homogenously. Figure 5.3a shows an SEM of the nanowires grown on a silicon (100) substrate from a solution which was not preheated, i.e., (ii) in Figure 5.2a; these nanowires are 604 ± 26 nm high and 61 ± 22 nm in diameter. In contrast,

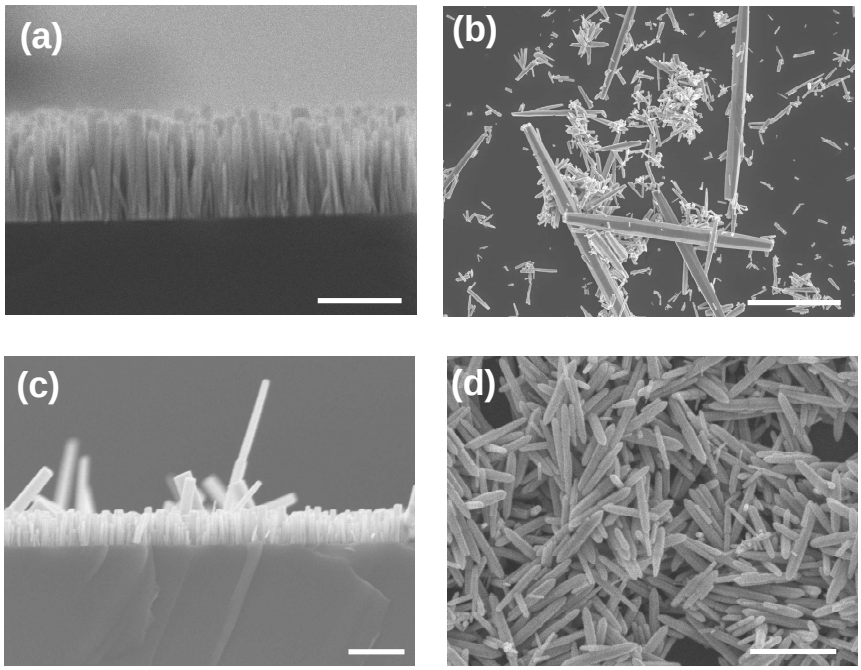

Figure 5.3 SEM images of ZnO nanowires grown at 90 ^{o}C for 4 hours. ZnO nanowires grown heterogeneously on Si using (a) the not preheating method and (c) the preheating method. In (a) the nanowires are 600 ± 25 nm long and 60 ± 25 nm in diameter, whereas in (c) they are 300 ± 25 nm long and 50 ± 20 nm in diameter. (b) and (d) show the homogeneous nanowire precipitates during (b) not preheated and (d) preheated growth, respectively. In (b) nanowire lengths range from fraction of a micron to 7 μm long while diameters range 50 to 500 nm. In (d) the nanowires are 830 ± 100 nm long and 120 ± 25 nm in diameter.

Figure 5.3c shows an SEM of the nanowires grown on a substrate from a solution which was preheated to 90 °C, i.e., (i) in Figure 5.2a; these nanowires are 307 ± 23 nm high and 46 ± 22 nm in diameter. The reason that the nanowires grown heterogeneously in the preheated solution are shorter and narrower than those grown in the not preheated solution is because over the course of the reaction there is a lower concentration of zinc in the preheated solution. The homogeneous growth and precipitation of $ZnO_{(s)}$ is the main sink of zinc in the growth solution; this will be shown shortly. When the reactants are preheated and mixed nanowires form instantaneously and homogeneously upon mixing. This rapid precipitation results in a very large drop in the total zinc ion concentration during the first minute followed by a fast decline during the rest of the growth. In contrast, the zinc concentration decreases slowly when the reactants are mixed at room temperature and heated to 90 ^{o}C (Figure 5.4). This slow decrease is due to the gradual temperature rise which brings the growth solution to supersaturation slowly. As a result, homogeneous nucleation and growth of nanowires begin only after the solution reaches ~60 °C. This allows the total zinc ion concentration to remain higher than that in the preheated growth solution. Thus, the heterogeneous nanowire growth rate, is higher when the reactants are mixed at room temperature and heated to 90 ^{o}C than the growth rate when the reactant solutions are preheated and mixed at 90 ^{o}C.

Figures 5.3b and d show the SEMs of nanowires that result from homogeneous nucleation and growth from a not-preheated (b) and a preheated (d) solution. The nanowires grown in the preheated solution are more uniform in length and diameter than those grown from a not-preheated solution. When the reactant solutions are preheated and mixed at the growth temperature, nucleation of ZnO nanowires in the solution is immediate. This immediate nucleation is followed by a longer growth period that last several hours. Thus, the nucleation and growth steps of the nanowire synthesis were temporally separated when the solution is preheated. This allows all the nanowires to nucleate at approximately the same time and grow simultaneously, thereby causing them to be uniform in size. In contrast, when the solution is not preheated, the nanowires nucleate and grow throughout the reaction resulting in a wide distribution of nanowire lengths and diameters.

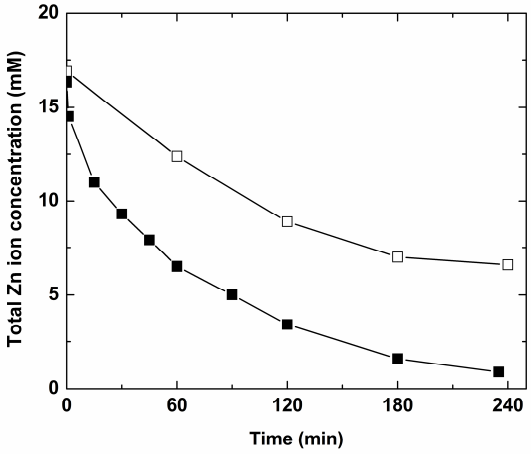

Figure 5.4 Total zinc ion concentration as a function of time during preheated (■) and not preheated (□) growth at 90 ^{o}C. The initial $Zn(NO_3)_2$ and methenamine concentrations were 16.8 mM and 25 mM, respectively.

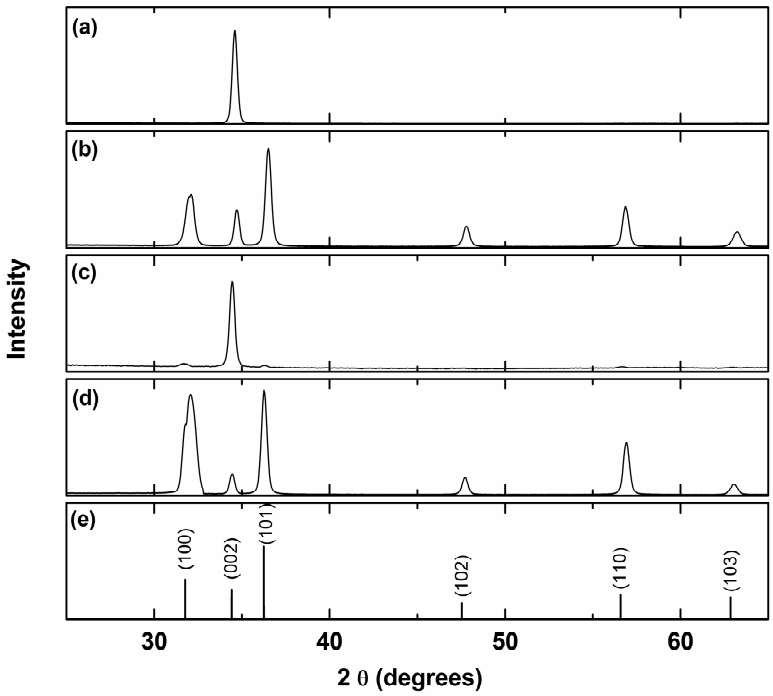

Figure 5.5 XRD from ZnO nanowires grown (a) heterogeneously on Si substrate and (b) homogeneously in solution using the transient growth method. (c) and (d) show the XRD from ZnO nanowires grown (c) heterogeneously on Si substrate and (d) homogeneously in solution using the isothermal growth method. (e) shows the powder diffraction pattern from wurtzite ZnO for comparison. The growth temperature and initial concentrations of $Zn(NO_3)_26H_2O$ and methenamine were 90^{o}C, 16.8 mM and 25 mM, respectively.

Although the dimensions ZnO nanowires synthesized in preheated and not preheated solutions are very different, all of the nanowires formed heterogeneously and homogeneously are wurtzite ZnO, as is shown in Figure 5.5. XRD of all nanowires matched that of wurtzite ZnO, regardless of whether they are grown homogeneously, heterogeneously, by preheating the reactants or by heating reactants mixed at room temperature. Moreover, XRD from nanowires collected from the solution at various times during growth all matched that of wurtzite ZnO. This sample set included the nanowires that precipitate immediately after the preheated reactants are mixed at 90 ^{o}C. Thus we conclude that only wurtzite ZnO nanowires form during growth.

5.4 Effect of Methenamine Concentration

Majority of the zinc put in the growth solution (99.5%) homogeneously precipitates as nanowires. Ultimately, the homogenous growth depletes the zinc concentration and brings the heterogeneous nanowire growth to a halt. Figure 5.6a shows the total mass of ZnO homogenous nanowire precipitates as a function of time for experiments where initial methenamine concentrations were varied while keeping the initial zinc nitrate hexahydrate concentrations constant at 16.8 mM. Assuming that all of the zinc initially placed in the solution eventually precipitates to form ZnO, the maximum weight of ZnO that can be formed from 10 ml of 16.8 mM $Zn(NO_3)_2 6H_2O$ solution is 13.7 mg (marked as the dotted line in Figure 5.6a). In all cases, the mass of the precipitates rises during the first 100-150 minutes and reaches a constant value. The significant scatter in the data reflects two sources of error. First, some amount of ZnO may be loss during centrifugation and washing steps. Second, after drying ZnO can start taking up water as ZnOH forms on the nanowire surfaces. This increases the weight. While this can be minimized by shortening the time between drying and weighing one could still see the mass change even as the precipitates were being weighed. Nevertheless, Figure 5.6a, shows that when more methenamine is added to the solution, homogeneous precipitation occurs faster and the precipitate weight reaches the final value sooner. We conclude that methenamine accelerates the growth reactions. This agrees with the results shown previously by Fujita et al.[2] and Chou et al.[7]

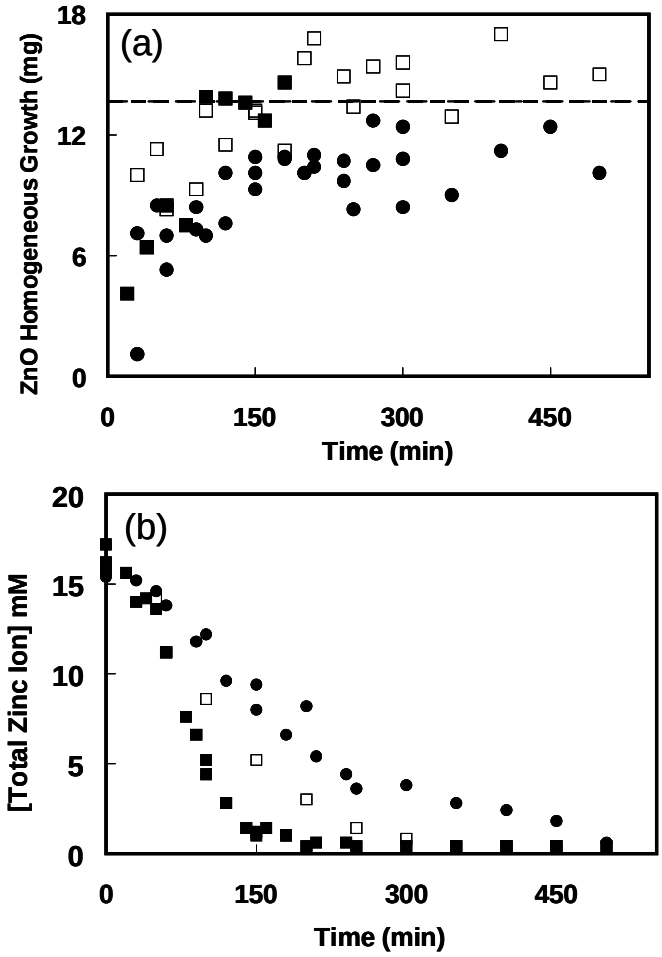

Figure 5.6 (a) Mass of the ZnO homogeneous precipitation versus time for 10 mL total volume reactions done in a centrifuge tube starting with 16.8 mM zinc nitrate hexahydrate and 50 mM (■), 25 mM (□) or 12.5 mM (●) methenamine. The dashed line is at 13.7 mg and estimates the total ZnO mass possible if all of the zinc initially in the solution becomes ZnO. (b) Total zinc ion concentration in the solution versus time for 10 mL total volume reactions done in centrifuge tubes starting with 16.8 mM zinc nitrate hexahydrate and 50 mM (■), 25 mM (□) or 12.5 mM (●) methenamine. The total zinc ion concentration was found by titrating the solution with EDTA. These reactions were not preheated and reached 90 °C after ~60 minutes.

The zinc depletion rate increases with increasing methenamine concentration (Figure 5.6b). This is consistent with increasing homogeneous ZnO nanowire growth rate with increasing methenamine concentration because homogeneous growth is the zinc sink. In addition, the time it takes the zinc ion concentration to drop from the initial concentration of 16.8 mM to its equilibrium value of ~0.4 mM is ~200, ~300 and ~500 minutes for the reactions with 50 mM, 25 mM and 12.5 mM methenamine, respectively (Figure 5.6b). These times match the time it takes to precipitate ~13.7 mg of ZnO (the total amount possible with 10 mL of 16.8 mM zinc nitrate hexahydrate) in reactions with each of these initial methenamine concentrations (Figure 5.6a). In summary, (i) nearly all of the zinc in solution precipitates as homogenous nanowires; (ii) homogenous growth rate determines the zinc depletion rate; and (iii) this rate increases with increasing methenamine concentration.

5.5 Speciation Diagrams

Thermodynamic reaction equilibrium calculations (or speciation calculations) help determine the expected concentrations of the dominant species in a solution. Accordingly, for the aqueous HMT-NH_3-$Zn(NO_3)_2$-$ZnO_{(s)}$ system, we calculated thermodynamic equilibrium concentrations and constructed speciation diagrams at room temperature and at 90 ^oC. Speciation calculations have been done previously on similar aqueous systems. Govender et al.[8] examined the HMT-$Zn(CH_3COO)_2$-$Zn(OH)_{2(s)}$ system, Ashfold et al.[6] the NH_3-Zn(NO3)-$ZnO_{(s)}$ system, Tay et al.[18] the NH_3-Zn(CH3COO)$_2$-$Zn(OH)_{2(s)}$ system, and Yamabi et al.[19] calculated the solubility of $ZnO_{(s)}$ in water.

The following reactions and species were considered in the speciation calculations.

$$ZnO(s) + 2H^+ \longleftrightarrow Zn^{2+} + H_2O \qquad (5.R8)$$

$$ZnO(s) + H^+ \longleftrightarrow ZnOH^+ \qquad (5.R9)$$

$$ZnO(s) + H_2O \longleftrightarrow Zn(OH)_2(aq) \qquad (5.R10)$$

$$ZnO(s) + 2H_2O \longleftrightarrow Zn(OH)_3 + H^+ \qquad (5.R11)$$

$$ZnO(s) + 3H_2O \longleftrightarrow Zn(OH)_4 + 2H^+ \qquad (5.R12)$$

$$Zn^{2+} + HMT \longleftrightarrow Zn - HMT^{2+} \qquad (5.R13)$$

$$HMT + H^{+} \longleftrightarrow H - HMT^{+} \qquad (5.R14)$$

$$Zn^{2+} + NO_3^{-} \longleftrightarrow Zn(NO_3)^{+} \qquad (5.R15)$$

$$Zn^{2+} + 2NO_3^{-} \longleftrightarrow Zn(NO_3)_2 \qquad (5.R16)$$

$$Zn^{2+} + 3NO_3^{-} \longleftrightarrow Zn(NO_3)_3^{-} \qquad (5.R17)$$

$$Zn^{2+} + 4NO_3^{-} \longleftrightarrow Zn(NO_3)_4^{2-} \qquad (5.R18)$$

$$Zn^{2+} + NH_3 \longleftrightarrow Zn(NH_3)^{2+} \qquad (5.R19)$$

$$Zn^{2+} + 2NH_3 \longleftrightarrow Zn(NH_3)_2^{2+} \qquad (5.R20)$$

$$Zn^{2+} + 3NH_3 \longleftrightarrow Zn(NH_3)_3^{2+} \qquad (5.R21)$$

$$Zn^{2+} + 4NH_3 \longleftrightarrow Zn(NH_3)_4^{2+} \qquad (5.R22)$$

$$NH_3 + H^{+} \longleftrightarrow NH_4^{+} \qquad (5.R23)$$

All of the zinc ions are in equilibrium with the solid $ZnO_{(s)}$ present in the solution. Assuming an ideal solution, 19 algebraic equations can be written and solved simultaneously for the concentrations of the 19 components in reactions (5.R8)-(5.R23) as a function of pH. These 19 equations include 16 reaction equilibrium expressions for reactions (5.R8)-(5.R23) which are of the form

$$K_j = \prod_{i=1}^{N_r} \hat{a}_i^{\upsilon_{ij}} \qquad (5.1)$$

where, υ_{ij} is the stoichiometric coefficient of species *i* in reaction *j*, K_j is the equilibrium constant for reaction *j*, $\hat{a}_i$ is the activity coefficient of reactant i, and N_r is the number of reactants. Assuming an ideal solution allows the reactant activity coefficients, $\hat{a}_i$, to be replaced with the reactant concentrations, c_i, such that equation (5.2) becomes,

$$K_j = \prod_{i=1}^{N_r} c_i^{\upsilon_{ij}} \qquad (5.2).$$

The equilibrium constant K_j is related to the standard Gibbs free energy change of the reaction j, ΔG_j°, by

$$K_j = e^{\frac{-\Delta G_j^{\circ}}{RT}} \qquad (5.3).$$

Table 5.1 Equilibrium constants for reactions (5.8R)-(5.23R). The equilibrium constants for reaction (5.R13)-(5.R22) were found from literature.[8,15,20] The other equilibrium constants were calculated from the ΔG_f° values in Table 5.2.

Reaction #	log K_j (25 ℃)	log K_j (90 ℃)
8	11.5	8.68
9	2.1	0.81
10	-5.8	-5.12
11	-17.2	-14.04
12	-30.0	-27.47
13	1.8	1.48
14	4.89	4.01
15	0.11	0.09
16	-0.82	-0.67
17	-0.6	-0.49
18	-1.3	-1.07
19	2.18	1.84
20	4.43	3.68
21	6.74	5.48
22	8.7	6.76
23	9.3	7.61

Table 5.2 Standard free energy, ΔG_f°, and enthalpy, ΔH_f°, of formation for the reactants in reactions (5.8R)-(5.23R), when available in literature.[18,19,21] Standard conditions are 1 atm and 25 °C.

Species	ΔG_f° kJ/mol	ΔH_f° kJ/mol
Zn^{2+} (aq)	-147	-153.64
$ZnOH^+$ (aq)	-330.1	-388.35
$Zn(OH)_2$ (aq)	-522.3	-611.95
$Zn(OH)_3$ (aq)	-694.3	-817.97
$Zn(OH)_4$ (aq)	-858.7	-1125.64
ZnO (s)	-318.32	-348.28
H_2O (l)	-237.18	-285.83
H^+ (aq)	0	0
OH^- (aq)	-157.29	-230
NH_3 (aq)	-26.57	-80.29
NH_4^+ (aq)	-79.37	-132.5
$Zn(NH_3)^{2+}$ (aq)	--	-244.81
$Zn(NH_3)_2^{2+}$ (aq)	--	-338.07
$Zn(NH_3)_3^{2+}$ (aq)	--	-434.68
$Zn(NH_3)_4^{2+}$ (aq)	--	-536.72

Table 5.1 shows the equilibrium constants for reactions (5.R8)-(5.R23) at 25 °C and 90 °C. For some of the reactions ΔG_j° was calculated, using the standard Gibbs free energy of formation of the reactants (ΔG_f°), and then used to calculate the reaction equilibrium constant using equation (5.3). For other reactions the equilibrium constant was found from literature.[8,15,20] The equilibrium constants at 90 °C for some of the reactions (5.R8)-(5.R23) were found using the standard enthalpy of formation of the reactants, ΔH_f°, and the Van't Hoff equation. Table 5.2 shows the reactant ΔG_f° and ΔH_f° values which are available in the literature.[18,19,21] For some reactants the ΔH_f° values were not available in the literature, so for those reactions involving these reactants the Gibbs free energy change was assumed to be independent of temperature in the narrow temperature range of interest. This is an appropriate assumption for a narrow range of temperatures because the exponential dependence of the equilibrium constants on temperature is the strongest while the temperature dependence of the Gibbs free energy is a higher order correction.

Traditionally, three atomic balance equations over nitrogen, oxygen and carbon would also be included. However, at equilibrium the total number of methenamine, ammonia and ammonium ions and nitrate ions is constant. Therefore, to simplify the calculations, molecular balances were done over methenamine, ammonia and ammonium ions and nitrate ions. The equations used were

$$[Zn-HMT^{2+}]+[HMT]+[H-HMT^{+}]=M \quad (5.4)$$

$$[NH_3]+[NH_4^+]=A \quad (5.5)$$

$$[NO_3^-]+[Zn(NO_3)^+]+2[Zn(NO_3)_2]+3[Zn(NO_3)_3^-]+4[Zn(NO_3)_4^{2-}]=N \quad (5.6)$$

where M, A and N are the total number of methenamine, ammonia and ammonium ions, and nitrate ions, respectively. M and N were set to the initial concentrations in the reaction solution, 25 mM and 32 mM respectively. A was set to 40 mM, this is the maximum concentration which occurs in the reaction solution according to the temporal evolution of the methenamine concentration shown below (Figure 5.11c).

The 16 reaction equilibrium equations of the form shown in equation (5.2) along with 3 molecular balances, equations (5.4)-(5.6), were all solved simultaneously for the concentration of the 19 reactants, shown in reactions (5.R8)-(5.R23), as a function of pH.

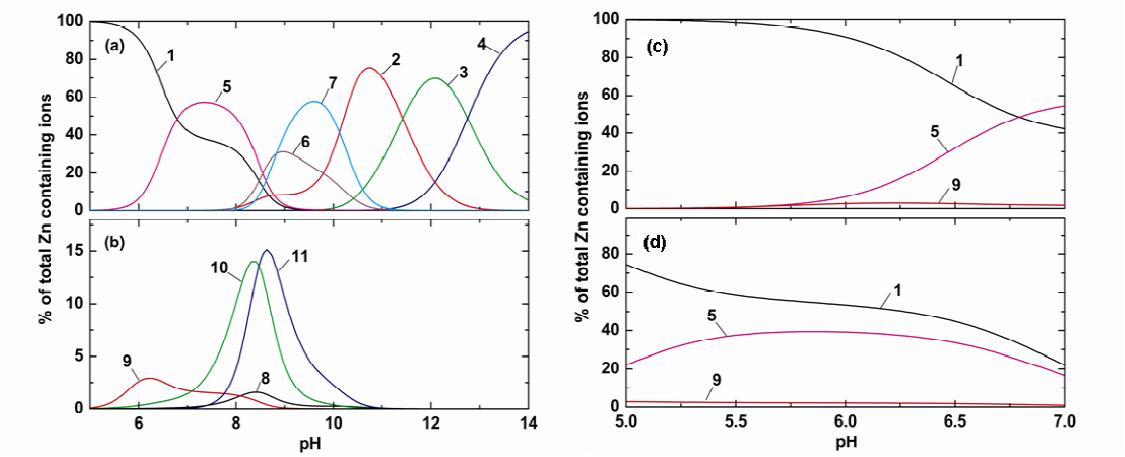

Figure 5.7 Concentrations of zinc containing ions, as a function of pH, in equilibrium with ZnO(s) in an aqueous solution containing 25 mM methenamine, 32 mM nitrate ions and 40 mM ammonia. The concentrations are expressed as a percentage of total Zn containing ions. (a) ,(b) and (c) are at 25 °C, and (d) is at 90 °C. Those species which are below 0.2% in the pH region displayed are not shown for clarity. (1) Zn^{2+}, (2) $Zn(OH)_2$, (3) $Zn(OH)_3^-$, (4) $Zn(OH)_4^{2-}$, (5) $ZnHMT^{2+}$, (6) $Zn(NH_3)_3^{2+}$, (7) $Zn(NH_3)_4^{2+}$, (8) $Zn(OH)^+$, (9) $Zn(NO)_3^+$, (10) $Zn(NH_3)^{2+}$, (11) $Zn(NH_3)_2^{2+}$.

The total solubility of ZnO as a function of solution pH was calculated by summing all the zinc containing ion concentrations at each pH value. The percentage that each zinc containing ion is of the total $ZnO_{(s)}$ solubility as a function of pH was calculated by dividing the concentration of each zinc ion (at each pH) by the total $ZnO_{(s)}$ solubility (at each pH) and multiplying by 100.

Figures 5.7a and b show the percentage that each zinc containing ion is of the total $ZnO_{(s)}$ solubility at 25 °C as a function of pH. Figure 5.2c shows that the experimentally relevant section of the speciation diagram is between 5.75 and 5.85. Figure 5.7c shows that in this pH range and at 25 °C most of the zinc containing ions are Zn^{2+} (~94%) with a small amount of $Zn(NO_3)^+$ (~4%) and zinc-methenamine complex Zn-HMT^{2+} (~2%) present. However, as the solution temperature is increased, the concentrations of zinc containing ions change as shown in Figure 5.7d. At 90 °C Zn^{2+} is still the dominant ion (55%) but there is also significant amounts of the zinc-methenamine complex Zn-HMT^{2+} (~38%). Other ions such as $Zn(OH)^+$, $Zn(OH)_2$, $Zn(NO_3)^-$ and $Zn(NH_3)^{2+}$ also exist in smaller amounts. While the reaction is clearly not in thermodynamic equilibrium these calculations suggest that the ZnO growth mechanism may involve Zn^{2+} and the zinc-methenamine complex, Zn-HMT^{2+}, as precursors.

5.8 Surface Characterization of ZnO Nanowires

Figure 5.8 shows the ATR-FTIR absorption spectrum of dry ZnO nanowires immediately after they are grown on a Ge ATR crystal but before rinsing with deionized water (unwashed). This spectrum of the unwashed nanowires is similar to that recorded by Chou et al.[7] for unwashed ZnO particles synthesized from zinc nitrate hexahydrate and methenamine. Figure 5.8 also shows the ATR-FTIR spectrum of the same nanowires after they were rinsed with deionized water and dried with flowing air. When the nanowires are allowed to dry after growth without rinsing with deionized water (i.e., unwashed wires), a salt containing zinc, methenamine, nitrate ions and water molecules deposits onto the surface of the nanowires and the infrared spectrum is dominated by this deposit. The IR peaks of the unwashed wires were assigned by comparing to spectra of methenamine, nitrate salts, and methenamine-nitrate-zinc-water salts found in

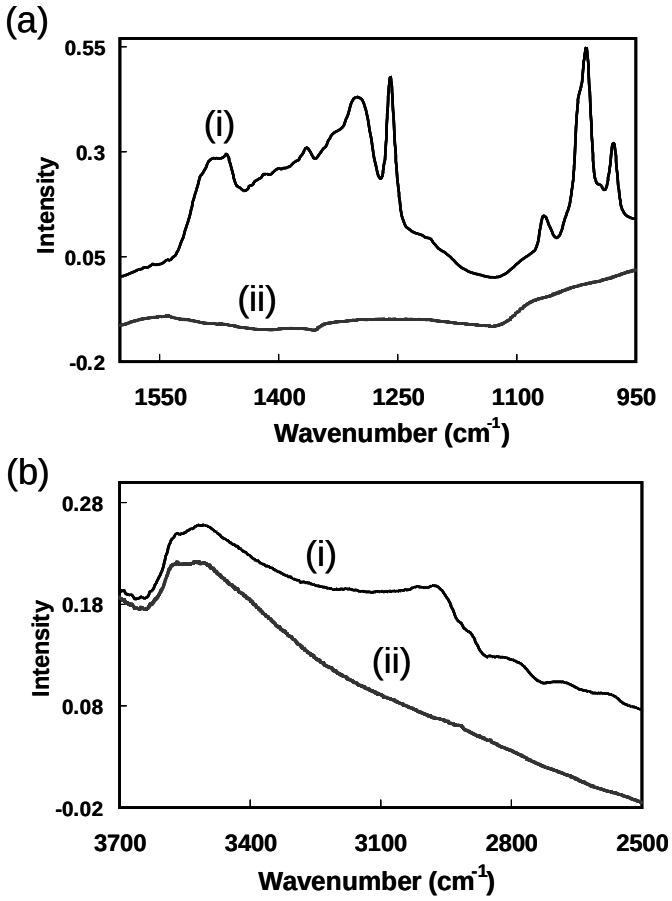

Figure 5.8 ATR-FTIR spectra of ZnO nanowires grown on a Ge ATR crystal for 4 hours not preheated at 90 °C in a solution of 16.8 mM zinc nitrate hexahydrate and 25 mM methenamine before (i) and after (ii) rinsing with deionized water. (a) Between 950 cm^{-1} and 1600 cm^{-1}. (b) Between 2500 cm^{-1} and 3700 cm^{-1}. Both of these spectra were taken with respect to the ZnO seeded (via drop casting ZnO nanoparticles) Ge ATR crystal.

literature.[13,22-26] When methenamine is bound to a zinc atom in a salt this causes the ν_{22} and ν_{21} C-N stretches and the C-N-C deformation mode, which are located at 1007 cm^{-1} and 1234 cm^{-1} and 1048 cm^{-1} respectively in neat methenamine to shift, broaden and split.[13,22] The "neat" methenamine IR spectrum we refer to in this chapter is that of crystalline methenamine in a KBr pellet.[22] In the IR spectrum of the unwashed wires the methenamine ν_{22} C-N stretch splits into two peaks, one at 978 cm^{-1} and one at 1012 cm^{-1}. The methenamine ν_{21} C-N stretch shifts to 1259 cm^{-1} and the C-N-C deformation mode shifts to 1066 cm^{-1}. The broad peaks at 1297 cm^{-1} and 1484 cm^{-1} are due to the N-O stretching bands of the nitrate ions. The weak absorptions between 1350 cm^{-1} and 1480 cm^{-1} are due to the CH_2 wags, deformations and scissors of the methenamine and the weak absorptions near 2980 cm^{-1} are due to methenamine CH_2 stretches. The broadabsorption near 3550 cm^{-1} is due to O-H stretches of adsorbed water and hydroxyls as well as the N-H stretches of methenamine.

The IR spectrum of the nanowires showed none of the absorptions assigned to the hydrated salt containing zinc, methenamine, nitrate ions after rinsing the unwashed nanowires with deionized water (Figure 5.8). We conclude that methenamine, nitrates and zinc were removed from the nanowire surface during rinsing with water. Only the absorption at 3550 cm^{-1}, which corresponds to O-H stretches, remains. This suggests that the nanowire surface is hydroxyl terminated when in the reaction solution. The 3550 cm^{-1} peak is assigned to O-H stretches and not to N-H absorptions, which also appear in this region of the spectrum, because no nitrogen was detected with XPS on the washed nanowires (Figure 5.9).

5.9 ZnO Nanowire Growth Mechanism

Tada[27] studied the decomposition of methenamine to ammonia (NH_3) and formaldehyde (H_2CO) in acidic conditions and found that the first step in this reaction is the protonation of one of the nitrogen atoms in methenamine. The nitrogen atoms of the methenamine molecule protonate and deprotonate on a very fast time scale compared to the reaction rates of the subsequent decomposition steps. Thus, during slow decomposition reactions the protonated ($H\text{-}HMT^+$) and unprotonated (HMT) forms of methenamine are in equilibrium with each other as shown in reaction (5.R14). The

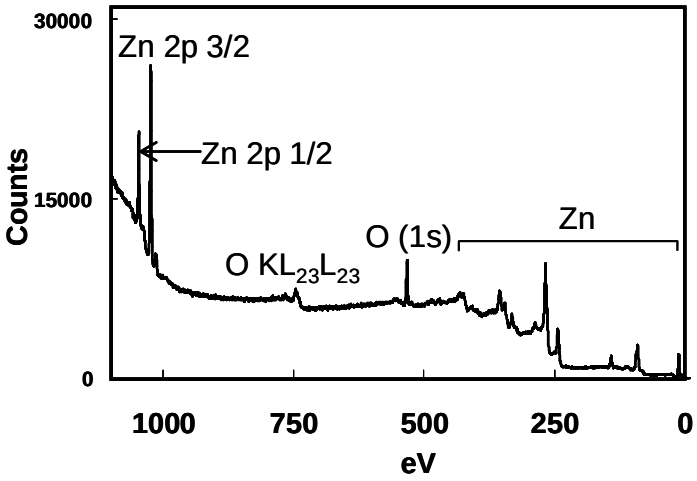

Figure 5.9 XPS spectrum of ZnO nanowires grown on a silicon substrate, seeded by drop casting ZnO nanoparticles, from an aqueous solution of 25 mM methenamine and 16.8 mM zinc nitrate hexahydrate not preheated at 90 °C. The nanowires were rinsed with deionized water before the spectra was taken. Only oxygen and zinc peaks were present in the spectrum.

equilibrium constant of this reaction was measured to be $K=10^{4.89}$.[8,20] In the second step of the decomposition mechanism, a second proton attaches to the already protonated nitrogen irreversibly breaking the C-N bond. Tada[27] found that once this C-N bond was broken the subsequent steps of the methenamine decomposition proceeded quickly, thus making this second step the rate limiting step.

We propose that, during ZnO nanowire growth, the methenamine decomposes through a similar mechanism, except that, instead of a proton, a zinc ion initiates the decomposition reaction by attaching to one of the nitrogen atoms on the methenamine. Figure 5.10 illustrates the proposed ZnO nanowire growth mechanism. In the first step, a Zn^{2+} ion binds to one of the nitrogen atoms on the methenamine molecule. The rapid binding and unbinding of the zinc to the nitrogen on the methenamine is fast relative to the subsequent reactions so that the Zn^{2+} ion, methenamine and zinc-methenamine complex (Zn-HMT^{2+}) are in pseudo equilibrium through reaction (5.R13) ($K=10^{1.8}$),[8,20] during the ZnO nanowire synthesis. This equilibrium is quantified by forward and reverse rate constants k_{1f} and k_{1r}. Assuming pseudo equilibrium between methenamine, Zn^{2+} ion and Zn-HMT^{2+} is appropriate because we expect molecules such as water and methenamine surrounding a Zn^{2+} ion in an aqueous solution to substitute at a rate of ~10^7 sec^{-1}. For example, this rate has been measured to be 3×10^7 s^{-1} for water,[28] and since the zinc-nitrogen bond formed between methenamine and Zn^{2+} should behave in a similar way to the zinc-oxygen bond formed between water and Zn^{2+}, the rate of methenamine substitution into the coordination sphere of Zn^{2+} should also be on the order of ~10^7 sec^{-1}. This is much faster than the decomposition of methenamine which happens on a time scale of minutes.

In the next step, one of two things can happen to the Zn-HMT complex. First, it can come in contact with the Zn-OH on the nanowire surface and the hydroxyls can act as a nucleophile, breaking the bond between the nitrogen bound to the zinc and an adjacent carbon atom. Tada[27] established such an attack on the Zn-N bond to be the rate limiting step in decomposition of methenamine. Following, the methenamine quickly decomposes to ammonia and formaldehyde and the zinc is incorporated into the ZnO solid. This

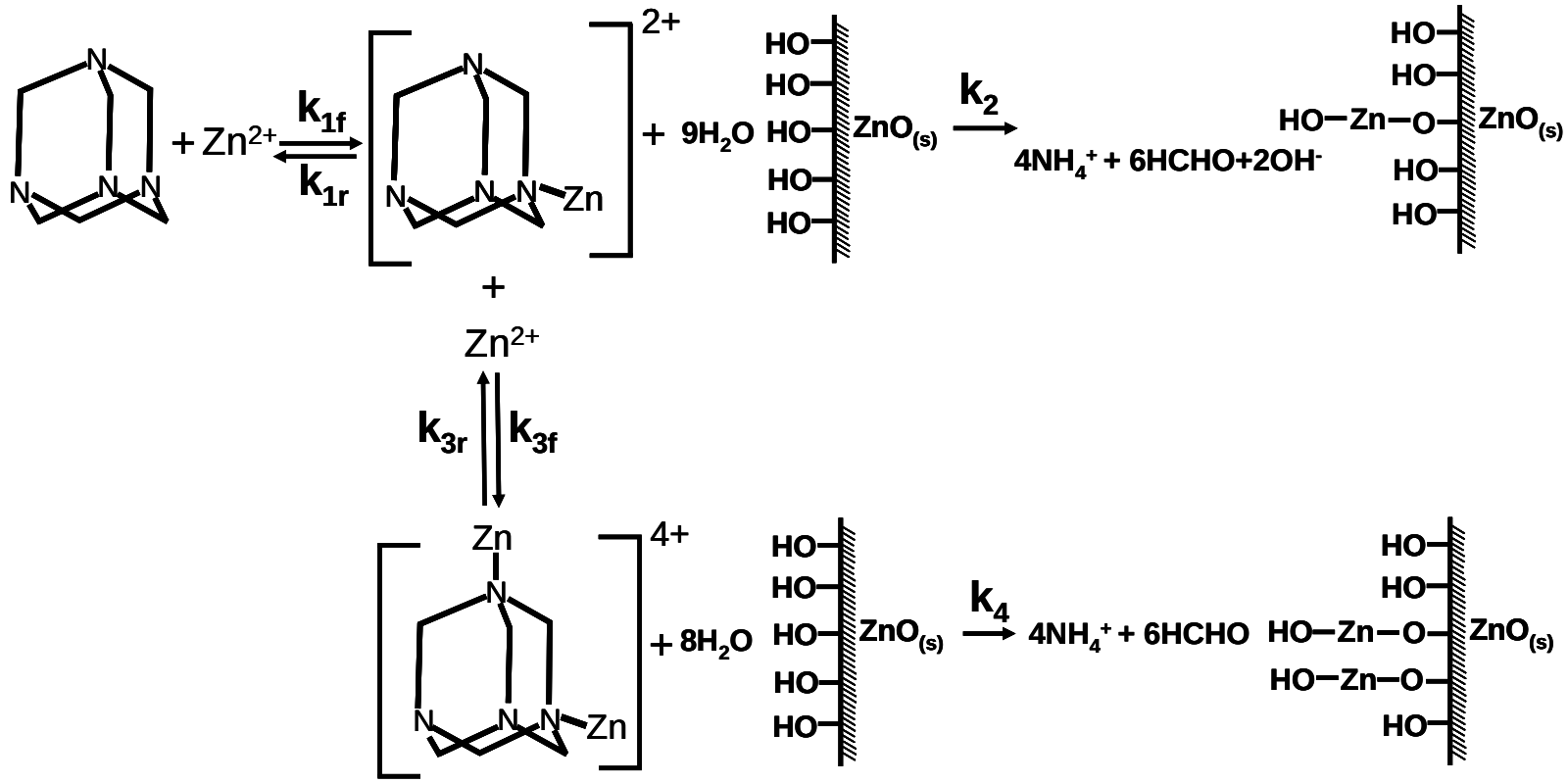

Figure 5.10 Schematic of the proposed mechanism of ZnO(s) formation from zinc nitrate hexahydrate and methenamine. Zinc-methenamine complexes, Zn-HMT^{2+} and Zn-HMT-Zn^{4+} form in the solution and react at the hydroxyl terminated $ZnO_{(s)}$ surface. Upon reaction the zinc incorporates into the $ZnO_{(s)}$ and the methenamine decomposes to ammonia and formaldehyde. The line with the hash marks indicates $ZnO_{(s)}$-solution-interface.

irreversible process of the zinc in the Zn-HMT^{2+} complex incorporating into ZnO can be approximated with one reaction rate constant k_2. The second possible reaction path for the Zn-HMT^{2+} is for another Zn^{2+} ion to bind to the Zn-HMT^{2+} before the methenamine decomposes, thus creating a Zn-HMT-Zn^{4+} complex. Since the addition of the second Zn^{2+} should be similar to the first, Zn-HMT^{2+}, Zn-HMT-Zn^{4+}, and Zn^{2+} are also taken to be in equilibrium with forward and reverse rates k_{3f} and k_{3r}, as is illustrated in Figure 5.10. Like Zn-HMT^{2+}, the Zn-HMT-Zn^{4+} can also react with the Zn-OH on the nanowire surface and incorporate zinc atoms into the growing ZnO solid while producing ammonia and formaldehyde. This reaction can also be modeled with one reaction rate constant k_4. It should be noted that the addition of the Zn^{2+} to Zn-HMT^{2+} may happen before or after the Zn-HMT^{2+} reacts with the $ZnO_{(s)}$ surface. For example, if it is possible for the Zn-HMT^{2+} to adsorb on the ZnO nanowire surface to form an adsorbed species with finite and relatively long lifetime, then reaction of a second Zn^{2+} with this adsorbate would trigger the decomposition of the Zn-HMT^{2+}complex. The main idea that this sequence of events is capturing is that as one methenamine molecule decomposes it can incorporate either one or two Zn^{2+} ions into the $ZnO_{(s)}$. We found this idea to be the key to fitting the kinetic data.

The reactions in Figure 5.10 are balanced by using the ammonium ion (NH_4^+) rather than ammonia (NH_3). This is because at the pH of the ZnO nanowire synthesis reaction, ~5.7, the NH_4^+ to NH_3 is ~80:1. Furthermore, hydroxyl ions are produced throughout the growth because the overall reaction of zinc and methenamine produces NH_3 and NH_4^+ ions, This is the reason for the slow rise in pH during the growth with preheated solutions (Figure 5.2c.) It should also be noted that while we identify the zinc complexes as Zn-HMT^{2+} and Zn-HMT-Zn^{4+}, in the aqueous solutions the Zn-HMT^{2+} and Zn-HMT-Zn^{4+} complexes are solvated by water as well as NO_3^- ions which balance the charge. The H_2O and NO_3^- molecules have been have been omitted from the complexes in Figure 5.10 for clarity.

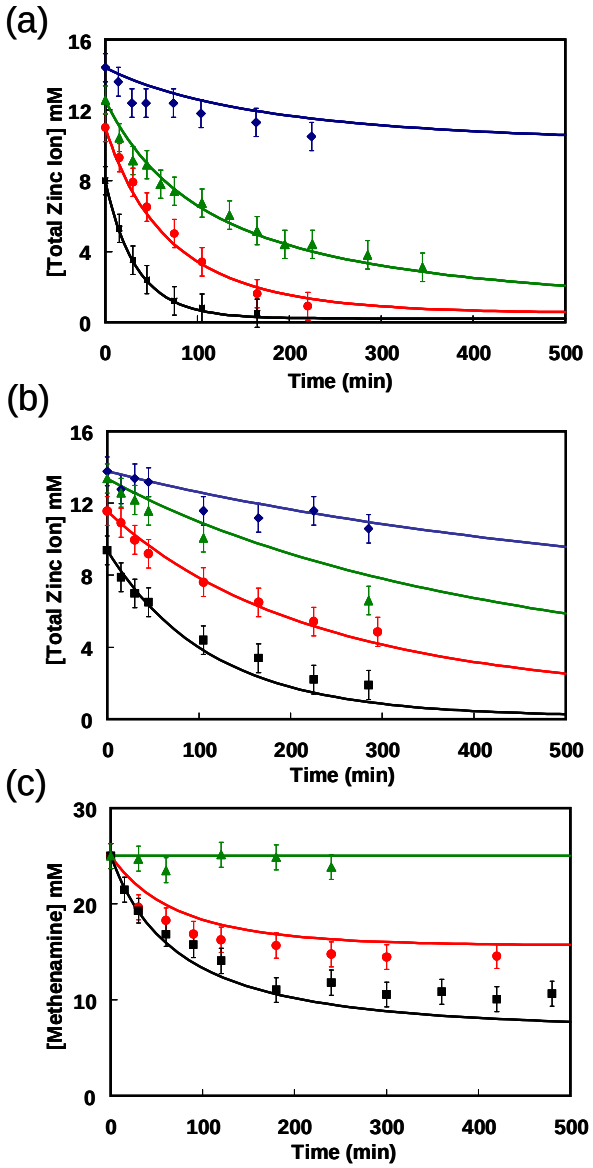

Figure 5.11 (a) Total zinc ion concentration as a function of time for reactions preheated at 90 °C. The points are experimentally found with EDTA titration and the lines are calculated from the proposed mechanism. The initial zinc concentration was 16.8 mM for all the reactions. The initial methenamine concentrations used were 50mM (■), 25 mM (●), 15 ± 2mM (▲) and 4 mM (●). (b) Total zinc ion concentration as a function of time for a reaction at 80 °C. The initial zinc concentration was 16.8 mM for all the reactions. The initial methenamine concentration used were 100 mM (■), 44 ± 6 mM (●), 25 mM (▲), 12.5 mM (●). (c) Concentration of methenamine as a function of time for a reaction preheated at 90 °C with an initial concentration of 25 mM methenamine and 33.6 mM (■) 16.8 mM (●) and 0 mM (▲) zinc nitrate hexahydrate. The reaction with 33.6 mM and 16.8 mM zinc nitrate hexahydrate was preheated and the reaction without zinc was not preheated. The points are experimental results from ^{1}H NMR and the lines are calculated from the proposed mechanism.

Using the proposed growth mechanism shown in Figure 5.10 equations for the depletion rate of methenamine and zinc are given by,

$$\frac{d[HMT]}{dt} = -[HMT][Zn]\left(\frac{K_1 + K_2[Zn]}{K_3 + K_4[Zn]}\right) \quad [5.7]$$

$$\frac{d[Zn]}{dt} = -[HMT][Zn]\left(\frac{K_1 + 2K_2[Zn]}{K_3 + K_4[Zn]}\right) \quad [5.8]$$

where,

$$K_1 = k_{1f}k_2 \quad [5.9]$$

$$K_2 = k_{1f}\left(\frac{k_{3f}k_4}{k_{3r} + k_4}\right) \quad [5.10]$$

$$K_3 = k_{1r} + k_2 \quad [5.11]$$

$$K_4 = \left(\frac{k_{3f}k_4}{k_{3r} + k_4}\right) \quad [5.12].$$

The Zn-HMT^{2+} concentration is given by,

$$[Zn - HMT^{2+}] = \frac{K_1/K_2\,[Zn][HMT]}{K_3 + K_4[Zn]} \quad [5.13].$$

[Zn] represents the concentration difference between the Zn^{2+} ion concentration and the equilibrium Zn^{2+} ion concentration. The equilibrium Zn^{2+} ion concentration was found by multiplying the total zinc ion concentration at equilibrium (found experimentally by titrating the solution after sufficient time for equilibrium to be reached, ~16 hours) by the fraction of the total zinc ion concentration which is Zn^{2+} (calculated from the thermodynamic reaction equilibrium calculation, Figure 7c). Equations (5.7), (5.8) and (5.13) were derived assuming pseudo steady state concentrations of Zn-HMT^{2+} and Zn-HMT-Zn^{4+}. The details of this derivation are given in Appendix 1. As was mentioned above, k_{1f} and k_{1r} are likely on the order of ~10^7 sec^{-1}. Thus the K_4, which does not contain k_{1f}, was taken to be negligible relative to K_1, K_2 and K_3. This reduces the equation (5.7) and (5.8) from a four parameter model to a two parameter model with constants K_1/K_3 and K_2/K_3.

The temporal evolution of methenamine and Zn^{2+} were calculated by numerically integrating equations (5.7) and (5.8) simultaneously. The EDTA titration measures the

total concentration of zinc ions in the solution. Thus, since Zn^{2+} and Zn-HMT^{2+} are the dominate zinc ion species (Figure 7c), the temporal profile of the sum of the Zn^{2+} and Zn-HMT^{2+} concentrations were compared to the experimental EDTA titration results. With the proper selection of K_1/K_3 and K_2/K_3 the predictions of this model for the methenamine and total zinc ion concentration profiles match those found experimentally. Figure 5.11a shows the comparison between measured and calculated temporal evolutions of the total zinc ion concentration at 90 °C for different initial methenamine concentrations. The K_1/K_3 and K_2/K_3 values used in this calculation are shown in Table 5.3. The initial zinc nitrate hexahydrate concentration was kept constant at 16.8 mM. Kinetic data collected under isothermal conditions (preheated solutions) was used to extract K_1/K_3 and K_2/K_3 because these reaction constants are functions of temperature. Figure 5.11b shows a similar comparison for experiments conducted at 80 °C. The corresponding K_1/K_3 and K_2/K_3 values that best matched the data are shown in Table 5.3. Again, the initial concentration of zinc nitrate hexahydrate was kept constant at 16.8 mM while the initial methenamine concentration was varied.

Table 5.3 The reaction rate constants, K_1/K_3 and K_2/K_3 at 90 °C and 80 °C which best match the experimental data.

Temperature (C)	K_1/K_3 mM^{-1} min^{-1}	K_2/K_3 mM^{-2} min^{-1}
90	6×10^{-4}	5×10^{-13}
80	9×10^{-5}	1×10^{-13}

When the preheated methenamine and zinc nitrate hexahydrate solution are mixed, precipitation occurs within the first few seconds (i.e., reaction (5.R3)) and there is an initial fast drop in zinc concentration. The mechanism presented above describes the growth kinetics after the solution has reached pseudo phase equilibrium and after the solid phase has nucleated. In order to remove the kinetics of this initial fast reaction, the first total zinc ion points shown in Figures 5.11 a and b are taken to be that measured 15 minutes into the reaction. The Zn^{2+} concentration at this point is then taken to be the initial Zn^{2+} concentration in the calculations. Thus, even though the initial concentration

of the all the reactions was 16.8 mM, the initial concentrations in Figure 5.11 a and b are lower.

Figure 5.11c shows a comparison between measured and calculated temporal evolutions of methenamine concentration at 90 °C for three initial zinc nitrate hexahydrate concentrations, 33.6 mM 16.8 mM and 0 mM. The initial concentration of methenamine was 25 mM. This figure clearly shows that, on the time scale of interest, methenamine decomposition occurs only when zinc is present. Furthermore, the methenamine depletes faster when more zinc in present. This data establishes that the presence of zinc accelerates the methenamine decomposition and that the decomposition rate is not independent of the reactions involving zinc as has been previously suggested.[6]

The agreement between the calculated and the measured temporal evolution of the total zinc ion and methenamine concentration suggests that the proposed mechanism captures the essential elements of the solution chemistry occurring during the ZnO nanowire growth process.

5.10 Evidence for the Presence of the Zinc-Methenamine Complex

Methenamine is a weak base; the protonated ($H\text{-}HMT^{+}$) and unprotonated (HMT) methenamine are in equilibrium with one another (reaction (5.R14)). The concentration of protonated methenamine increases as the pH of the solution decreases. The fraction of protonated methenamine in the solution was calculated as a function of pH at 25 °C and is shown in Figure 5.12a. The amount of protonated methenamine at different pH values can be measured from the ^{1}H NMR spectra of methenamine. Figure 5.12a shows that the position of the methenamine proton peak shifts downfield as the pH of the methenamine solution is lowered upon addition of HCl. The methenamine peak shifts downfield due to the protonation of the nitrogen atom, which in turn deshields the protons on the carbon atoms. As the pH is lowered further and more methenamine is protonated, reaction (5.R14) shifts to the right while the methenamine peak shifts downfield. At any given moment in the methenamine solution protonated and unprotonated methenamine exists in equilibrium. Only a single methenamine ^{1}H NMR peak is observed (Figure 5.12b) because the protonation and deprotonation rates at equilibrium are very fast compared to the time scale of the NMR scan (i.e. the difference in frequency between the protonated

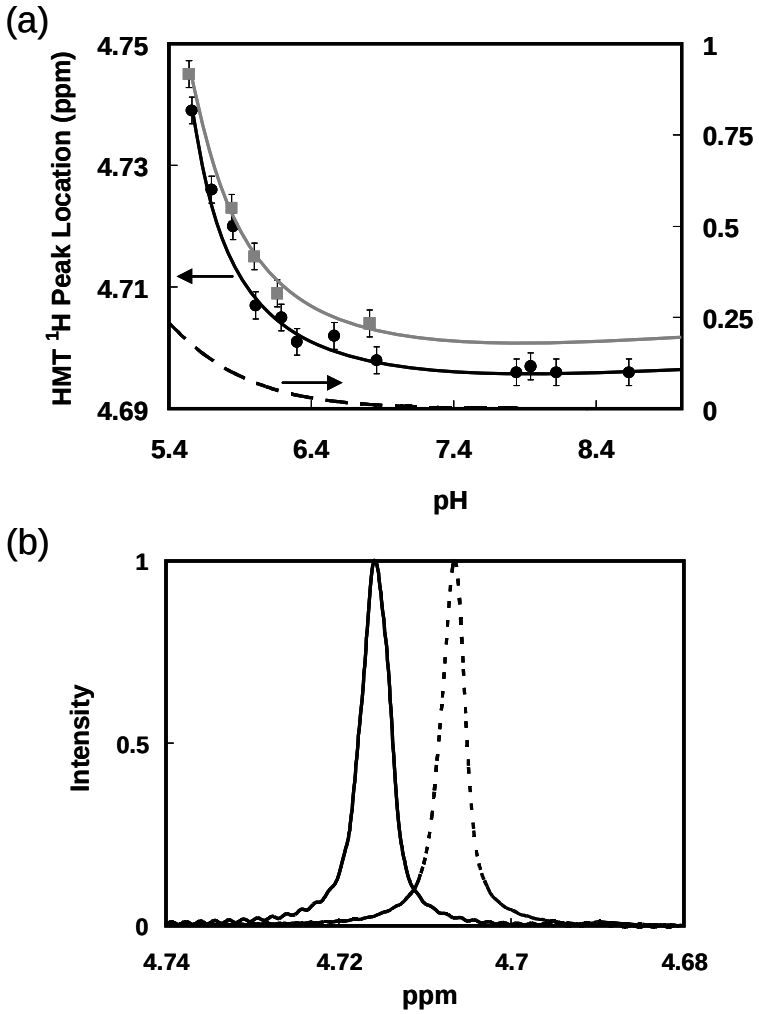

Figure 5.12 (a) ^{1}H NMR peak position of CH_2 protons in methenamine as a function of pH in absence (●) and in presence (■) of zinc (16.8 mM) in 25 mM methenamine D_2O solution. (b) shows the NMR shift with addition of Zn at constant pH of 6. The solid lines are fits to aid the eye. The dashed line is the fraction of protonated methenamine as a function of pH at 25 ^oC calculated using the equilibrium constant for reaction (5.R14) in Table 5.1.

and unprotonated methenamine peaks.) Therefore, the protonated and unprotonated methenamine peaks are not resolved in the ^{1}H NMR spectrum and the methenamine peak location is an average of the locations of the methenamine peaks when methenamine is protonated and when it is not. This average peak location is determined by the relative amounts of protonated and unprotonated methenamine in solution and shifts closer to that of the protonated peak downfield as the pH is lowered and more protonated methenamine is present. The pH value at which the methenamine peak starts to shift downfield matches to the pH at which the fraction of protonated methenamine is calculated to increase using the equilibrium constant for reaction (5.R14).[8,20]

When zinc is present in the solution, it also binds to the nitrogen on the methenamine, and the resulting zinc-methenamine complex, zinc and methenamine are all in equilibrium with each other, reaction (5.R13). Binding of zinc to the methenamine also deshields the protons on the carbons and shifts the methenamine peak downfield. In aqueous solutions of methenamine and zinc nitrate hexahydrate, both reactions (5.R13) and (5.R14) occur at the same time: zinc ions as well as protons are bound and released rapidly from the nitrogen on the methenamine. Again, these equilibria are much faster relative to the time scale of the NMR scan, and only a single methenamine NMR peak is detected presenting presence of zinc ions as shown in Figure 5.12b. When zinc ions are present and bound to methenamine, the protons attached to the carbon are even more deshielded than when just the protons are present and, at any given pH, the methenamine peak shifts further downfield as shown in Figure 5.12a. This larger proton NMR peak shift with zinc added to the methenamine solution is one of the evidence for the presence of the zinc-methenamine complex in the nanowire growth solution.

Further evidence for the presence of the zinc-methenamine complex in the growth solution comes from the ATR-FTIR spectra of salts deposited on a Ge ATR crystal when aqueous solutions containing zinc, methenamine and nitrate ions dry on these surfaces. When zinc binds to methenamine to form a molecular salt complex, the ν_{22} and ν_{21} modes of neat methenamine located at 1007 cm^{-1} and 1234 cm^{-1}, which are assigned as C-N stretches, split into two or more peaks.[13,22] The number and location of the resulting absorption peaks are sensitive to the geometry, and in particular, to the symmetry of

methenamine complex.[12,13,28] In general, as the methenamine symmetry is lowered the C-N stretches split into more peaks.[13,23] The symmetry of the methenamine molecule is T_d. When methenamine is a monodentate ligand and is attached to one zinc ion, its symmetry is lowered to C_{3v}. When methenamine acts as a bidentate ligand and is bonded to two zinc atoms, the symmetry is further lowered to C_{2v}. In the bidentate geometry, methenamine bridges two zinc ions (i.e., Zn-HMT-Zn^{4+} as it was denoted above). When methenamine acts as a monodentate ligand or a bridge-like ligand the C-N stretching absorption peak splits into two and three peaks, respectively.[12]

Grodzicki et al. have studied the infrared absorption spectra of the hydrated salts formed by zinc, methenamine and one of several different anions including the nitrate ion.[12,13,29] Grodzicki et al. formed these molecular salts by drying and thermally dehydrating aqueous solutions of zinc nitrate hexahydrate and methenamine.[13,29] They proposed two possible chemical formulas for the salts that form directly from the solution by drying, $[Zn(H_2O)_2(HMT)_2](NO_3)_2 \bullet 4H_2O$ and $[Zn(H_2O)_4(HMT)_2](NO_3)_2 \bullet 2H_2O$. In both of these salt structures Grodzicki et al.[13] determined that the methenamine is bound to the zinc though a single coordination bond rather than through a bridge-like bond. They also found that, for both of these salts, the C-N stretch (ν_{22}), which appears at 1007 cm^{-1} in the neat methenamine spectra, splits into two peaks, one at 1000 cm^{-1} and another at 1025 cm^{-1}. They also observed that the C-N stretch (ν_{21}) which is normally at 1234 cm^{-1} in the neat methenamine spectra splits into two peaks, one at 1236 cm^{-1} and another at 1255 cm^{-1}.

Using ATR-FTIR, we examined the C-N stretching absorption of salt complexes that form when aqueous solution of zinc nitrate hexahydrate and methenamine dried on the Ge ATR crystal surface. Figure 5.13a shows the ATR-FTIR spectra of a 16 mM aqueous zinc nitrate hexahydrate solution dried on the Ge ATR crystal. The three broad peaks in the spectra are located at 1024 cm^{-1}, 1290 $cm^{-1}$and 1479 cm^{-1} and are due to the ν_2, ν_5 and ν_1 modes respectively.[25] These modes have been assigned to N-O stretching of the nitrate.[25] An aqueous solution containing 100 mM methenamine was dried on the Ge ATR crystal and the ATR-FTIR spectra is shown in Figure 5.13b. The strong peaks at 1002 cm^{-1} and 1236 cm^{-1} are due to the ν_{22}, and ν_{21} C-N stretching modes, respectively.[22]

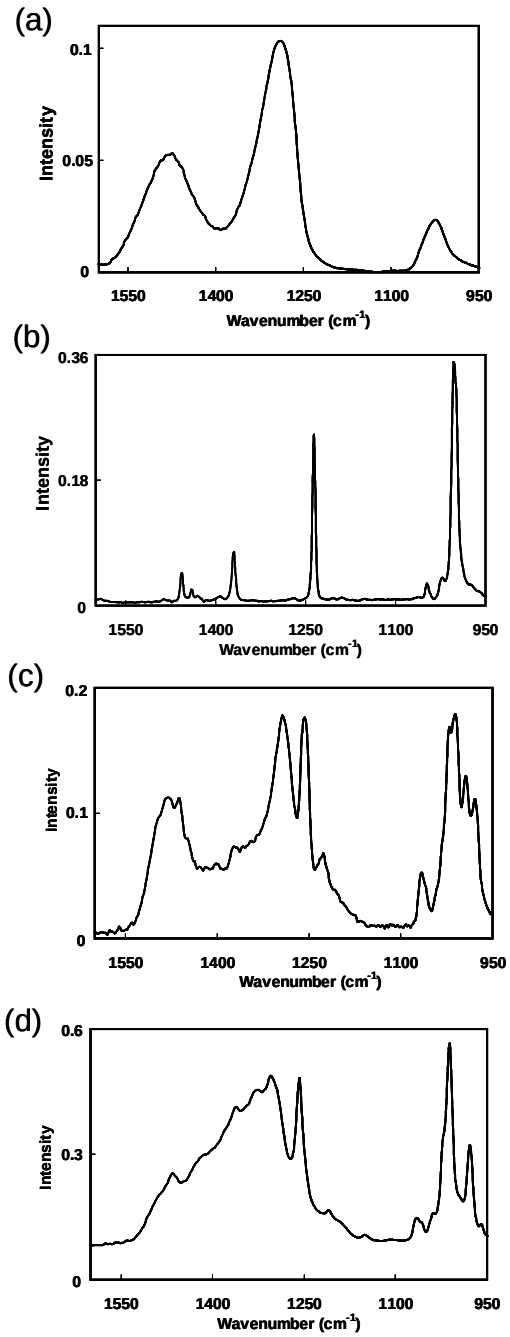

Figure 5.13 ATR-FTIR spectra of aqueous solutions dried on a Ge ATR crystal. (a) 16 mM zinc nitrate hexahydrate at 25 °C, (b) 100 mM methenamine at 25 °C. (c) spectrum of 16.8 mM zinc nitrate hexahydrate and 25 mM methenamine at 25 °C and (d) heated at 90 °C for 4 hours

The weak peaks at 1022 cm^{-1} and 1047 cm^{-1} are due to C-N-C deformations, and the peaks between 1360 cm^{-1} and 1470 cm^{-1} are from CH_2 wag, deformation and scissors.[20,24] Besides slight shifting of the C-N stretching and C-N-C deformation modes, this spectra is very similar to neat methenamine.[22] Figure 5.13c shows the ATR-FTIR spectrum of an aqueous solution of 25 mM methenamine and 16.8 mM zinc nitrate hexahydrate dried on the Ge ATR crystal. The ATR-FTIR spectrum of the methenamine and zinc nitrate hexahydrate mixture is not simply the superposition of the zinc nitrate hexahydrate spectrum and the methenamine spectrum. The $\nu_{22,}$ C-N stretching mode which is one peak at 1002 cm^{-1} in the spectra of methenamine dried on the Ge ATR crystal (Figure 5.13b) splits into three strong, sharp peaks at 978 cm^{-1}, 994 cm^{-1}, and 1011 cm^{-1}. Also, the $\nu_{21,}$ C-N stretching mode which is one peak at 1234 cm^{-1} in the spectra of methenamine dried on the Ge ATR crystal splits into two peaks, one medium peak at 1227 cm^{-1} and one strong peak at 1257 cm^{-1}. Furthermore, the C-N-C deformations which were at 1022 cm^{-1} and 1047 cm^{-1} in the spectra of methenamine dried on the Ge ATR crystal shift to 1020 cm^{-1} and 1066 cm^{-1}, respectively. The peaks between 1270 cm^{-1} and 1550 cm^{-1} are roughly the superposition of the ν_5 and ν_1 N-O stretching modes of the nitrate and the CH_2 wag, deformation and scissor peaks of methenamine. Figure 5.13d shows the ATR-FTIR spectra of an aqueous 25 mM methenamine and 16.8 mM zinc nitrate hexahydrate mixture which was heated at 90 °C (not preheated) for 4 hours prior to drying on the Ge ATR crystal. This spectra differs from that of the salt deposited from the methenamine and zinc nitrate hexahydrate solution which was not heated (compare Figure 5.13 c and d) The ν_{22} C-N stretch at 1007 cm^{-1} in the neat methenamine spectra splits into four peaks, two strong peaks at 977 cm^{-1} and 1010 cm^{-1} and two weak peaks at 960 cm^{-1} and 1039 cm^{-1}. The ν_{21} C-N stretch at 1234 cm^{-1} in the neat methenamine spectra splits into two peaks, one strong peak at 1257 cm^{-1} and one weak peak at 1211 cm^{-1}. However, the C-N-C deformations which were at 1022 cm^{-1} and 1047 cm^{-1} in the spectra of methenamine dried on the Ge ATR crystal still shift to 1020 cm^{-1} and 1066 cm^{-1}. The peaks between 1270 cm^{-1} and 1550 cm^{-1} are due to the ν_5 and ν_1 N-O stretching modes of the nitrate and the CH_2 wag, deformation and scissor peaks of methenamine. The ν_5 and ν_1 N-O stretching modes are weaker and broader as compared to those in the spectra of

Table 5.4 Summary of infrared absorptions due to C-N related modes in HMT and HMT containing zinc complexes. All wavelengths are in cm^{-1}. The two columns on the far right correspond to the IR absorptions of salts deposited on the ATR crystal when a solution containing 25 mM HMT and 16.8 mM $Zn(NO_3)_2$ dries on the ATR crystal.

Assignment	Neat HMT [Ref. 22]	$Zn(NO_3)_2$•2(HMT)•$6H_2O$ [Ref. 13]	HMT	HMT and Zinc Nitrate Hexahydrate at 25 °C	HMT and Zinc Nitrate Hexahydrate at 90 °C
CN stretch (ν_{22})	1007	1000	1002	978	960
		1025		994	977
				1011	1010
					1039
CN stretch (ν_{21})	1234	1236	1236	1227	1211
		1255		1257	1257
CNC def	1020	not available	1022	1020	1020
CNC def	1048	not available	1047	1066	1066
CN stretch (ν_{21})	1234	1236	1236	1227	1211
		1255		1257	1257

the room temperature methenamine and zinc nitrate hexahydrate mixture. This could be due to the nitrate molecules having a different coordination in the molecular salt complex formed from the heated mixtures as compared to the room temperature mixtures. The ATR-FTIR spectra of the heated mixture is similar to that of the unwashed wires (compare Figure 5.13d and Figure 5.8a) Table 5.4 summarizes the C-N stretch peak splitting found by Grodzicki et al.[13] and the C-N stretch peak splitting and C-N-C deformation peak shifting we found in ATR-FTIR spectra of the salts deposited on the Ge ATR crystal both from solutions heated and not heated.

It is evident that a molecular salt complexes containing zinc, methenamine, nitrate ions and water are deposited on the Ge ATR crystal because peaks corresponding to molecules of zinc, methenamine, nitrate ions and water are present in the spectra (the water bending peaks at ~1650 are present although not shown). Furthermore, the methenamine molecules are bound to the zinc atom in the salt and this is shown by the C-N stretch splitting shown in Figure 5.13 c and d which is similar to that found by Grodzicki et al.[13] Differences between the peak splitting observed herein and that reported by Grodzicki et al.[13] is likely due to the variations in the ratios of zinc to methenamine in the solution from which the salts were deposited. Grodzicki et al.[29] prepared the salts from solutions with zinc to methenamine ratios of 1:2 whereas our room temperature and heated solutions had ratios of ~1:1.5 and ~1:16, respectively. These differing concentrations result in there being different amounts of mondentate and bridging methenamine molecules present in our salts as compared to those prepared by Grodzicki et al. which leads to differences in how the peaks split.[13] Regardless of how the methenamine is coordinated to the zinc, the salts formed in this work definitely contain bonds between zinc and methenamine which is evident by the C-N stretch splitting. This provides further proof that a zinc-methenamine complex (which also includes some water and nitrate ions) exists in the solution since similar bonds which appear in the salt will exist in the solution.

5.11 Labile Attachment of Methenamine to the ZnO Nanowires

As was mentioned above, rinsing the nanowires after growth with deionized water removes all of the methenamine absorption peaks from the infrared spectrum, leaving

only the infrared absorption due to hydroxyl groups on the surface. This indicated that methenamine is not covalently bound to the ZnO nanowire surface because it can be completely removed from the wires upon rinsing with deionized water. If the methenamine-nanowire-surface bond is labile then methenamine could be washed off and replaced by OH leaving no evidence of methenamine presence. One way to determine if a labile methenamine-ZnO surface bond is possible would be to use in situ ATR-FTIR. Such an experiment is challenging due to very strong water absorption. Instead, we studied the infrared spectrum of aqueous methenamine solutions as they dried on an ATR crystal covered with ZnO nanowires. To do this we grew ZnO nanowires on a Ge ATR crystal, rinsed them with deionized water after growth and allowed them to dry. Following, we placed a few drops of an aqueous solution of 25 mM methenamine at room temperature on to the washed nanowires and allowed it to dry as we recorded ATR-FTIR spectra of the methenamine on the nanowires (Figure 5.14). The ATR-FTIR spectrum of an aqueous solution of 100 mM methenamine dried on the Ge ATR crystal is also shown in Figure 5.14. The ν_{22} C-N stretch, which is at 1007 cm^{-1} in neat methenamine,[22] shifts to 1005 cm^{-1} and broadens when the methenamine is on the ZnO nanowires. This same peak shifts to 1002 cm^{-1} without broadening when the methenamine is on the Ge surface. The ν_{21} C-N stretch, which is at 1234 cm^{-1} in the neat methenamine spectra, shifts to 1238 cm^{-1} when the methenamine is on the ZnO nanowire surface and shifts to 1236 cm^{-1} when the methenamine is on the Ge crystal. In contrast to these changes, the IR absorption due to the CH_2 wag, deformation and scissor modes in methenamine neither shift nor broaden when methenamine solutions dry on Ge or ZnO (Figure 5.14). The C-N stretches of methenamine dried on Ge and ZnO surfaces being not identical to that of neat methenamine indicates that the methenamine associates with the ZnO and Ge surfaces, perhaps through van der Waals forces or hydrogen bonding. Moreover the C-N stretching absorption shifts and broadens more on the ZnO surface than on the Ge surface. This suggests that the interaction between the methenamine and the ZnO surface is stronger than that between the methenamine and the Ge surface. The fact that the methenamine does associate with the ZnO surface relatively strongly suggests that the methenamine is interacting with the ZnO surface, most likely via a zinc-

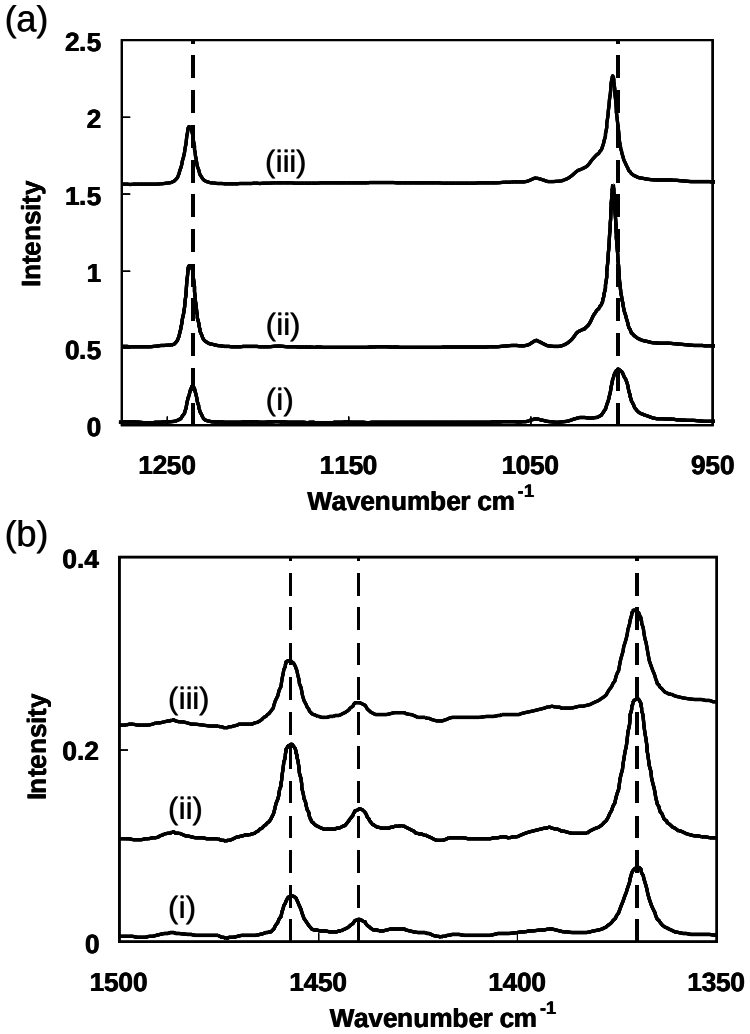

Figure 5.14 ATR-FTIR spectra of (i) a room temperature aqueous solution of 100 mM methenamine dried on a Ge ATR crystal, (ii) a room temperature 25 mM aqueous methenamine dried on washed ZnO nanowires grown on a Ge ATR crystal, (ii) ZnO nanowires on a Ge ATR crystal after heating in a 25 mM aqueous solution at 90 °C for 4 hours. The background for spectrum (i) is the pristine Ge ATR crystal and for spectra (ii) and (iii) the background is washed ZnO nanowires on the Ge ATR crystal. (a) Shows the region between 925 cm^{-1} and 1275 cm^{-1} and (b) shows the region between 1350 cm^{-1} and 1500 cm^{-1}. The dotted lines denote the peak locations of spectrum (i). The spectra have been shifted vertically for clarity.

nitrogen interaction, during the nanowire growth as has been previously suggested.[7,9-11] In order to investigate the effect of temperature on the ATR-FTIR spectra of the methenamine on the nanowires, the nanowires on the Ge ATR crystal were placed in an aqueous solution of 25 mM methenamine and heated to 90 °C for four hours. Following, the nanowire covered Ge ATR crystal was removed from the heated methenamine solution and dried. Figure 5.14 shows that the ATR-FTIR spectrum of these methenamine covered ZnO nanowires is identical to the ATR-FTIR spectrum of room temperature methenamine solution dried on the nanowires. Thus, temperature does not change how the methenamine interacts with the ZnO nanowire surface.

5.12 Conclusions

ZnO nanowire growth from an aqueous solution of zinc nitrate hexahydrate and methenamine was studied in detail. A ZnO nanowire growth mechanism was proposed which predicts that the precursor is a zinc-methenamine complex (Zn-HMT^{2+} and Zn-HMT-Zn^{4+}) which reacts at the hydroxyl terminated nanowire surface. This growth mechanism was supported by characterizing and modeling the synthesis using several analytical techniques as well as kinetic and thermodynamic models.

References

(1) Verges, M. A.; Mifsud, A.; Serna, C. J. *J. Chem. Soc. Faraday T.* **1990**, *86*, 959.

(2) Fujita, K.; Matsuda, K.; Mitsuzawa, S. *B. Chem. Soc. Jpn.* **1992**, *65*, 2270.

(3) Vayssieres, L.; Keis, K.; Lindquist, S. E.; Hagfeldt, A. *J. Phys. Chem. B* **2001**, *105*, 3350.

(4) Li, Q.; Kumar, V.; Li, Y.; Zhang, H.; Marks, T. J.; Chang, R. P. H. *Chem. Mater.* **2005**, *17*, 1001.

(5) Liu, J.; She, J.; Deng, S.; Chen, J.; Xu, N. *J. Phys. Chem. C* **2008**, *112*, 11685.

(6) Ashfold, M. N. R.; Doherty, R. P.; Ndifor-Angwafor, N. G.; Riley, D. J.; Sun, Y. *Thin Solid Films* **2007**, *515*, 8679.

(7) Chou, K.-S.; Chen, W.-H.; Huang, C.-S. *J. Chin. Inst. Chem. Eng.* **1990**, *21*, 327.

(8) Govender, K.; Boyle, D. S.; Kenway, P. B.; O'Brien, P. *J. Mater. Chem.* **2004**, *14*, 2575.

(9) Sugunan, A.; Warad, H. C.; Boman, M.; Dutta, J. *J. Sol-Gel Sci.Techn.* **2006**, *39*, 49.

(10) Ho, G. W.; Wong, A. S. W. *Appl.Phys. A-Mater.* **2007**, *86*, 457.

(11) Qiu, J. J.; Li, X. M.; He, W. Z.; Park, S. J.; Kim, H. K.; Hwang, Y. H.; Lee, J. H.; Kim, Y. D. *Nanotechnology* **2009**, *20* 155603.

(12) Grodzicki, A.; Szlyk, E. *Pol. J. Chem.* **1984**, *58*, 999.

(13) Grodzicki, A.; Szlyk, E. *Pol. J. Chem.* **1984**, *58*, 1009.

(14) Greene, L. E.; Law, M.; Tan, D. H.; Montano, M.; Goldberger, J.; Somorjai, G.; Yang, P. *Nano Lett.* **2005**, *5(7)*, 1231.

(15) Harris, D. C. *Quantitative Chemical Analysis*; W.H. Freeman and Company: New York, 1991.

(16) McPeak, K. M.; Baxter, J. B. *Ind. Eng. Chem. Res.* **2009**, *48*, 5954.

(17) Olofsson, G.; Hepler, L. G. *J. Solution Chem.* **1975**, *4*, 127.

(18) Tay, C. B.; Le, H. Q.; Chua, S. J.; Loh, K. P. *J. Electrochem. Soc.* **2007**, *154*, K45.

(19) Yamabi, S.; Imai, H. *J. Mater. Chem.* **2002**, *12*, 3773.

(20) Isaeva, U. I.; Imanakunov, B. I. *Inst. Neorg. Fiz. Khim.* **1982**, *4*, 46.

(21) Stumm, W.; Morgan, J. J. *Aquatic Chemistry: Chemical Equilibria and Rates in Natural Waters*; Wiley-Interscience: New York, 1995.

(22) Bertie, J. E.; Solinas, M. *J. Chem. Phys.* **1974**, *61*, 1666.

(23) Ahuja, I. S.; Yadava, C. L.; Singh, R. *J. Mole.Struct.* **1982**, *81*, 229.

(24) Negita, H.; Nishi, Y.; Koga, K. *Spectrochim Acta* **1965**, *21*, 2144.

(25) Nakamoto, K. *Infrared and Raman Spectra of Inorganic and Coordination Compounds : Applications in Coordination, Organometallic, and Bioinorganic Chemistry* 5ed.; Wiley-Interscience: New York, 1997; Vol. B.

(26) Jensen, J. O. *Spectrochim. Acta A* **2002**, *58*, 1347.

(27) Tada, H. *J. Am. Chem. Soc.* **1960**, *82*, 255.

(28) Eigen, M. *Pure Appl. Chem.* **1963**, *6*, 97.

(29) Grodzicki, A.; Szlyk, E. *Pol. J. Chem.* **1984**, *58*, 991.

Chapter 6 : Transport Limited Growth of ZnO Nanowires*

6.1 Introduction

In order for ZnO nanowires DSSCs to have efficiencies comparable or greater than TiO_2 nanoparticle DSSC the surface area of the ZnO nanowire photoanodes must to be increased by an order of magnitude.[1] One approach to increasing the ZnO nanowire surface area is to grow taller nanowires. However, the extraordinarily slow growth rate of the nanowires (< 1μm/hr) makes this approach impractical. A second approach is to grow denser and thinner nanowires. However, it will be shown shortly that increasing the nanowire number density slows the growth rate even further. Overcoming these limitations will require fundamental and detailed understanding of the ZnO nanowire growth.

Several studies of the ZnO nanowire growth from aqueous solutions of zinc nitrate hexahydrate and methenamine found a correlation between the nanowire number density (nanowires/cm^2) and the nanowire height and diameter.[2-5] Specifically, when denser nanowire films were obtained they tended to consist of shorter nanowires with smaller diameters. These studies attributed this correlation to "limited mass supplied from the solution",[2] a "competition process"[3] amongst the neighboring nanowires, and faster zinc precursor consumption over dense areas leading to lower local concentrations and growth rates.[4,5]

Coltrin et al. have developed a two dimensional model of the growth of ZnO nanowires on patterned silver substrates that took into account the mass transport of reactants to the substrate surface, the reaction and diffusion of the ZnO precursor at the nanowire surface and the desorption of hydrogen from the surface of the nanowires.[6] From their model and experiments they concluded that the rate limiting step in the nanowire growth is the desorption of hydrogen from the nanowire surface.

In this chapter, we show that ZnO nanowire growth from an aqueous solution of

*This chapter is adapted from:
Boercker, J. E.; Schmidt, J. B.; Aydil, E. S. *Cryst.Growth Des.* **2009**, *9*, 2783.

zinc nitrate hexahydrate and methenamine is limited by the mass transport of the ZnO precursor to the substrate surface. We show that mass transport limited nanowire growth results in the inverse relationship between nanowire number density and nanowire dimensions (height and diameter) as experimentally observed by us and others.[2-5] We also explore the implications of mass transport limitations on the uniformity of the nanowire growth and suggest a method for accelerating the growth rate. Moreover, we show that the anisotropic growth of ZnO nanowires is not due to mass transport limitations as previously suggested[4] but is a direct result of the difference in growth kinetics between the $(10\bar{1}0)$ and (0001) surfaces.

6.2 Experimental Procedures

ZnO nanowires were grown from an aqueous solution of zinc nitrate hexahydrate and methenamine on silicon substrates seeded with flat ZnO platelets.[7] Silicon (100) substrates (~23 mm × ~17 mm × 0.5 mm) were cleaned by sonication in a mixture of water, isopropanol, and acetone (1:1:1 by volume) for 20 minutes and then blown dried with a stream of argon. Following the seeding process developed by Greene et al.,[7] one drop of a 5 mM zinc acetate ethanol solution was spread uniformly across each substrate by slowly rotating and gently tilting the substrate manually. After ~10 seconds, the substrate was rinsed with a brief squirt of ethanol and blown dry with argon. This process was repeated five times and, following, the substrate was annealed at 350° C for 20 minutes. The process of seeding with zinc acetate solution and annealing was repeated a second time to ensure that the substrate was uniformly covered with seeds.

For experiments designed to explore the nanowire growth near a boundary between a seeded and unseeded region, the seeds were removed from a 5 mm wide region around the edges of the substrate by wiping this region with a cotton swab dipped in ~1 M hydrochloric acid and then blowing the edges dry with argon. Following, the edges were wiped three times with a cotton swab soaked in distilled water and blown dry with argon to remove the residual hydrochloric acid. This left an approximately 8 mm thick region of seeded area in the middle of the substrate. This area was sufficiently far away from the edges of the aluminum holder used to suspend the substrates in the growth solution so that the effects observed in these experiments are due to the boundary

between the seeded and unseeded regions and not due to edge effects introduced by the presence of the holder.

The ZnO seed density was varied by varying the concentration of the zinc acetate seeding solution (0.3 to 5 mM),[8] the number of times zinc acetate was drop cast (3 to 5 times) before annealing, and the number of times the seeding process, including the annealing step, was repeated (once or twice).

Nanowires were grown by placing the substrates face down at a 45° angle on an aluminum holder (Figure 6.1a) in a 100 mL aqueous solution of 16 mM zinc nitrate hexahydrate and 25 mM methenamine, and heating the solution at 90° C in an oven for various lengths of time. It took ~2 hours for the solution to approach thermal equilibrium with the oven temperature. After growth, the nanowire covered substrates were rinsed with water and dried in an argon stream. Almost no nanowire growth was observed in unseeded areas.

To compare the morphologies of heterogeneously and homogeneously grown ZnO nanowires to each other, we grew ZnO nanowires homogeneously in a 300 mL solution of 16 mM zinc nitrate hexahydrate and 25 mM methenamine at 90° C. A 15 mL aliquot of the solution containing homogeneously grown ZnO nanowires was periodically removed, centrifuged, and washed three times with water to isolate a powder of ZnO nanowires. The ZnO nanowires were dispersed in acetone, and drop cast onto silicon wafers for subsequent examination by scanning electron microscopy (SEM) and X-ray microdiffraction.

In some experiments, the growth solution was stirred using a ~2.1 cm long magnetic stir bar spinning beneath the substrate. For these experiments the substrate was placed horizontally and face down in an aluminum holder (Figure 6.1b). The solution was heated to 95 °C using a feed back controlled hotplate with stirring capability. The stirring rates were varied between 0 rpm and 600 rpm. Figure 6.1c illustrates the fluid flow induced below the substrate due to stirring and the "stagnant" diffusion boundary layer of thickness δ that is presumed to exist near the substrate surface.

The average dimensions of the ZnO nanowires were determined using SEM (JEOL 6700). To obtain statistically significant results, dimensions of 10-70 nanowires

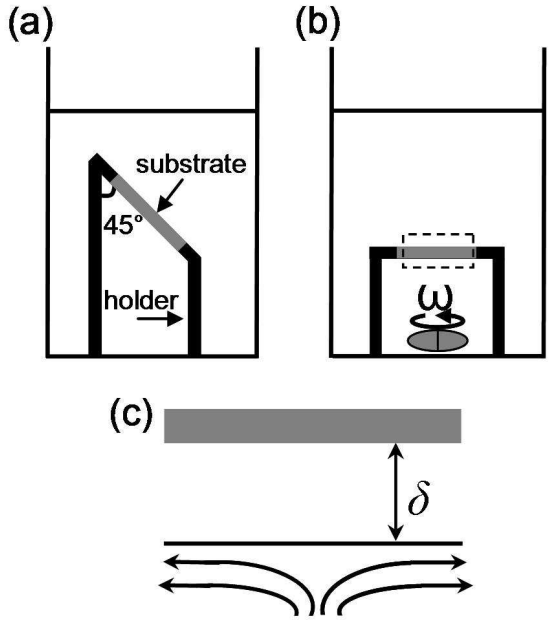

Figure 6.1 (a) Schematic of the growth configuration showing the substrate placed growth-face down on an aluminum holder at 45° with respect to the bottom of the beaker. (b) Schematic of the growth configuration used to vary the diffusion boundary layer thickness by stirring. (c) Magnification of the substrate within the dashed box of b showing the diffusion boundary layer with thickness δ.

were measured and averaged. X-ray microdiffraction, (Bruker-AXS Microdiffractometer) was used to determine the crystal structure of the nanowires.

6.3 Model Description

In interpreting our experimental results we have made use of simple but nontrivial models of the solution phase species transport and the nanowire growth. These models are described below. The modeling results and the insight they provide are discussed together with the experimental observations. The goal of the modeling was to provide insight into the scaling relations between experimentally controlled variables and the nanowire growth rate and dimensions. We did not aim to fit the experimental data by varying the model parameters. Instead, we chose reasonable values that are either measured experimentally or are representative of the experimental conditions.

In order to examine the inverse relationship between nanowire number density and nanowire height and diameter, a one-dimensional model of the species transport near the substrate surface was developed. The model geometry is shown in Figure 6.2. We solve the diffusion equation for ZnO precursor concentration, *c*, in a boundary layer of thickness δ under quasi-steady state conditions. We assume that there are no homogeneous reactions near the substrate and that the zinc precursor is consumed through first order heterogeneous reactions that lead to nanowire growth on the substrate. In principle, the precursor can react with ZnO nanowires that have nucleated and grown in the liquid phase. If there are significant amount of nanowires in the boundary layer, they can act as sinks. However, estimates of the surface area of the nanowires growing on the substrate and the surface area of the homogeneously growing nanowires in the boundary layer shows that the former is approximately 30 times larger than the latter so that the nanowires in the boundary layer do not act as significant sinks. The factor of 30 is a lower bound and was calculated assuming that all the zinc in the growth solution yields homogeneously grown ZnO nanowires that are ~7 μm long and 0.6 μm in diameter; these values are the experimentally measured average dimensions of the nanowires in the solution phase at the end of the growth period. Thus, neglecting homogeneous reactions in the boundary layer is justified.

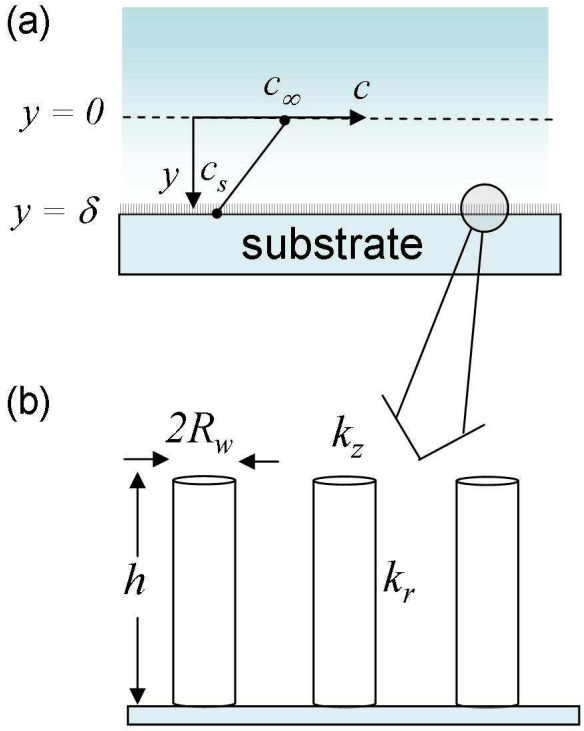

Figure 6.2 (a) Geometry of the one-dimensional model used to calculate the temporal evolution of the nanowire height and diameter. The concentration boundary layer extends a distance δ from the substrate. c is the concentration of the nanowire precursor and varies along y. c_∞ is the bulk precursor concentration and c_S is the concentration at the nanowire surface. (b) A magnified view of the portion of (a) indicated by the circle. R_W and h are the nanowire radius and height, respectively. k_Z and k_r are the first order surface reaction rate constants on the top (0001) and sides of the nanowires $(10\bar{1}0)$, respectively.

The nanowire radius, R_w and height, h, are functions of time and increase at different rates. The reaction kinetics on the (0001) and $(10\bar{1}0)$ surfaces are parameterized by first order reaction coefficients k_z and k_r, respectively. The surface reaction rates were taken to be first order in the precursor concentration because we found, through titration with EDTA, that the depletion rate of the total zinc (all zinc compounds) in the solution is first order. Under these assumptions the precursor concentration in the boundary layer is linear and drops from the bulk concentration, c_∞, to the concentration in the solution just above the nanowires, c_s. Strictly speaking, c is the concentration above the equilibrium saturation concentration of the precursor (i.e. the zinc-methenamine complexes discussed in Chapter 5). The flux and c_s are evaluated using the boundary conditions; at $y=0$ the concentration is equal to the bulk solution concentration of the precursor, c_∞, and at $y=\delta$ the consumption rate by surface reactions must be equal to the flux to the surface. Since $\delta >> h$ the nanowires are coarse grained and treated like a sink at the substrate surface. The dimensions of the nanowires determine the total precursor consumption rate. With these assumptions, the concentration of the precursor varies linearly with distance into the boundary layer and decreases to

$$c = \frac{c_\infty}{(1+\Phi)} \tag{6.1}$$

near the nanowire surface, where

$$\Phi = \frac{N(k_z \pi R_w^2 + 2k_r \pi R_w h)\delta}{D} \tag{6.2}$$

is the dimensionless Thiele modulus, a measure of the ratio of the surface reaction rate to the diffusion rate. In these equations, D is the diffusion coefficient of the ZnO precursor, and N is the nanowire number density (nanowires/cm^2). A mass balance at the surface of the nanowires leads to two ordinary differential equations in time, t, for the height and radius of the nanowires,

$$\frac{dh}{dt} = \frac{k_z c_\infty}{\rho(1+\Phi)} \tag{6.3}$$

and

$$\frac{dR_w}{dt} = \frac{k_r c_\infty}{\rho(1+\Phi)} \tag{6.4}$$

where ρ is the ZnO molar density. Moreover, we use the experimental observation that the depletion of total zinc in the solution is pseudo-first order at this temperature and assume that this also applies to the ZnO precursor. Thus, equations (6.3) and (6.4) are coupled to

$$\frac{dc_\infty}{dt} = -kc_\infty \tag{6.5}$$

and we use the experimentally determined value of k in the calculations (0.129 min^{-1}). The homogeneous chemistry and kinetics is in reality more complicated as was discussed in Chapter 5. However at 90 °C and with initial concentrations of zinc nitrate hexahydrate and methenamine of 16 mM and 25 mM respectively, equation (6.5) accurately depicts the temporal evolution of the ZnO precursor in solution. The temporal variation of the nanowire height and diameter were found by integrating equations (6.3)-(6.5) numerically. The initial height and diameter were both taken to be 10 nm (approximate size of the seeds) the results are not sensitive to any reasonable choice of these values. The initial bulk precursor concentration was set at 16 mM, a typical experimental value for total zinc concentration. The boundary layer thickness was set to 300 μm, a typical value of the diffusion length in solution (see below). The diffusion coefficient was set to that of Zn^{2+} in water,[9] 2.91×10^{-5} cm^2/s and k_z and k_r were chosen such that the final nanowire height and diameters were approximately those measured experimentally. This yields, 0.1 cm/min and 0.01 cm/min, for k_z and k_r respectively. The nanowire planar number density, N, was varied to study the effect of nanowire density on the final nanowire height and diameter.

A two-dimensional transport model of the spatial variation of the ZnO precursor concentration was developed to study the growth near the boundary between a seeded area of the substrate (where nanowires grow) and an unseeded area (where nanowires do not grow). The two-dimensional model geometry is shown in Figure 6.3. Neglecting homogeneous reactions within a distance δ of the substrate, we solved the steady-state diffusion equation

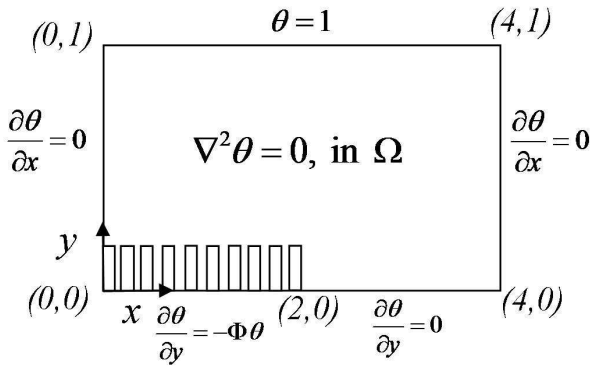

Figure 6.3 Geometry and illustration of the two-dimensional model used for calculating the ZnO precursor concentration around the boundary between seeded and unseeded sections of the substrate. The substrate is at y=0 and spans $0 \leq x \leq 4$.

$$\nabla^2\theta = 0 \tag{6.6}$$

for dimensionless precursor concentration, θ (θ = c/ c_∞), within the domain, Ω, shown in Figure 6.3. The boundary conditions are

$$\theta = 1 \qquad \text{at} \quad y = 1; \quad 0 \le x \le 4 \tag{6.7}$$

$$\frac{\partial\theta}{\partial y} = -\Phi\theta \quad \text{at} \quad y = 0; \quad 0 \le x \le 2 \tag{6.8}$$

$$\frac{\partial\theta}{\partial y} = 0 \qquad \text{at} \quad y = 0; \quad 2 \le x \le 4 \tag{6.9}$$

$$\frac{\partial\theta}{\partial x} = 0 \qquad \text{at} \quad x = 0; \quad 0 \le y \le 1 \tag{6.10}$$

$$\frac{\partial\theta}{\partial x} = 0 \qquad \text{at} \quad x = 4; \quad 0 \le y \le 1 \tag{6.11}$$

where x and y are non-dimensional distances along the x and y axes, respectively, both non-dimensionalized by the boundary layer thickness, δ. Equation (6.7) asserts that the precursor concentration at a distance δ from the substrate surface is the bulk concentration, c_∞. Equation (6.8) equates the flux of the precursor to the surface to the rate of reactions that lead to nanowire growth. Equations (6.9)-(6.11) are the no flux boundary conditions. Calculation domain, Ω is taken to be sufficiently wide in the x direction (4 δ) such that the concentration profiles are well developed along the x direction away from the boundary and boundary conditions (6.10) and (6.11) are good approximations. Taking it wider than 4 δ does not change the results and conclusions significantly. Equation (6.6) was solved with the boundary conditions (6.7)-(6.11) using a finite element method as implemented in the COMSOL Multiphysics package.

6.4 One-Dimensional Transport Model: Theory and Experiments

The one-dimensional model depicted in Figure 6.2 was used to explore the dependence of final nanowire height and diameter on the nanowire number density, *N*. (In batch growth, using these reaction conditions, the precursor concentration is depleted with time according to equation (6.5) and nanowire dimensions reach a steady value as $t \to \infty$; we refer to these values as final nanowire height and diameter.) The Thiele

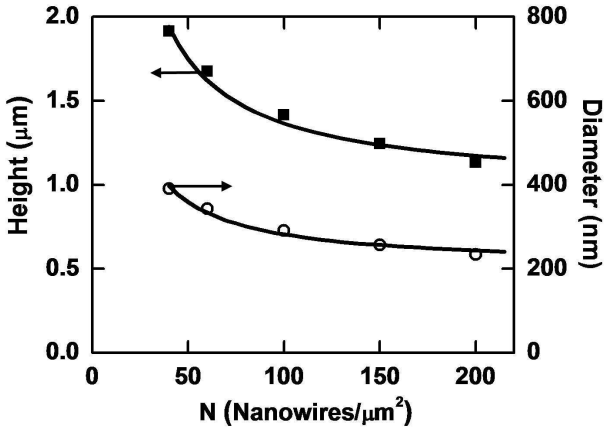

Figure 6.4 Nanowire height (■) and diameter (○) as a function of nanowire density as predicted by the one dimensional growth model shown in Figure 6.2 with $\Phi >> 1$. The lines are drawn to aide the eye and decrease as $\propto 1/N$.

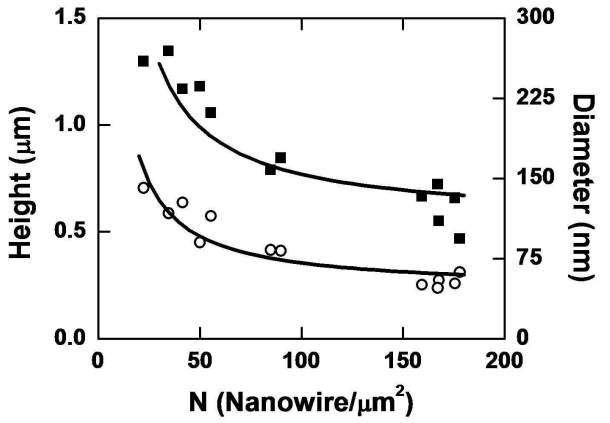

Figure 6.5 Experimentally determined nanowire height (■) and diameter (○) after four hours of growth as a function of nanowire density. The lines are drawn to aide the eye and decreases as $\propto 1/N$.

modulus, Φ, is a measure of how the ZnO nanowire precursor diffusion compares to the precursor reaction rate at the nanowire surface. When $\Phi >> 1$ the nanowire growth is limited by the diffusion of the precursor to the nanowire surface. Conversely, when $\Phi << 1$ the nanowire growth is limited by the reaction of the precursor at the nanowire surface. Figure 6.4 shows the predictions of the one-dimensional model for the final nanowire dimensions as a function of the nanowire number density. This model predicts that when the growth is mass transport limited (i.e., $\Phi >> 1$) the nanowire height and diameter scale as $\sim 1/N$. When the reaction rate constants in the model, k_z and k_r, are decreased such that $\Phi << 1$ (i.e., the growth is reaction rate limited) the nanowire height and diameter become independent of N. When the growth is mass transport limited more nanowires, and therefore higher nanowire surface area, will result in a larger precursor depletion near the surface and hence a lower surface concentration, c_s. For large Φ the surface concentration, c_s, is inversely proportional to Φ. Since the growth rate is proportional to c_s, and Φ is proportional to N the nanowire dimensions decrease as $\sim 1/N$. On the other hand when $\Phi << 1$ the diffusion of the precursor to the nanowire surface is significantly faster than the depletion rate, even with substrates with large N. Consequently, the nanowire height and diameter become independent of N.

To experimentally establish the relationship between nanowire height and diameter and number density, nanowires were grown on substrates with various seed densities. As shown in Figure 6.5, both nanowire height and diameter were found to be proportional to $1/N$, the same scaling predicted by the one-dimensional model when $\Phi >> 1$. Thus, we conclude that the ZnO nanowire growth process is indeed mass transport limited.

6.5 Two-Dimensional Transport Model: Theory and Experiments

Mass transport limitation has consequences on the uniformity of the ZnO precursor concentration, and hence ZnO growth, near the boundary between the seeded and the unseeded regions of the substrate. Specifically, as the seed and, therefore, the nanowire number density, N, decreases from $\sim 100\ \mu m^{-2}$ in the seeded regions to zero in the unseeded regions, the precursor concentration should rise from c_s to c_∞ across a lateral

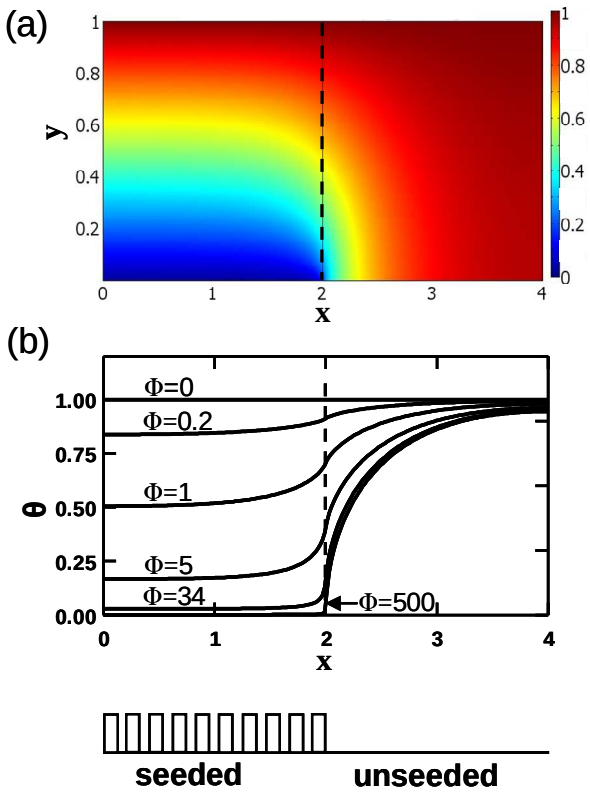

Figure 6.6 (a) Dimensionless ZnO precursor concentration around the boundary between seeded and unseeded sections of the substrate calculated using the model shown in Figure 3 with Φ=32. (b) Dimensionless ZnO precursor concentration at the surface (y=0) as a function of position along the x-axis at various Φ values.

length scale characterized by the diffusion length. Figure 6.6a shows the two dimensional ZnO precursor concentration profile above the boundary between the seeded region and the unseeded region calculated using the model shown in Figure 6.3. Since $\Phi >> 1$, the concentration over the seeded region where the nanowires are growing is lower than that over the part of the substrate without the seeds. The nanowires deplete the precursor over the seeded regions of the substrate, whereas there is no depletion, above the unseeded regions. Figure 6.6b shows the concentration profile at the surface of the substrate, (i.e., $y=0$), for various values of Φ. When $\Phi << 1$ the concentration profile is uniform because the growth is reaction rate limited. As Φ increases, the growth becomes mass transport limited and a concentration gradient develops across the boundary between the seeded and unseeded regions. The concentration profile in Figure 6.6b indicates that there is a significant surface concentration increase at the boundary between the seeded and unseeded regions. Thus, the nanowires on the seeded side near this boundary are predicted to grow faster and taller.

To explore this prediction with experiments, a substrate was patterned and seeded only in the middle of the substrate, leaving ~5 mm wide regions on either side of this region unseeded. Nanowires grew only in the middle of the substrate Figure 6.7a. Figure 6.7b shows the spatial variation of the nanowire height between the middle of the seeded region and the boundary between the seeded and unseeded regions. Figure 6.7c shows cross sectional SEM images at various points labeled in Figure 6.7b. Figure 6.7d shows the spatial variation of the nanowire height on an expanded scale, within a few hundred microns of the boundary between the seeded and unseeded regions. Indeed, as this boundary is approached, within a distance of ~300 μm, the height of the nanowires increases from ~400 nm to ~1 μm. This increase is due to higher ZnO precursor concentration near the boundary between the seeded and unseeded regions as compared to the rest of the seeded region away from this boundary.

6.6 Increasing the Growth Rate with Stirring

The discovery that the ZnO growth is mass transport limited immediately suggests a method for increasing the growth rate. One obvious improvement would be to stir the solution to increase the growth rate while still maintaining a high number density

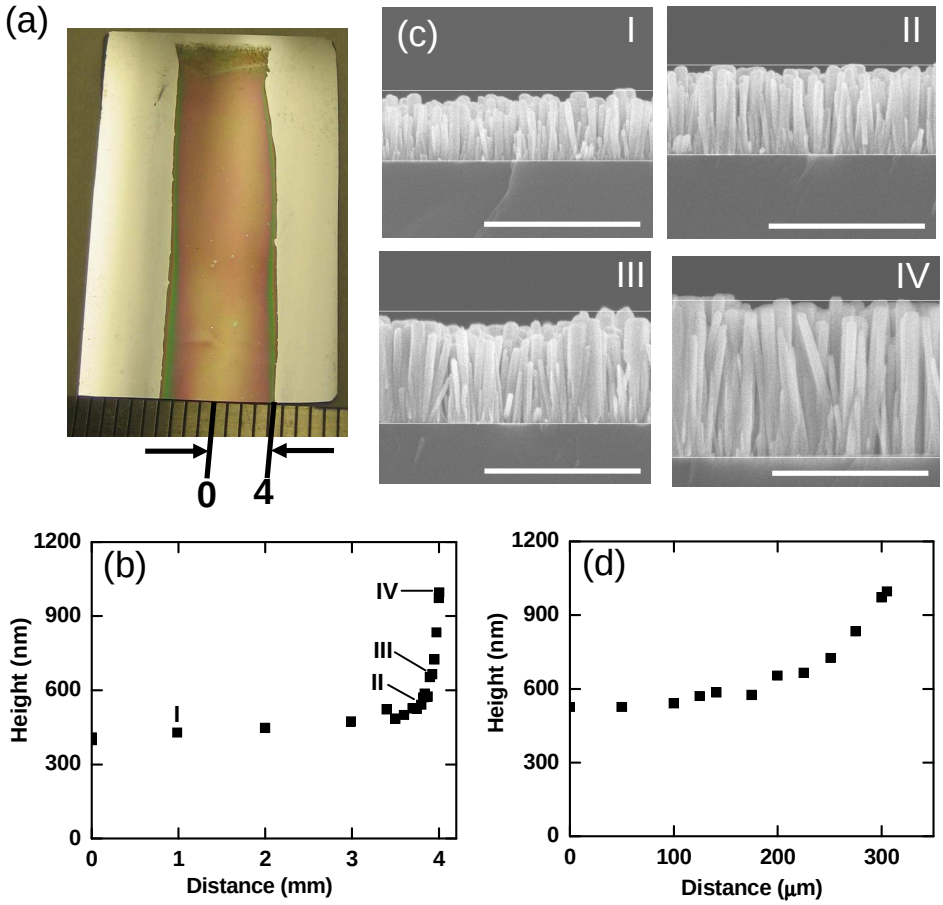

Figure 6.7 (a) Digital camera image of ZnO nanowires grown for four hours on a silicon substrate patterned with a ~8 mm wide strip of seeds in the middle of the substrate. The darker part of the substrate is where the nanowires have grown and the lighter parts are unseeded regions where there are no nanowires. (b) Spatial variation of the nanowire height between the middle of the substrate, taken to be the origin (0 mm), and the boundary between the seeded and unseeded region. This 4 mm distance corresponds to the distance indicated at the bottom of (a). (c) Cross-sectional SEM images of the nanowire array at different locations as numbered in (b). The scale bars are all 1 μm. (d) The same spatial variation of the nanowire height as in (b) but shown only within 305 μm from the boundary between the seeded and unseeded regions. The origin (0 mm) is taken to be 305 μm from the boundary within the seeded region.

of nanowires. Stirring the solution will decrease the diffusion boundary layer thickness above the substrate, δ, and increase c_s and the growth rate. Indeed, Figure 6.8a shows that the nanowire height reached after 4 hours of growth increases with the stirring speed, ω. In these experiments, the solution was stirred using the set up shown in Figure 6.1b and the substrate was patterned with seeds in the middle as shown in Figure 6.7a. Figure 6.8a displays the nanowire heights within 1 mm of the boundary between the seeded andunseeded regions for various spinning rates. Even when the solution is stirred, the nanowire heights near the boundary are larger than those that are in the middle of the seeded region. This indicates that the growth process is still mass transport limited even when the solution is stirred vigorously. The height of the nanowires and hence the growth rate scales as $\omega^{1/2}$ (Figure 6.8b) consistent with the expected scaling of the boundary layer thickness with stirring speed for rotational flow. In rotational flow, the boundary layer thickness is proportional to the square root of the Ekman number, *Ek*, ($\delta \propto \sqrt{Ek}$).[10] The Ekman number is a measure of the viscous force as compared to the Coriolis force and is defined as $Ek = \nu/\omega L^2$ where ν, and L are the kinematic viscosity of the solution and the characteristic length, respectively.[10] Thus, $\delta \propto \sqrt{Ek} \propto \omega^{-1/2}$ and the nanowire height, *h*, is directly proportional to $\omega^{1/2}$ (i.e., $h \propto \Phi^{-1} \propto \delta^{1} \propto \omega^{1/2}$).

When the stir bar was not centered perfectly at the center of the substrate we observed that the nanowire heights were not symmetric due to the boundary layer thickness changing non-uniformly across the substrate. This underscores the necessity of ensuring symmetric flow across the substrate surface. Also, in the experiments shown in Figure 6.8, it was necessary for the seed density and hence the nanowire number density to be kept approximately constant to observe the effect of the stirring speed. Since the height of the nanowire array is also a strong function of the nanowire number density, slight variations in seed density affects the results.

6.7 Anisotropic Nanowire Growth

It has been suggested that mass transfer limited growth may be responsible for anisotropic growth and the resulting high aspect ratio nanowires.[4] It is believed that the growth on the top surface (c-face) of the nanowires depletes most of the precursor and

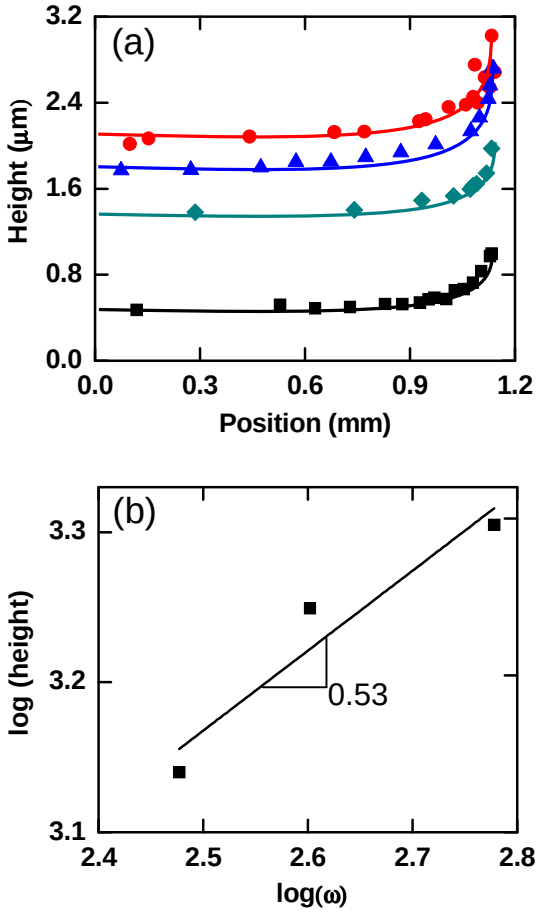

Figure 6.8 (a) Nanowire height as a function of position for stir bar rotation speeds, ω, of 0 (■), 300 (♦), 400 (▲), and 600 (●) rpm. Lines are drawn in to aid the eye. The nanowires were grown for 4 hours. (b) Log-log plot showing the square root scaling of the nanowire height (away from the boundary between the seeded and unseeded regions) and the stir bar rotation speed.

causes the precursor concentration to drop to nearly zero around the sides of the nanowires. We have found, however, that the diffusion length scale is much larger than the height of the nanowire, i.e., $\delta >> h$. This implies that there cannot be a steep concentration gradient on the length scale of the nanowire height and that the concentration of the precursor is approximately the same at the top and around the sides of the nanowires. Below, we show evidence that the anisotropic growth is due to the differences in the growth kinetics of the $(10\bar{1}0)$ and (0001) surfaces in methenamine and zinc nitrate hexahydrate and not due to the mass transport limited growth.

We examined the origin of the anisotropic growth by comparing the heterogeneous nanowire growth on the substrate to the homogenous nanowire growth within the reaction solution. Figure 6.9 compares the x-ray diffraction pattern of the ZnO nanowires grown heterogeneously on the substrate (Figure 6.9a) to the x-ray diffraction pattern of the ZnO nanowires collected from the solution phase (Figure 6.9b). Both x-ray diffraction patterns index to the wurtzite ZnO structure, which indicates that ZnO is found heterogeneously on the substrate and homogenously in the solution. Only the (002) and (004) peaks of the ZnO can be seen in the diffraction pattern for the heterogeneous growth because the ZnO nanowires are aligned with respect to the substrate surface. Since both the heterogeneous and homogeneous growth is wurtzite ZnO, the precursor and growth mechanism should be similar for both types of growth.

The heterogeneous and homogeneous nanowires were examined in detail using SEM. Figure 6.10a shows histograms of the diameters for both the heterogeneously and homogeneously grown nanowires. Figure 6.10c shows a similar graph for the nanowire heights. Typical SEM images of the heterogeneous and homogeneous growth are shown in Figures 6.10b and 6.10d, respectively. The heights and diameters of the homogenously grown nanowires are much larger than those of the heterogeneously grown nanowires because homogeneous growth has little or no mass transport limitations. Consequently, the precursor concentration is higher near the surface of a homogenously grown nanowire, which results in a faster growth rate. In addition, the height and diameter distribution of the homogenously grown nanowires are much wider

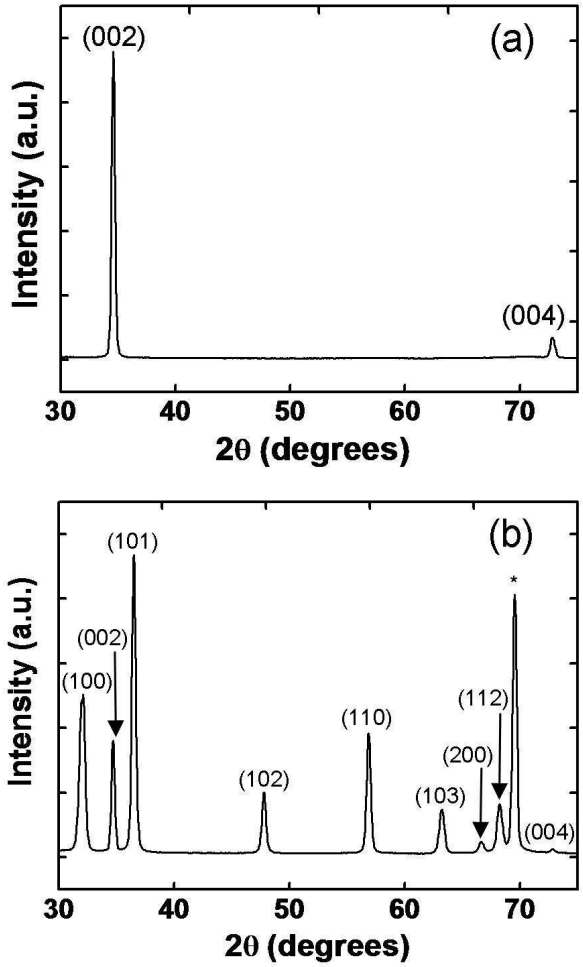

Figure 6.9 X-ray diffraction pattern of ZnO nanowires grown (a) heterogeneously on a Si substrate and (b) homogeneously in the bulk solution. Both XRD patterns index to wurtzite ZnO. The * corresponds to the (400) peak of the silicon substrate.

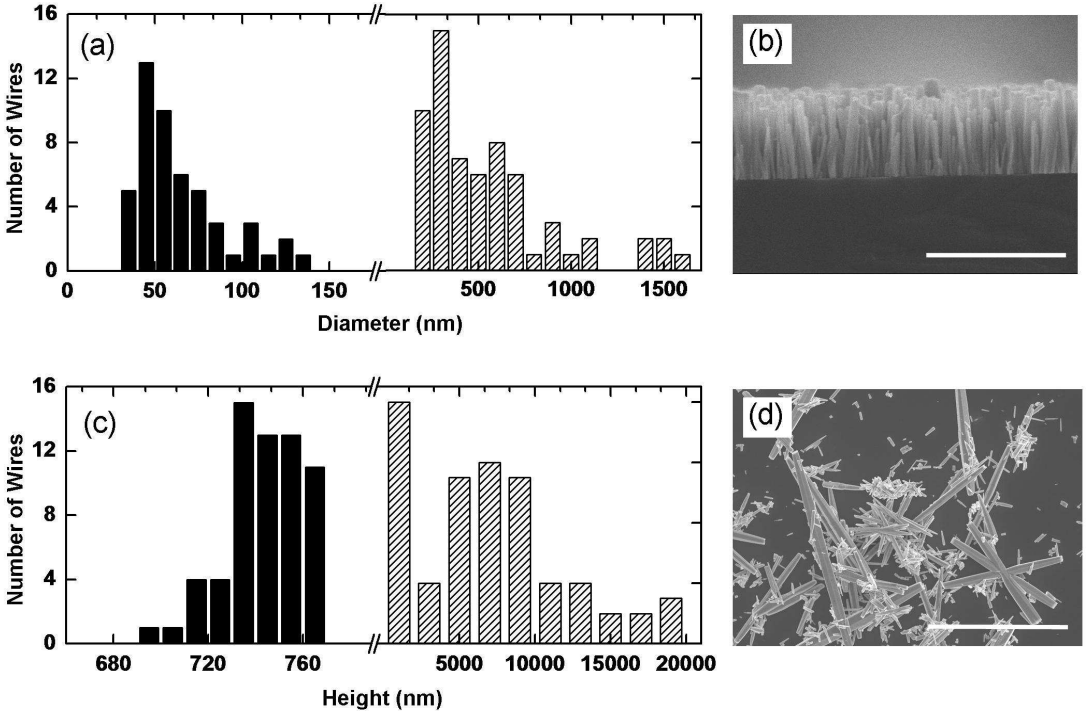

Figure 6.10 Diameter (a) and height (c) distributions of nanowires grown heterogeneously (solid bars) on a substrate and homogeneously (striped bars) in solution. SEM images of the heterogeneously (b) and homogeneously (d) grown nanowires. The scale bar in (b) is 1 μm and the scale bar in (d) is 10 μm. These nanowires were grown at 90 °C for 8 hours.

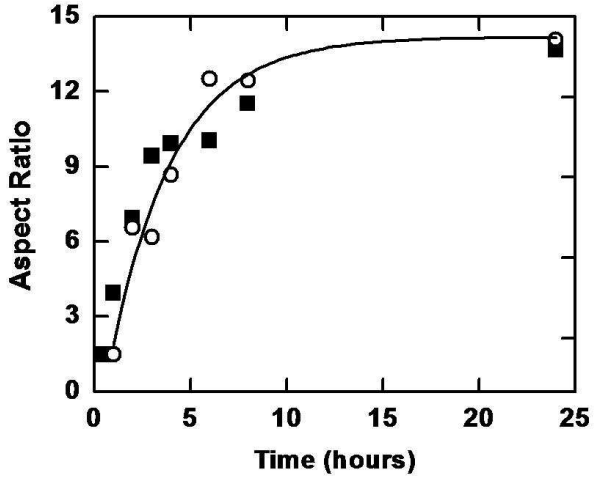

Figure 6.11 Temporal evolution of the nanowire aspect ratio for heterogeneous (■) and homogeneous (○) growth.

than the corresponding distributions for heterogeneously grown nanowires. The wider distribution in homogeneous growth results because the nucleation and growth are not separated in time and continue to occur together throughout the growth. In contrast, heterogeneous growth is nucleated all at the same time by seeding the substrate.

A cursory examination of Figure 6.10 would lead one to conclude that the heterogeneous and homogeneous growth look very different. However, a careful examination of the average aspect ratio, ($h/2R_w$) shows that the temporal evolution of this value is the same for both heterogeneous and homogeneous growth (Figure 6.11). This indicates that even with little or no mass transport limitations in the solution, the homogeneously nucleated nanowires still grow faster along the c-axis. Moreover, it would be difficult to explain the anisotropic homogeneous growth with mass transport limitations. This result also shows that the ratio of the c-axis growth rate to the lateral growth rate (i.e., k_z/k_r) is the same for both the homogeneous and heterogeneous growth. This is conclusive evidence that the anisotropic growth of the ZnO is intrinsic to the growth kinetics of ZnO in methenamine and zinc nitrate hexahydrate and is not caused by mass transport limited growth.

6.8 Conclusions

The heterogeneous growth of ZnO nanowires in an aqueous solution of methenamine and zinc nitrate hexahydrate was shown to be mass transport limited. As a result the growth rate is inversely proportional to the nanowire number density which limits the growth of dense nanowire arrays at a practical rate. This limitation can be overcome by stirring the growth solution near the substrate and growth rates four times that obtained in stagnant solutions have been achieved with modest stirring rates. The mass transport limited growth leads to nonuniform growth near boundaries between seeded and unseeded regions. Finally, the anisotropic nanowire growth is not due to the mass transport limited growth but is due to the intrinsic growth kinetics of the $(10\bar{1}0)$ and (0001) surfaces of ZnO in zinc nitrate hexahydrate and methenamine.

References

(1) Baxter, J. B.; Walker, A. M.; van Ommering, K.; Aydil, E. S. *Nanotechnology* **2006**, *17*, S304.

(2) Yan, X.; Li, Z.; Chen, R.; Gao, W. *Cryst. Growth Des.* **2008**, *8*, 2406.

(3) Cui, J. B.; Daghlian, C. P.; Gibson, U. J.; Pusche, R.; Geithner, P.; Ley, L. *J. Appl. Phys.* **2005**, *97*, 044315.

(4) Liu, J.; She, J.; Deng, S.; Chen, J.; Xu, N. *J. Phys. Chem. C* **2008**, *112*, 11685.

(5) Guo, M.; Diao, P.; Cai, S. M. *J. Solid State Chem.***2005**, *178*, 1864.

(6) Coltrin, M. E.; Hsu, J. W. P.; Scrymgeour, D. A.; Creighton, J. R.; Simmons, N. C.; Matzke, C. M. *J. Cryst. Growth* **2008**, *310*, 584.

(7) Greene, L. E.; Law, M.; Tan, D. H.; Montano, M.; Goldberger, J.; Somorjai, G.; Yang, P. *Nano Lett.* **2005**, *5(7)*, 1231.

(8) Ma, T.; Guo, M.; Zhang, M.; Zhang, Y.; Wang, X. *Nanotechnology* **2007**, *18*, 035605.

(9) Oelkers, E. H.; Helgeson, H. C. *Geochim. Cosmochim. Ac.* **1988**, *52*, 63.

(10) Greenspan, H. P.; Batchelor, G. K.; Miles, J. W. *The Theory of Rotating Fluids*; University Printing House: Cambridge, **1968**.

Chapter 7 : Summary and Future Directions

7.1 Summary

The unique operation principles of excitonic solar cells, allows the use of inexpensive components and low cost processing techniques. For these reasons, excitonic solar cells have the potential to lower the cost of solar–to-electric energy conversion. In particular, the TiO_2 nanoparticle dye-sensitized solar cell, which is currently the most efficient excitonic solar cell (~11%)[1] is very promising. Indeed, several companies have started manufacturing DSSCs. However, the record efficiency achieved with DSSCs is nowhere near the theoretical maximum efficiency for DSSCs (~24% assuming a dye HOMO-LUMO gap of 2 eV).[2] Thus, there is the potential to increase the efficiency of DSSCs. Increasing the thickness of the photoanode, allowing for more dye adsorption, is one way to increase the DSSC efficiency. However, this method is limited because the electron collection efficiency decreases as the photoanode thickness increases. Replacing the nanoparticle photoanodes with nanowire photoanodes has been shown to increase electron collection by providing a direct electron pathway to the collection electrode. However, due to their lower surface area, nanowire DSSC efficiency has not exceeded that of nanoparticle DSSCs. Thus, the synthesis of nanowire films with high surface area has the potential to benefit DSSCs as well as other types of excitonic solar cells. To this end, we have studied the synthesis of TiO_2 and ZnO nanowires and have made some progress towards the synthesis of high surface area nanowire films.

Polycrystalline anatase TiO_2 nanowire films were successfully synthesized on flexible titanium foil substrates and the three step hydrothermal process which transforms single crystal sodium titanate nanotubes, $Na_2Ti_2O_4(OH)_2$, to polycrystalline anatase TiO_2 nanowires was examined in detail. The TiO_2 nanowires are randomly oriented and entangled together to form a nanostructured film with an overall surface area similar to that of nanoparticle DSSCs. These TiO_2 nanowire films were incorporated as the photoanode in DSSCs.

Compared to nanoparticle DSSCs in literature, the TiO_2 nanowire DSSCs synthesized have similar electron transport rates but slower recombination rates which

results in increased electron collection efficiency. However, the overall efficiency of these TiO_2 nanowire based DSSCs is still a factor of three to four less than that of nanoparticle DSSCs found in the literature. There are several possible reasons for this lower efficiency. First, the highest nanoparticle DSSCs efficiency achieved in our lab is ~3% which is a factor of three to four less than the record 11%.[1] The reason for this lower efficiency is because there are several steps involved in making an efficient DSSC and not all have been optimized in our group. Some of these steps include purifying the dye, sealing the cells and optimizing the electrolyte composition. All these steps have to be mastered and optimized to reach record efficiencies. We have chosen to study the effects of morphology on electron transport by comparing different photoanode morphologies. Future studies should focus on optimization of the other steps and DSSC components in order to increase the efficiency of the nanowire based cells made in our lab. Second, the TiO_2 nanowires are on opaque Ti foil, which necessitates the cell to be illuminated from the cathode side. This lowers the cells efficiency because less light is incident on the photoanode due to low transmission through the Pt electrode and the electrolyte. Third, because the nanowires are polycrystalline the electrons must cross grain boundaries, which limits the electron transport and thus the improvement to the electron collection efficiency due to the nanowire morphology. However, even the single crystal rutile TiO_2 wires, which have been recently realized on a transparent conducting oxide substrates and integrated into DSSCs,[3] have similar transport and recombination time constants as TiO_2 nanoparticle DSSCs.[4,5] The reason for the lack of improvement of the electron collection efficiency in the single crystal rutile nanowires is likely due to a high defect density on the surfaces of the nanowires which results in electron transport involving diffusion through traps rather than by direct transport through the nanowire conduction band. Further investigation of this hypothesis would be worth while in order to improve the electron collection efficiency through the nanowires as well as to address the question of whether or not nanowire films will indeed significantly increase the efficiency of excitonic solar cells.

Unlike the single crystal rutile TiO_2 nanowires, single crystal wurtzite ZnO nanowires show a significantly faster transport rate as well as a slightly improved

recombination rate as compared to nanoparticle DSSCs.[6] Typical nanoparticle DSSCs have transport and recombination rates of 1-10 ms and 10-100 ms, respectively.[4,5] Whereas, ZnO nanowire DSSCs have transport and recombination rates of 0.1-10 ms and 100-1000 ms, respectively.[6] With the improved collection efficiency found in the ZnO nanowires, photoanodes as thick at 100 μm could be realized without a significant loss in injected electron collection efficiency.[6] However, despite the increased electron collection efficiency, DSSCs have achieved efficiencies of only ~2.4%.[7] These limited efficiencies are due to insufficient surface area of ZnO nanowire arrays. We have studied the synthesis of ZnO nanowires from aqueous solutions of zinc nitrate hexahydrate and methenamine in detail and have gained a fundamental and detailed knowledge of the growth mechanism. This may lead to control of the nanowire growth and thereby the ability to increase the ZnO nanowire film surface area. We have proposed a growth mechanism for the nanowire synthesis in which a zinc-methenamine complex reacts at the surface of hydroxyl terminated nanowires. Upon reaction, the zinc is incorporated into the ZnO solid and the methenamine decomposes to ammonia and formaldehyde. Using analytical chemistry as well as thermodynamic and kinetic models we have supported our proposed mechanism. The knowledge of the nanowire synthesis on the molecular level is interesting not only from a fundamental scientific point of view may potentially lead to better control of the nanowire growth in the future. We also found that the nanowire growth is mass transport limited and that stirring the solution increases the growth rate by a factor of four and improves the heterogeneously grown nanowire yield. This result highlights the advantages of stirring during chemical bath deposition processes, which is valuable since it is common for this technique to be mass transport limited, as is the case for the deposition of CdS films (personal communication with Selin Tosun, July 19, 2009).

7.2 Future Directions

We have made progress towards synthesizing high surface area TiO_2 and ZnO nanowire films which can be introduced as the photoanode in DSSCs. However, for the DSSC efficiency to be improved, sufficient surface area and increased electron collection efficiency must be realized simultaneously. This is proving to be a difficult task. The

solution synthesized, single crystal, ZnO nanowire films provide increased electron collection efficiency as compared to nanoparticles films, but are deficient in surface area. Whereas, the opposite is true for the single crystal TiO_2 nanowire films; they have sufficient surface area but the expected increase in collection efficiency has not been realized. If the extinction coefficient of the dye could be increased and/or the absorbance of the dye could be broadened to include the near IR this would lower the photoanode surface area required for maximum photon absorption. This would then make the realization of a photoanode which simultaneously possesses sufficient surface area and high collection efficiency more attainable. Furthermore, it is not clear if single crystal nanowires provide increased electron collection efficiencies by providing direct transport to the photoanode as it was initially conjectured. Clearly, the validity of this hypothesis depends on the nanowires since enhancement in electron transport has been demonstrated in ZnO nanowires but not in TiO_2 nanowires. The reasons for this surprising difference must be explored further.

The single crystal ZnO nanowire films synthesized in this thesis do not have adequate surface area to take advantage of their high collection efficiency to increase the DSSC performance. Yoshida et al.[8] have found a novel way to combine high surface area and increased electron collection in a ZnO photoanode. They have synthesized the ZnO DSSC with the highest efficiency to date of 7.2%.[9] Yoshida et al.[8] have deposited a porous ZnO nanostructure onto FTO substrates by electrodeposition of zinc salts, e.g. $ZnCl_2$, in oxygen-saturated aqueous solutions with an organic dye present. The dyes used are sufficient for use in DSSCs, e.g. eosin Y (available from Aldrich). The dye acts as a structure direction agent (SDA) and "templates" the ZnO as is it deposited. The dye and the ZnO became intermixed on the nanometer scale which leads to a unique interconnected, crystalline ZnO structure with vertical pores.[8] The width of the pores is similar in size to the dye molecules, making the surface area per unit height of the ZnO nanostructure exceptionally high. With this porous structure ~3-5 μm thick films (~10 μm nanoparticle films are required) are sufficient to provide enough surface area for maximum photon absorption. The dye, which is initially deposited during the electrodeposition, deposits as aggregates and therefore the as deposited films do not

result in high DSSCs efficiencies. However, the dye can be removed with a dilute KOH solution and a fresh monolayer of dye can be deposited by placing the ZnO photoanode in fresh dye solution. As Yoshida et al.[8] have pointed out, since all of the dye is removed when the deposited electrode is placed in the KOH solution, all of the ZnO surface is attainable by the KOH solution. This means that the electrolyte is able to reach the dye molecules for regeneration during cell operation. The photoanode is not one large single crystal but it is single crystal on the micrometer length scale, which is a significantly larger single crystal area than that which occurs in ~5-15 nm ZnO nanoparticles films.

This electrodeposition process is attractive not only because of the high surface area ZnO films it creates but because it is simple, inexpensive and can be done at temperatures as low as 40 °C. These attributes make this method attractive for manufacturing low cost DSSCs on plastic substrates. Incidentally, ZnO is virtually the only semiconductor which is crystalline immediately upon electrodeposition.[8] Other semiconductors need a post deposition high temperature anneal to crystallize. Yoshida et al.[8] also find increased electron transport in the electrodeposited porous films as compared to ZnO nanoparticle films. They claim this is due to the single crystallinity of the porous films. It is also possible to form different ZnO nanostructure film morphologies depending on the dye present during the electrodeposition.[8] For example, the eosinY dye creates a vertically oriented porous nanostructure with the ZnO c-axis perpendicular to the substrate. In contrast, when the dye coumarin343 (available from Aldrich) is added to the deposition solution, a film with a lamellar structure composed of nanoplates with the ZnO c-axis parallel to the substrate is formed. This difference in morphology is because the eosinY and coumarin343 dyes preferentially adsorb to different faces of ZnO and therefore direct the growth differently.[8] This recent work illustrates that there are alternative morphologies to nanowires for increasing the DSSC efficiencies which may even prove more important than nanowires even though recent work has touted the advantages of one-dimensional nanostructures.[4,10,11] It might be that a highly porous yet still crystalline structure is a good way to get both the high surface area and increased electron transport simultaneously. It would be interesting to look at the ZnO film electrodeposition process in more detail and to try to increase the surface area

even further and make the crystalline domains larger. Anatase TiO_2 porous photoanodes have also been achieved by a combination of amorphous titanate electrodeposition and post-deposition annealing of the resulting film at 450 °C.[12] While the annealing step limits the usefulness of this technique on plastic substrates, the DSSCs made from these films achieve an overall power conversion efficiency of ~0.8% with a film thickness of ~500 nm, a quite high value for such a thin film.[12] Thus, exploring how to electrodeposit thick, crystalline and high surface area, TiO_2 films directly onto conducting substrates using different dyes as structure direction agents may be a fruitful area of research.

Improving the dye by making it less expensive and able to absorb further into the near infrared is an area of research with a lot of potential to increase the DSSC efficiency. For example, if a dye which is able to absorb from 300-700 nm is replaced with one which can absorb from 300-1000 nm, then the fraction of the absorbed photons increases from 46% to 65% of the total number of incident photons in the AM 1.5 spectrum. This is a 40% increase which, assuming the open circuit voltage and the fill factor do not change with increased dye absorption, should result in a 40% increase in the short circuit current and overall efficiency. Currently the best dyes (e.g., N3, N719 and "black dye" from Solaronix), contain Ru metal which is rare and increases the price of the dyes. In addition, the low molar extinction coefficients[8] of the dyes result in large amounts of dye being required for high efficiencies. Thus, synthesis of new inexpensive, high molar extinction coefficient dyes which absorb in the near IR would greatly improve the efficiency and cost of DSSCs.

Another issue which requires further research regarding the Ru based dyes from Solaronix is that they work well with TiO_2, however they do not work well with ZnO. One problem with using the Ru based dyes with ZnO photoanodes is that the dyes have carboxylic acid groups which attach to the ZnO surface in order to anchor the dye. However, this lowers the local pH at the ZnO surface. Since ZnO is more soluble at lower pH values, this causes some of the zinc atoms at the surface to dissolve and become zinc ions. These zinc ions then complex with the dye irreversibly creating zinc-dye-aggregates which absorb photons but do not efficiently inject electrons into the ZnO.[13]

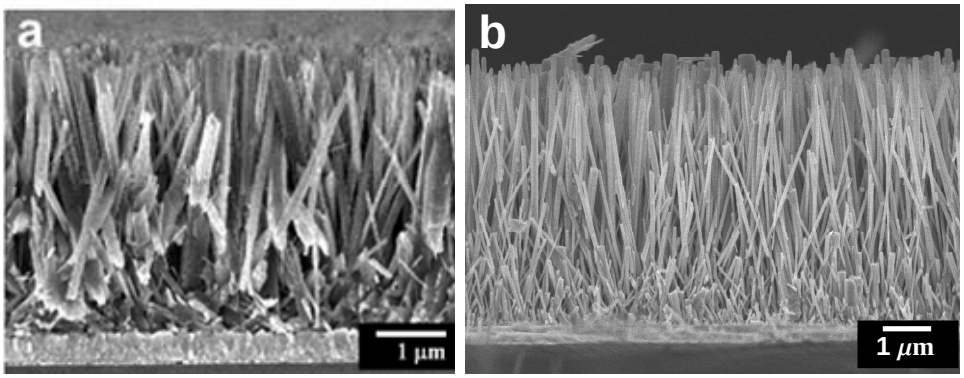

Figure 7.1 (a) Rutile TiO_2 nanowire film with height, diameter and number density of ~4 μm, ~90 nm and ~40 nanowires/μm^2, respectively.[3] (b) ZnO nanowire film with height, diameter and number density of ~5 μm, ~100 nm and ~22 nanowires/μm^2, respectively.

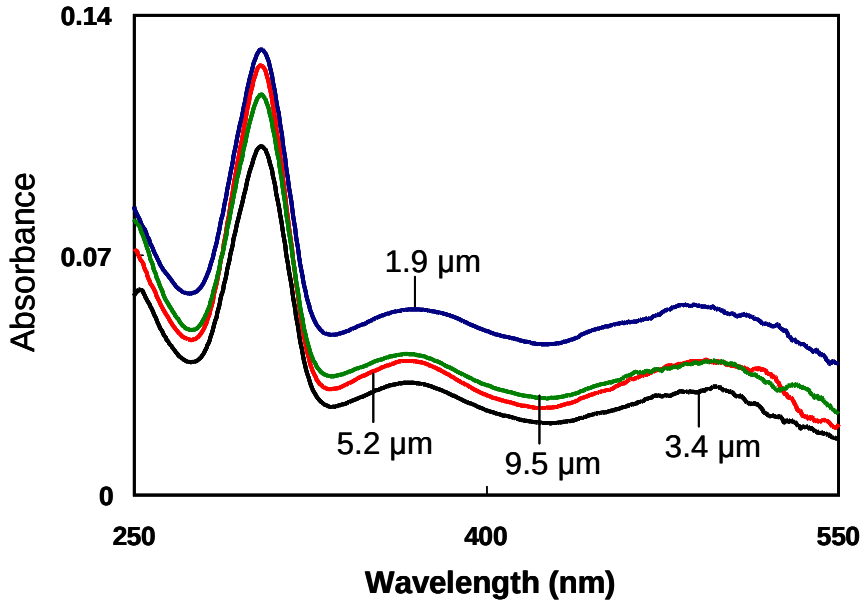

Figure 7.2 Absorbance of the N719 (Solaronix) dye desorbed in 0.1 M aqueous KOH solution from ZnO nanowire DSSCs with heights of 1.9 μm, 3.4 μm, 5.2 μm and 9.5 μm indicated by the vertical lines. The absorbance does not increase systematically with nanowire height.

Thus, the aggregates lower the electron injection quantum yield and hence the overall power conversion efficiency.[14]

We also believe that another problem with using the Ru based dyes with ZnO is that the dyes do not bind as densely to the ZnO surface as they do to the TiO_2 surfaces. We believe this because an order of magnitude more dye is adsorbed onto the rutile single crystal TiO_2 nanowire films as compared to the single crystal wurtzite ZnO nanowire films, even though the number densities, diameters and lengths of the nanowires are similar, Figure 7.1. The amount of dye desorbed from the 4 μm TiO_2 nanowire film corresponds to a roughness factor (i.e. nanowire surface area/projected film area) of 150, whereas the roughness factor found by dye desorption from a 4 μm ZnO nanowire film is ~20. However, the roughness factors estimated from the nanowire dimensions and number density measured from SEM gives a roughness factor for the TiO_2 and ZnO nanowires of 45 and 36, respectively. It could be that there is surface roughness on the TiO_2 which allows for an order of magnitude higher surface area, however, looking at Figure 7.1 this seem unlikely. Also, we have observed that the amount of dye adsorbed onto the ZnO nanowires does not always increase as the nanowire height increases (Figure 7.2). Therefore, it is likely that the dye does not adsorb as much or pack as densely on to ZnO nanowires as it does on to TiO_2 nanowires, thus lowering the efficiency of ZnO nanowire DSSCs. A good way to confirm that the dye packs differently on the TiO_2 and ZnO nanowires would be to measure the surface areas of the ZnO and TiO_2 nanowire films using another technique other than dye desorption. If the ZnO and TiO_2 nanowire films have the same surface area, then less dye must adsorb on the ZnO nanowire films because it packs less densely on ZnO as compared to TiO_2. For example, BET measurements using a Kr absorption isotherm could be done on the nanowires to find an independent surface area value. Kr should be used and not N_2 since the Kr absorption tends to be more sensitive than N_2 absorption,[15] and this sensitivity is needed since one 4 cm^2 substrate has a relatively small surface area.

Since the Ru based dyes work best with TiO_2 it has had the effect of making ZnO photoanodes seem inferior to TiO_2, when in reality it is likely that the reason for the lower ZnO performance is that the appropriate dye for ZnO has not been found yet.[8]

Thus, there is a need for dyes which are more suitable for ZnO. Such a dye must bind densely to the ZnO nanowires/particles, not cause the ZnO to dissolve, allow for fast electron injection, have a high extinction coefficient, and absorb into the near IR. Moreover, this dye must achieve all these requirements at low cost.

Yoshida et al.[8] have been working on finding dyes, which meet the requirements stated above and have had some success. They have found several potential dyes and have tested them on their electrodeposited porous crystalline ZnO photoelectrodes. In particular, they have found that the D149 dye (Mitshubishi Paper Mills Ltd.), which absorbs from 300-700 nm, works well with ZnO. Using this dye and electrodeposited porous crystalline ZnO photoelectrodes, an overall power conversion efficiency of 5.56% has been achieved.[8] Yoshida et al. have also found that porous crystalline ZnO photoelectrodes in conjunction with the squarylium dye (available from Aldrich), which absorbs from 500-700[8] nm, or heptamethine-cyanine dye (must be synthesized), which absorbs from 600-900[8] nm, results in DSSCs with overall power conversion efficiencies of 1.5%[16] and 0.67%[17], respectively. They have also tried coadsorbing dyes which are compatible with ZnO and absorb in different regions of the solar spectrum. They have found that the DSSCs assembled with two dyes have efficiencies higher than those with a single dye and that the dyes maintain their sensitization capability even when they are coabsorbed on the same photoanode. Thus, combining dyes in order to cover the whole solar spectrum is a possibility if a single dye with a broad absorption spectra cannot be found. While Yoshida et al.[8] have made significant progress, more research needs to be done to engineer the best dye for high efficiency ZnO DSSCs.

Single crystal ZnO nanowires provide increased electron collection efficiency as compared to TiO_2 nanoparticles,[6] however, single crystal rutile TiO_2 nanowires have similar collection efficiencies as TiO_2 nanoparticles (unpublished results, personal communication with Bin Liu, April 8, 2009). It is not clear why this is the case and it presents a fundamental question as to whether or not all single crystal nanowires, and in particular rutile TiO_2 nanowires, have the ability to significantly increase electron transport as has been predicted.[9,10] It has been shown that the ZnO nanoparticle photoanodes have better charge transport properties than TiO_2 nanoparticle

photoanodes,[18] thus it may be that lower electron collection efficiency is intrinsic to TiO_2 and therefore TiO_2 nanowires will not be able to increase the efficiency of DSSCs. However, it might also be possible to modify the synthesis process such that these rutile TiO_2 nanowires exhibit higher electron collection efficiencies. The slower electron transport could be due to a high defect density in these nanowires which results in the electron transport involving traps and not direct transport though the conduction band. Therefore, if a synthesis method was developed which lowered the defect density this could result in higher electron collection efficiencies. In addition single crystal anatase TiO_2 nanowire films on a transport conducting oxide have yet to be realized and they may behave differently than rutile nanowires. Thus, developing a synthesis method for low defect density single crystal anatase TiO_2 films may be valuable.

Another potentially profitable research project would be to determine if defect-derived surface states are likely to be present on the side surfaces of the single crystal rutile nanowires by examining the (110) TiO_2 rutile crystal face using femtosecond time-resolved two-photon photoemission spectroscopy (TR-2PPE). The (110) crystal face should be examined since this is the orientation of nanowire sidewalls.[3] The $(10\bar{1}0)$ crystal face of ZnO, which is the same face as the side walls of the ZnO nanowires used in DSSCs, has been examined using TR-2PPE.[19] It was found that there is an exponentially decreasing density of defect-derived surface states within the band gap which may be responsible for the carrier trapping observed in the electron transport in ZnO nanowires.[19] Thus, studying the rutile TiO_2 (110) face with TR-2PPE, might suggest whether defect-derived surface states are responsible for the lower collection efficiency in the rutile TiO_2 nanowires as compared to ZnO nanowires. This may help to answer the fundamental question of whether or not single crystal rutile TiO_2 nanowires will be able to increase the efficiency of DSSCs.

The research and findings described in this thesis have furthered the understanding of TiO_2 and ZnO nanowire synthesis techniques. This understanding may be used in the future to create high surface area nanowires for DSSCs. However, there are still many research paths to pursue, and challenges to overcome, to significantly increase the efficiency of DSSCs. Nevertheless, other nanowire based excitonic solar cells have

different requirements for the nanowire film, which may be met more easily. For example, the nanowire based quantum dot solar cell only requires that the nanowires provide fast electron transport and does not require a high surface area nanowire film. Thus, an improvement to the QDSC efficiency by incorporating ZnO nanowires has been recently achieved.[20]

References

(1) Chiba, Y.; Islam, A.; Watanabe, Y.; Komiya, R.; Koide, N.; Han, L. Y. *Jpn. J. Appl. Phys. 2* **2006**, *45*, L638.

(2) Shockley, W.; Queisser, H. J. *J. Appl. Phys.* **1961**, *32*, 510.

(3) Liu, B.; Aydil, E. S. *J. Am. Chem. Soc.* **2009**, *131*, 3985.

(4) Zhu, K.; Neale, N. R.; Miedaner, A.; Frank, A. J. *Nano Lett.* **2007**, *7*, 69.

(5) Frank, A. J.; Kopidakis, N.; van de Lagemaat, J. *Coordin. Chem. Rev.* **2004**, *248*, 1165.

(6) Enache-Pommer, E., University of Minnesota, 2009.

(7) Guo, M.; Diao, P.; Wang, X.; Cai, S. *J. Solid State Chem.* **2005**, *178*, 3210.

(8) Tsukasa Yoshida; Jingbo Zhang; Daisuke Komatsu; Seiichi Sawatani; Hideki Minoura; Thierry Pauporté; Daniel Lincot; Torsten Oekermann; Derck Schlettwein; Hirokazu Tada; Dieter Wöhrle; Kazumasa Funabiki; Masaki Matsui; Hidetoshi Miura; Hisao Yanagi *Adv. Funct. Mater.* **2009**, *19*, 17.

(9) Gonzalez-Valls, I.; Lira-Cantu, M. *Energ. Environ. Sci.* **2009**, *2*, 19.

(10) Baxter, J. B.; Aydil, E. S. *Appl. Phys. Lett.* **2005**, *86*, 53114.

(11) Law, M.; Greene, L. E.; Johnson, J. C.; Saykally, R.; Yang, P. D. *Nat. Mater.* **2005**, *4*, 455.

(12) Wessels, K.; Maekawa, M.; Rathousky, J.; Yoshida, T.; Wark, M.; Oekermann, T. *Micropor. Mesopor. Mat.* **2008**, *111*, 55.

(13) Keis, K.; Lindgren, J.; Lindquist, S.-E.; Hagfeldt, A. *Langmuir* **2000**, *16*, 4688.

(14) Anderson, N. A.; Ai, X.; Lian, T. *J. Phys. Chem. B* **2003**, *107*, 14414.

(15) Yanazawa, H.; Mastunaga, H.; Itoh, H.; Nakai, K.; Suzuki, I. *J. Vac. Sci. Technol. B* **2002**, *20*, 1833.

(16) Otsuka, A.; Funabiki, K.; Sugiyama, N.; Yoshida, T. *Chem.* Lett. **2006**, *35*, 666.

(17) Otsuka, A.; Funabiki, K.; Sugiyama, N.; Mase, H.; Yoshida, T.; Minoura, H.; Matsui, M. *Chem. Lett.* **2008**, *37*, 176.

(18) Keis, K.; Magnusson, E.; Lindström, H.; Lindquist, S.-E.; Hagfeldt, A. *Sol. Energ. Mat. Sol. C.***2002**, *73*, 51.

(19) Tisdale, W. A.; Muntwiler, M.; Norris, D. J.; Aydil, E. S.; Zhu, X. Y. *J .Phys. Chem. C* **2008**, *112*, 14682.

(20) Leschkies, K. S.; Jacobs, A. G. ; Norris, D. J.; Aydil, E. S. *Appl. Phys. Lett.* **2009**, *submitted*.

Bibliography

(1) Ackermann, J.; Videlot, C.; El Kassmi, A.; Guglielmetti, R.; Fages, F. *Advanced Functional Materials* **2005**, *15*, 810-817.

(2) Adachi, M.; Murata, Y.; Takao, J.; Jiu, J. T.; Sakamoto, M.; Wang, F. M. *Journal of the American Chemical Society* **2004**, *126*, 14943-14949.

(3) Ahuja, I. S.; Yadava, C. L.; Singh, R. *Journal of Molecular Structure* **1982**, *81*, 229-234.

(4) Al-Ibrahim, M.; Roth, H. K.; Zhokhavets, U.; Gobsch, G.; Sensfuss, S. *Solar Energy Materials and Solar Cells* **2005**, *85*, 13-20.

(5) Anderson, N. A.; Ai, X.; Lian, T. *The Journal of Physical Chemistry B* **2003**, *107*, 14414-14421.

(6) Arici, E.; Sariciftci, N. S.; Meissner, D. *Advanced Functional Materials* **2003**, *13*, 165-171.

(7) Ashfold, M. N. R.; Doherty, R. P.; Ndifor-Angwafor, N. G.; Riley, D. J.; Sun, Y. *Thin Solid Films* **2007**, *515*, 8679-8683.

(8) Bahnemann, D. W.; Kormann, C.; Hoffmann, M. R. *Journal of Physical Chemistry* **1987**, *91*, 3789-3798.

(9) Barbe, C. J.; Arendse, F.; Comte, P.; Jirousek, M.; Lenzmann, F.; Shklover, V.; Gratzel, M. *Journal of the American Ceramic Society* **1997**, *80*, 3157-3171.

(10) Baxter, J. B., Univeristy of California, Santa Barbara, 2005.

(11) Baxter, J. B.; Aydil, E. S. *Applied Physics Letters* **2005**, *86*, 53114-1.

(12) Baxter, J. B.; Walker, A. M.; van Ommering, K.; Aydil, E. S. *Nanotechnology* **2006**, *17*, S304-S312.

(13) Beek, W. J. E.; Wienk, M. M.; Janssen, R. A. J. *Journal of Materials Chemistry* **2005**, *15*, 2985-2988.

(14) Beek, W. J. E.; Wienk, M. M.; Kemerink, M.; Yang, X. N.; Janssen, R. A. J. *Journal of Physical Chemistry B* **2005**, *109*, 9505-9516.

(15) Benkstein, K. D.; Kopidakis, N.; van de Lagemaat, J.; Frank, A. J. *The Journal of Physical Chemistry B* **2003**, *107*, 7759-7767.

(16) Bertie, J. E.; Solinas, M. *The Journal of Chemical Physics* **1974**, *61*, 1666-1677.

(17) Bierman, M. J.; Lau, Y. K. A.; Kvit, A. V.; Schmitt, A. L.; Jin, S. *Science* **2008**, *320*, 1060-1063.

(18) Bisquert, J.; Zaban, A.; Greenshtein, M.; Mora-Sero, I. *Journal of the American Chemical Society* **2004**, *126*, 13550-13559.

(19) Boercker, J. E.; Enache-Pommer, E.; Aydil, E. S. *Nanotechnology* **2008**, *19*, 10.

(20) Boercker, J. E.; Schmidt, J. B.; Aydil, E. S. *Crystal Growth & Design* **2009**, *9*, 2783-2789.

(21) Boschloo, G.; Haggman, L.; Hagfeldt, A. *Journal of Physical Chemistry B* **2006**, *110*, 13144-13150.

(22) Boyle, D. S.; Govender, K.; O'Brien, P. *Chemical Communications* **2002**, *80*, 80-81.

(23) Boyle, D. S.; Govender, K.; O'Brien, P. *Thin Solid Films* **2003**, *431*, 483-487.

(24) Brown, P.; Takechi, K.; Kamat, P. V. *Journal of Physical Chemistry C* **2008**, *112*, 4776-4782.

(25) Brus, L. *The Journal of Physical Chemistry* **2002**, *90*, 2555-2560.

(26) C. N. Duckworth; A. W. Brinkman; J. Woods *Physica Status Solidi (a)* **1983**, *75*, K99-K102.
(27) Cameron, P. J.; Peter, L. M. *Journal of Physical Chemistry B* **2003**, *107*, 14394-14400.
(28) Cameron, P. J.; Peter, L. M.; Hore, S. *Journal of Physical Chemistry B* **2005**, *109*, 930-936.
(29) Cao, X. B.; Chen, P.; Guo, Y. *Journal of Physical Chemistry C* **2008**, *112*, 20560-20566.
(30) Chang, C.-H.; Lee, Y.-L. *Applied Physics Letters* **2007**, *91*, 053503.
(31) Chappel, S.; Chen, S.-G.; Zaban, A. *Langmuir* **2002**, *18*, 3336-3342.
(32) Chen, Y. W.; Qiao, Q.; Liu, Y. C.; Yang, G. L. *Journal of Physical Chemistry C* **2009**, *113*, 7497-7502.
(33) Cheng, A.-J.; Tzeng, Y.; Zhou, Y.; Park, M.; Wu, T.-h.; Shannon, C.; Wang, D.; Lee, W. *Applied Physics Letters* **2008**, *92*, 092113.
(34) Cheng, H.-M.; Chiu, W.-H.; Lee, C.-H.; Tsai, S.-Y.; Hsieh, W.-F. *The Journal of Physical Chemistry C* **2008**, *112*, 16359-16364.
(35) Chiba, Y.; Islam, A.; Watanabe, Y.; Komiya, R.; Koide, N.; Han, L. Y. *Japanese Journal of Applied Physics Part 2-Letters & Express Letters* **2006**, *45*, L638-L640.
(36) Chou, K.-S.; Chen, W.-H.; Huang, C.-S. *Journal of the Chin. I. Ch. E.* **1990**, *21*, 327-334.
(37) Coakley, K. M.; McGehee, M. D. *Applied Physics Letters* **2003**, *83*, 3380-3382.
(38) Coakley, K. M.; McGehee, M. D. *Chemistry of Materials* **2004**, *16*, 4533-4542.
(39) Coakley, K. M.; Srinivasan, B. S.; Ziebarth, J. M.; Chiatzun, G.; Yuxiang, L.; McGehee, M. D. *Advanced Functional Materials* **2005**, *15*, 1927-32.
(40) Coltrin, M. E.; Hsu, J. W. P.; Scrymgeour, D. A.; Creighton, J. R.; Simmons, N. C.; Matzke, C. M. *Journal of Crystal Growth* **2008**, *310*, 584-593.
(41) Cui, D. H.; Xu, J.; Zhu, T.; Paradee, G.; Ashok, S.; Gerhold, M. *Applied Physics Letters* **2006**, *88*.
(42) Cui, J. B.; Daghlian, C. P.; Gibson, U. J.; Pusche, R.; Geithner, P.; Ley, L. *Journal of Applied Physics* **2005**, *97*, 044315-044315.
(43) Cui, J. B.; Daghlian, C. P.; Gibson, U. J.; Pusche, R.; Geithner, P.; Ley, L. *Journal of Applied Physics* **2005**, *97*, 044315.
(44) Diguna, L. J.; Shen, Q.; Kobayashi, J.; Toyoda, T. *Applied Physics Letters* **2007**, *91*.
(45) Dloczik, L.; Engelhardt, R.; Ernst, K.; Lux-Steiner, M. C.; Könenkamp, R. *Sensors and Actuators B: Chemical* **2002**, *84*, 33-36.
(46) Dloczik, L.; Ileperuma, O.; Lauermann, I.; Peter, L. M.; Ponomarev, E. A.; Redmond, G.; Shaw, N. J.; Uhlendorf, I. *Journal of Physical Chemistry B* **1997**, *101*, 10281-10289.
(47) DOE; http://www1.eere.energy.gov/windandhydro/pdfs/43025.pdf: Jul 23, 2009.
(48) DOE; http://www.energy.gov/energysources/index.htm: July 23, 2009.
(49) DOE; http://www.eia.doe.gov/cneaf/electricity/epm/table4_1.html: July 23, 2009.
(50) EDN; http://www.edn.com/article/CA6432171.html: July 23, 2009.
(51) Eigen, M. *Pure and Applied Chemistry* **1963**, *6*, 97-115.

(52) Ellingson, R. J.; Beard, M. C.; Johnson, J. C.; Yu, P.; Micic, O. I.; Nozik, A. J.; Shabaev, A.; Efros, A. L. *Nano Letters* **2005**, *5*, 865-871.
(53) Enache-Pommer, E., University of Minnesota, 2009.
(54) Enache-Pommer, E.; Boercker, J.; Aydil, E. *Applied Physics Letter* **2007**, *91*, 123116.
(55) Enache-Pommer, E.; Boercker, J.; Aydil, E. *Applied Physics Letter* **2007**, *91*, 123116.
(56) Enache-Pommer, E.; Liu, B.; Aydil, E. *PCCP submitted* **2009**.
(57) Enright, B.; Fitzmaurice, D. *The Journal of Physical Chemistry* **1996**, *100*, 1027-1035.
(58) Ferrere, S.; Zaban, A.; Gregg, B. A. *Journal of Physical Chemistry B* **1997**, *101*, 4490-4493.
(59) Fisher, A. C.; Peter, L. M.; Ponomarev, E. A.; Walker, A. B.; Wijayantha, K. G. U. *The Journal of Physical Chemistry B* **2000**, *104*, 949-958.
(60) Frank, A. J.; Kopidakis, N.; van de Lagemaat, J. *Coordination Chemistry Reviews* **2004**, *248*, 1165-1179.
(61) Frank, A. J.; Kopidakis, N.; van de Lagemaat, J. *Coordination Chemistry Reviews* **2004**, *248*, 1165-1179.
(62) Fujita, K.; Matsuda, K.; Mitsuzawa, S. *Bulletin of the Chemical Society of Japan* **1992**, *65*, 2270-2271.
(63) Galoppini, E.; Rochford, J.; Chen, H. H.; Saraf, G.; Lu, Y. C.; Hagfeldt, A.; Boschloo, G. *Journal of Physical Chemistry B* **2006**, *110*, 16159-16161.
(64) Galoppini, E.; Rochford, J.; Chen, H. H.; Saraf, G.; Lu, Y. C.; Hagfeldt, A.; Boschloo, G. *Journal of Physical Chemistry B* **2006**, *110*, 16159-16161.
(65) Gao, X. F.; Li, H. B.; Sun, W. T.; Chen, Q.; Tang, F. Q.; Peng, L. M. *Journal of Physical Chemistry C* **2009**, *113*, 7531-7535.
(66) Ghosh, A. K.; Wakim, F. G.; Addiss, R. R. *Physical Review* **1969**, *184*, 979.
(67) Gonzalez-Valls, I.; Lira-Cantu, M. *Energy & Environmental Science* **2009**, *2*, 19-34.
(68) Govender, K.; Boyle, D. S.; Kenway, P. B.; O'Brien, P. *Journal of Materials Chemistry* **2004**, *14*, 2575-2591.
(69) Gratzel, M. *Pure and Applied Chemistry* **2001**, *73*, 459-467.
(70) Gratzel, M. *Nature* **2001**, *414*, 338-344.
(71) Gratzel, M. *Journal of Photochemistry and Photobiology C-Photochemistry Reviews* **2003**, *4*, 145-153.
(72) Gratzel, M. *Journal of Photochemistry and Photobiology A-Chemistry* **2004**, *164*, 3-14.
(73) Gratzel, M. *Inorganic Chemistry* **2005**, *44*, 6841-6851.
(74) Greene, L. E.; Law, M.; Tan, D. H.; Montano, M.; Goldberger, J.; Somorjai, G.; Yang, P. *Nano Letter* **2005**, *5(7)*, 1231.
(75) Greene, L. E.; Law, M.; Yuhas, B. D.; Yang, P. D. *Journal of Physical Chemistry C* **2007**, *111*, 18451-18456.
(76) Greenham, N. C.; Xiaogang, P.; Alivisatos, A. P. *Physical Review B (Condensed Matter)* **1996**, *54*, 17628-37.

(77) Greenspan, H. P.; Batchelor, G. K.; Miles, J. W. *The Theory of Rotating Fluids*; University Printing House: Cambridge, 1968.
(78) Gregg, B. A. *Journal of Physical Chemistry B* **2003**, *107*, 4688-4698.
(79) Grodzicki, A.; Szlyk, E. *Polish Journal of Chemistry* **1984**, *58*, 999-1007.
(80) Grodzicki, A.; Szlyk, E. *Polish Journal of Chemistry* **1984**, *58*, 1009-1016.
(81) Grodzicki, A.; Szlyk, E. *Polish Journal of Chemistry* **1984**, *58*, 991-998.
(82) Gubbala, S.; Chakrapani, V.; Kumar, V.; Sunkara, M. K. *Advanced Functional Materials* **2008**, *18*, 2411-2418.
(83) Gundlach, L.; Ernstorfer, R.; Willig, F. *Progress in Surface Science* **2007**, *82*, 355-377.
(84) Guo, M.; Diao, P.; Cai, S. M. *Applied Surface Science* **2005**, *249*, 71-75.
(85) Guo, M.; Diao, P.; Cai, S. M. *Applied Surface Science* **2005**, *249*, 71-75.
(86) Guo, M.; Diao, P.; Cai, S. M. *Journal of Solid State Chemistry* **2005**, *178*, 1864-1873.
(87) Guo, M.; Diao, P.; Wang, X.; Cai, S. *Journal of Solid State Chemistry* **2005**, *178*, 3210-3215.
(88) Gur, I.; Fromer, N. A.; Geier, M. L.; Alivisatos, A. P. *Science* **2005**, *310*, 462-465.
(89) H. Gerischer *Photochemistry and Photobiology* **1972**, *16*, 243-260.
(90) Hagfeldt, A.; Gratzel, M. *Accounts of Chemical Research* **2000**, *33*, 269-277.
(91) Halls, J. J. M.; Walsh, C. A.; Greenham, N. C.; Marseglia, E. A.; Friend, R. H.; Moratti, S. C.; Holmes, A. B. *Nature* **1995**, *376*, 498-500.
(92) Hanna, M. C.; Nozik, A. J. *Journal of Applied Physics* **2006**, *100*, 074510.
(93) Harris, D. C. *Quantitative Chemical Analysis*; W.H. Freeman and Company: New York, 1991.
(94) He, C.; He, Q. G.; He, Y. J.; Li, Y. F.; Bai, F. L.; Yang, C. H.; Ding, Y. Q.; Wang, L. X.; Ye, J. P. *Solar Energy Materials and Solar Cells* **2006**, *90*, 1815-1827.
(95) Heo, Y. W.; Varadarajan, V.; Kaufman, M.; Kim, K.; Norton, D. P.; Ren, F.; Fleming, P. H. *Applied Physics Letters* **2002**, *81*, 3046-3048.
(96) Hesske, H.; Gloe, K. *The Journal of Physical Chemistry A* **2007**, *111*, 9848-9853.
(97) Ho, G. W.; Wong, A. S. W. *Applied Physics a-Materials Science & Processing* **2007**, *86*, 457-462.
(98) Ho, G. W.; Wong, A. S. W. *Applied Physics a-Materials Science & Processing* **2007**, *86*, 457-462.
(99) Hoffert, M. I.; Caldeira, K.; Jain, A. K.; Haites, E. F.; Harvey, L. D. D.; Potter, S. D.; Schlesinger, M. E.; Schneider, S. H.; Watts, R. G.; Wigley, T. M. L.; Wuebbles, D. J. *Nature* **1998**, *395*, 881-884.
(100) Hore, S.; Palomares, E.; Smit, H.; Bakker, N. J.; Comte, P.; Liska, P.; Thampi, K. R.; Kroon, J. M.; Hinsch, A.; Durrant, J. R. *Journal of Materials Chemistry* **2005**, *15*, 412-418.
(101) Hore, S.; Vetter, C.; Kern, R.; Smit, H.; Hinsch, A. *Solar Energy Materials and Solar Cells* **2006**, *90*, 1176-1188.
(102) Hsiao, P. T.; Wang, K. P.; Cheng, C. W.; Teng, H. S. *Journal of Photochemistry and Photobiology A-Chemistry* **2007**, *188*, 19-24.

(103) Hsu, Y. F.; Xi, Y. Y.; Djurisic, A. B.; Chan, W. K. *Applied Physics Letters* **2008**, *92*, 133507.
(104) Hu, Z.; Herrera Santos, J. F.; Oskam, G.; Searson, P. C. *Journal of colloid and interface science* **2005**, *288*, 313-316.
(105) Hu, Z.; Oskam, G.; Penn, R. L.; Pesika, N.; Searson, P. C. *The Journal of Physical Chemistry B* **2003**, *107*, 3124-3130.
(106) Hu, Z.; Oskam, G.; Searson, P. C. *Journal of colloid and interface science* **2003**, *263*, 454-460.
(107) Hu, Z.; Ramirez, D. J. E.; Cervera, B. E. H.; Oskam, G.; Searson, P. C. *Journal of Physical Chemistry B* **2005**, *109*, 11209-14.
(108) Huang, J.-S.; Lin, C.-F. *Journal of Applied Physics* **2008**, *103*, 014304.
(109) Huang, S. Y.; Schlichthorl, G.; Nozik, A. J.; Gratzel, M.; Frank, A. J. *The Journal of Physical Chemistry B* **1997**, *101*, 2576-2582.
(110) Huynh, W. U.; Dittmer, J. J.; Alivisatos, A. P. *Science* **2002**, *295*, 2425-2427.
(111) Imai, H.; Ohgi, H.; Takezawa, Y.; Yahiro, J. *Electroceramics in Japan Viii* **2005**, *301*, 211-214.
(112) Isaeva, U. I.; Imanakunov, B. I. *Inst. Neorg. Fiz. Khim.* **1982**, *4*, 46.
(113) Jensen, J. O. *Spectrochimica Acta Part A: Molecular and Biomolecular Spectroscopy* **2002**, *58*, 1347-1364.
(114) Jin Young, K.; Kwanghee, L.; Coates, N. E.; Moses, D.; Thuc-Quyen, N.; Dante, M.; Heeger, A. J. *Science* **2007**, *317*, 222-5.
(115) Jiu, J. T.; Isoda, S.; Wang, F. M.; Adachi, M. *Journal of Physical Chemistry B* **2006**, *110*, 2087-2092.
(116) Jiu, J. T.; Wang, F. M.; Isoda, S.; Adachi, M. *Chemistry Letters* **2005**, *34*, 1506-1507.
(117) Johnson, O. W.; Ohlsen, W. D.; Kingsbury, P. I. *Physical Review* **1968**, *175*, 1102.
(118) Kaidashev, E. M.; Lorenz, M.; von Wenckstern, H.; Rahm, A.; Semmelhack, H. C.; Han, K. H.; Benndorf, G.; Bundesmann, C.; Hochmuth, H.; Grundmann, M. *Applied Physics Letters* **2003**, *82*, 3901-3.
(119) Kannan, B.; Castelino, K.; Majumdar, A. *Nano Letters* **2003**, *3*, 1729-1733.
(120) Kasuga, T.; Hiramatsu, M.; Hoson, A.; Sekino, T.; Niihara, K. *Langmuir* **1998**, *14*, 3160-3163.
(121) Kasuga, T.; Hiramatsu, M.; Hoson, A.; Sekino, T.; Niihara, K. *Advanced Materials* **1999**, *11*, 1307-1311.
(122) Keis, K.; Lindgren, J.; Lindquist, S.-E.; Hagfeldt, A. *Langmuir* **2000**, *16*, 4688-4694.
(123) Keis, K.; Magnusson, E.; Lindström, H.; Lindquist, S.-E.; Hagfeldt, A. *Solar Energy Materials and Solar Cells* **2002**, *73*, 51-58.
(124) Kelzenberg, M. D.; Turner-Evans, D. B.; Kayes, B. M.; Filler, M. A.; Putnam, M. C.; Lewis, N. S.; Atwater, H. A. *Nano Letters* **2008**, *8*, 710-714.
(125) Kim, J. Y.; Lee, K.; Coates, N. E.; Moses, D.; Nguyen, T. Q.; Dante, M.; Heeger, A. J. *Science* **2007**, *317*, 222-225.
(126) Klimov, V. I. *Applied Physics Letters* **2006**, *89*, 123118.

(127) Koleilat, G. I.; Levina, L.; Shukla, H.; Myrskog, S. H.; Hinds, S.; Pattantyus-Abraham, A. G.; Sargent, E. H. *ACS nano* **2008**, *2*, 833-840.
(128) Kong, F. T.; Dai, S. Y.; Wang, K. J. *Plasma Science & Technology* **2006**, *8*, 531-534.
(129) Kongkanand, A.; Tvrdy, K.; Takechi, K.; Kuno, M.; Kamat, P. V. *Journal of the American Chemical Society* **2008**, *130*, 4007-4015.
(130) Koster, L. J. A.; Mihailetchi, V. D.; Blom, P. W. M. *Applied Physics Letters* **2006**, *88*.
(131) Koster, L. J. A.; van Strien, W. J.; Beek, W. J. E.; Blom, P. W. M. *Advanced Functional Materials* **2007**, *17*, 1297-1302.
(132) Kwong, C. Y.; Choy, W. C. H.; Djurisic, A. B.; Chui, P. C.; Cheng, K. W.; Chan, W. K. *Nanotechnology* **2004**, *15*, 1156-1161.
(133) Lang, D. V. *Journal of Applied Physics* **1974**, *45*, 3023-3032.
(134) Law, M.; Greene, L. E.; Johnson, J. C.; Saykally, R.; Yang, P. D. *Nature Materials* **2005**, *4*, 455-459.
(135) Law, M.; Greene, L. E.; Johnson, J. C.; Saykally, R.; Yang, P. D. *Nature Materials* **2005**, *4*, 455-459.
(136) Law, M.; Greene, L. E.; Johnson, J. C.; Saykally, R.; Yang, P. D. *Nature Materials* **2005**, *4*, 455-459.
(137) Law, M.; Greene, L. E.; Radenovic, A.; Kuykendall, T.; Liphardt, J.; Yang, P. D. *Journal of Physical Chemistry B* **2006**, *110*, 22652-22663.
(138) Lee, Y.-J.; Sounart, T. L.; Scrymgeour, D. A.; Voigt, J. A.; Hsu, J. W. P. *Journal of Crystal Growth* **2007**, *304*, 80-85.
(139) Lee, Y. L.; Chang, C. H. *Journal of Power Sources* **2008**, *185*, 584-588.
(140) Lee, Y. L.; Huang, B. M.; Chien, H. T. *Chemistry of Materials* **2008**, *20*, 6903-6905.
(141) Lenzmann, F.; Kroon, J. M. *Advances in OptoElectronics* **2007**, *2007*, 10.
(142) Lenzmann, F.; Krueger, J.; Burnside, S.; Brooks, K.; Gratzel, M.; Gal, D.; Ruhle, S.; Cahen, D. *The Journal of Physical Chemistry B* **2001**, *105*, 6347-6352.
(143) Leschkies, K. S.; Beatty, T. J.; Kang, M. S.; Norris, D. J.; Aydil, E. *ACS nano* **2009**, *accepted*.
(144) Leschkies, K. S.; Divakar, R.; Basu, J.; Enache-Pommer, E.; Boercker, J. E.; Carter, C. B.; Kortshagen, U. R.; Norris, D. J.; Aydil, E. S. *Nano Letters* **2007**, *7*, 1793-1798.
(145) Leschkies, K. S.; Jacobs, A. G.; Norris, D. J.; Aydil, E. S. *Applied Physics Letters* **2009**, *submitted*.
(146) Li, Q.; Kumar, V.; Li, Y.; Zhang, H.; Marks, T. J.; Chang, R. P. H. *Chemistry of Materials* **2005**, *17*, 1001-1006.
(147) Li, Q. C.; Kumar, V.; Li, Y.; Zhang, H. T.; Marks, T. J.; Chang, R. P. H. *Chemistry of Materials* **2005**, *17*, 1001-1006.
(148) Li, Y.; Meng, G. W.; Zhang, L. D.; Phillipp, F. *Applied Physics Letters* **2000**, *76*, 2011-2013.
(149) Lifshitz, I. M.; Slyozov, V. V. *Journal of Physics and Chemistry of Solids* **1961**, *19*, 35-50.

(150) Liou, S.-C.; Hsiao, C.-S.; Chen, S.-Y. *Journal of Crystal Growth* **2005**, *274*, 438-446.
(151) Lira-Cantu, M.; Norrman, K.; Andreasen, J. W.; Krebs, F. C. *Chemistry of Materials* **2006**, *18*, 5684-5690.
(152) Liu, B.; Aydil, E. S. *Journal of the American Chemical Society* **2009**, *131*, 3985-3990.
(153) Liu, B.; Aydil, E. S. *Journal of the American Chemical Society* **2009**, *131*, 3985-3990.
(154) Liu, B.; Boercker, J. E.; Aydil, E. S. *Nanotechnology* **2008**, *19*.
(155) Liu, D.; Kamat, P. V. *Journal of Physical Chemistry* **1993**, *97*, 10769-10773.
(156) Liu, J.; She, J.; Deng, S.; Chen, J.; Xu, N. *Journal of Physical Chemistry C* **2008**, *112*, 11685-11690.
(157) Liu, J.; She, J. C.; Deng, S. Z.; Chen, J.; Xu, N. S. *Journal of Physical Chemistry C* **2008**, *112*, 11685-11690.
(158) Liu, S.-Y.; Chen, T.; Wan, J.; Ru, G.-P.; Li, B.-Z.; Qu, X.-P. In *Applied Physics A: Materials Science & Processing* 2009; Vol. 94, p 775-780.
(159) Lopez-Luke, T.; Wolcott, A.; Xu, L. P.; Chen, S. W.; Wcn, Z. H.; Li, J. H.; De La Rosa, E.; Zhang, J. Z. *Journal of Physical Chemistry C* **2008**, *112*, 1282-1292.
(160) Lori E. Greene; Matt Law; Joshua Goldberger; Franklin Kim; Justin C. Johnson; Yanfeng Zhang; Richard J. Saykally; Peidong Yang *Angewandte Chemie International Edition* **2003**, *42*, 3031-3034.
(161) Luther, J. M.; Law, M.; Beard, M. C.; Song, Q.; Reese, M. O.; Ellingson, R. J.; Nozik, A. J. *Nano Letters* **2008**, *8*, 3488-3492.
(162) M. H. Huang; Y. Wu; H. Feick; N. Tran; E. Weber; P. Yang *Advanced Materials* **2001**, *13*, 113-116.
(163) Ma, T.; Guo, M.; Zhang, M.; Zhang, Y.; Wang, X. *Nanotechnology* **2007**, *18*, 035605-035605.
(164) Macak, J. M.; Tsuchiya, H.; Ghicov, A.; Schmuki, P. *Electrochemistry Communications* **2005**, *7*, 1133-1137.
(165) Macák, J. M.; Tsuchiya, H.; Schmuki, P. *Angewandte Chemie International Edition* **2005**, *44*, 2100-2102.
(166) Markov, I. V. *Crystal Growth for Beginners*; World Scientific: New Jersey, 2003.
(167) Martinson, A. B. F.; Elam, J. W.; Hupp, J. T.; Pellin, M. J. *Nano Letters* **2007**, *7*, 2183-2187.
(168) Martinson, A. B. F.; Elam, J. W.; Hupp, J. T.; Pelline, M. J. *Nano Letters* **2007**, *published online*.
(169) Martinson, A. B. F.; McGarrah, J. E.; Parpia, M. O. K.; Hupp, J. T. *Physical Chemistry Chemical Physics* **2006**, *8*, 4655-4659.
(170) Maslin, M. *Global warming: a very short introduction*; Oxford University Press: New York, 2004.
(171) Matsumura, M.; Nomura, Y.; Tsubomura, H. *Bulletin of the Chemical Society of Japan* **1977**, *50*, 2533-2537.
(172) McDonald, S. A.; Konstantatos, G.; Zhang, S. G.; Cyr, P. W.; Klem, E. J. D.; Levina, L.; Sargent, E. H. *Nature Materials* **2005**, *4*, 138-U14.

(173) McPeak, K. M.; Baxter, J. B. *Industrial & Engineering Chemistry Research* **2009**, *48*, 5954.
(174) Meyer, B.; Marx, D. *Physical Review B* **2003**, *67*, 035403.
(175) Miyagi, T.; Kamei, M.; Mitsuhashi, T.; Yamazaki, A. *Applied Physics Letters* **2003**, *83*, 1782-1784.
(176) Miyagi, T.; Kamei, M.; Mitsuhashi, T.; Yamazaki, A. *Applied Physics Letters* **2003**, *83*, 1782-1784.
(177) Mor, G. K.; Shankar, K.; Paulose, M.; Varghese, O. K.; Grimes, C. A. *Nano Letters* **2006**, *6*, 215-218.
(178) Nakade, S.; Kanzaki, T.; Wada, Y.; Yanagida, S. *Langmuir* **2005**, *21*, 10803-10807.
(179) Nakamoto, K. *Infrared and Raman Spectra of Inorganic and Coordination Compounds : Applications in Coordination, Organometallic, and Bioinorganic Chemistry* 5ed.; Wiley-Interscience: New York, 1997; Vol. B.
(180) Nazeeruddin, M. K.; De Angelis, F.; Fantacci, S.; Selloni, A.; Viscardi, G.; Liska, P.; Ito, S.; Takeru, B.; Gratzel, M. G. *Journal of the American Chemical Society* **2005**, *127*, 16835-16847.
(181) Nazeeruddin, M. K.; Pechy, P.; Renouard, T.; Zakeeruddin, S. M.; Humphry-Baker, R.; Comte, P.; Liska, P.; Cevey, L.; Costa, E.; Shklover, V.; Spiccia, L.; Deacon, G. B.; Bignozzi, C. A.; Gratzel, M. *Journal of the American Chemical Society* **2001**, *123*, 1613-1624.
(182) Negita, H.; Nishi, Y.; Koga, K. *Spectrochimica Acta* **1965**, *21*, 2144-2145.
(183) Ngamsinlapasathian, S.; Pavasupree, S.; Suzuki, Y.; Yoshikawa, S. *Solar Energy Materials and Solar Cells* **2006**, *90*, 3187-3192.
(184) Nian, J. N.; Teng, H. S. *Journal of Physical Chemistry B* **2006**, *110*, 4193-4198.
(185) Norris, D. J.; Efros, A. L.; Erwin, S. C. *Science* **2008**, *319*, 1776-1779.
(186) *Quantum Dot Photonic Crystals*; Norris, D. J.; Vlasov, Y. A., Eds.; Kluwer: New York, 2003.
(187) Oelkers, E. H.; Helgeson, H. C. *Geochimica et Cosmochimica Acta* **1988**, *52*, 63-85.
(188) Ohsaki, Y.; Masaki, N.; Kitamura, T.; Wada, Y.; Okamoto, T.; Sekino, T.; Niihara, K.; Yanagida, S. *Physical Chemistry Chemical Physics* **2005**, *7*, 4157-4163.
(189) Olofsson, G.; Hepler, L. G. *Journal of Solution Chemistry* **1975**, *4*, 127-143.
(190) Olson, D. C.; Piris, J.; Collins, R. T.; Shaheen, S. E.; Ginley, D. S. *Thin Solid Films* **2006**, *496*, 26-9.
(191) Olson, D. C.; Piris, J.; Collins, R. T.; Shaheen, S. E.; Ginley, D. S. *Thin Solid Films* **2006**, *496*, 26-29.
(192) Olson, D. C.; Shaheen, S. E.; Collins, R. T.; Ginley, D. S. *Journal of Physical Chemistry C* **2007**, *111*, 16670-16678.
(193) Oosterhout, S. D.; van Bavel, S. S.; Wienk, M. M.; Janssen, R. A. J. In *Excitonic Solar Cell Conference* Warwick U.K., 2008, p 96.
(194) Oregan, B.; Gratzel, M. *Nature* **1991**, *353*, 737-740.
(195) Oregan, B.; Gratzel, M. *Nature* **1991**, *353*, 737-740.
(196) O'Regan, B.; Gratzel, M. *Nature* **1991**, *353*, 737.

(197) Oskam, G.; Bergeron, B. V.; Meyer, G. J.; Searson, P. C. *The Journal of Physical Chemistry B* **2001**, *105*, 6867-6873.
(198) Otsuka, A.; Funabiki, K.; Sugiyama, N.; Mase, H.; Yoshida, T.; Minoura, H.; Matsui, M. *Chemistry Letters* **2008**, *37*, 176-177.
(199) Otsuka, A.; Funabiki, K.; Sugiyama, N.; Yoshida, T. *Chemistry Letters* **2006**, *35*, 666-667.
(200) Ozgur, U.; Alivov, Y. I.; Liu, C.; Teke, A.; Reshchikov, M. A.; Dogan, S.; Avrutin, V.; Cho, S. J.; Morkoc, H. *Journal of Applied Physics* **2005**, *98*.
(201) Pacholski, C.; Kornowski, A.; Weller, H. *Angewandte Chemie - International Edition* **2002**, *41*, 1188-1191.
(202) Pan, K.; Zhang, Q. L.; Wang, Q.; Liu, Z. Y.; Wang, D. J.; Li, J. H.; Bai, Y. B. *Thin Solid Films* **2007**, *515*, 4085-4091.
(203) Park, N. G.; van de Lagemaat, J.; Frank, A. J. *The Journal of Physical Chemistry B* **2000**, *104*, 8989-8994.
(204) Park, W. I.; Kim, D. H.; Jung, S.-W.; Yi, G.-C. *Applied Physics Letters* **2002**, *80*, 4232-4234.
(205) Paulose, M.; Shankar, K.; Varghese, O. K.; Mor, G. K.; Grimes, C. A. *Journal of Physics D-Applied Physics* **2006**, *39*, 2498-2503.
(206) Paulose, M.; Shankar, K.; Varghese, O. K.; Mor, G. K.; Hardin, B.; Grimes, C. A. *Nanotechnology* **2006**, *17*, 1446-1448.
(207) Pavasupree, S.; Ngamsinlapasathian, S.; Nakajima, M.; Suzuki, Y.; Yoshikawa, S. *Journal of Photochemistry and Photobiology A-Chemistry* **2006**, *184*, 163-169.
(208) Pavasupree, S.; Ngamsinlapasathian, S.; Suzuki, Y.; Yoshikawa, S. *Journal of Nanoscience and Nanotechnology* **2006**, *6*, 3685-3692.
(209) PBS; http://www.pbs.org/now/science/coal.html: July 23, 2009.
(210) Peet, J.; Kim, J. Y.; Coates, N. E.; Ma, W. L.; Moses, D.; Heeger, A. J.; Bazan, G. C. *Nature Materials* **2007**, *6*, 497-500.
(211) Peiro, A. M.; Ravirajan, P.; Govender, K.; Boyle, D. S.; O'Brien, P.; Bradley, D. D. C.; Nelson, J.; Durrant, J. R. *Journal of Materials Chemistry* **2006**, *16*, 2088-2096.
(212) Peng, B.; Jungmann, G.; Jager, C.; Haarer, D.; Schmidt, H. W.; Thelakkat, M. *Coordination Chemistry Reviews* **2004**, *248*, 1479-1489.
(213) Pesika, N. S.; Hu, Z. S.; Stebe, K. J.; Searson, P. C. *Journal of Physical Chemistry B* **2002**, *106*, 6985-6990.
(214) Pesika, N. S.; Stebe, K. J.; Searson, P. C. *Journal of Physical Chemistry B* **2003**, *107*, 10412-15.
(215) Peter, L. M.; Wijayantha, K. G. U. *Electrochimica Acta* **2000**, *45*, 4543-4551.
(216) Peterson, R. B.; Fields, C. L.; Gregg, B. A. *Langmuir* **2004**, *20*, 5114-5118.
(217) Petit, J. R.; Jouzel, J.; Raynaud, D.; Barkov, N. I.; Barnola, J. M.; Basile, I.; Benders, M.; Chappellaz, J.; Davis, M.; Delaygue, G.; Delmotte, M.; Kotlyakov, V. M.; Legrand, M.; Lipenkov, V. Y.; Lorius, C.; Pepin, L.; Ritz, C.; Saltzman, E.; Stievenard, M. *Nature* **1999**, *399*, 429-436.
(218) Peumans, P.; Uchida, S.; Forrest, S. R. *Nature* **2003**, *425*, 158-162.
(219) Plank, N. O. V.; Snaith, H. J.; Ducati, C.; Bendall, J. S.; Schmidt-Mende, L.; Welland, M. E. *Nanotechnology* **2008**, *19*.

(220) Pradhan, B.; Batabyal, S. K.; Pal, A. J. *Solar Energy Materials and Solar Cells* **2007**, *91*, 769-773.
(221) Qifeng Zhang; Christopher S. Dandeneau; Xiaoyuan Zhou; Guozhong Cao *Advanced Materials* **2009**, *9999*, NA.
(222) Qiu, J. J.; Li, X. M.; He, W. Z.; Park, S. J.; Kim, H. K.; Hwang, Y. H.; Lee, J. H.; Kim, Y. D. *Nanotechnology* **2009**, *20*.
(223) Qiu, J. J.; Li, X. M.; He, W. Z.; Park, S. J.; Kim, H. K.; Hwang, Y. H.; Lee, J. H.; Kim, Y. D. *Nanotechnology* **2009**, *20*.
(224) R. Memming *Photochemistry and Photobiology* **1972**, *16*, 325-333.
(225) R. Memming *Photochemistry and Photobiology* **1972**, *16*, 325-333.
(226) Ravirajan, P.; Haque, S. A.; Durrant, J. R.; Poplavskyy, D.; Bradley, D. D. C.; Nelson, J. *Journal of Applied Physics* **2004**, *95*, 1473-1480.
(227) Ravirajan, P.; Peiro, A. M.; Nazeeruddin, M. K.; Graetzel, M.; Bradley, D. D. C.; Durrant, J. R.; Nelson, J. *Journal of Physical Chemistry B* **2006**, *110*, 7635-7639.
(228) Sahu, D. R.; Lin, S. Y.; Huang, J. L. *Applied Surface Science* **2006**, *252*, 7509-7514.
(229) Saito, M.; Fujihara, S. *Energy & Environmental Science* **2008**, *1*, 280-283.
(230) Sakohara, S.; Ishida, M.; Anderson, M. A. *Journal of Physical Chemistry B* **1998**, *102*, 10169-75.
(231) Sakohara, S.; Tickanen, L. D.; Anderson, M. A. *Journal of Physical Chemistry* **1992**, *96*, 11086.
(232) Sariciftci, N. S.; Braun, D.; Zhang, C.; Srdanov, V. I.; Heeger, A. J.; Stucky, G.; Wudl, F. *Applied Physics Letters* **1993**, *62*, 585-7.
(233) Sayama, K.; Sugihara, H.; Arakawa, H. *Chemistry of Materials* **1998**, *10*, 3825-3832.
(234) Schaller, R. D.; Klimov, V. I. *Physical Review Letters* **2004**, *92*, 186601.
(235) Schmidt-Mende, L.; MacManus-Driscoll, J. L. *Materials Today* **2007**, *10*, 40-48.
(236) Shockley, W.; Queisser, H. J. *Journal of Applied Physics* **1961**, *32*, 510-519.
(237) Shrotriya, V.; Li, G.; Yao, Y.; Chu, C. W.; Yang, Y. *Applied Physics Letters* **2006**, *88*.
(238) Sommeling, P. M.; O'Regan, B. C.; Haswell, R. R.; Smit, H. J. P.; Bakker, N. J.; Smits, J. J. T.; Kroon, J. M.; van Roosmalen, J. A. M. *Journal of Physical Chemistry B* **2006**, *110*, 19191-19197.
(239) Song, J.; Lim, S. *Journal of Physical Chemistry C* **2007**, *111*, 596-600.
(240) Song, M. Y.; Ahn, Y. R.; Jo, S. M.; Kim, D. Y.; Ahn, J. P. *Applied Physics Letters* **2005**, *87*, 113113-113113.
(241) Song, M. Y.; Kim, D. K.; Ihn, K. J.; Jo, S. M.; Kim, D. Y. *Nanotechnology* **2004**, *15*, 1861-1865.
(242) Stumm, W.; Morgan, J. J. *Aquatic Chemistry: Chemical Equilibria and Rates in Natural Waters*; Wiley-Interscience: New York, 1995.
(243) Sugita, M.; Tsuji, M.; Abe, M. *Bulletin of the Chemical Society of Japan* **1990**, *63*, 1978-1984.
(244) Sugunan, A.; Warad, H. C.; Boman, M.; Dutta, J. *Journal of Sol-Gel Science and Technology* **2006**, *39*, 49-56.

(245) Sugunan, A.; Warad, H. C.; Boman, M.; Dutta, J. *Journal of Sol-Gel Science and Technology* **2006**, *39*, 49-56.
(246) Sun, B. Q.; Marx, E.; Greenham, N. C. *Nano Letters* **2003**, *3*, 961-963.
(247) Sun, Y.; Ndifor-Angwafor, N. G.; Riley, D. J.; Ashfold, M. N. R. *Chemical Physics Letters* **2006**, *431*, 352-357.
(248) Sun, Y.; Riley, D. J.; Ashfold, M. N. R. *Journal of Physical Chemistry B* **2006**, *110*, 15186-15192.
(249) Suzuki, Y.; Ngamsinlapasathian, S.; Yoshida, R.; Yoshikawa, S. *Central European Journal of Chemistry* **2006**, *4*, 476-488.
(250) Tada, H. *Journal of the American Chemical Society* **1960**, *82*, 255-263.
(251) Tak, Y.; Yong, K. *The Journal of Physical Chemistry B* **2005**, *109*, 19263-19269.
(252) Takanezawa, K.; Hirota, K.; Wei, Q. S.; Tajima, K.; Hashimoto, K. *Journal of Physical Chemistry C* **2007**, *111*, 7218-7223.
(253) Tan, B.; Toman, E.; Li, Y. G.; Wu, Y. Y. *Journal of the American Chemical Society* **2007**, *129*, 4162-+.
(254) Tan, B.; Wu, Y. Y. *Journal of Physical Chemistry B* **2006**, *110*, 15932-15938.
(255) Tang, H.; Zhu, L.; Ye, Z.; He, H.; Zhang, Y.; Zhi, M.; Yang, F.; Yang, Z.; Zhao, B. *Materials Letters* **2007**, *61*, 1170-1173.
(256) Tani, T.; Watanabe, N.; Takatori, K. *Journal of Nanoparticle Research* **2003**, *5*, 39-46.
(257) Tay, C. B.; Le, H. Q.; Chua, S. J.; Loh, K. P. *Journal of the Electrochemical Society* **2007**, *154*, K45-K50.
(258) Tian, Z. R. R.; Voigt, J. A.; Liu, J.; McKenzie, B.; Xu, H. F. *Journal of the American Chemical Society* **2003**, *125*, 12384-12385.
(259) Tisdale, W. A.; Muntwiler, M.; Norris, D. J.; Aydil, E. S.; Zhu, X. Y. *The Journal of Physical Chemistry C* **2008**, *112*, 14682-14692.
(260) Tokumoto, M. S.; Briois, V.; Santilli, C. V.; Pulcinelli, S. H. *Journal of Sol-Gel Science and Technology* **2003**, *26*, 547-551.
(261) Tokumoto, M. S.; Pulcinelli, S. H.; Santilli, C. V.; Briois, V. *Journal of Physical Chemistry B* **2003**, *107*, 568-74.
(262) Tsai, C. C.; Teng, H. S. *Chemistry of Materials* **2006**, *18*, 367-373.
(263) Tsukasa Yoshida; Jingbo Zhang; Daisuke Komatsu; Seiichi Sawatani; Hideki Minoura; Thierry Pauporté; Daniel Lincot; Torsten Oekermann; Derck Schlettwein; Hirokazu Tada; Dieter Wöhrle; Kazumasa Funabiki; Masaki Matsui; Hidetoshi Miura; Hisao Yanagi *Advanced Functional Materials* **2009**, *19*, 17-43.
(264) Uchida, S.; Chiba, R.; Tomiha, M.; Masaki, N.; Shirai, M. *Electrochemistry* **2002**, *70*, 418-420.
(265) Usami, A. *Chemical Physics Letters* **1997**, *277*, 105-108.
(266) van de Lagemaat, J.; Frank, A. J. *The Journal of Physical Chemistry B* **2001**, *105*, 11194-11205.
(267) Vanlaeke, P.; Swinnen, A.; Haeldermans, I.; Vanhoyland, G.; Aernouts, T.; Cheyns, D.; Deibel, C.; D'Haen, J.; Heremans, P.; Poortmans, J.; Manca, J. V. *Solar Energy Materials and Solar Cells* **2006**, *90*, 2150-2158.
(268) Vayssieres, L. *Advanced Materials* **2003**, *15*, 464-466.
(269) Vayssieres, L. *Advanced Materials* **2003**, *15*, 464-466.

(270) Vayssieres, L. *Advanced Materials* **2003**, *15*, 464-466.
(271) Vayssieres, L.; Keis, K.; Hagfeldt, A.; Lindquist, S. E. *Chemistry of Materials* **2001**, *13*, 4395.
(272) Vayssieres, L.; Keis, K.; Lindquist, S. E.; Hagfeldt, A. *Journal of Physical Chemistry B* **2001**, *105*, 3350-3352.
(273) Vayssieres, L.; Keis, K.; Lindquist, S. E.; Hagfeldt, A. *Journal of Physical Chemistry B* **2001**, *105*, 3350-3352.
(274) Verges, M. A.; Mifsud, A.; Serna, C. J. *Journal of the Chemical Society-Faraday Transactions* **1990**, *86*, 959-963.
(275) Viswanatha, R.; Sapra, S.; Satpati, B.; Satyam, P. V.; Dev, B. N.; Sarma, D. D. *Journal of Materials Chemistry* **2004**, *14*, 661-668.
(276) Vogel, R.; Hoyer, P.; Weller, H. *Journal of Physical Chemistry* **1994**, *98*, 3183-3188.
(277) Wagner, C. *Z. Elektrochem* **1961**, *65*, 581.
(278) Wang, H.; Oey, C. C.; Djurisic, A. B.; Xie, M. H.; Leung, Y. H.; Man, K. K. Y.; Chan, W. K.; Pandey, A.; Nunzi, J. M.; Chui, P. C. *Applied Physics Letters* **2005**, *87*.
(279) Wang, P.; Zakeeruddin, S. M.; Comte, P.; Charvet, R.; Humphry-Baker, R.; Gratzel, M. *The Journal of Physical Chemistry B* **2003**, *107*, 14336-14341.
(280) Wang, P.; Zakeeruddin, S. M.; Moser, J. E.; Nazeeruddin, M. K.; Sekiguchi, T.; Gratzel, M. *Nature Materials* **2003**, *2*, 402-407.
(281) Wang, S. F.; Tseng, T. Y.; Wang, Y. R.; Wang, C. Y.; Lu, H. C. *Ceram. Int.* **2009**, *35*, 1255-1260.
(282) Wang, Z. S.; Kawauchi, H.; Kashima, T.; Arakawa, H. *Coordination Chemistry Reviews* **2004**, *248*, 1381-1389.
(283) Watanabe, T.; Hayashi, H.; Imai, H. *Solar Energy Materials and Solar Cells* **2006**, *90*, 640-648.
(284) Wei, M. D.; Konishi, Y.; Zhou, H. S.; Sugihara, H.; Arakawa, H. *Journal of the Electrochemical Society* **2006**, *153*, A1232-A1236.
(285) Wei, M. D.; Qi, Z. M.; Ichihara, M.; Zhou, H. S. *Acta Materialia* **2008**, *56*, 2488-2494.
(286) Wessels, K.; Maekawa, M.; Rathousky, J.; Yoshida, T.; Wark, M.; Oekermann, T. *Microporous and Mesoporous Materials* **2008**, *111*, 55-61.
(287) Willander, M.; Yang, L. L.; Wadeasa, A.; Ali, S. U.; Asif, M. H.; Zhao, Q. X.; Nur, O. *Journal of Materials Chemistry* **2009**, *19*, 1006-1018.
(288) Womelsdorf, H.; Hoheisel, W.; Passing, G. Germany, 2000.
(289) Wong, E. M.; Bonevich, J. E.; Searson, P. C. *Journal of Physical Chemistry B* **1998**, *102*, 7770-5.
(290) Wu, J.-J.; Chen, G.-R.; Yang, H.-H.; Ku, C.-H.; Lai, J.-Y. *Applied Physics Letters* **2007**, *90*, 213109.
(291) Wu, J.-J.; Chen, G.-R.; Yang, H.-H.; Ku, C.-H.; Lai, J.-Y. *Applied Physics Letters* **2007**, *90*, 213109.
(292) Wu, W.; Hu, G.; Cui, S.; Zhou, Y.; Wu, H. *Crystal Growth & Design* **2008**, *8*, 4014-4020.

(293) Wu, Y.; Wadia, C.; Ma, W. L.; Sadtler, B.; Alivisatos, A. P. *Nano Letters* **2008**, *8*, 2551-2555.
(294) Y. Sun; G. M. Fuge; N. A. Fox; D. J. Riley; M. N. R. Ashfold *Advanced Materials* **2005**, *17*, 2477-2481.
(295) Yagi, E.; Hasiguti, R. R.; Aono, M. *Physical Review B* **1996**, *54*, 7945.
(296) Yamabi, S.; Imai, H. *Journal of Materials Chemistry* **2002**, *12*, 3773-3778.
(297) Yan, X.; Li, Z.; Chen, R.; Gao, W. *Crystal Growth & Design* **2008**, *8*, 2406-2410.
(298) Yanazawa, H.; Mastunaga, H.; Itoh, H.; Nakai, K.; Suzuki, I. *Journal of Vacuum Science & Technology B: Microelectronics and Nanometer Structures* **2002**, *20*, 1833-1835.
(299) Yang, J. J.; Jin, Z. S.; Wang, X. D.; Li, W.; Zhang, J. W.; Zhang, S. L.; Guo, X. Y.; Zhang, Z. J. *Dalton Transactions* **2003**, 3898-3901.
(300) Yongfang, L.; Fenglian, B.; Chang, H.; Qingguo, H.; Youjun, H.; Chunhe, Y.; Yuqin, D.; Lingxuan, W.; Jianping, Y. *Solar Energy Materials and Solar Cells* **2006**, *90*, 1815-27.
(301) Yoon, J. H.; Jang, S. R.; Vittal, R.; Lee, J.; Kim, K. J. *Journal of Photochemistry and Photobiology A-Chemistry* **2006**, *180*, 184-188.
(302) Yu, G.; Gao, J.; Hummelen, J. C.; Wudl, F.; Heeger, A. J. *Science* **1995**, *270*, 1789-91.
(303) Yu, G.; Heeger, A. J. *Journal of Applied Physics* **1995**, *78*, 4510-15.
(304) Yu, P. R.; Zhu, K.; Norman, A. G.; Ferrere, S.; Frank, A. J.; Nozik, A. J. *Journal of Physical Chemistry B* **2006**, *110*, 25451-25454.
(305) Yu, Y. X.; Xu, D. S. *Applied Catalysis B-Environmental* **2007**, *73*, 166-171.
(306) Zaban, A.; Greenshtein, M.; Bisquert, J. *Chemphyschem* **2003**, *4*, 859-864.
(307) Zaban, A.; Micic, O. I.; Gregg, B. A.; Nozik, A. J. *Langmuir* **1998**, *14*, 3153-3156.
(308) Zeng, T. W.; Lin, Y. Y.; Lo, H. H.; Chen, C. W.; Chen, C. H.; Liou, S. C.; Huang, H. Y.; Su, W. F. *Nanotechnology* **2006**, *17*, 5387-5392.
(309) Zhang, R.; Kumar, S.; Zou, S.; Kerr, L. L. *Crystal Growth & Design* **2007**, *8*, 381-383.
(310) Zhang, Y.; Xie, T. F.; Jiang, T. F.; Wei, X.; Pang, S.; Wang, X.; Wang, D. *Nanotechnology* **2009**, *20*.
(311) Zhao, Y. N.; Jin, J.; Yang, X. Q. *Materials Letters* **2007**, *61*, 384-388.
(312) Zhao, Y. N.; Lee, U. H.; Suh, M.; Kwon, Y. U. *Bulletin of the Korean Chemical Society* **2004**, *25*, 1341-1345.
(313) Zhong Lin, W. *Journal of Physics: Condensed Matter* **2004**, *16*, 829-58.
(314) Zhong, Q. P.; Matijevic, E. *Journal of Materials Chemistry* **1996**, *6*, 443-447.
(315) Zhou, Y.; Wu, W.; Hu, G.; Wu, H.; Cui, S. *Materials Research Bulletin* **2008**, *43*, 2113-2118.
(316) Zhu, H. Y.; Gao, X. P.; Lan, Y.; Song, D. Y.; Xi, Y. X.; Zhao, J. C. *Journal of the American Chemical Society* **2004**, *126*, 8380-8381.
(317) Zhu, H. Y.; Lan, Y.; Gao, X. P.; Ringer, S. P.; Zheng, Z. F.; Song, D. Y.; Zhao, J. C. *Journal of the American Chemical Society* **2005**, *127*, 6730-6736.
(318) Zhu, K.; Neale, N. R.; Miedaner, A.; Frank, A. J. *Nano Letters* **2007**, *7*, 69-74.
(319) Zhu, K.; Neale, N. R.; Miedaner, A.; Frank, A. J. *Nano Letters* **2007**, *7*, 69-74.

Appendix 1: Derivation of ZnO Nanowire Growth Mechanism Model

Referring to Figure 5.10 in Chapter 5 the following differential equations describe the depletion of Zn^{2+}, HMT, Zn-HMT^{2+}, and Zn-HMT-Zn^{4+} ,

$$\frac{d[HMT]}{dt} = -k_{1f}[Zn][HMT] + k_{1r}[ZnHMT] \quad \text{(A.1)}$$

$$\frac{d[Zn]}{dt} = -k_{1f}[Zn][HMT] + k_{1r}[ZnHMT] - k_{3f}[Zn][ZnHMT] + k_{3r}[Zn_2HMT] \quad \text{(A.2)}$$

$$\frac{d[ZnHMT]}{dt} = k_{1f}[Zn][HMT] - k_{1r}[ZnHMT] - k_2[ZnHMT] - k_{3f}[Zn][ZnHMT] + k_{3r}[Zn_2HMT] \quad \text{(A.3)}$$

$$\frac{d[Zn_2HMT]}{dt} = k_{3f}[Zn][ZnHMT] - k_{3r}[Zn_2HMT] - k_4[Zn_2HMT] \quad \text{(A.4).}$$

Assuming a pseudo steady-state of the Zn-HMT^{2+} and Zn-HMT-Zn^{4+} intermediates (i.e. equations A.3 and A.4 are equal to zero) the Zn-HMT-Zn^{4+} can be written as function of Zn-HMT^{2+} and Zn^{2+} and the Zn-HMT^{2+} can be written as a function of Zn^{2+} and HMT,

$$[Zn_2HMT] = \frac{k_{3f}[Zn][ZnHMT]}{k_{3r} + k_4} \quad \text{(A.5)}$$

$$[ZnHMT] = \frac{k_{1f}[Zn][HMT]}{k_{1r} + k_2 + \left[k_{3f} - \frac{k_{3r}k_{3f}}{k_{3r} + k_4}\right][Zn]} \quad \text{(A.6)}$$

Substituting these into the equations A.1 and A.2 and then after some mathematical manipulation the depletion rate of Zn^{2+} and HMT can be written as.

$$\frac{d[HMT]}{dt} = -[Zn][HMT]\left(\frac{K_1 + K_2[Zn]}{K_3 + K_4[Zn]}\right) \quad \text{(A.7)}$$

$$\frac{d[Zn]}{dt} = -[Zn][HMT]\left(\frac{K_1 + 2K_2[Zn]}{K_3 + K_4[Zn]}\right) \quad \text{(A.8)}$$

Where,

$$K_1 = k_{1f} k_2 \tag{A.9}$$

$$K_2 = k_{1f}\left(\frac{k_{3f} k_4}{k_{3r} + k_4}\right) \tag{A.10}$$

$$K_3 = k_{1r} + k_2 \tag{A.11}$$

$$K_4 = \left(\frac{k_{3f} k_4}{k_{3r} + k_4}\right) \tag{A.12}.$$